

ADVANCED STEEL CONSTRUCTION

An International Journal

Volume 16 Number 1

March 2020

CONTENTS

Technical Papers

Mechanical Performance of Welded Hollow Spherical Joints at Elevated Temperatures

Hong-bo Liu, Ying-jie Zhang, Lan Wang, Zhi-hua Chen

Axial Compressive Behavior of Self-Stressing Steel Slag Aggregate Concrete Filled Steel Tubular Columns with Bond-Slip Damage

Feng Yu, Chi Yao, Yi Hu, Yuan Fang, Kang Niu and Guo-sheng Xiang

Multi Storey Composite Framed Structures Due To Edge Column Loss

Guo-qiang Li, Jing-zhou Zhang and Jian Jiang

Shear Resistance of Novel Perforated Shaped Steel-Engineered Cementitious Composite (ECC) Connectors

Li-min Tian, Ting Liu, Tian-ji Li, and Hai-liang Lin

Influence of The Core-Restrainer Clearance on The Mechanical Performance of Sandwich Buckling-Restrained Braces

Lu-qi Xie, Jing Wu, Jian-hua Shi and Yun-qing Zhu

Lateral Torsional Buckling Strength of Steel I Beams Within Preflexed Beams in Pre Bending Stage

Lin-jie Tian, Zhe Li, Ming Yang, Shan Chang and Jian-qi Qian

In-Plane Nonlinear Analysis and Buckling of Shear-Deformable Circular Arches

Gen-shu Tong, Yong-lin Pi and Wei Gao

Experimental Study on Bearing Capacity of Austenitic Stainless Steel Lipped Channel Columns

Sheng-gang Fan, Run-min Ding, Yun-long Han, Mei-he Chen, Cheng-liang Liu and Yue-lin Tao

Experimental Evaluation of The Full-Range Behaviour of Steel Beam-To-Column Connections

Shen Yan, Kim J.R. Rasmussen, Lu-li Jiang, Chen Zhu and Hao Zhang

Seismic Responses of Rc Braced Frames with Buckling-Restrained Braces Connected to Corbels

An-chin Wu, Keh-chyuan Tsai, Ting-li Lin, Ching-yi Tsai and Kung-juin Wang

Copyright © 2020 by :

The Hong Kong Institute of Steel Construction

Website: <http://www.hkisc.org>

ISSN 1816-112X

Science Citation Index Expanded, Materials Science Citation Index and ISI Alerting

Cover: Peak Galleria, Hong Kong, China

e-copy of IJASC is free to download at "www.ascjournal.com" in internet and mobile apps.

ADVANCED STEEL CONSTRUCTION

VOL.16, NO.1 (2020)

ADVANCED STEEL CONSTRUCTION

an International Journal

ISSN 1816-112X

Volume 16 Number 1

March 2020



Editors-in-Chief

S.L. Chan, *The Hong Kong Polytechnic University, Hong Kong, China*

W.F. Chen, *University of Hawaii at Manoa, USA*

R. Zandonini, *Trento University, Italy*



ISSN 1816-112X

Science Citation Index Expanded,
Materials Science Citation Index
and ISI Alerting

EDITORS-IN-CHIEF

**Asian Pacific, African
and organizing Editor**
S.L. Chan
*The Hong Kong Poly. Univ.,
Hong Kong, China*

American Editor
W.F. Chen
Univ. of Hawaii at Manoa, USA

European Editor
R. Zandonini
Trento Univ., Italy

ASSOCIATE EDITORS

Y.P. Liu
The Hong Kong Poly. Univ., Hong Kong, China

S.W. Liu
Sun Yat-Sen Univ., China

INTERNATIONAL EDITORIAL BOARD

F.G. Albermani
Central Queensland Univ., Australia

I. Burgess
Univ. of Sheffield, UK

F.S.K. Bijlaard
Delft Univ. of Technology, The Netherlands

R. Bjorhovde
The Bjorhovde Group, USA

M.A. Bradford
The Univ. of New South Wales, Australia

D. Camotim
Technical Univ. of Lisbon, Portugal

C.M. Chan
Hong Kong Univ. of Science & Technology, Hong Kong, China

T.H.T. Chan
Queensland Univ. of Technology, Australia

T.M. Chan
The Hong Kong Poly. Univ., Hong Kong, China

Z.H. Chen
Tianjin Univ., China

S.P. Chiew
Nanyang Technological Univ., Singapore

W.K. Chow
The Hong Kong Poly. Univ., Hong Kong, China

G.G. Deierlein
Stanford Univ., California, USA

L. Dezi
Univ. of Ancona, Italy

D. Dubina
The Politehnica Univ. of Timisoara, Romania

R. Greiner
Technical Univ. of Graz, Austria

L. Gardner
Imperial College of Science, Technology and Medicine, UK

Y. Goto
Nagoya Institute of Technology, Japan

L.H. Han
Tsinghua Univ. China

S. Herion
University of Karlsruhe, Germany

G.W.M. Ho
*Ove Arup & Partners Hong Kong Ltd., Hong Kong,
China*

B.A. Izzuddin
*Imperial College of Science, Technology and
Medicine, UK*

J.P. Jaspart
Univ. of Liege, Belgium

S. A. Jayachandran
IIT Madras, Chennai, India

S.E. Kim
Sejong Univ., South Korea

S. Kitipornchai
The Univ., of Queensland, Australia

D. Lam
Univ. of Bradford, UK

H.F. Lam
City Univ. of Hong Kong, Hong Kong, China

G.Q. Li
Tongji Univ., China

J.Y.R. Liew
National Univ. of Singapore, Singapore

E.M. Lui
Syracuse Univ., USA

Y.L. Mo
Univ. of Houston, USA

J.P. Muzeau
CUST, Clermont Ferrand, France

D.A. Nethercot
*Imperial College of Science, Technology and
Medicine, UK*

Y.Q. Ni
The Hong Kong Poly. Univ., Hong Kong, China

D.J. Oehlers
The Univ. of Adelaide, Australia

J.L. Peng
Yunlin Uni. of Science & Technology, Taiwan, China

K. Rasmussen
The Univ. of Sydney, Australia

J.M. Rotter
The Univ. of Edinburgh, UK

C. Scawthorn
Scawthorn Porter Associates, USA

P. Schaumann
Univ. of Hannover, Germany

Y.J. Shi
Tsinghua Univ., China

G.P. Shu
Southeast Univ. China

L. Simões da Silva
*Department of Civil Engineering, University of
Coimbra, Portugal*

J.G. Teng
The Hong Kong Poly. Univ., Hong Kong, China

G.S. Tong
Zhejiang Univ., China

K.C. Tsai
National Taiwan Univ., Taiwan, China

C.M. Uang
Univ. of California, USA

B. Uy
University of Western Sydney, Australia

M. Veljkovic
Univ. of Lulea, Sweden

F. Wald
Czech Technical Univ. in Prague, Czech

Y.C. Wang
The Univ. of Manchester, UK

Y.L. Xu
The Hong Kong Poly. Univ., Hong Kong, China

D. White
Georgia Institute of Technology, USA

E. Yamaguchi
Kyushu Institute of Technology, Japan

Y.B. Yang
National Taiwan Univ., Taiwan, China

Y.Y. Yang
China Academy of Building Research, Beijing, China

B. Young
The Univ. of Hong Kong, Hong Kong, China

X.L. Zhao
Monash Univ., Australia

X.H. Zhou
Chongqing University, China

Z.H. Zhou
The Hong Kong Poly. Univ., Hong Kong, China

S.Y. Zhu
The Hong Kong Poly. Univ., Hong Kong, China

R.D. Ziemian
Bucknell Univ., USA

Cover: Peak Galleria, Hong Kong, China

e-copy of IJASC is free to download at "www.ascjournal.com" in internet and mobile apps.

General Information

Advanced Steel Construction, an international journal

Aims and scope

The International Journal of Advanced Steel Construction provides a platform for the publication and rapid dissemination of original and up-to-date research and technological developments in steel construction, design and analysis. Scope of research papers published in this journal includes but is not limited to theoretical and experimental research on elements, assemblages, systems, material, design philosophy and codification, standards, fabrication, projects of innovative nature and computer techniques. The journal is specifically tailored to channel the exchange of technological know-how between researchers and practitioners. Contributions from all aspects related to the recent developments of advanced steel construction are welcome.

Disclaimer. No responsibility is assumed for any injury and / or damage to persons or property as a matter of products liability, negligence or otherwise, or from any use or operation of any methods, products, instructions or ideas contained in the material herein.

Subscription inquiries and change of address. Address all subscription inquiries and correspondence to Member Records, IJASC. Notify an address change as soon as possible. All communications should include both old and new addresses with zip codes and be accompanied by a mailing label from a recent issue. Allow six weeks for all changes to become effective.

The Hong Kong Institute of Steel Construction

HKISC

c/o Department of Civil and Environmental Engineering,
The Hong Kong Polytechnic University,
Hungghom, Kowloon, Hong Kong, China.

Tel: 852- 2766 6047 Fax: 852- 2334 6389

Email: ceslchan@polyu.edu.hk Website: <http://www.hkisc.org/>

ISSN 1816-112X

Science Citation Index Expanded, Materials Science Citation Index and ISI Alerting

Copyright © 2020 by:

The Hong Kong Institute of Steel Construction.



ISSN 1816-112X

Science Citation Index Expanded,
Materials Science Citation Index and
ISI Alerting

EDITORS-IN-CHIEF

Asian Pacific, African and organizing Editor

S.L. Chan

*The Hong Kong Polyt. Univ.,
Hong Kong, China*

Email: ceslchan@polyu.edu.hk

American Editor

W.F. Chen

Univ. of Hawaii at Manoa, USA

Email: waifah@hawaii.edu

European Editor

R. Zandonini

Trento Univ., Italy

Email: riccardo.zandonini@ing.unitn.it

Advanced Steel Construction

an international journal

VOLUME 16 NUMBER 1

March 2020

Technical Papers

Mechanical Performance of Welded Hollow Spherical Joints at Elevated Temperatures 1

Hong-bo Liu, Ying-jie Zhang, Lan Wang, Zhi-hua Chen*

Axial Compressive Behavior of Self-Stressing Steel Slag Aggregate Concrete Filled Steel Tubular Columns with Bond-Slip Damage 13

Feng Yu, Chi Yao, Yi Hu, Yuan Fang, Kang Niu and Guo-sheng Xiang*

Multi Storey Composite Framed Structures Due To Edge Column Loss 20

Guo-qiang Li, Jing-zhou Zhang and Jian Jiang*

Shear Resistance of Novel Perforated Shaped Steel-Engineered Cementitious Composite (ECC) Connectors 30

Li-min Tian, Ting Liu, Tian-ji Li, and Hai-liang Lin*

Influence of The Core-Restrainer Clearance on The Mechanical Performance of Sandwich Buckling-Restrained Braces 37

Lu-qi Xie, Jing Wu, Jian-hua Shi and Yun-qing Zhu*

Lateral Torsional Buckling Strength of Steel I Beams Within Preflexed Beams in Pre Bending Stage 47

Lin-jie Tian, Zhe Li, Ming Yang, Shan Chang and Jian-qi Qian*

In-Plane Nonlinear Analysis and Buckling of Shear-Deformable Circular Arches 55

Gen-shu Tong, Yong-lin Pi and Wei Gao*

Experimental Study on Bearing Capacity of Austenitic Stainless Steel Lipped Channel Columns 65

Sheng-gang Fan, Run-min Ding, Yun-long Han, Mei-he Chen, Cheng-liang Liu and Yue-lin Tao*

Experimental Evaluation of The Full-Range Behaviour of Steel Beam-To-Column Connections 77

Shen Yan, Kim J.R. Rasmussen, Lu-li Jiang, Chen Zhu and Hao Zhang*

Seismic Responses of Rc Braced Frames with Buckling-Restrained Braces Connected to Corbels 85

An-chin Wu, Keh-chyuan Tsai, Ting-li Lin, Ching-yi Tsai and Kung-juin Wang*

MECHANICAL PERFORMANCE OF WELDED HOLLOW SPHERICAL JOINTS AT ELEVATED TEMPERATURES

Hong-bo Liu^{1,3,4*}, Ying-jie Zhang³, Lan Wang², Zhi-hua Chen^{1,3,4}

¹ State Key Laboratory of Hydraulic Engineering Simulation and Safety, Tianjin University, Tianjin 300072, China

² Tianjin Fire Research Institute of MEM, Tianjin 300000, China

³ Department of Civil Engineering, Tianjin University, Tianjin 300072, China

⁴ Key Laboratory of Coast Civil Structure and Safety, Ministry of Education (Tianjin University), Tianjin 300072, China

* (Corresponding author: E-mail: hbliu@tju.edu.cn)

ABSTRACT

Welded hollow spherical joints (WHSJs) have been extensively applied to spatial grid structures. However, the failure mechanism and assessment method of WHSJ under fire conditions have been rarely studied. In this study, the failure mechanism and high-temperature attenuation pattern of the axial compression performance of WHSJ at fire-induced high temperatures were explored via high-temperature axial compression experiments by using 18 specimens. A finite element (FE) model was constructed by using the ABAQUS software. The reliability of this FE model was verified by experimental results. The influencing patterns of the type of steel, stiffening rib arrangement, size of the WHSJ, and the test temperature on the high-temperature axial compression performance of WHSJ were discussed through the FE model. A simplified calculation method of the compressive bearing capacity of WHSJ at elevated temperatures was proposed on the basis of the test data and the FE parameterized analysis results. The findings of the simplified calculation method conformed to experimental and numerical simulation results.

ARTICLE HISTORY

Received: 11 March 2019
Revised: 11 August 2019
Accepted: 14 September 2019

KEYWORDS

Welded hollow spherical joint;
Under fire;
Axial compression experiment;
Compressive bearing capacity;
Initial axial stiffness;
High-temperature attenuation mechanism

Copyright © 2020 by The Hong Kong Institute of Steel Construction. All rights reserved.

1. Introduction

Joints in the spatial grid structure mainly include WHSJ, bolted hollow spherical joints, hub-type joints, cast steel joints, tubular joints, and Temcor joints (Fig. 1) [1,2,3,4,5]. WHSJ were proposed by Professor Liu [6] from Tianjin University in 1965. With a clear load path and convenient connection with other components, WHSJ have become one of the joint forms used mostly in China.

Fire hazards constitute the main disaster that causes architectural structural damages. At elevated temperatures attributed to a fire disaster, the mechanical properties of steel materials change remarkably. The yield strength of steel materials at 400 °C decreases to 50% of that at room temperature, and steel materials lose their bearing capacity at temperatures higher than 600 °C [7]. The failure of WHSJ during fire disasters may cause the collapse of overall structures. Therefore, the study of the mechanical properties of WHSJ at elevated temperatures plays an important role in examining the overall performance of spatial grid structures that use these joints during fire disasters.



(a) Welded hollow spherical joint (b) Bolted hollow spherical joint

Fig. 1 Typical joint forms used in the spatial grid structure.

Studies on WHSJ have mainly focused on the mechanical properties of WHSJ at room temperature, and a relatively ideal analysis and design method has been established. Xue [8] studied the failure mechanism of WHSJ with round steel tubes under compressive load and proposed a practical calculation method of its bearing capacity. Ding et al. [9] constructed the tensile and compressive mechanical calculation models of WHSJ with circular steel tubes. Han [10] performed tests and numerical simulations and developed a calculation formula of the tensile and compressive bearing capacity of WHSJ with round steel

tubes through regression analysis. The diameter limit is extended to 900 mm. Li [11] examined the influences of axial force, bending moment, and their combination on the bearing capacity of WHSJ with round steel tubes and proposed a relevant formula. Liu et al. [12] suggested calculation formulas for the tensile and compressive bearing capacity of WHSJ with H-shaped steel tubes through experimental studies and numerical simulation. Han and Liu [13] introduced a theory and practical formula of the initial rigidity of WHSJ and analyzed the influences of joint rigidity on the overall reticulated shell. Zhao [14] examined the effects of WHSJ on the mechanical properties of a single-layered reticulated structure through numerical simulation and found that such effects are related to structure size. Zhao and Wang et al. [15,16] analyzed the influences of welded residual stress on the mechanical properties of WHSJ through numerical simulation. Zhao [17,18] discussed the effects of corrosion at different places on the bending rigidity of WHSJ through a series of nonlinear numerical analyses. The probabilistic distribution model of corroded WHSJ with random pit corrosion has also been proposed. Furthermore, the design methods of WHSJ are introduced to the Technical Regulation of the Space Grid Structure (JGJ7-2010) [19].

The performance of WHSJ at elevated temperatures has been rarely investigated. Liu and Lu et al. [20,21,22] experimentally studied the post-fire residual load-bearing capacity and initial axial stiffness of WHSJ. The design methods of predicting the post-fire residual bearing capacity of WHSJ under axial compression or eccentric compression have also been proposed. Xue [23] performed a high-temperature axial compression experimental study on WHSJ and obtained the temperature field distribution and load-displacement relation curve of these joints.

The bearing capacity of WHSJ at elevated temperatures has yet to be quantitatively analyzed. The rigidity of WHSJ at elevated temperatures has been rarely explored. In this study, the mechanical behaviors of WHSJ at elevated temperatures, such as initial axial stiffness, yield loads, and load-bearing capacities, were examined through tests and numerical simulation. A simplified calculation formula of the bearing capacity of the WHSJ at elevated temperatures was proposed on the basis of numerical analysis results.

2. Experimental investigation

2.1. Test specimen design

In consideration of various parameters, including type of steel, stiffening

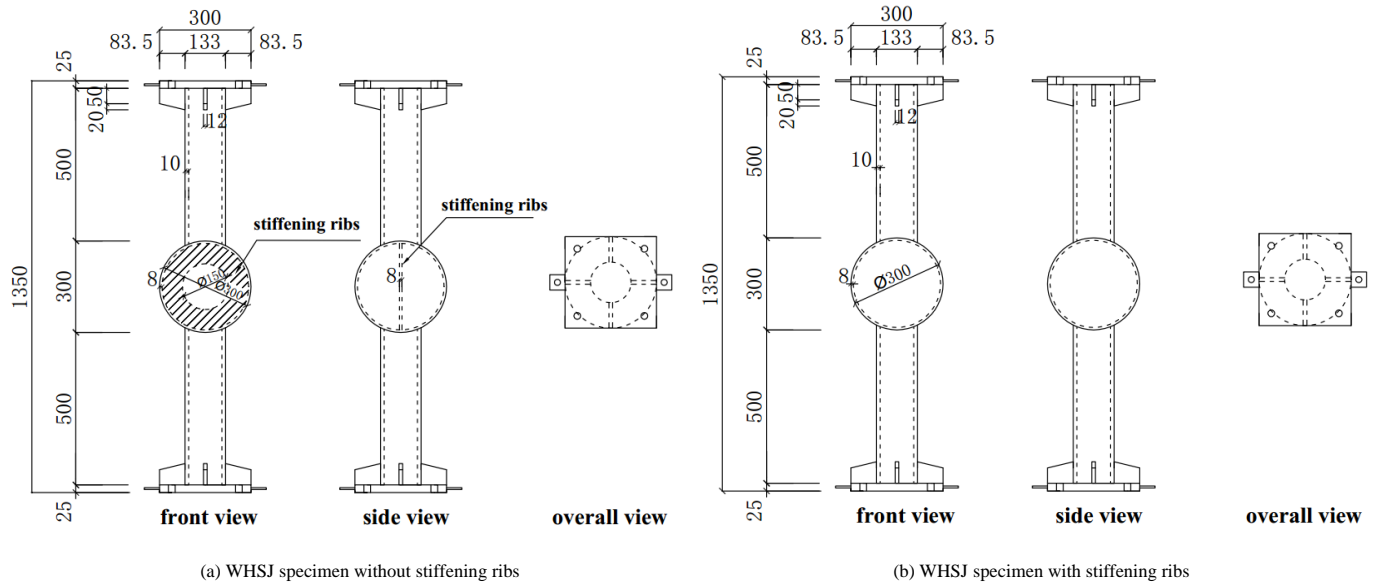


Fig. 2 Dimension of the specimens (unit: mm)

Table 1
Specimen parameters

Group No.	Joint No.	D /mm	t /mm	Steel grade	Stiffening ribs present	$T/^\circ\text{C}$	Quantity
1	WS-345-20	300	8	Q345	No	20	1
2	WS-345-300	300	8	Q345	No	300	3
3	WS-345-500	300	8	Q345	No	500	3
4	WS-345-700	300	8	Q345	No	700	3
5	WSR-345-20	300	8	Q345	Yes	20	1
6	WSR-345-500	300	8	Q345	Yes	500	3
7	WS-235-20	300	8	Q235	No	20	1
8	WS-235-500	300	8	Q235	No	500	3

Specimens were named according to a certain principle.

For example, in WS-345-300-1 or WSR-345-300-1, WS and WSR denote the joint specimen without stiffening ribs and with stiffening ribs, respectively; 345 represents the steel grade of the specimens (Q345); 300 reflects the test temperature (300 $^\circ\text{C}$); and 1 indicates the number of parallel specimens, which correspond to the first parallel specimen. The detailed information of the specimens is shown in Table 1. The same batch of the steel materials was chosen to test the material properties. The results are presented in Table 2.

Table 2
Material properties

Specimen No.	E/GPa	f_y /MPa	f_u /MPa	δ
Q235-1	204.9	298.12	457.19	41.1%
Q235-2	205.7	302.45	449.76	37.3%
Q235-3	204.2	291.69	445.15	38.2%
Average	204.9	297.42	450.70	38.9%
Q345-1	206.4	390.15	605.14	35.2%
Q345-2	204.7	386.70	600.45	34.3%
Q345-3	205.6	388.86	599.12	34.0%
Average	205.6	388.57	601.57	34.5%

2.2. Experimental scheme

The experiment involved two steps. First, the specimens were heated from

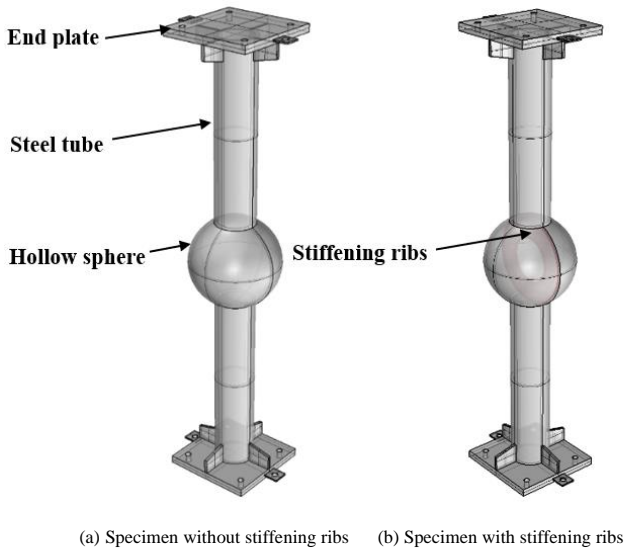


Fig. 3 3D visualization of the WHSJ specimens

rib arrangement, and test temperature, 18 WHSJ specimens were designed and prepared. All of the specimens were composed of hollow spheres, steel tubes, and end plates (Fig. 2 and Fig. 3). The outer diameter (D) and the wall thickness (t) of the hollow sphere were 300 and 8 mm, respectively. The outer diameter (d), the wall thickness (t_s), and the length (L) of the steel tube were 133, 10, and 500 mm, respectively. The end plate size was 300 mm \times 300 mm \times 25 mm.

room temperature to high temperatures. Second, the high temperature was kept, and the axial compression load was applied. The specimens were heated in a temperature-controlled furnace (Fig. 4). Two thermocouples were placed in a furnace cavity to test air temperature in the furnace. The joint surface was bonded to three thermocouples to test the temperatures of the joint at different positions. The furnace temperature during the heating process was initially raised to 80% of the target temperature at a rate of 10 °C/min and then maintained for 10 min. Subsequently, the furnace temperature was raised to the target temperature at a rate of 5 °C/min and then maintained for 30 min. This heating process was adopted to ensure the uniform temperature distribution of the specimens (Fig. 5). In the experiment, air temperature was basically consistent with the joint surface temperature. Axial compressive load was applied to the heated specimens by using a 1200 kN testing machine (Fig. 6). First, preloading was performed. The load was controlled at 10% of the expected load-bearing capacity and lower than 50 kN. Then, formal loading was performed at a displacement rate of 2 mm/min. The load-displacement curves of the specimens were automatically recorded by the software.



Fig. 4 Temperature-controlled furnace

2.3. Test results and discussion

2.3.1. Failure modes

The failure modes of the specimens were similar. All of the specimens developed bending invagination at the connection between the spherical joint and the steel tube (Fig. 7). The failure mode can be characterized as an elastoplastic buckling collapse proposed by Han et al. [10]. Moreover, two steel tubes of some specimens were not on the same straight line after the WHSJs failed (Fig. 8). At a high temperature, the steel tubes were protected by asbestos, but the spherical joint had no protection from thermal insulation materials. Furthermore,

air temperature in the furnace was not completely uniform, and the properties of the steel materials changed with temperature. The specimens had initial defects. Therefore, different uncertain factors might cause interferences to the specimens.

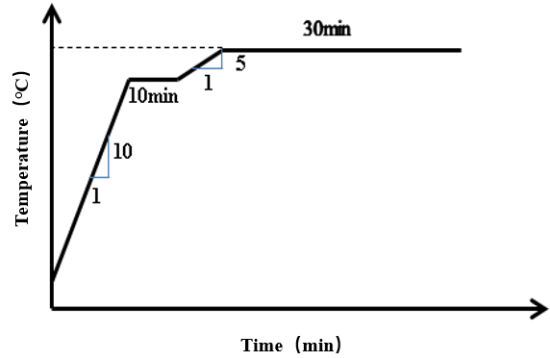


Fig. 5 Heating process

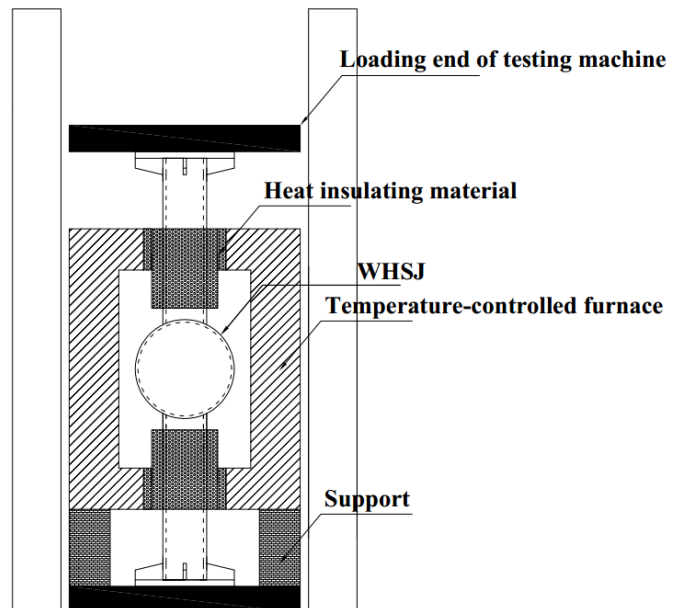
The test phenomena of the specimens differed at various temperatures. The rust on the spherical joint fell off slightly at $T=300\text{ }^{\circ}\text{C}$, whereas the weld bead at the connection between the steel tube and the joint turned slightly blue. Some rust on the spherical joint fell off at $T=500\text{ }^{\circ}\text{C}$. The joint was dark red, and the weld bead at the connection between the steel tube and the joint became light blue. At $T=700\text{ }^{\circ}\text{C}$, the rust on the spherical joint largely fell off. The spherical joint appeared bright red, and the weld bead at the connection between the steel tube and the joint became deep blue (Fig. 9).

2.3.2 Initial axial rigidity

The load-displacement curves of all of the specimens are shown in Fig. 10. The curves of some specimens (e.g., WS-345-20 and WSR-345-500-1) were slightly gentle at the initial stage, and the displacement value was between 0 and 1.5 mm, which might be caused by the processing error of these specimens. This stage was the compaction stage of the end plate, which did not influence the test results. At high temperatures ($300\text{ }^{\circ}\text{C}$ and $500\text{ }^{\circ}\text{C}$) and when the value of the load reaches about 130kN, a small stable section of the load-displacement curves formed, which was observed in other tests by using this testing machine. The causes of this phenomenon should be the system setting of the test device connected to the testing machine. The load-displacement curves of each group of parallel specimens except WS-345-300 were close. This finding confirmed the high reliability of the load-displacement curves of the specimens.



(a) photo of setup



(b) sketch of setup

Fig. 6 Loading device



(a) WS-345-20 and WS-345-300 -1~3

(b) WS-345-500-1~3

(c) WS-345-700-1~3



(d) WSR-345-200 and WSR-345-500 -1~3



(e) WS-235-20 and WS-235-500-1~3

Fig. 7 Failure modes**Fig. 8** Misaligned tubes

(a) WS-345-300

(b) WS-345-500

(c) WS-345-700

Fig. 9 Test phenomena of the specimens at different high temperatures

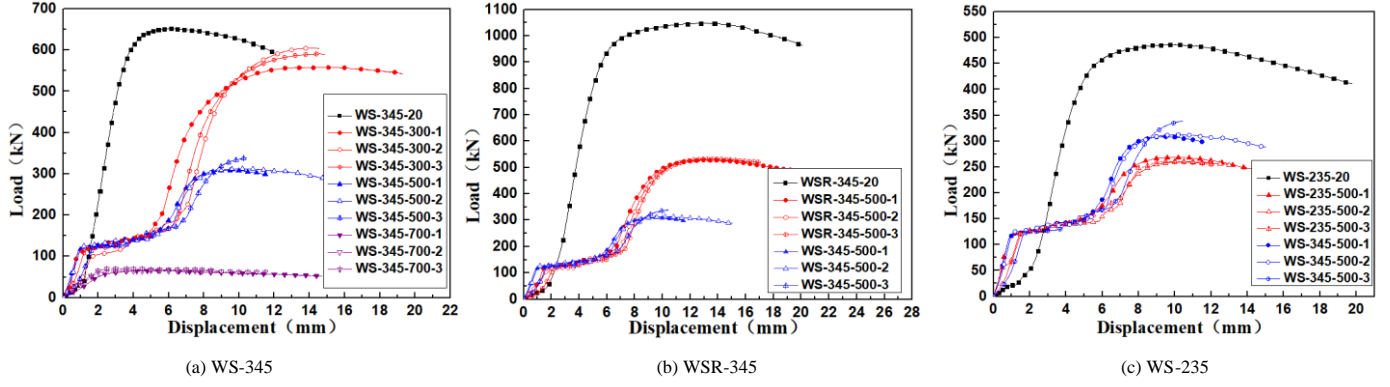


Fig. 10 Load-displacement curves of specimens

The failure process of WHSJ under the action of axial load can be divided into three stages [10], as shown in Fig. 11. At the elastic stage, the stiffness of the joint is constant; at the elastoplastic stage and the plastic stage, the load increases slowly as the displacement escalates gradually. The stiffness of the joint degenerates to zero when the ultimate load is reached.

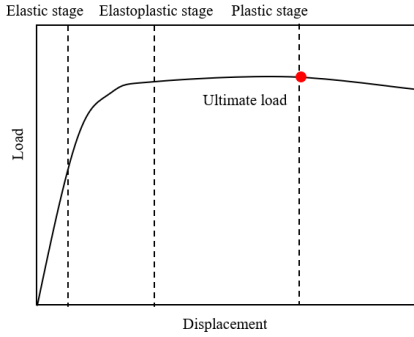


Fig. 11 Load-displacement curve of WHSJ under axial compression

In this study, the initial stiffness at the elastic stage was analyzed and the initial axial rigidity of the WHSJ was defined as follows:

$$K = N/\Delta \quad (1)$$

where K is the initial axial rigidity of the WHSJ, N is the axial load at the elastic stage, and Δ is the vertical displacement of the WHSJ at the elastic stage.

The axial deformation of the upper and lower steel tubes is overlooked because of the limitation of the test conditions. Therefore, Δ is approximately equal to the displacement of the specimens in this experiment. The reduction coefficient of the initial axial rigidity of the WHSJ at a high temperature ($k_{E,T}$) is defined as the ratio between the initial axial rigidity of the WHSJ at a high temperature (K_T) and the initial axial rigidity of the WHSJ at room temperature (K_{20}). K and $k_{E,T}$ are listed in Table 3 and plotted in Fig. 12(a) and (b), respectively. The reduction of the initial axial rigidity of the WHSJ is accelerated at temperatures exceeding 500 °C. The axial rigidity of the WHSJ at 300 °C is approximately 10% lower than that at room temperature. Such rigidity is about 30% lower at 500 °C and approximately 85% lower at 700 °C compared with that at room temperature. The stiffening rib arrangement and yield strength of the steel materials slightly influence $k_{E,T}$.

2.3.3 Yield load and ultimate load

The determination of the yield load and the ultimate load of the specimens is shown in Fig. 13. The experimentally obtained yield load at high temperatures (N_{YT}) and the ultimate load at high temperatures (N_{uT}) are shown in Fig. 14(a) and (b), respectively. The reduction coefficient of yield load at high temperatures (η_{YT}) is defined as the ratio between the yield load at a high temperature (N_{YT}) and the yield load at room temperature (N_Y), which is shown in Figure 15 (a). The reduction coefficient of the ultimate load at high temperatures (η_{uT}) can be defined similarly, which is shown in Fig. 15 (b). The yield load, the ultimate load, and their reduction coefficient are listed in Table 3. The reduction of the yield load and the ultimate load accelerates significantly at temperatures greater than 300 °C. The yield load and the ultimate load at 300 °C are approximately

10% lower than those at room temperature, and they further decrease to approximately 50% at 500 °C and approximately 90% at 700 °C. The reduction coefficient of the yield load of the same specimens is close to that of the ultimate load. The stiffening rib arrangement and yield strength of steel materials can slightly influence η_{uT} and η_{YT} .

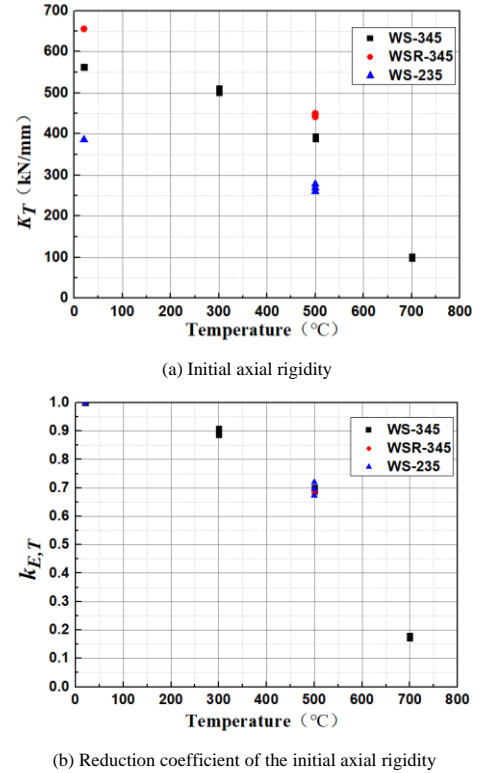


Fig. 12 Initial axial rigidity and its reduction coefficient

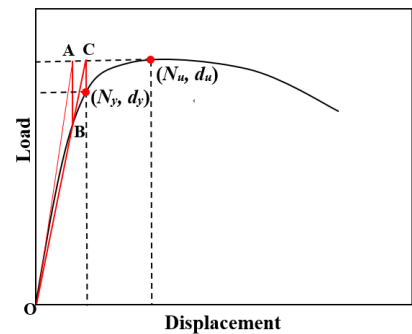


Fig.13 Determination of the yield load and the ultimate load
(Note: The line OA is the tangent at the dot.)

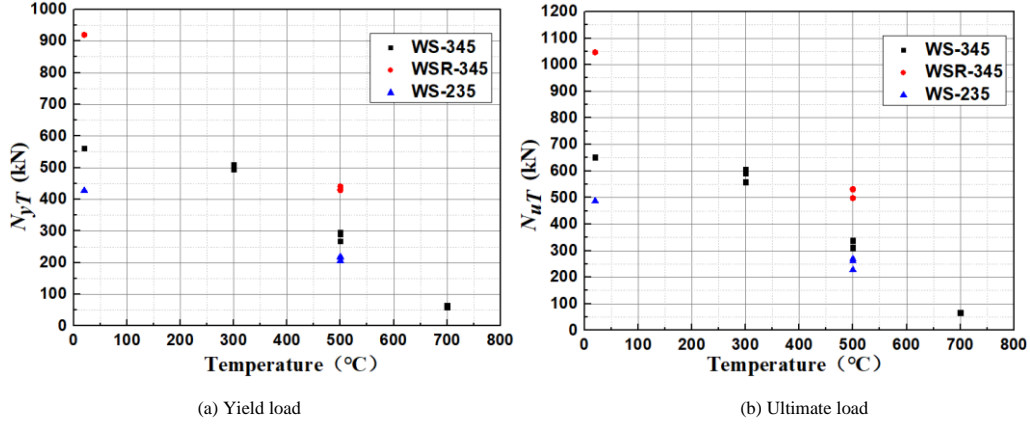


Fig. 14 Yield load and ultimate load of the specimens

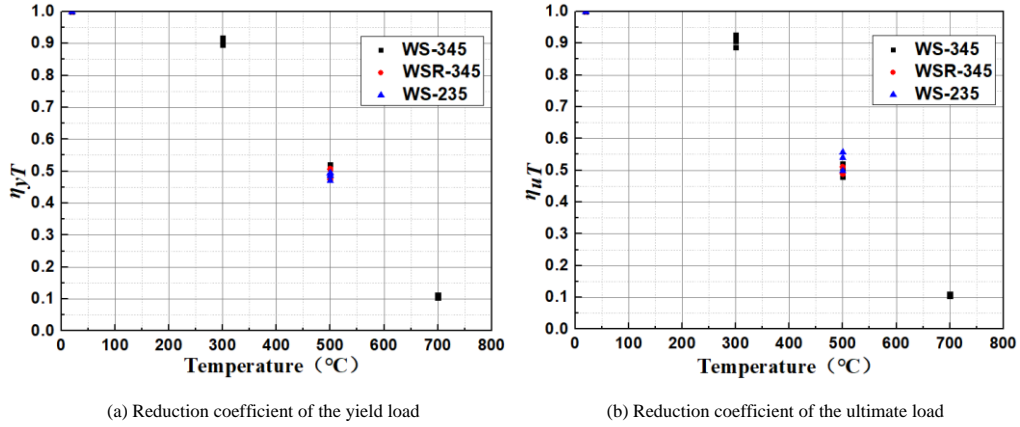


Fig. 15 Reduction coefficient of the yield load and ultimate load

Table 3

Test results

Joint No.	Rigidity /kN/mm	$k_{E,T}$	Yield load /kN	η_{yT}	Ultimate load /kN	η_{uT}
WS-345-20	563	1	561	1	652.6	1
WS-345-300	506	0.90	507	0.90	584.9	0.90
WS-345-500	391	0.69	277	0.49	320.4	0.49
WS-345-700	100	0.18	60	0.11	65.4	0.10
WS-235-20	386	1	423	1	486.7	1
WS-235-500	269	0.70	213	0.50	252.7	0.52
WSR-345-20	656	1	922	1	1047.9	1
WSR-345-500	447	0.68	429	0.47	520.2	0.50

Note: Data at a high temperature represent the mean value of three specimens in a group.

3. Finite element analysis

Finite element analysis (FEA) was conducted by using the ABAQUS. The analysis type was static, which considered the nonlinearity of the materials and the geometry.

3.1 Constitutive model of materials at high temperatures

The mechanical properties of materials, including elasticity modulus, yield strength, and ultimate strength, may change at high temperatures. Structural analysis accuracy at a high temperature is mainly determined by the stress–strain relation of materials, that is, the determination of different mechanical indices. The smooth curve model (Fig. 16) is defined in EUROCODE3 [24]. In this model, the stress hardening of the steel materials is neglected. The reduction coefficients of the yield strength and the initial elasticity modulus of the steel materials at different temperatures are shown in Table 4. Poisson's ratio of the steel materials at high temperatures is set equal to that at room temperature (0.3) because this ratio is less sensitive to high temperature.

3.2 Finite element model

The geometric details of the FE model are consistent with those of the test

specimens presented in Section 2.1. The measured thickness of base metal plate of WHSJs is 7.8 mm (a mean value). Compared to the base metal plate, the thickness of the hollow sphere decreases due to the formation of the oxide film and the stretching of the steel sheet during the process of stamping, and the reduction varies with the locations of the hollow sphere. The reduction coefficient of the thickness of WHSJs (μ_t) is defined by Eq. (2):

$$\mu_t = \frac{t}{t_0} \quad (2)$$

where t and t_0 refer to the thickness of WHSJs and the base metal plate, respectively. The value of μ_t , which is proposed by Chen [25,26], is between 0.85 and 1. In the finite element simulation of this paper, the value of μ_t is 0.95. Therefore, the thickness of the finite element model of WHSJs established in this paper is 7.4 mm.

The 3D eight-node solid element with reduced integration (C3D8R) was used to mesh the model. The stress at the connection between the spherical joint and the steel tubes is relatively high. The meshing density of this region increases. Meshing size can evidently influence the accuracy of the FE model results. Therefore, the sensitivity analysis of the meshing size was performed first. The spherical joint model is meshed by three meshing sizes (8,467 elements, 16,776 elements, and 24,112 elements). The corresponding load–displacement curves are shown in Fig. 17. The calculation results of the FE model with 16,776

elements are close to that of its counterpart with 24,112 elements. This finding suggests that the former meshing size is accurate enough and can meet the accuracy requirements of the FE model. Therefore, the spherical joint model is divided into 16,776 elements (Fig. 18).

In terms of the excellent thermal conductivity of the steel materials, the temperature of the whole specimen can be viewed in uniform distribution. As such, the same material properties and field temperature are applied to the FE model under fire disasters.

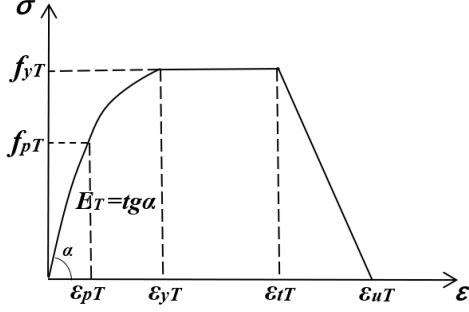


Fig. 16 Constitutive model of materials at high temperatures

Table 4

Reduction coefficient of the mechanical properties of the steel materials at high temperatures [24]

Temperature /°C	Reduction coefficient of the yield strength	Reduction coefficient of the initial elasticity modulus
20	1.000	1.000
100	1.000	1.000
200	1.000	0.900
300	1.000	0.800
400	1.000	0.700
500	0.780	0.600
600	0.470	0.310
700	0.230	0.130
800	0.110	0.090
900	0.060	0.0675
1000	0.040	0.0450
1100	0.020	0.0225
1200	0.000	0.000

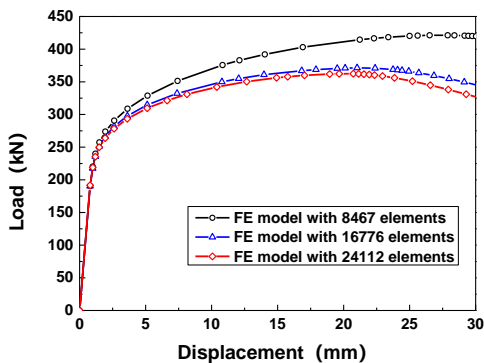


Fig. 17 The influence of meshing sizes

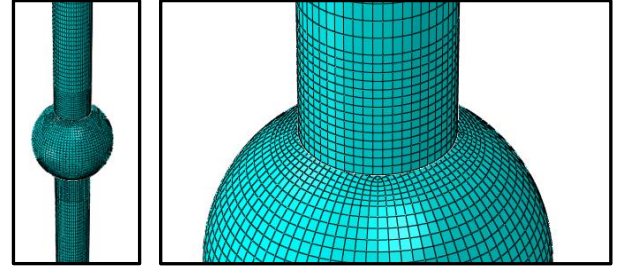


Fig. 18 FE model of the specimen

3.3 Verification of finite element simulation

The FEA results are compared with the test results. The typical failure modes and load-displacement curves are shown in Fig. 19 and Fig. 20, respectively. The ultimate bearing capacity and initial axial rigidity of the specimens are presented in Tables 5 and 6, respectively. The failure modes of the spherical joint in the test are consistent with those in FEA. All of the specimens developed bending invagination at the connection between the joint and the steel tubes. The test results agree well with the simulation results in terms of ultimate bearing capacity, initial axial rigidity, and their reduction coefficients. The bearing capacity and rigidity errors of the specimens at 700 °C are relatively high, reaching 25.2% and 32%. Other specimens show small error (<20%).

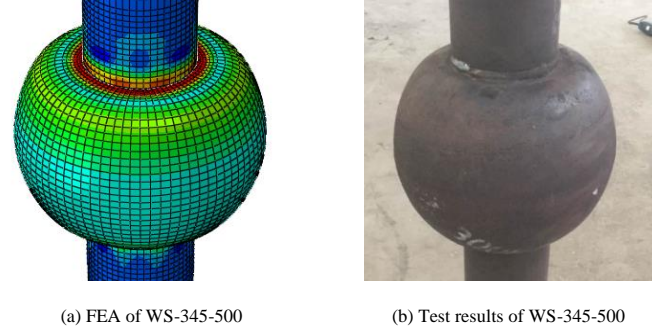


Fig. 19 Comparison of typical failure modes between simulation and test results

The differences between the test and FEA in fig. 20 are caused by several reasons. 1) The thickness of the hollow sphere decreases due to the formation of the oxide film and the stretching of the steel sheet during the process of stamping, and the reduction coefficient of thickness of WHSJ (μ_t), which is determined by Eq. (2), ranges from 0.85 to 1 according to the recommendations in literatures [25,26]. The influence of μ_t on the bearing capacity is shown in Fig. 21. It indicates that the bearing capacity of WHSJ decreases by 12% with the μ_t decreasing by 0.05. 2) The simulated temperature is approximately 50 °C lower than the test value because the rise of specimen temperature lagged behind the rise of air temperature, resulting in the bearing capacity of WHSJ decreases by about 10%, as shown in Fig. 22. 3) There are residual stress and the loss of material after the process of stamping, which might have detrimental influences on the bearing capacity of the WHSJ. 4) There is discreteness in the quality of the specimen, leading to the values which are inconsistent with the ideal results.

3.4. Correction of the initial axial rigidity

Steel tube deformation may remarkably influence the initial rigidity of the WHSJ during fire disasters because the connecting steel tubes are long. The calculation formula of the initial axial rigidity of the WHSJ is shown in Eq. (1), but this formula neglects the influences of the axial deformation of steel tubes. In this section, the accurate calculation formula of the axial deformation of the WHSJ is proposed by considering the axial deformation of steel tubes:

$$\Delta = (\Delta_2 - \Delta_3) / 2 \quad (3)$$

where Δ₂ is the total displacement of specimens, and Δ₃ is the displacement of steel tubes.

The influences of steel tube deformation on the initial axial rigidity of the

WHSJ at different temperatures are explored through FEA based on WS-345 (Fig. 23). The initial axial rigidity of the joint is significantly smaller when the steel tube deformation is neglected than that when the axial deformation of the steel tubes is considered. Steel tubes develop substantial deformation at high

temperatures, and this phenomenon cannot be disregarded in calculating the axial rigidity of the joint. The relation curve between the initial axial rigidity of the WHSJ after the correction and the test temperature is shown in Fig. 24. The axial rigidity of the WHSJ at a high temperature declines gradually and begins to decrease obviously at temperatures higher than 500 °C.

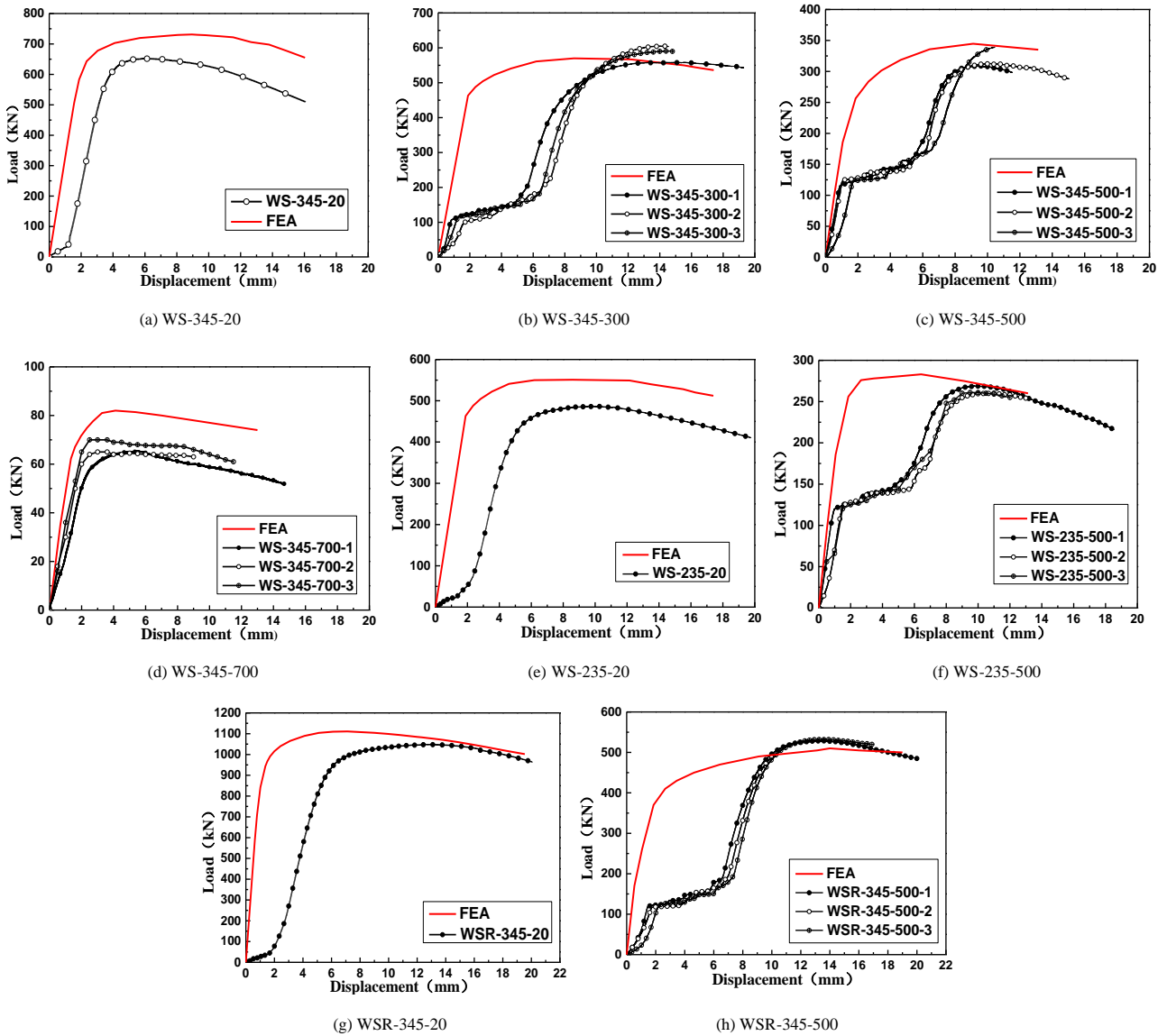


Fig. 20 Comparison of load-displacement curves between simulation and test results

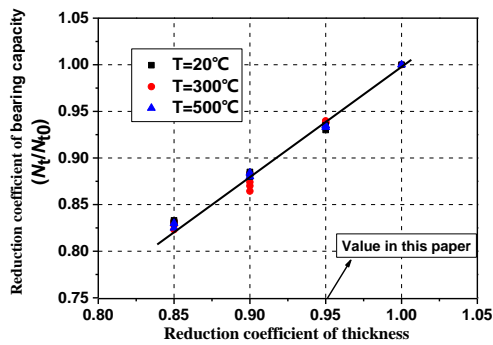


Fig. 21 The influence of reduction coefficient of thickness on bearing capacity

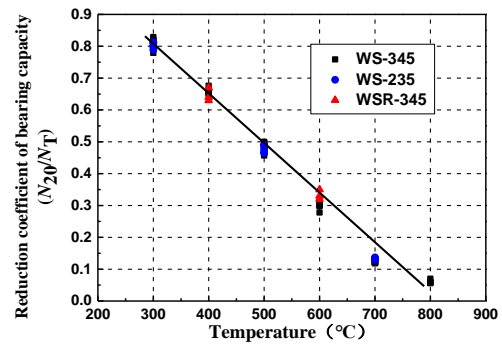


Fig. 22 The influence of temperature on bearing capacity

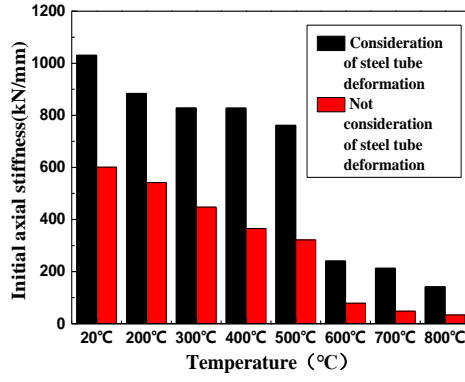


Fig. 23 Initial axial rigidity of the joint

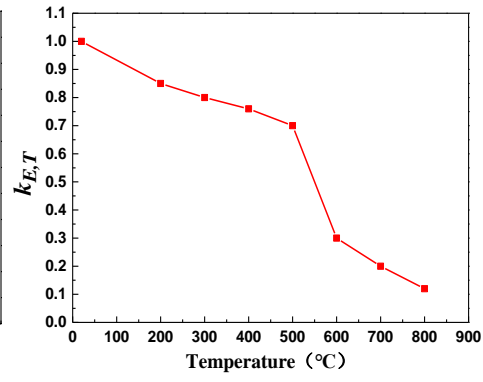


Fig. 24 Reduction coefficient of the initial axial rigidity

Table 5

Comparison of ultimate bearing capacity error

Specimen No.	N_t (kN)	N_f (kN)	$(N_f - N_t) / N_t$ (%)	η_t	η_f	$(\eta_f - \eta_t) / \eta_t$ (%)
WS-345-20	652.6	746.7	14.4	1	1	--
WS-345-300	584.9	555.7	-5.0	0.90	0.74	-17.8
WS-345-500	320.4	348.5	8.8	0.49	0.47	-4.0
WS-345-700	65.4	81.9	25.2	0.10	0.11	-10.0
WS-235-20	486.7	574.3	18.0	1	1	--
WS-235-500	252.7	283.6	12.2	0.52	0.49	5.8
WSR-345-20	1047.9	1110.9	6.0	1	1	--
WSR-345-500	520.2	505.9	-2.7	0.50	0.46	-8.0

Notes: N_t is the tested bearing capacity. N_f is the simulation bearing capacity. η_t is the reduction coefficient of tested bearing capacity. η_f is the reduction coefficient of simulated bearing capacity.

Table 6

Comparison of initial axial rigidity errors

Specimen No.	K_t	K_f	$(K_f - K_t) / K_t$ (%)	k_t	k_f	$(k_f - k_t) / k_t$ (%)
WS-345-20	563	621	10.3	1	1	--
WS-345-300	506	548	8.3	0.90	0.82	-8.9
WS-345-500	391	442	13.0	0.69	0.71	2.9
WS-345-700	100	132	32	0.18	0.21	16.7
WS-235-20	386	445	15.3	1	1	--
WS-235-500	269	329	18.2	0.70	0.74	5.7
WSR-345-20	656	693	5.6	1	1	--
WSR-345-500	447	500	11.9	0.68	0.72	5.9

Notes: K_t is the tested rigidity. K_f is the simulated rigidity. k_t is the reduction coefficient of the tested rigidity. k_f is the reduction coefficient of the simulated rigidity.

3.5. Strain analysis

The load-strain relation curve at different positions (1–6) of WS-345 at a high temperature is shown in Fig. 25. The results demonstrate that the steel tube (positions 1–6) of the specimens is maintained at the elasticity stage, which is attributed to the large thickness of the steel tube. The strain development of the spherical joint changes significantly with positions and temperature. In general, strain strength decreases dramatically along the radial direction of the spherical joint (from position 2 to position 4). Under a specific axial load, the maximum strain level is at the connection between the spherical joint and the steel tubes (positions 2 and 5). This phenomenon is consistent with the failure modes of the spherical joint in Fig. 7. For specimens at room temperature and at a low temperature (<500 °C), only the connection between the spherical joint and the steel

tubes enters the yield stage under a high load, whereas the remaining regions still maintain the elastic state. As temperature increases, the yield region expands. For example, positions 2, 3, and 4 of WS-345-700 reach the yield stage under a high load.

4. Simplified calculation method

In the Technical Regulation of Spatial Grid Structure (JGJ7-2010), the calculation formula of the compressive bearing capacity of the WHSJ at room temperature is:

$$N_u = \left(0.32 + 0.6 \frac{d}{D} \right) \eta_D \pi t d f \quad (4)$$

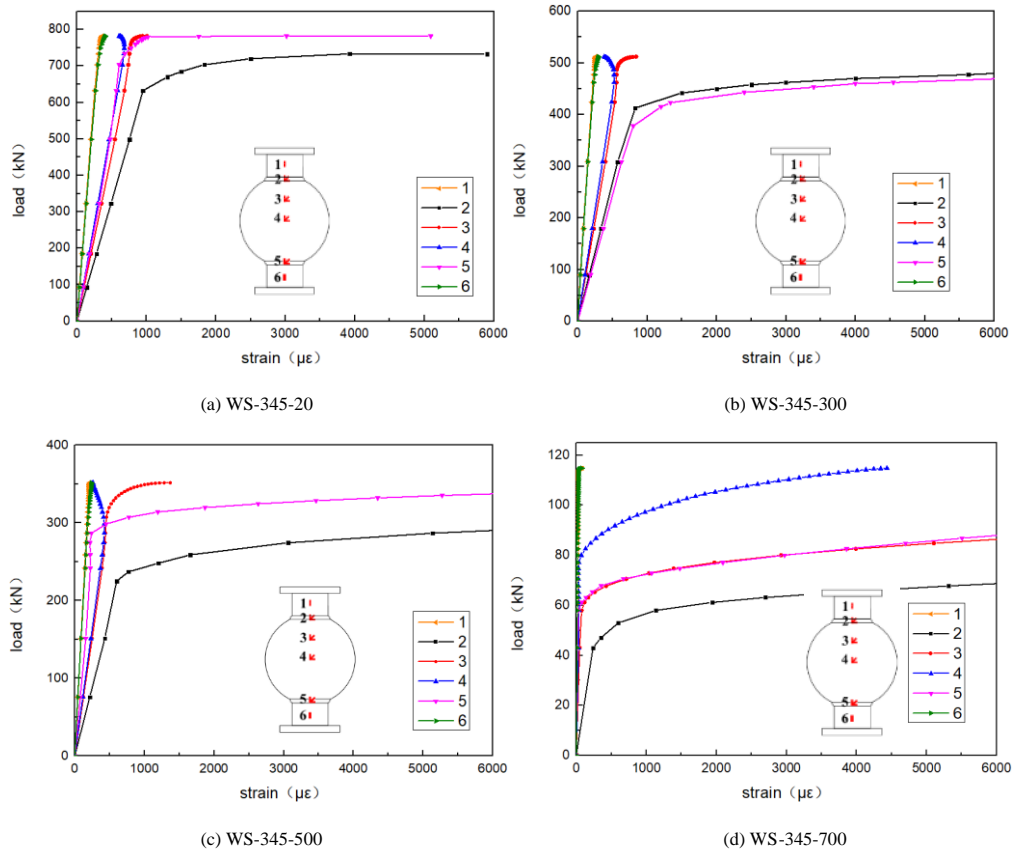
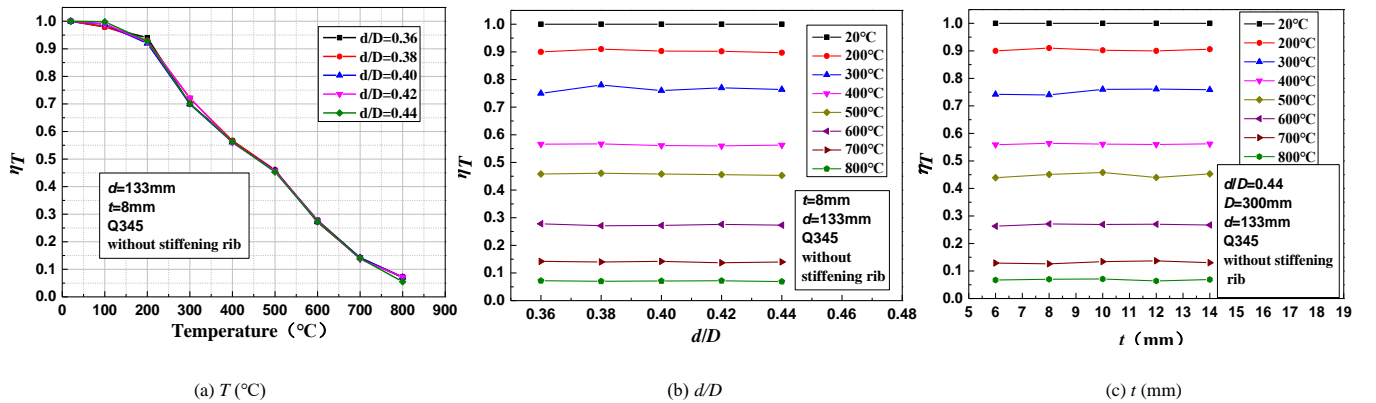
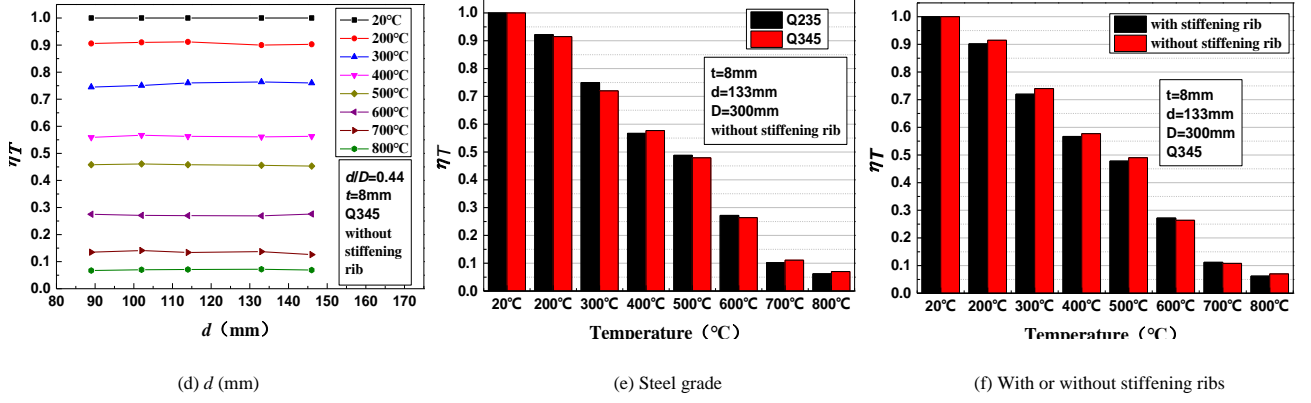


Fig. 25 Load-strain curves of WS-345

Table 7
Values of parameters

Parameters	Values	Reference values
Joint temperature T (°C)	20, 100, 200, 300, 400, 500, 600, 700, 800	—
Steel grade	Q235, Q345	Q345
Existence of stiffening ribs on spherical joint	With and without stiffening ribs	Without stiffening ribs
d/D	0.36, 0.38, 0.4, 0.42, 0.44	0.44
d (mm)	89, 102, 114, 133, 146	133
t (mm)	6, 8, 10, 12, 14	8



Fig. 26 Effects of key parameters on η_T

For the convenience of calculating the compressive bearing capacity of the WHSJ at a high temperature, a simplified calculation formula is proposed. In this formula, the concept of the reduction coefficient of the ultimate bearing capacity (η_T) is introduced:

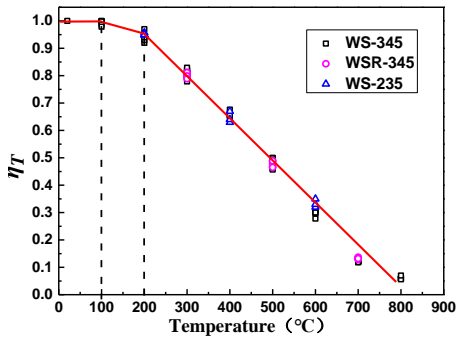
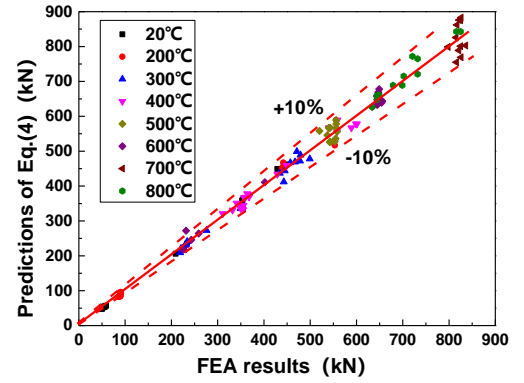
$$N_{UT} = \eta_T N_U \quad (5)$$

where N_{UT} is the axial compressive bearing capacity of the WHSJ at a high temperature, and N_U is the axial compressive bearing capacity of the WHSJ at room temperature and can be calculated according to Eq. (4).

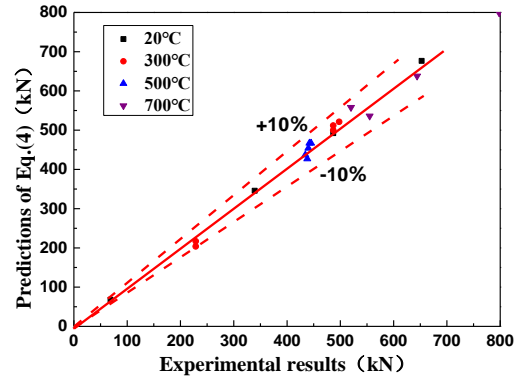
The influences of key parameters on η_T are studied on the basis of parameterization analysis results. Dimension parameters are designed in accordance with the Technical Regulation of Spatial Grid Structure (JGJ7-2010). All of the parameters are listed in Table 7, and their influences on η_T are shown in Fig. 26. η_T is mainly determined by T and slightly influenced by other factors. The relation curve between η_T and T can be obtained from regression analysis (Fig. 27). The equation is shown as follows:

$$\eta_T = \begin{cases} 1 & 20^\circ\text{C} < T \leq 100^\circ\text{C} \\ 1.04 - 4 \times 10^{-4} T & 100^\circ\text{C} < T \leq 200^\circ\text{C} \\ 1.27 - 1.55 \times 10^{-3} T & 200^\circ\text{C} < T \leq 800^\circ\text{C} \end{cases} \quad (6)$$

The axial compressive bearing capacity of the WHSJ, which is predicted in Eq. (5), is compared with the FEA results and the test results (Fig. 28(a) and (b)), thereby achieving high consistency. This result verifies the accuracy of the simplified calculation method.

Fig. 27 The relation curve between η_T and T 

(a) Simplified calculation method and FEA results



(b) Simplified calculation method and test results

Fig. 28 Verification of the simplified calculation method

5. Conclusions

WHSJs have been extensively applied to spatial grid structures. The study of the mechanical behavior of WHSJ at elevated temperatures provide important basis for assessing the fire damage of the whole structure. This paper presented experimental and numerical studies on the mechanical behavior of WHSJ at elevated temperatures. The failure mechanism and high-temperature attenuation pattern of the axial compression performance of WHSJ at elevated temperatures were explored via high-temperature axial compression experiments by using 18 specimens. A FE model was constructed and the reliability of this FE model was verified by experimental results. Simplified calculation methods, based on test results and parametric studies, were proposed to predict the load-bearing capacity of WHSJ at elevated temperatures. The findings of the simplified calculation method conformed to experimental results and numerical simulation results. Some major conclusions can be drawn:

The failure mode of the WHSJ at a high temperature is similar to that at room temperature. Bending invagination occurs at the connection between the spherical joint and the steel tubes, indicating plastic failure.

The ultimate load and the yield load of the WHSJ at 300 °C are 10% lower than those at room temperature. The ultimate load and the yield load of the WHSJ at 500 °C are about 50% lower than those at room temperature. At 700 °C,

they decrease by 90% compared with those at room temperature. The stiffening rib arrangement and the steel grade slightly influence the reduction coefficients of the yield load and the ultimate load of the WHSJ at a high temperature. The reduction coefficients of the ultimate load and the yield load of the spherical joint are consistent.

The initial axial rigidity of the WHSJ is significantly influenced by steel tube deformation that should be considered in calculating the initial axial rigidity of the joint. The initial axial rigidity of the WHSJ at 300 °C decreases by about 20% compared with those at room temperature and further decreases greatly after 500 °C.

The tested results of bearing capacity, the reduction coefficient of bearing capacity, rigidity, and the reduction coefficient of rigidity are consistent with the simulation results. The errors between the test results and the simulation results are lower than 20% except those in some specimens.

Parameterized analysis indicates that the reduction coefficient of the bearing capacity of the WHSJ (η_T) is mainly determined by test temperature. However, η_T is less sensitive to other factors. The simplified calculation method based on abundant FEA results can reasonably predict the axial compressive bearing capacity of the WHSJ at high temperatures.

Acknowledgments

This study was financially supported by the National Natural Science Foundation of China (Grant No. 51678404).

References

- [1] Fan F., Ma H.H. and Chen G.B., "Experimental study of semi-rigid joint systems subjected to bending with and without axial force", *Journal of Constructional Steel Research*, 68(1), 126-137, 2012.
- [2] Xu S., Chen Z.H. and Wang X.D., "Hysteretic out-of-plane behavior of the Temcor joint", *Thin-Walled Structures*, 94, 585-592, 2015.
- [3] Gao F., Shao Y.B. and Gho W.M., "Stress and Strain Concentration Factors of Completely Overlapped Tubular Joints Under Lap Brace IPB Load", *Journal of Constructional Steel Research*, 63(3), 305-316, 2007.
- [4] Du W.F., Sun Y. and Yang M.J., "Bearing capacity of the cast-steel joint with branches under eccentric load", *Journal of Constructional Steel Research*, 135, 285-291, 2017.
- [5] Han Q.H., Liu Y.M. and Zhang J.Y., "Mechanical behaviors of the Assembled Hub (AH) joints subjected to bending moment", *Journal of Constructional Steel Research*, 138, 806-822, 2017.
- [6] Liu X.L., "Design and Construction of Plate Grid Structures", Press of Tianjin University, Tianjin, China, 2000.
- [7] Hou X.M., Zheng W.Z. and Kodul V., "Effect of temperature on mechanical properties of prestressing bars", *Construction and Building Materials*, 61, 24-32, 2014.
- [8] Xue W.L. and Zhang Q.L., "Destructive mechanism and experimental study of welded hollow spherical joints connected with circular steel tubes", *Journal of Building Structures*, 30(5), 155-161, 2009.
- [9] Ding Y., Qi L. and Li Z.X., "Mechanical calculation model for welded hollow spherical joint in spatial latticed structures", *Advanced Steel Construction*, 7(4), 330-343, 2011.
- [10] Han Q.H. and Liu X.L., "Ultimate Bearing Capacity of the Welded Hollow Spherical Joints in Spatial Reticulated Structures", *Engineering Structures*, 26(1), 73-82, 2004.
- [11] Li X., "Load-carrying Capacity and Practical Design Method of Welded Hollow Spherical Joints in Space Latticed Structures", *Advanced Steel Construction*, 6(4), 976-1000, 2010.
- [12] Liu H.B., Ying J.J. and Chen Z.H., "Ultimate tensile and compressive performances of welded hollow spherical joints with H-beam", *Journal of Constructional Steel Research*, 150, 195-208, 2018.
- [13] Han Q.H., Liu Y.M. and Xu Y., "Stiffness Characteristics of Joints and Influence on the Stability of Single-Layer Latticed Domes", *Thin-Walled Structures*, 107, 514-25, 2016.
- [14] Zhao Z.W., Liu H.Q. and Liang B., "Influence of welded hollow spherical joints on the mechanical behavior of single-layer reticulated shell structures", *Journal of the Brazilian Society of Mechanical Sciences and Engineering*, 40, 386, 2018.
- [15] Zhao Z.W., Zhu H. and Chen Z.H., "Mechanical behavior of single-layer reticulated shell connected by welded hollow spherical joints with considering welding residual stress", *Welding in the World*, 60(1), 61-69, 2016.
- [16] Wang P.P., Lei H.G. and Wang F., "Numerical Simulation Analysis of Residual Stress in Welded Hollow Spherical Joint with Circular Steel Tubes", *Architectural Engineering and New Materials*, 308-314, 2015.
- [17] Zhao Z.W., Liu H.Q. and Liu B., "Assessment of the bending capacity of welded hollow spherical joints with pit corrosion", *Thin-Walled Structures*, 131, 274-285, 2018.
- [18] Zhao Z.W., Liu H.Q. and Liu B., "Bending capacity of corroded welded hollow spherical joints", *Thin-Walled Structures*, 127, 523-539, 2018.
- [19] GJ 7-2010, Technical Specification for Space Frame Structures, Ministry of Construction of the People's Republic of China, Beijing, 2010.
- [20] Lu J., Liu H.B. and Chen, Z.H., "Post-fire Behavior of Welded Hollow Spherical Joints Subjected to Eccentric Loads", *International Journal of Steel Structures*, 18(2), 456-472, 2018.
- [21] Liu H.B., Lu J. and Chen Z.H., "Residual behavior of welded hollow spherical joints after exposure to elevated temperatures", *Journal of Constructional Steel Research*, 137, 102-118, 2017.
- [22] Lu J., Liu H.B. and Chen Z.H., "Behavior of Welded Hollow Spherical Joints After Exposure to ISO-834 Standard Fire", *Journal of Constructional Steel Research*, 140, 108-124, 2018.
- [23] Xue S.D. and Qiu L., "Experimental investigation on compression performance of welded hollow spherical joints in fire", *Journal of Building Structures*, 32(2), 113-119, 2011.
- [24] Eurocode3: Design of steel structures. Part 1-2: General rules - Structural fire design. Brussels, Belgium, European Committee for Standardization, 2005.
- [25] Liu X.L. and Chen Z.H., "Failure Mechanism Analysis and Bearing Capacity Test Study of Grid Welded Hollow Spherical Joints", *Journal of Building Structures*, 3, 38-44, 1994.
- [26] Chen Z.H. and Liu X.L., "Study on Calculation Formula of Bearing Capacity of Welded Hollow Spherical Joints", *Proceedings of the 11th Academic Conference on Space Structure*, 2005.

AXIAL COMPRESSIVE BEHAVIOR OF SELF-STRESSING STEEL SLAG AGGREGATE CONCRETE FILLED STEEL TUBULAR COLUMNS WITH BOND-SLIP DAMAGE

Feng Yu ¹, Chi Yao ¹, Yi Hu ², Yuan Fang ^{1,*}, Kang Niu ¹ and Guo-sheng Xiang ¹

¹ Department of Civil Engineering and Architecture, Anhui University of Technology, Ma'anshan, China

² China MCC 17 Group Co., Ltd, Ma'anshan, China

* (Corresponding author: Email:fyuan86@126.com)

ABSTRACT

The axial compressive behavior of self-stressing steel slag aggregate concrete filled steel tubular (CFST) columns with bond-slip damage is investigated in this paper. Six bond-slip damaged specimens and two undamaged specimens with different diameter-thickness ratios and expansion ratios are tested. According to the test, the outward deformation dominates the failure of the axial loaded bond-slip damaged specimens. The ultimate bearing capacity is lower with higher diameter-thickness ratio, while the increase of the expansion ratio will bring benefits to bond-slip damaged specimens. The bond-slip damage has a little influence on the ultimate capacity. The ultimate displacement will be decreased by increasing the diameter-thickness ratio. The effect of expansion ratio on the longitudinal displacement is not obvious. The stiffness degradation can be mitigated by raising the expansion ratio. The ultimate axial and circumferential strains increase as the expansion ratio increases while they decrease with the diameter-thickness ratio of bond-slip damaged specimens increasing. In addition, the accuracy of existing CFST design specifications for predicting the strength of bond-slip damaged specimens is evaluated.

ARTICLE HISTORY

Received: 12 April 2019
Revised: 06 September 2019
Accepted: 14 September 2019

KEYWORDS

CFST;
Slag;
Expansion ratio;
Diameter-thickness ratio;
Ultimate bearing capacity;
Stress-strain curve

Copyright © 2020 by The Hong Kong Institute of Steel Construction. All rights reserved.

1. Introduction

Steel slag produced from steel-making is one of the main types of solid waste. To date, a huge amount of steel slag has been discarded leading to a considerable land occupation and the pollution in air and water [1-2]. The Steel Slag Aggregate Concrete (SSAC), using the steel slag as the concrete aggregate, is proposed for recycling the industrial waste and preserving natural resources [3]. SSAC offers advantages such as low hydration heat, high strength and good durability [4-6]. However, the oxides, *MgO* and *free-CaO* in the steel slag might lead to micro-expansion of SSAC [7-10], which limits the application in civil engineering. To inhibit the volume instability, the self-stressing steel slag aggregate CFST column is proposed in this analysis.

CFST column utilizing the beneficial properties of concrete and steel has a high bearing capacity, good ductility and excellent seismic performance [11-14]. The bonding force significantly affect the mechanical properties of the composite member. Apparently, because of the volume shrinkage of the ordinary concrete during the curing, the bonding force would be decreased, and the slip defects would occur leading to the reduction of the bearing capacity, the safety and the durability of the structures [15-17].

By employing SSAC, the mechanical properties of the composite member could be effectively improved due to the slight expansion of SSAC. In recent years, Ferhoun [18] studied the behavior of the eccentrically loaded cold-formed steel tube with the crushed crystallized slag aggregate concrete and proved that the recycled slag could be integrated in the concrete manufacture. Zeghiche [19] parametrically investigated the influences of concrete strength and section geometry on the behavior of cold formed steel tube with crystallized slag aggregate concrete.

The investigations of defects mainly focused on the initial stress and eccentricities. Wei et. al. [20] revealed that the initial stress could significantly decrease the ultimate bearing capacity of single-set. Xiong et. al. [21] carried out a comprehensive numerical study on the mechanical behavior of CFST columns and discussed the influences of the eccentricity, length-thinness ratio, and initial stress ratio. Hu et. al. [22] conducted the experiments on the influences of the heat treatment and the arch rib deviation on the ultimate bearing capacity of steel tube arch. However, little research had been conducted on the member with the initial bond-slip imperfection.

In this study, Six bond-slip damaged specimens and two undamaged specimens under axial compression are tested. The effects of the diameter-thickness ratio and the expansion ratio on the mechanical behavior of bond-slip damaged specimens are detailed investigated. The influences of the bond-slip damage on the bearing capacity, longitudinal displacement, and stiffness of specimen are examined. Additionally, the bearing capacity of bond-slip damaged specimens is evaluated by the current CFST specifications.

2. Experimental program

2.1. Specimen design

In this analysis, eight self-stressing steel slag aggregate CFST columns including six bond-slip damaged specimens and two undamaged specimens, are designed and tested. The bond-slip damage is achieved through the push-out method from the undamaged column. The process includes three steps, namely (1) reserving 50 mm at the bottom of the specimens in the process of casting; (2) placing a circular steel plate slightly smaller than the inner diameter of the steel tube on the top of the core SSAC, and (3) loading the columns on the hydraulic compression testing machine until the specimen bond-slip fails (Fig. 1).



Fig. 1 The process of achieving bond-slip damage

The outer steel tube of specimens is made of Q235 steel. The tubes are 500 mm long with 140 mm outer diameter and 2.09 mm, 3.63 mm or 4.23 mm thickness. The pouring depths of SSAC are 450 mm and 500 mm in bond-slip damaged specimens and the undamaged specimens, respectively. Different diameter-thickness ratios (i.e., 33.10, 38.46, and 66.99), and expansion ratios (i.e., 2.8×10^{-4} , and -3.5×10^{-4}) are adopted. More details are listed in Table 1.

2.2. Material properties

To investigate the influences of the expansion ratio on the mechanical behaviors of bond-slip damaged stub columns, two types of SSAC, such as the Ex-1 with the expansion ratio of 2.8×10^{-4} and the Ex-2 with the expansion ratio of -3.5×10^{-4} , are prepared, where the Ex-2 series is used to simulate the ordinary concrete. According to GB/T50082-2009 [23], the expansion ratio is determined by SSAC block test, as shown in Fig. 2. The expansion ratio of SSAC can be calculated as:

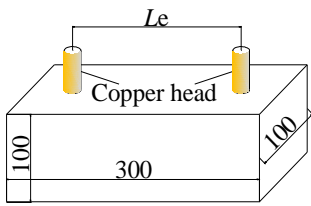
$$E_x = (L_t - L_0) / L_0 \quad (1)$$

Where, E_x is the expansion ratio of SSAC on the t -day, L_e denotes the gauge length of the test block, L_0 represents the initial length of the test block on the third day, and L_t is the length of the test block after t days.

Table 1
Parameters of specimens

Specimen	t_s /mm	D /mm	D/t_s	$E_x/10^{-4}$	Type
TCZY1-1	2.09	140	66.99	2.8	BSDS
TCZY2-2				-3.5	
TCZY3-1	3.64	140	38.46	2.8	
TCZY4-2				-3.5	
TCZY5-1	4.23	140	33.10	2.8	
TCZY6-2				-3.5	
ZY7-1	3.64	140	38.46	2.8	Undamaged specimen
ZY8-2				-3.5	

Note: t_s , D and E_x are the measured thickness, outside diameter of steel tube and expansion ratio of the SSAC, respectively. BSDS represents the bond-slip damaged specimen.



(a) Schematic diagram of SSAC



(b) Photo of the test block

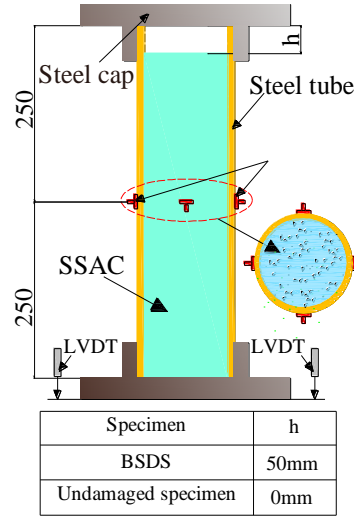
Fig. 2 Test for measuring E_x of SSAC

According to “Metallic material - Tensile testing (GB/T228-2010)” Part I [24], the coupon test method is adopted to evaluate the mechanical properties of the steel tubes. The steel material properties are shown in Table 2. SSAC is made of graded gravel, steel slag (fine aggregate), P. O 42.5 cement, city tap water. The steel slag is continuously graded, and the particle size range of the steel slag is 0.15 mm to 2.36 mm. The components of SSAC at different expansion ratios and the mechanical properties of SSAC are listed in Table 3.

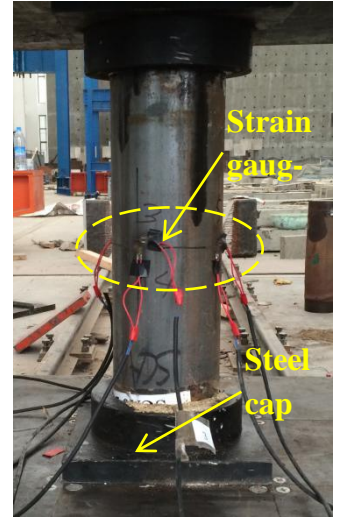
2.3. Test setup and procedure

The experiments were conducted in the Structure and Earthquake Resistance Laboratory of Anhui University of Technology. A 5000 kN hydraulic compression testing machine was employed for applying the monotonic static load, as shown in Fig.3. Two steel caps were prepared for both ends of speci-

men. The axial and circumferential strain gauges (eight strain gauges) were evenly arranged at mid-height of columns, and two linear variable displacement transducers (LVDTs) were applied to measure the specimen's longitudinal deflections, as shown in Fig.3(a). Multi-stage loading was adopted in the experiments, and the initial load increment was 1/10 of the estimated ultimate strength. When the specimens became inelastic, the load increment changed to 1/15 of the estimated ultimate strength.



(a) Schematic diagram of specimens



(b) Photo of the test setup

Note: BSDS represents the bond-slip damaged specimen.

Fig. 3 Test setup and measuring points arrangement

3. Test procedure and failure modes

Initially, the compressive load was mainly undertaken by the outer steel tube. As the load increased to 30% - 45% of the ultimate strength, the local outward buckling appeared at the top of the steel tube. With the increase of load, the black rust on the surface of the outer steel tube gradually fell off, and the local outward buckling became obvious. The longitudinal deformation greatly increased while the compressive load approximately kept constant. As the load further increased, the top loading plate reached to SSAC. The outer steel tube and core SSAC carried load together. The stiffness of specimen increased significantly. As the load increased to 50% - 60% of the ultimate strength, the slight noise of core SSAC cracking can be heard occasionally. When the load increased to 75% - 85% of the ultimate strength, outward buckling appeared at middle of specimen, and large areas of black rust fell off. Cracks of core SSAC were frequently heard. Finally, specimens lost their bearing capacities and exhibited outward buckling failures as shown in Fig.4.

Table 2
Material properties of steel tube

Steel Grade	Diameter /mm	Thickness /mm	Ultimate bearing capacity /MPa	Yield Strength /MPa	Young's modulus /MPa	Poisson's ratio
Q235	2.09	140	223	176	2.01×10^5	0.301
Q235	3.64	140	296	233		
Q235	4.23	140	301	237		

Table 3
The components of the two series of SSAC and mechanical properties

Type	Expansion ratio / 10^{-4}	Material usage / $\text{kg} \cdot \text{m}^{-3}$				Particle size of steel slag /mm	Cube compressive Strength /MPa	Young's modulus /MPa	Poisson's ratio
		Tap water	Cement	Coarse aggregate	Steel slag				
E_{x-1}	2.8	202.1	366.1	962.1	622.1	0.15~0.30 (75%) 0.30~0.60 (25%)	22.9	2.73×10^4	0.231
E_{x-2}	-3.5	202.1	366.1	962.1	622.1	1.18~2.36	35.3	3.62×10^4	0.242

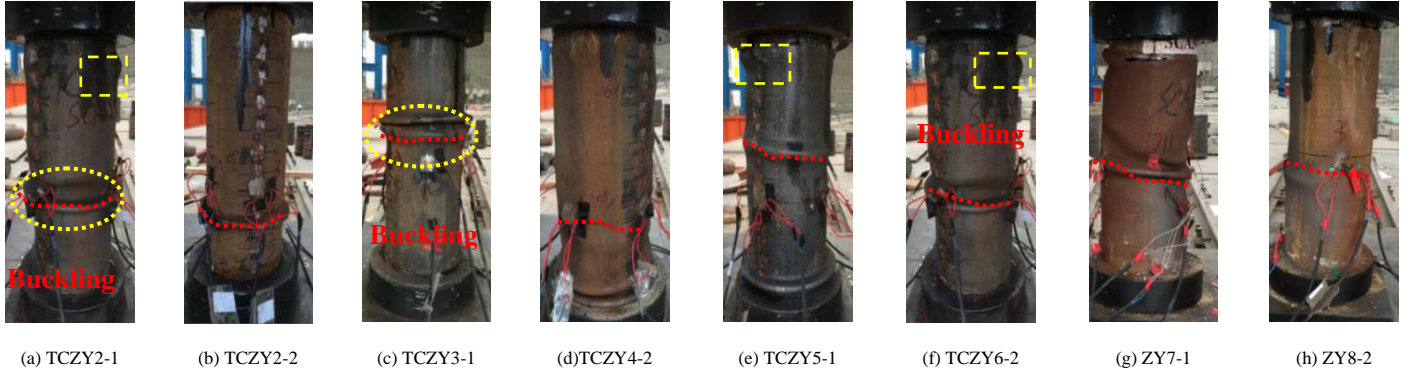
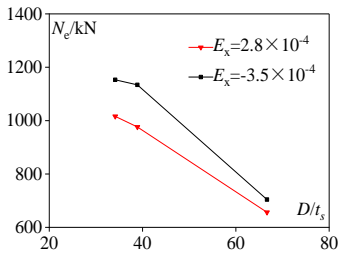
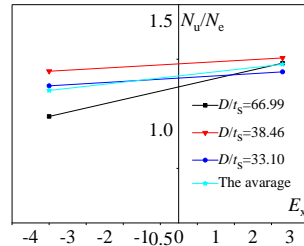


Fig. 4 Failure modes of specimens

4. Experimental results and analysis

4.1. Bearing capacity

The ultimate bearing capacity of bond-slip damaged specimens with different diameter-thickness ratios is depicted in Fig. 5. Apparently, the increase in the diameter-thickness ratio of bond-slip damaged specimens decreases the ultimate bearing capacity. For the columns with -3.5×10^{-4} expansion ratio, the ultimate bearing capacity of bond-slip damaged specimens with the diameter-thickness ratio 66.99 is 39% lower than the bond-slip damaged specimens with the diameter-thickness ratio 33.10. This is mainly because the confinement effect decreases as the diameter-thickness ratio of bond-slip damaged specimens increases.

Fig. 5 Effect of D/t_s on bearing capacityFig. 6 Effect of E_x on N_u/N_e

The Incremental Range of the Ultimate Bearing Capacity (N_u/N_e), the ratio between the ultimate bearing capacity (N_u) and the nominal compressive strength ($N_e = f_y A_k + f_c A_c$), is adopted to evaluate the influence of the expansion ratio on the ultimate bearing capacity of bond-slip damaged specimens, as showed in Fig. 6. N_u/N_e increases as the expansion ratio of bond-slip damaged specimens increases. The average N_u/N_e of bond-slip damaged specimens with expansion ratio of -3.5×10^{-4} is 11.8% lower than the bond-slip damaged specimens with the expansion ratio of 2.8×10^{-4} . Take the bond-slip damaged specimens with the diameter-thickness ratio of 66.99 as an example, when the expansion ratio increases from -3.5×10^{-4} to 2.8×10^{-4} , N_u/N_e of bond-slip damaged specimens increases by 24.7%. Therefore, the decrease of

the diameter-thickness ratio or the increase of the SSAC expansion ratio in a reasonable range can effectively improve the ultimate bearing capacity.

Specimens TCZY4-2 and ZY8-2 are employed to reveal the effect of bond-slip damage on the bearing capacity. The load-deflection curves of the specimens are plotted in Fig. 7. Obviously, the undamaged specimen exhibits three stages, namely, the elastic stage, the elastoplastic stage and the plastic stage. For bond-slip damaged specimens, an additional strengthening stage is appeared within the second and third stages. The proportion limit of the undamaged specimen is 809.6 kN, which is 4.05 times than that of the bond-slip damaged specimen. This may be due to the different mechanic performances. The axial load of bond-slip damaged specimens is only carried by the steel tube, while the axial load of undamaged specimen is carried by both the core SSAC and steel tube. As the load increases, the specimen enters the second stage. The difference between the undamaged specimen and bond-slip damaged specimen is obvious in this stage. The yield strength of undamaged specimen and bond-slip damaged specimens are 936.2 kN and 300.1 kN, respectively. After that, the bearing capacity of bond-slip damaged specimens increases significantly, while that of undamaged specimen does not. Finally, the ultimate bearing capacity of undamaged specimen and bond-slip damaged specimens are approximate consistent. The bond-slip damage has a little influence on the ultimate strength, while the bond-slip damage has a remarkable influence on yield strength. The detailed experimental results of specimens on bearing capacity and displacement are shown in Table 4.

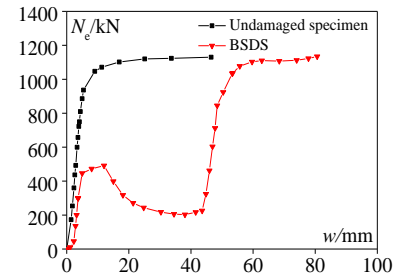


Fig. 7 Effect of bond-slip damage on bearing capacity

Table 4

Experimental results of specimens on bearing capacity and displacement

Specimen	Proportion limit/kN	Elastic displacement/mm	Yield load/kN	Yield displacement/mm	Ultimate load/kN	Ultimate displacement/mm
TCZY1-1	143.2	0.8	251.8	3.0	656.0	60.0
TCZY2-2	147.7	0.9	252.7	3.1	704.0	60.0
TCZY3-1	202.5	3.1	298.6	3.6	976.2	79.0
TCZY4-2	200.1	3.2	300.1	3.7	1134.0	80.6
TCZY5-1	318.4	1.3	490.2	2.5	1016.0	82.1
TCZY6-2	329.8	1.4	487.7	2.4	1153.0	83.3
ZY7-1	736.3	4.3	832.2	5.3	979.3	45.4
ZY8-2	809.6	4.4	936.2	5.4	1130.2	46.5

4.2. Load-displacement

The effects of the expansion ratio and the diameter-thickness ratio on the load-displacement relationship are depicted in Fig.8. Initially, the load-displacement relationship is approximate linear. As the load increases, the load-displacement curve deviates from the linearity. The axial load decreases slightly while the longitudinal displacement of bond-slip damaged specimens increases greatly. Outward buckling appears at mid-height of the steel tube and the longitudinal displacement of specimen quickly approach to 50 mm. As the axial load increases further, the bond-slip damaged specimen enters the hardening range. Finally, the outward deformation dominates the failure of the bond-slip damaged specimens, and the overall deformation is large.

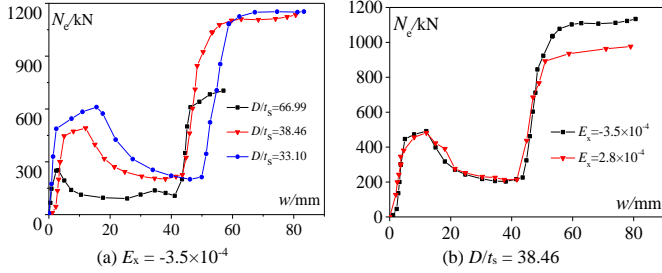


Fig. 8 Effect of two studied parameters on load-displacement relationship of BSDS

The increase of the diameter-thickness ratio would decrease the longitudinal displacement of bond-slip damaged specimens, as shown in Fig.8(a). This may come from that the confinement effect of steel tube on core SSAC decreases as the diameter-thickness ratio increases, and core SSAC is more susceptible to outward failure, leading to the decrease of ultimate deformation.

The load-displacement relationship curves of bond-slip damaged specimens with different expansion ratios are presented four stages, as shown in Fig.8(b). The effect of expansion ratio on the longitudinal displacement of bond-slip damaged specimens is not obvious.

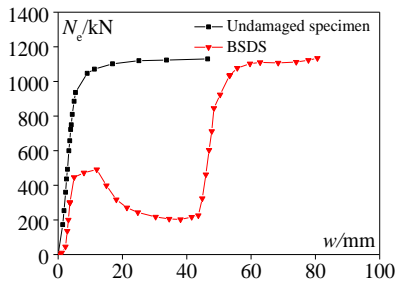


Fig. 9 Effect of bond-slip damage on load-displacement curves

Take specimens TCZY4-2 and ZY8-2 as example, the effect of bond-slip damage on load-displacement curves is depicted in Fig.9. Compared with undamaged specimen, the slope of the bond-slip damaged specimens in the elastic stage is smaller, and the longitudinal displacement of bond-slip damaged specimens in the elastoplastic stage is remarkable. These indicate that the bond force can significantly reduce the longitudinal displacement of the specimen. A hardening range is appeared in the load-displacement curve of bond-slip damaged specimens, and the curve is approximate linear in this stage. When the bond-slip damaged specimens and undamaged specimen are close to failure, the load-displacement relationship curves finally show a horizontal section. Obviously, the ultimate deformation of bond-slip damaged specimens is larger than that of the undamaged specimen.

4.3. Stiffness

Fig.10. depicts the relationship between the stiffness (K_s) and load (N_s) of bond-slip damaged specimens. The load-stiffness curve of bond-slip damaged specimens roughly divides into four parts. The first stage is the horizontal part, and the stiffness of the bond-slip damaged specimens changes little. In this part, only the outer steel tube carried the axial load, and the bond-slip damaged specimens is in the elastic stage. As the load increases, the bond-slip damaged specimens enters the second stage (the descending part). With the yielding of steel tube, the stiffness of bond-slip damaged specimens degenerates rapidly. When the loading plate reaches to SSAC, the bond-slip damaged specimens enters the third stage (the recovery part). The outer steel tube and

core SSAC begin to carry the load together, and the composite stiffness of bond-slip damaged specimens increases. As the load further increases, the bond-slip damaged specimens enters the last stage (the second descending part), and the stiffness of bond-slip damaged specimens drops sharply.

As the confinement effect of the outer tube is inadequate due to the increase of the diameter-thickness ratio, a high diameter-thickness ratio would decrease the stiffness of the bond-slip damaged specimens, shorten the recovery part of load-stiffness curve and aggravate the stiffness degradation.

Fig.11. shows the effect of expansion ratio on the stiffness of bond-slip damaged specimens. In the horizontal part and the descending part, the influence of the expansion ratio on the load-stiffness curve of bond-slip damaged specimens is not significant. The axial stiffness is mainly related to the steel tube. The bond-slip damaged specimens with a higher expansion ratio has a longer recovery part, a shorter second descending part with a rapid stiffness degradation. This may come from that the premature development of SSAC micro-cracks can be confined effectively by the outer steel tube. However, the development of SSAC micro-cracks couldn't be confined by the yielding steel tube at the later loading stage, and the core SSAC with a higher expansion ratio is more likely to crush without the effective constraint of outer steel tube.

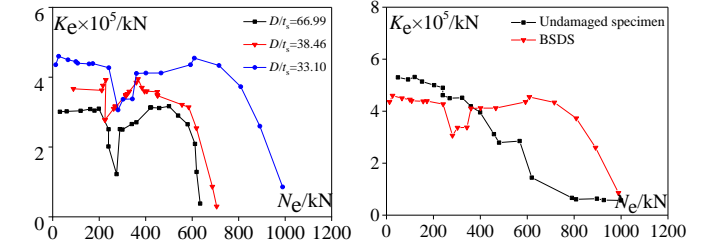


Fig. 10 Effect of D/t_s on stiffness

Fig. 11 Effect of E_s on stiffness

Specimens TCZY4-2 and ZY8-2 are employed to investigate the effect of bond-slip damage on load-stiffness curves, as shown in Fig.12. Compared with the bond-slip damaged specimens, the early stiffness of undamaged specimen is larger, this is mainly because the early stiffness of undamaged specimen is the combined stiffness, while the early stiffness of bond-slip damaged specimens is approximate equal to that of the outer steel tube. When the loading plate reaches to SSAC, the stiffness of bond-slip damaged specimens increases. As the load further increases, the load-stiffness curves of bond-slip damaged specimens and undamaged specimen tend to overlap.

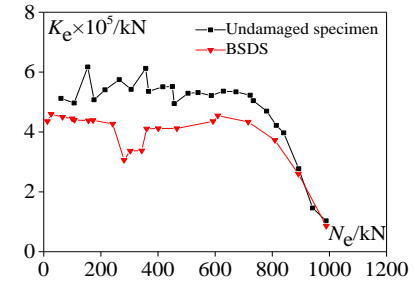
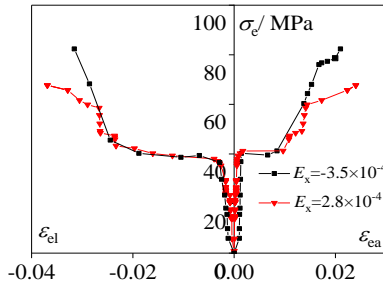
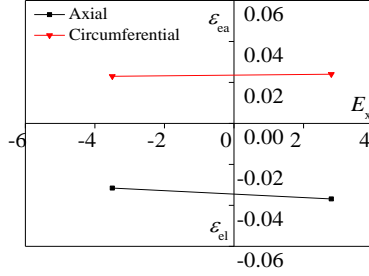


Fig. 12 Effect of bond-slip damage on load-stiffness curves

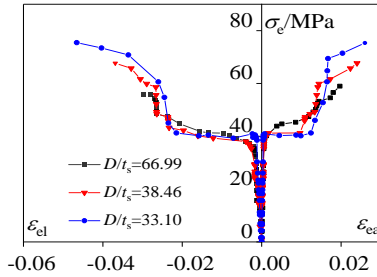
4.4. Stress-strain

The effects of expansion ratio and diameter-thickness on stress-strain relationship of bond-slip damaged specimens are depicted in Fig.13. - Fig.16, where ϵ_{ea} , ϵ_e are the measured circumferential strain and axial strain at middle height of specimen.

The expansion ratio has a little influence on the bond-slip damaged specimens in the elastic and elastoplastic stages. The stress-strain curves of bond-slip damaged specimens with two expansion ratios are approximate consistent in these two stages. However, the bond-slip damaged specimens with higher SSAC expansion ratio has a larger slope in the hardening stage, as shown in Fig.13. This is mainly because the premature development of the SSAC micro-cracks can be confined effectively by the steel tube, and the early stiffness degeneration ratio is low with higher expansion ratio. The ultimate axial and circumferential strains increase as the expansion ratio increase, while the influence of the expansion ratio on the circumferential strain is more obvious, as shown in Fig.14. For example, the ultimate axial and circumferential strains of the specimen with diameter-thickness ratio of 38.46 increase by 16.9% and 4.5% respectively, when increasing the expansion ratio from -3.5×10^{-4} to 2.8×10^{-4} .

Fig. 13 Effect of E_x on stress-strain relationshipFig. 14 Effect of E_x on ultimate strain

The influence of diameter-thickness ratio on the stress-strain relationship is not obvious in the first and second stages. In the hardening stage, the slope of bond-slip damaged specimens decreases as the diameter-thickness ratio increases, as shown in Fig.15. This may come from that the increase in the diameter-thickness ratio decreases the composite stiffness of bond-slip damaged specimens in the hardening stage.

Fig. 15. Effect of D/t_s on stress-strain relationship

The ultimate axial and circumferential strains decrease as the diameter-thickness ratio of bond-slip damaged specimens increases, as shown in Fig.16. This is mainly because the confinement effect of outer steel tube on core SSAC decreases as the diameter-thickness ratio increases, and outward buckling failure of core SSAC is more likely to occur, leading to the decrease of ultimate strains.

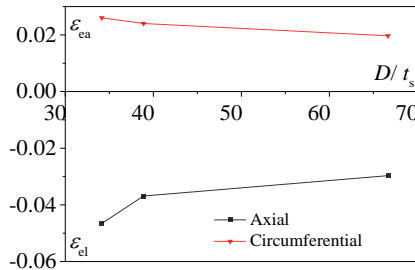
Fig. 16 Effect of D/t_s on ultimate strain

Fig.17. depicts the stress-strain relationship of specimens TCZY4-2 and ZY8-2. Compared with the undamaged specimen, an additional hardening stage is appeared in the stress-strain relationship curve of bond-slip damaged specimens. The ultimate axial and circumferential strains of the bond-slip damaged specimens are obvious greater than those of the undamaged specimens. However, the ultimate stress of bond-slip damaged specimens is approximate consistent with that of the undamaged specimens.

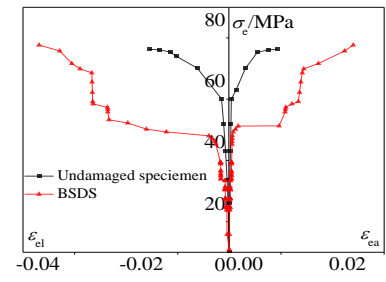


Fig. 17 Effect of bond-slip damage on stress-strain curves

5. Design recommendations

In this part, the applicability of the current CFST design methods for predicting the bearing capacity of bond-slip damaged specimens is examined. The ultimate bearing capacity of bond-slip damaged specimens estimated by GB50936-2014, AIJ-CFT (1997), ANSI/AISC360-16 (2016), and Eurocode 4 (2004) are compared to the test data.

5.1. Chinese code GB50936-2014[25]

On the basis of a large number of experimental and analytical investigations, the unified theory is adopted for predicting the strength of CFST members under axial compression in Chinese code GB50936-2014. The formula is as follow.

$$N \leq N_u = f_{sc} A_{sc} \quad (2)$$

$$f_{sc} = (1.212 + B\theta + C\theta^2) f_c \quad (3)$$

$$B = 0.176 f_y / 213 + 0.974 \quad (4)$$

$$C = -0.104 f_c / 14.4 + 0.031 \quad (5)$$

where f_{sc} represents the design value of compressive strength of CFST member, A_{sc} denotes the section area of CFST member, B , C are the calculated coefficient, which are fitted by a large number of experimental results, θ is the confinement index, $\theta = f_y A_s / f_c A_c$.

5.2. Japan code AIJ-CFT (1997) [26]

In Japan code AIJ-CFT, the axial strength of CFST member is calculated by proportionally combining the bearing capacity of internal concrete and external steel tube. The formula for predicting the strength of CFST under axial load is as follow.

$$N = 1.27 A_s F + k f_{cd} A_c \quad (6)$$

$$F = \min(f_y, 0.7 f_u) \quad (7)$$

in which, F is the characteristic value of strength of steel tube, f_u is the ultimate bearing capacity of steel tube, k is the reduction coefficient of compressive strength of concrete cylinder, and $k = 0.85$.

5.3. American specification - ANSI/AISC 360-16 (2016) [27]

The specification evaluates the overall stability of composite members through the conventional stability design equation as provided in Eq. (8). The contribution of the inner concrete is converted into the nominal compressive strength of steel given in Eq. (9). The strength of CFST members could be designed according to pure steel components.

$$N = \phi_c P_n \quad (8)$$

$$\begin{cases} P_n = P_{no} 0.658^{P_{no}/P_c} & P_{no}/P_c \leq 2.25 \\ P_n = 0.877 P_c & P_{no}/P_c \geq 2.25 \end{cases} \quad (9)$$

in which, N denotes the design value of axial compression column, P_n is nominal axial strength; $\phi_c = 0.75$; $P_{no} = f_y A_s + 0.85 f_{cd} A_c + f_{ysr} A_{sr}$; f_{ysr} and f_y are the specified yield stress of reinforcing bars and steel section, respectively; f_{cd} is the specified concrete compressive strength; A_c , A_s , and A_{sr} were the cross-sectional area of steel, concrete, and reinforcing bars, respective-

ly; P_e represents the elastic critical buckling load, $P_e = \pi^2(EI_{eff})/(KL)^2$; K is the effective length factor; L is the laterally unbraced length of the member; $EI_{eff} = E_c I_s + 0.5E_s I_{sr} + C_1 E_c I_c$; EI_{eff} is the section effective bending stiffness; E_c and E_s are Young's modulus of concrete and steel, respec-

tively; I_c , I_s and I_{sr} are the moment of inertia of concrete, steel tube, and reinforcing bars about the section elastic neutral axis, respectively; $C_1 = 0.1 + 2A_s/(A_c + A_s) \leq 0.3$.

Table 5

Contrast between theoretical calculated and experimental results of columns

Specimen number	Experimental data	GB50936-2014		AIJ-CFT (1997)		ANSI/AISC 360-16 (2016)		Eurocode 4 (2004)	
	N_u /kN	N_{c1} /kN	$\frac{N_u}{N_{c1}}$	N_{c2} /kN	$\frac{N_u}{N_{c2}}$	N_{c3} /kN	$\frac{N_u}{N_{c3}}$	N_{c4} /kN	$\frac{N_u}{N_{c4}}$
TCZY1-1	656	525	1.25	439	1.49	319	2.06	573	1.15
TCZY2-2	704	709	0.99	583	1.21	425	1.66	742	0.95
TCZY3-1	976	758	1.29	610	1.60	462	2.11	876	1.11
TCZY4-2	1134	937	1.21	747	1.52	563	2.01	1038	1.09
TCZY5-1	1016	827	1.23	731	1.39	506	2.01	967	1.05
TCZY6-2	1153	1003	1.15	866	1.33	606	1.90	1126	1.02
Mean of N_u/N_e		1.1866		1.4235		1.9589		1.0627	
Mean square error of N_u/N_e		0.0092		0.0170		0.0222		0.0042	

Note: N_u denotes the experimental ultimate bearing capacity, N_e stand for the calculation result according to various specifications.

5.4. European specification - Eurocode 4 (2004) [28]

In European specification - Eurocode 4, the full section of specimen coming into plasticity is assumed for estimating the strength of CFST members under axial load. That is, when the axially loaded CFST members reaches the ultimate strength, the outer steel tube and the concrete core reach their ultimate compressive bearing capacity, simultaneously.

$$N \leq \chi N_u \quad (10)$$

$$N_u = \eta_{ao} f_y A_s + f_{cd} A_c (1 + \eta_{co} f_{yk} / df_{ck}) + f_{ysr} A_{sr} \quad (11)$$

Where N_u represents the plastic axial capacity of the composite section; χ is the reduction factor; η_{ao} and η_{co} are the factors related to the confinement of concrete; f_{ck} is the concrete cylinder characteristic compressive strength measured from the compressive test at 28 days; f_{yk} is the steel characteristic yield strength.

Comparisons between the theoretical predicted values form the test results and the above CFST design specifications are shown in Table.5. American ANSI/AISC 360-16(2016) and Japan AIJ-CFT(1997) underestimate the strength of bond-slip damaged specimens under axial compression, and Chinese GB50936-2014 is a little conservative. The average difference between the test data and the predicted values by the Eurocode 4 (2004) is 1.063, and the mean square error is 0.004, which indicates that the Eurocode 4 (2004) has a high precision. Therefore, it's recommended to adopt the Eurocode 4 (2004) to estimate the ultimate bearing capacity of bond-slip damaged specimens under axial compression.

6. Conclusions

Six bond-slip damaged specimens and two undamaged specimens are designed and tested in this study. The influences of the diameter-thickness ratio, the expansion ratio and bond-slip damage on the bearing capacity, longitudinal displacement, stiffness and strain of specimens are analyzed and discussed. The bearing capacity of bond-slip damaged specimens is evaluated by the current CFST specifications. The main conclusions can be drawn as follows.

(1) The failure process of undamaged specimens presents three stages as elastic, elastoplastic, and plastic stages. An additional hardening stage can be found in the bond-slip damaged specimens. The failure modes of both bond-slip damaged specimens and undamaged specimen are outward deformation.

(2) The ultimate strength of bond-slip damaged specimens would be decreased by increasing the diameter-thickness ratio. Contrarily, the increase of the expansion ratio would bring benefits to bond-slip damaged specimens. The bond-slip damage has a little influence on the ultimate strength.

(3) The initial damage reduces the member stiffness. The ultimate displacement of bond-slip damaged specimens is larger than that of the undamaged specimen. The increase of the diameter-thickness ratio decreases the ultimate displacement of bond-slip damaged specimens, while the effect of

expansion ratio on the ultimate displacement of bond-slip damaged specimens is not significant.

(4) The increase in the diameter-thickness ratio would weaken the confine effects on the inner concrete, which reduces the stiffness of the bond-slip damaged specimens and aggravates the stiffness degradation. The early stiffness of undamaged specimen is larger than that of bond-slip damaged specimens. With the deformation increasing, the stiffness of the two series specimens become comparable.

(5) The specimens with the large expansion ratio or the small diameter-thickness ratio have superior strain capacity.

(6) The accuracy of the CFST design specifications for estimating the strength of the bond-slip damaged specimens is evaluated. The comparisons illustrate the method in Eurocode 4 (2004) can provide the most coherent results for bond-slip damaged specimens than other specifications.

Acknowledgements

This study was funded by the National Natural Science Foundation of China (No. 51578001, 51878002, 51608003, and 51008001), Key Research and Development Plan of Anhui Province (No. 1704a0802131), and the Outstanding Young Talent Support Program of Anhui Province (No. gxyqZD2016072).

References

- [1] Jiang Y., Ling T.C., Shi C.J. and Pan S.Y., "Characteristics of steel slags and their use in cement and concrete—a review", *Resources Conservation and Recycling*, 136, 187-197, 2018.
- [2] Mayes W.M., Younger P.L. and Aumônier J., "Hydrogeochemistry of alkaline steel slag leachates in the uk", *Water Air and Soil Pollution*, 195(1-4), 35-50, 2008.
- [3] Roslan N.H., Ismail M., Abdulmajid Z., Ghoreishamiri S. and Muhammad B., "Performance of steel slag and steel sludge in concrete", *Construction and Building Materials*, 104, 16-24, 2016.
- [4] Saxena S. and Tembhurkar A.R., "Impact of use of steel slag as coarse aggregate and wastewater on fresh and hardened properties of concrete", *Construction and Building Materials*, 165, 126-137, 2018.
- [5] Han F. and Zhang Z., "Properties of 5-year-old concrete containing steel slag powder", *Powder Technology*, 334, 27-35, 2018.
- [6] Santamaria A., Orbe A. and José JTS., "A study on the durability of structural concrete incorporating electric steelmaking slags", *Construction and Building Materials*, 161, 94-111, 2018.
- [7] Wang Q., Wang D. and Zhuang S., "The soundness of steel slag with different free CaO and MgO contents", *Construction and Building Materials*, 151, 138-146, 2017.
- [8] Shanahan N. and Markandeya A., "Influence of slag composition on cracking potential of slag-portland cement concrete", *Construction and Building Materials*, 164, 820-829, 2018.
- [9] Pang B., Zhou Z. and Xu H., "Utilization of carbonated and granulated steel slag aggregate in concrete", *Construction and Building Materials*, 84, 454-467, 2015.
- [10] Liu J. and Wang D., "Influence of steel slag-silica fume composite mineral admixture on the properties of concrete", *Powder Technology*, 320, 230-238, 2017.
- [11] Han L.H., Li W. and Bjorhovde R., "Developments and advanced applications of concrete-filled steel tubular (CFST) structures: members", *Journal of Constructional Steel Research*, 100, 211-228, 2014.
- [12] Shi Y.L., Wang Y.W. and Wang W.D., "Analytical behavior of concrete-filled steel tubular stub column with internal steel reinforced under axial compression", *Earthquake Resistant*

- Engineering & Retrofitting, chain, 2013.
- [13] Chen J., Wang J. and Li W., "Experimental behaviour of reinforced concrete-filled steel tubes under eccentric tension", *Journal of Constructional Steel Research*, 136, 91-100, 2017.
- [14] Zhou T., Jia Y., Xu M., Wang X. and Chen Z., "Experimental study on the seismic performance of L-shaped column composed of concrete-filled steel tubes frame structures", *Journal of Constructional Steel Research*, 114, 77-88, 2015.
- [15] Chen Y., Feng R., Shao Y. and Zhang X., "Bond-slip behaviour of concrete-filled stainless steel circular hollow section tubes" *Journal of Constructional Steel Research*, 130, 248-263, 2017.
- [16] Tomii M., "Bond Check for Concrete-Filled Steel Tubular Columns", *Composite & Mixed Construction*, ASCE, 2015.
- [17] Tao Z., Song T.Y., Uy B. and Han L.H., "Bond behavior in concrete-filled steel tubes", *Journal of Constructional Steel Research*, 120, 81-93, 2016.
- [18] Ferhoun N., "Experimental behaviour of cold-formed steel welded tube filled with concrete made of crushed crystallized slag subjected to eccentric load", *Thin-Walled Structures*, 80(1), 159-166, 2014.
- [19] Zeghiche, N. F. J., Numerical analysis of cold-formed steel welded tube filled with, concrete made of crystallized slag aggregate. *International Journal of Applied Electromagnetics & Mechanics*, 16(1), 112, 2014.
- [20] Wei J.G., Huang F.Y. and Chen B.C., "Research on the influence of initial stress to ultimate load carrying capacity of concrete filled steel tubular (single tube) arches", *Engineering Mechanics*, 27(7), 103-112, 2010.
- [21] Xiong D.X., Zha X.X., "A numerical investigation on the behaviour of concrete-filled steel tubular columns under initial stresses", *Journal of Constructional Steel Research*, 63(5), 599-611, 2007.
- [22] Hu J.L., Yan Q.S., Yu X.L. and Zheng H.B., "Ultimate bearing capacity analysis of concrete filled steel tubular arch considering the initial defects' influence", *Advanced Materials Research*, 446-449, 1248-1251, 2012.
- [23] Standard Test Method for Long-term and Durability of Ordinary Concrete Use of GB/T50082-2009., *Architecture and Building Press*, Beijing, China, 2009.
- [24] Method of Tensile Test at Room Temperature Use of GB/T228-2010., *Architecture and Building Press*, Beijing, China, 2010.
- [25] Technical Code for Concrete Filled Steel Tubular Structures Use of GB50936-2014., the Ministry of housing and urban-rural development of the people's republic of China, Beijing, China, 2014.
- [26] Design Method for Concrete Filled Steel Tubular Structures., the Japan institute of architecture, Japan, 1997.
- [27] Specification for Structural Steel Buildings (ANSI/AISC-360-16)., Chicago, Illinois, American: AISC Committee, 2016.
- [28] Design of Composite Steel and Concrete Structures., European Committee for Standardization, European, 2004.

MULTI-STOREY COMPOSITE FRAMED-STRUCTURES DUE TO EDGE-COLUMN LOSS

Guo-qiang Li ^{1,2}, Jing-zhou Zhang ^{1,*} and Jian Jiang ³

¹ College of Civil Engineering, Tongji University, Shanghai, China

² State Key Laboratory for Disaster Reduction in Civil Engineering, Shanghai, China

³ Jiangsu Key Laboratory of Environmental Impact and Structural Safety in Engineering, China University of China University of Mining and Technology, Xuzhou, China

* (Corresponding author: E-mail: 1410206zhangjingzhou@tongji.edu.cn)

ABSTRACT

This paper proposes an analytical method to predict the progressive collapse resistance of multi-storey composite framed-structures due to different scenarios of edge column loss. These include the removal of edge-intermediate (EI) or edge-corner (EC) column. The proposed method accounts for the tensile membrane action of slabs and vierendeel effect of the steel frames. The reliability of the proposed method is verified against validated numerical simulations. Parametric studies show that for EI column loss scenario, the vierendeel effect increases the plastic capacity of the structure but has limited influence on the ultimate capacity. However, the vierendeel effect significantly enhances the structural resistance against EC column loss (>60%). It is thus over conservative to determine the progressive collapse resistance of multi-storey structures based on that of single-storey structures where no vierendeel effect is considered. Catenary action in steel beams has not noticeably developed under the removal of a corner column. In this case, it is recommended to calculate the ultimate bearing capacity of structures under a corner column removal according to the yield-line theory.

ARTICLE HISTORY

Received: 12 February 2019
Revised: 24 May 2019
Accepted: 5 September 2019

KEYWORDS

Collapse resistance;
Multi-storey;
Composite framed-structure;
Catenary action;
Vierendeel effect

Copyright © 2020 by The Hong Kong Institute of Steel Construction. All rights reserved.

1. Introduction

The concern with collapse resistance and robustness enhancement of buildings in structural design is initiated due to the accidental collapse event of Ronan Point tower in UK (1968), triggered by an explosion-induced loss of corner column at eighteenth storey [1]. Research efforts have been subsequently refocused and intensified following the collapse of Alfred P. Murrah building [2] and World Trade Center Towers [3] in USA. These events signify a growing potential for engineering buildings to suffer from extreme actions such as fire, explosion and impact, wherein they are prone to globally collapse without sufficient robustness even due to a limited local failure (i.e. disproportionate collapse). Hence, mitigating the susceptibility of structures against disproportionate collapse is of great importance in view of the potential casualties and property losses in case of collapse.

Composite framed-structures with steel skeletons and concrete floor systems have been widely used in various buildings due to their high constructional efficiency and excellent seismic performance [4]. In the case of a column loss, tensile membrane actions in reinforced-concrete slabs and catenary actions in steel beams are mobilized at large deflections to prevent the potential progressive collapse of composite framed-structures. Currently, experimental studies have been extensively launched to investigate the global performance of three-dimensional composite framed-structures due to a column loss [5-8]. Column removal tests by Johnson et al. [5] indicated that common composite framed-structures generally had significant capabilities to redistribute loads even without particular construction measures against progressive collapse. However, the ultimate bearing capacities of these structures failed to satisfy those required under the extreme event. In the experiments by Fu et al. [8], the effects of the composite action degree between slabs and beams, slab aspect ratio and boundary condition of the substructure on the progressive collapse resistance were investigated. It was concluded that the capability of vertical load redistribution was mainly influenced by the slab aspect ratio and connection ductility. Composite action had limited effect on the collapse resistance of substructures. Considering the huge financial cost of experimental studies, numerical analyses on the progressive collapse resistance of composite framed-structures have been successively carried out [9-12]. In the simulation models from Alashker et al. [11], the effects of structural parameters including steel deck thickness, slab reinforcement and the number of bolts in the shear tab on the behavior of structural systems were studied. It was found that the collapse resistance of structures was mainly provided by the steel deck. Increasing the number of bolts failed to significantly enhance the overall collapse resistance. Li et al. [12] numerically studied the robustness of a composite framed-structure in several column loss scenarios (external and interior columns in lower, middle and upper floors). The results revealed that compared with the lower-storey

column loss, less robustness against progressive collapse was found in the upper-storey column loss scenario.

Research involving robustness analysis essentially aim to facilitate the structural safety design in practice. However, when the structural parameters change, relaunching the experimental and numerical investigations can be costly. Hence analytical method with simple calculations is more necessary to quantitatively guide the structural safety design. Such analytical studies focusing on the collapse resistance of composite framed-structures are relatively rare in the literature [13-16]. Izzuddin et al. [13] proposed an assessment framework to investigate the robustness of composite framed-structures due to an edge-intermediate column loss, wherein the structure was simplified to steel-concrete composite beams which facilitated its application in practical engineering. However, it failed to fully account for the beneficial effect of tensile membrane action in the floor systems, thus leading to less accuracy of the method to certain extent. Li et al. [14] analytically dealt with the collapse resistance of composite framed-structures due to an edge-intermediate column loss, wherein the contribution percentage of the slab and steel skeleton to the total resistance of the structure were quantified, respectively. However, the objective of their research was limited to single-storey structures, wherein the conclusions were questionable for multi-storey structures. Fig. 1 shows the difference of bending moment distribution between typical single-storey and multi-storey (taking two-storey

for example) structures due to a side column loss. It can be seen that for two-storey framed-structures, bending moment along beam section reverses its direction near the beam-column connection. The positive bending moment emerging at the beam end therefore increases the effective bending stiffness of the beam. This phenomenon, named as vierendeel effect, can enhance the plastic bearing capacity of two-storey framed-structures to more than twice that of corresponding single-storey framed-structures.

In general, analytical approaches on collapse resistance of composite framed-structures, accounting for both tensile membrane actions in floor systems and vierendeel effect in steel skeletons are rare. What's more, compared with the edge-intermediate and interior column loss scenarios, the edge-corner column loss scenario is always ignored considering its small probability of occurrence. These limitations in recent research impede the development of structural safety design of multi-storey buildings.

Accordingly, this paper proposed an energy-based method to directly predict the behavior of multi-storey composite framed-structures consisting of steel beams and concrete slabs due to an edge-column loss. It includes the removal of edge-intermediate (EI) or edge-corner (EC) column. The membrane action in the concrete floor systems and vierendeel effect in the multi-storey steel frames were fully considered. Simplified resistance-displacement curves were proposed to capture the primary mechanical features of structures at large deflections. The reasonability and

reliability of the proposed analytical method were verified against validated numerical analyses.

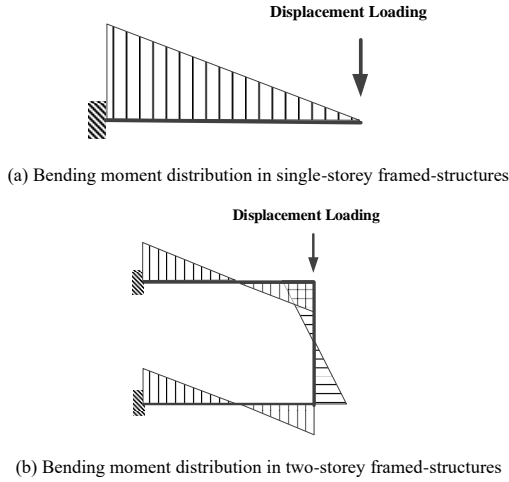


Fig. 1 Development of vierendeel effect in two-storey framed-structures due to a side column loss

2 Analytical method

2.1. Model simplification

To evaluate the robustness of a structure subjected to an edge column loss, the most reasonable approach is to directly investigate the global behavior of the remaining structure. To save the computational cost but without missing the key mechanical characteristics, a beam-slab substructure adjacent to the removed column was extracted and investigated for two removal scenarios: edge-intermediate (EI) column and edge-corner (EC) column, as shown in Fig.

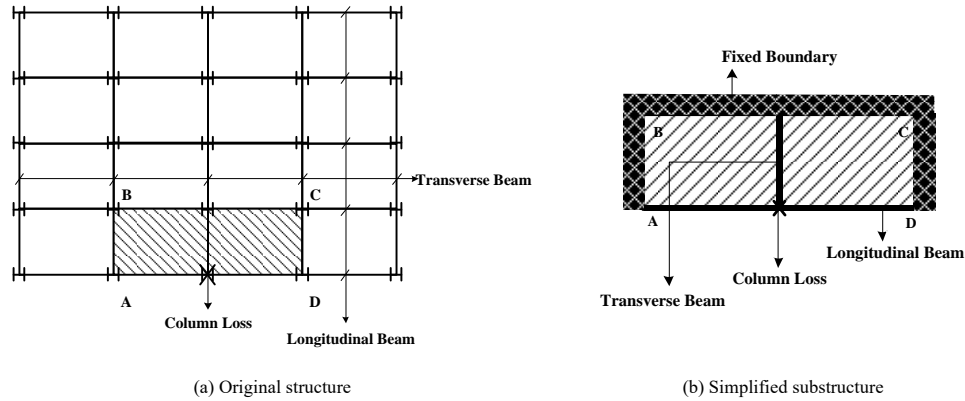


Fig. 2 Simplified model for edge-intermediate (EI) column loss

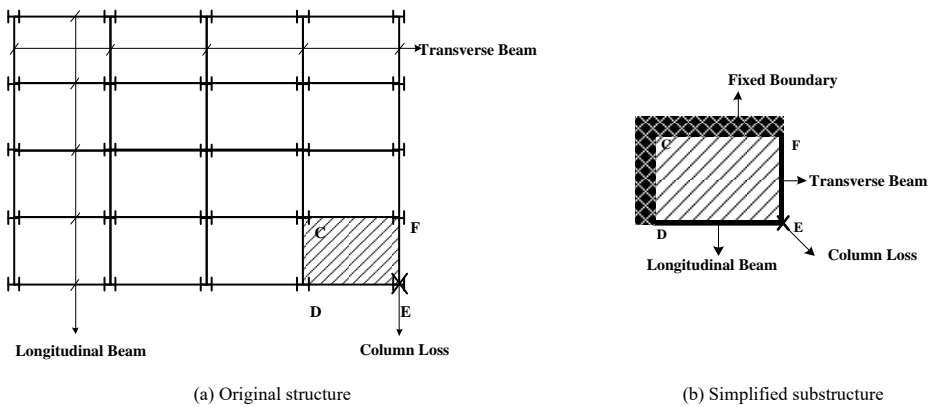


Fig. 3 Simplified model for edge-corner (EC) column loss

2.2.1. Plastic bearing capacity of multi-storey substructures due to an EI column loss

Fig. 5 illustrates the yield line pattern for single-storey substructures. The

2 and Fig. 3, respectively. For the scenario of EI column loss, the substructure ABCD was extracted from the whole structure, wherein the boundary conditions for edges AB, BC and CD are assumed to be fully restrained due to surrounding substructures. Edge AD was assumed to be free. In the case of EC column loss, analogously, the edges CD and CF were postulated to be fixed, and the edges DE and EF were left to be free. The reasonability of this simplification has been verified by Zhang and Li [16], wherein the resistance-displacement curves for the full structures and extracted substructures due to a middle column loss were compared. It was concluded that the plastic bearing capacity of the whole structure was slightly smaller than that of the simplified substructure. At large deflections, the progressive collapse resistance for the substructure agreed well with that of the corresponding full structure. Therefore, in the following sections, the full structure was represented by the idealized corresponding substructure. This study focused on the steel moment frame with flat concrete slab (the steel deck being excluded), where all steel beams were fully welded to the columns and no secondary beam was considered. The strength of the welding was identical to that of the steel beam.

2.2. Edge-intermediate (EI) column removal scenario

A tri-linear resistance-displacement curve was analytically determined by Li et al. [14] for single-storey substructures due to an EI column loss. This curve is found to be also suitable for multi-storey substructures in the event of an EI column loss. As shown in Fig. 4, F_y and F_u are the plastic and ultimate bearing capacity of the substructure, respectively. The determination of v_A and v_B was described in reference [14]. The failure displacement v_c can be calculated from the current building regulation [17]. However, herein the displacement v_c was directly obtained from numerical analyses to achieve a fair comparison between the numerical and analytical ultimate bearing capacity. For given F_y and F_u , the resistance-displacement curve can be determined for multi-storey substructures due to an EI column loss. The plastic and ultimate bearing capacity of multi-storey substructures were determined as follows

positive plastic hinge of the steel beam in Y-direction was not accounted for considering that the boundary condition at beam end C is free. However, for the yield line pattern of multi-storey substructures shown in Fig. 6, positive

moment hinges were assumed to emerge at the end of the transverse beams CG and DH, due to the rotational restraints provided by the column CD (shown in Fig. 7). The deflection at the removed column location (Point D) was assumed to be 1. Based on the yield-line theory, the total internal work done due to the rotation in plastic hinges and along the yield lines is given by (the curved negative yield lines A₁A and E₁E are assumed to be linear, with length l)

$$W_{in} = \sum_{i=1}^N \left(\frac{2\alpha_i M_{yi} l_i}{l_i} + \frac{2M_{xi} l_i}{\alpha_i L_i} + \frac{2M'_{xi} l_i}{\alpha_i L_i} + \frac{2(M_{LNi} + M_{LPi})}{\alpha_i L_i} + \frac{M_{TNi} + M_{TPi}}{l_i} \right) \quad (1)$$

where N is the total storey number; i is the number of a certain storey; M'_{xi} and M_{xi} are the negative and positive yield bending capacity per unit width of slabs about Y direction at storey i , respectively; M_{yi} is the positive yield bending capacity per unit width of slabs about X direction at storey i ; M_{LNi} and M_{LPi} are the negative and positive plastic capacity of beams in X direction at storey i , respectively; M_{TNi} and M_{TPi} are the negative and positive plastic capacity of beams in Y direction at storey i , respectively. The development of M_{TPi} is dependent on the column plastic bending capacity. M_{TPi} was determined as the minimum value of the plastic bending capacity of the transverse beam and column. The value of parameter α_i should be taken as no greater than 0.5.

For a concentrated load, the work done by the external force is expressed as:

$$W_{ext} = F_y \quad (2)$$

$$F_y = \sum_{i=1}^N \left(\alpha_i B_i + \frac{A_i}{\alpha_i} + \frac{M_{TNi} + M_{TPi}}{l_i} \right) \quad (3)$$

where

$$A_i = 2 \frac{M_{xi} l_i + M'_{xi} l_i + M_{LNi} + M_{LPi}}{L_i} \quad B_i = 2 \frac{M_{yi} l_i}{l_i} \quad (4)$$

The parameter α_i can be determined according to the minimum load principle [18]:

$$\frac{dF_y}{d\alpha_i} = 0 \quad (5)$$

The solution to Eq. (5) is given by:

$$\alpha_i = \sqrt{\frac{A_i}{B_i}} \quad (6)$$

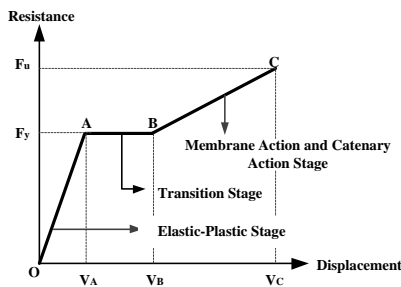


Fig. 4 Simplified resistance-displacement curve for multi-storey substructures due to an EI column loss [14]

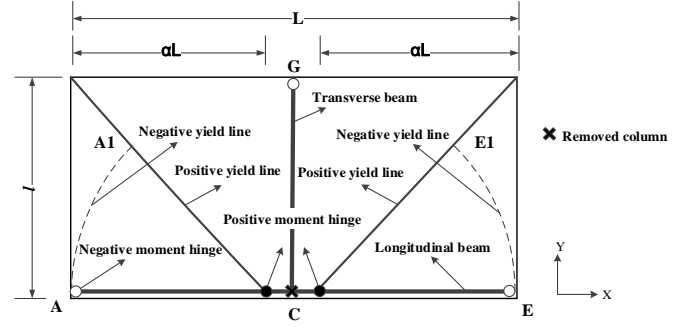


Fig. 5 Schematic of yield line pattern for single-storey substructures [14]

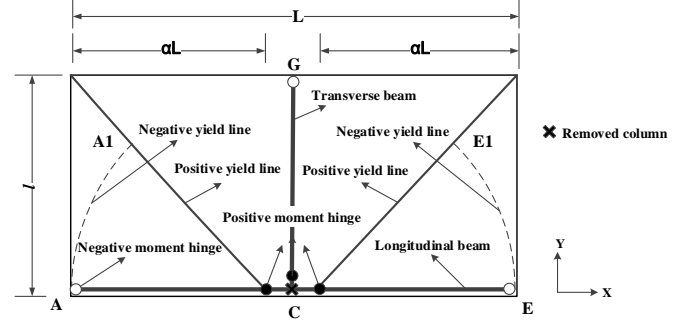


Fig. 6 Schematic of yield line pattern for multi-storey substructures

2.2.2. Ultimate bearing capacity of multi-storey substructures due to an EI column loss

The ultimate bearing capacity F_u of multi-storey substructures due to an EI column loss was determined by simply summing up the capacity for each storey of the substructure, wherein the vierendeel effect was not accounted for. The reason is shown in Fig. 8. The beam ends C and D can freely rotate due to the presence of plastic hinges at large deflections. At this moment, considering that the resisting mechanism gradually changes from bending action to catenary action in the steel beams, the ultimate bearing capacity for skeleton GCDH is essentially the sum of that for the two individual skeletons GC and HD. The detailed deduction process of ultimate bearing capacity for single-storey substructures due to an EI column loss is included in reference [14], which is derived based on the principle of minimum potential energy [19]. The ultimate bearing capacity F_u for multi-storey substructures is directly given by:

$$F_u = \sum_{i=1}^N \left(C_{xei} (T_{xi} l_i + 2F_{uLi}) + 2C_{yai} T_{yi} L_i b_i \frac{v}{2l_i} + 2C_{xai} T_{xi} l_i b_i \frac{v}{\alpha_i L_i} + 2F_{uLi} \frac{v}{\alpha_i L_i} + 2C_{ymi} M_{yi} \alpha_i \frac{L_i}{l_i} + 2C_{xmi} M_{xi} \frac{l_i}{\alpha_i L_i} + 2M'_{xi} \frac{l_i}{\alpha_i L_i} \right) \quad (7)$$

where C_{xei} represents the contribution due to extensions of rebar and steel beams at storey i ; C_{yai} and C_{xai} represent the effect of membrane force-induced bending moments at storey i ; C_{ymi} and C_{xmi} denote interactions between the tensile force and yield bending capacity of sections along yield lines at storey i . The detailed expressions of these parameters is included in reference [14].

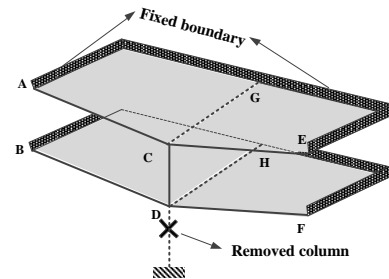


Fig. 7 Configuration of multi-storey substructures due to an EI column loss (taking a two-storey system for example)

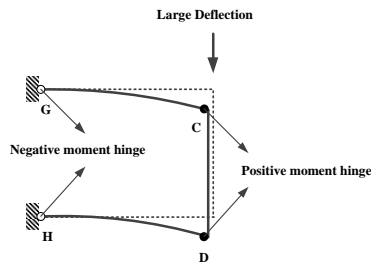


Fig. 8 Deformation configuration of skeleton GCDH at large deflections

2.3. Edge-corner (EC) column removal scenario

For a multi-storey substructure under an EC column loss, the plastic and ultimate bearing capacities were assumed to be identical in this study. This is because that in this scenario, the catenary action in cantilever steel beams fails to sufficiently develop due to its inadequate axial restraint. The resistance for the substructures due to an EC column loss is incapable of apparently re-ascending at large deflections. The deduction process of ultimate bearing capacity in this case was elucidated as follows. Fig. 9 shows the yield line pattern for single-storey substructures due to an EC column loss, wherein positive moment hinges were not considered due to the free boundary condition of beam end T. For multi-storey substructures, however, positive moment hinges were assumed to exist at the beam end T, considering the column-induced rotational restraints (shown in Fig. 10 and Fig. 11). The deflection at the location of the removed column (Point U) was assumed to be 1. The total internal work done is given by:

$$W_{in} = \sum_{i=1}^N \left(\frac{M'_{xi} l_i}{L_i} + \frac{M'_{yi} L_i}{l_i} + \frac{M_{LNi} + M_{LPi}}{L_i} + \frac{M_{TNi} + M_{TPi}}{l_i} \right) \quad (8)$$

For a concentrated load, the work done by the external force is given by:

$$W_{ex} = F_y \quad (9)$$

Thus, the yield load is calculated as:

$$F_y = \sum_{i=1}^N \left(\frac{M'_{xi} l_i}{L_i} + \frac{M_{yi} L_i}{l_i} + \frac{M_{LNi} + M_{LPi}}{L_i} + \frac{M_{TNi} + M_{TPi}}{l_i} \right) \quad (10)$$

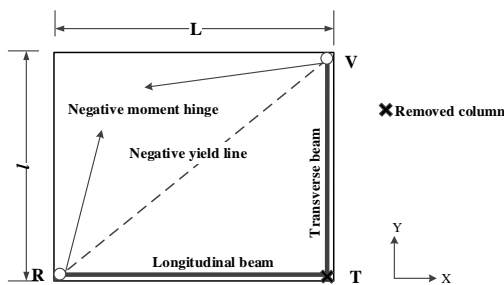


Fig. 9 Schematic of yield line pattern for single-storey substructures due to an EC column loss

3. Verifications

The multi-storey framed-structure is represented by the two-storey framed-structure in the numerical models for simplicity. In the following sections, the notations “IntT” and “IntS” were used to simply represent the case for two-storey and single-storey substructures subjected to an EI column loss, respectively. The notations “CorT” and “CorS” were used to represent the case for two-storey and single-storey substructures subjected to an EC column loss, respectively. The reliability and effectiveness of the finite element approaches being used in the numerical models have been validated against several experiments by Guo et al. [7] and. Yi et al. [20]. The Finite Element models were established in ABAQUS [21]. Eight-node solid element was used to simulate concrete slab. Two-node truss element was employed to

model rebar. Steel columns and beams are modeled by Four-node shell element. “Embedded” Command was used to connect the rebar and concrete slab. “Tie” Command was employed to connect the steel beam and concrete slab. All steel members, including the beams and columns were merged as a new assembly to achieve rigid beam-column connections. The stress-strain relationship of steel was assumed to be bi-linear. The ductile damage model was used to account for the failure of steel. The concrete was modelled by plastic damage model, wherein the compressive stress-inelastic strain and tensile stress-cracking strain relationships were defined to account for the compressive and tensile behavior of concrete, respectively. The details are included in reference [14].

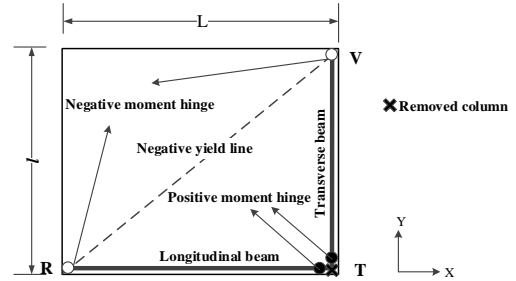


Fig. 10 Schematic of yield line pattern for multi-storey substructures due to an EC column loss

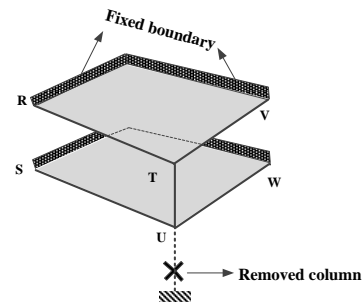


Fig. 11 Configuration of multi-storey substructures due to an EC column loss (taking a two-storey system for example)

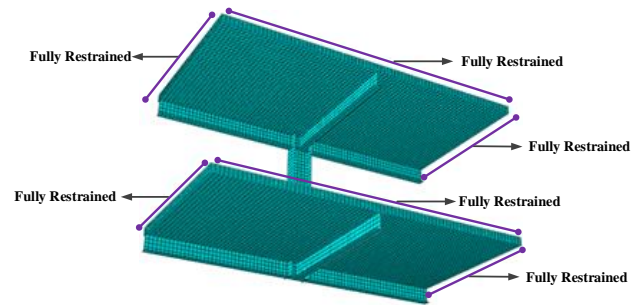


Fig. 12 Boundary conditions and mesh size of the finite element models for the IntT-series substructure

3.1. Edge-intermediate (EI) column removal scenario

A total of 13 numerical models for the IntT-series substructures were established. The boundary conditions and mesh size of the numerical models are shown in Fig. 12. Three edges (including the beam ends) of the substructure were fixed. A displacement-control loading was imposed at the predefined column-loss position of the substructure. The section dimension of the transverse beams is the same with that of the longitudinal beams. The slab has identical reinforcement in transverse and longitudinal directions. The material properties in the beam are the same to those measured in the experiment [7]. The same materials were used for the steel beams and columns. The details of the design parameters are shown in Table. 1. The substructure IntT1 is the baseline specimen. Compared with IntT1, the short span of IntT2, IntT3 and IntT4 are reduced by 12.5%, increased by 12.5% and 25%, respectively. The slab thickness of IntT5, IntT6 and IntT7 are reduced by 25%, increased by 25% and 50%, respectively. The reinforcement

Table 1

Details of the IntT-series substructures

No.	Variable	Planar Size ($L \times l$)	Slab Thickness	Reinforcement		Beam Section
				Top	Bottom	
IntT1	Aspect ratio	4000×2000	100	Φ12@120	Φ12@180	200×100×5.5×8
IntT2		4000×1750	100	Φ12@120	Φ12@180	200×100×5.5×8
IntT3		4000×2250	100	Φ12@120	Φ12@180	200×100×5.5×8
IntT4		4000×2500	100	Φ12@120	Φ12@180	200×100×5.5×8
IntT5	Slab thickness	4000×2000	75	Φ12@120	Φ12@180	200×100×5.5×8
IntT6		4000×2000	125	Φ12@120	Φ12@180	200×100×5.5×8
IntT7		4000×2000	150	Φ12@120	Φ12@180	200×100×5.5×8
IntT8	Rebar diameter	4000×2000	100	Φ14@120	Φ14@180	200×100×5.5×8
IntT9		4000×2000	100	Φ16@120	Φ16@180	200×100×5.5×8
IntT10		4000×2000	100	Φ10@120	Φ10@180	200×100×5.5×8
IntT11	Beam section height	4000×2000	100	Φ12@120	Φ12@180	120×100×5.5×8
IntT12		4000×2000	100	Φ12@120	Φ12@180	160×100×5.5×8
IntT13		4000×2000	100	Φ12@120	Φ12@180	240×100×5.5×8

Note: Dimensions in mm.

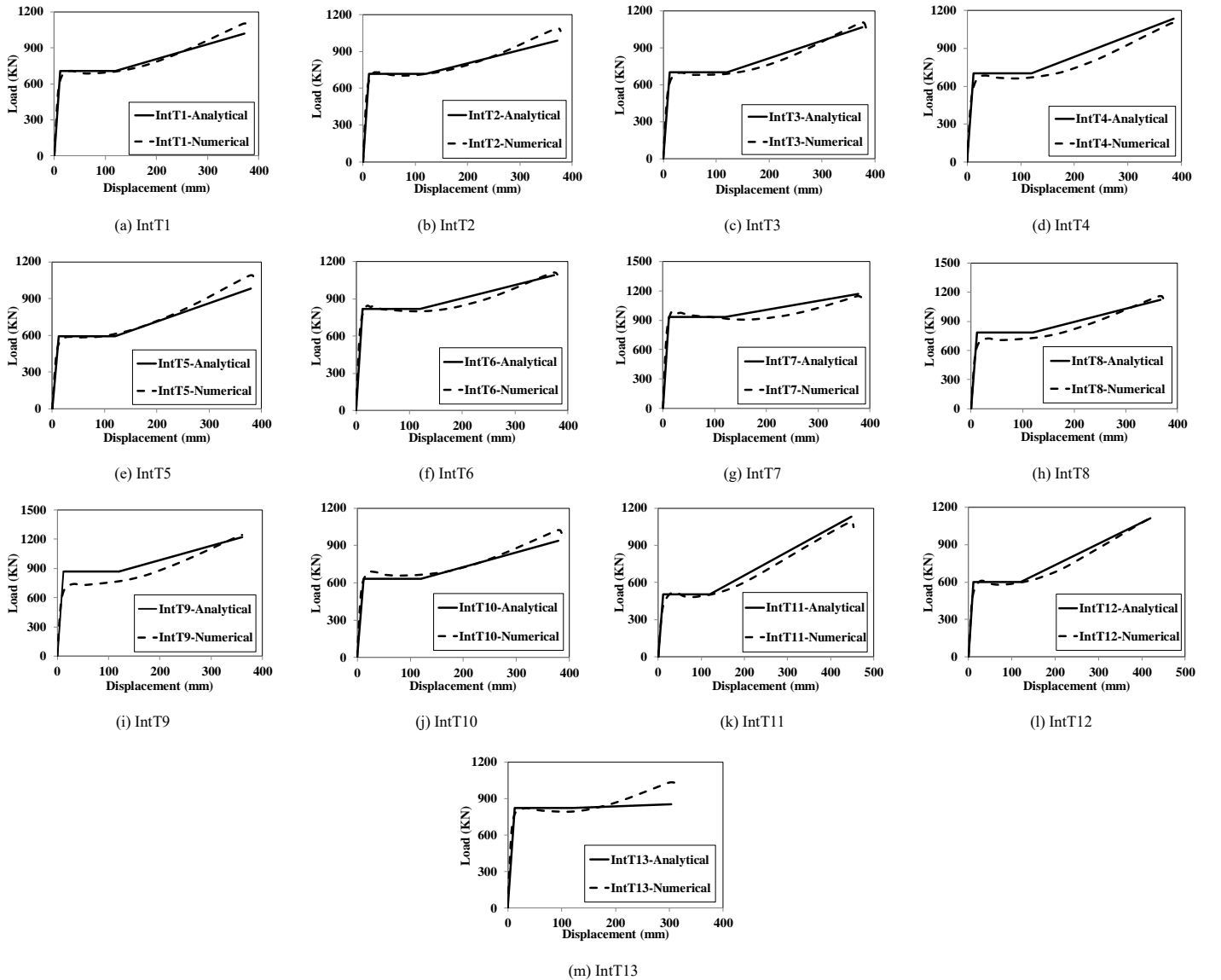
**Fig. 13** Comparisons of the numerical and analytical load-displacement curves for substructures IntT1-IntT13

Table 2

Relative errors of the analytical ultimate bearing capacity for IntT-series substructures

No.	Numerical Ultimate Capacity (kN)	Analytical Ultimate Capacity (kN)	Relative Errors (%)
IntT1	1103.8	1020.3	7.6%
IntT2	1086.9	989.3	9.0%
IntT3	1103.6	1066.5	3.4%
IntT4	1100.2	1133.6	-3.0%
IntT5	1092.5	981.0	10.2%
IntT6	1111.9	1092.9	1.7%
IntT7	1148.0	1172.1	-2.1%
IntT8	1162.7	1119.7	3.7%
IntT9	1242.8	1220.5	1.8%
IntT10	1023.9	939.7	8.2%
IntT11	1089.6	1130.2	-3.7%
IntT12	1108.7	1114.0	-0.5%
IntT13	1034.4	853.9	17.5%

ratio of IntT8, IntT9 and IntT10 are increased by 36.1% and 77.8%, reduced by 30.6%, respectively. The beam section height of IntT11, IntT12 and IntT13 are reduced by 40% and 20%, increased by 20%, respectively. The central distance between the two concrete slabs is 1.8 m. The section dimension of the steel column is 250 mm (section height) \times 200 mm (section width) \times 16 mm (flange thickness) \times 12 mm (web thickness).

The reasonability of the simplified resistance-displacement curve in Section 2.2 is exhibited in Fig. 13. For the substructures IntT1-IntT13, the main mechanical features during large deflections can be captured by the tri-linear curve. The analytical method was found to provide relatively accurate predictions on both the plastic and ultimate bearing capacity of the substructures. However, for the substructures IntT8 and IntT9, the predicted

plastic capacity was slightly greater than that for numerical analyses. This is because the reinforcement ratio of the substructures IntT8 and IntT9 are 36% and 78% greater than that of IntT1, respectively. The slab of the two substructures were over-reinforced, and thus only partial rebar along yield lines sufficiently yields. In practice, however, the substructures with over-reinforced slab should be avoided.

To further quantify the difference between the numerical and analytical ultimate bearing capacity, a relative error is defined:

$$\text{Relative error}_j (\%) = \frac{q_{j\text{-numerical}} - q_{j\text{-analytical}}}{q_{j\text{-numerical}}} \quad (11)$$

where $q_{j\text{-numerical}}$ is the numerically predicted ultimate bearing capacity; $q_{j\text{-analytical}}$ is the analytically predicted ultimate bearing capacity.

Table. 2 shows the relative errors of the analytically predicted ultimate bearing capacity for the substructures IntT1-IntT13. It can be seen that the relative errors were generally within 10%. However, a conservative error of 17.5% was found for the substructure IntT13. This is because the fracture-induced failure at the bottom flange prematurely occurred due to a large section height of the steel beams. At this limit state, the catenary action in steel beams had not sufficiently developed, wherein the enhancement of vierendeel effect on the resistance of the substructure IntT13 was not negligible. This resulted in somewhat conservative analytical predictions of ultimate bearing capacity compared with numerical results.

3.2. Edge-corner (EC) column removal scenario

A total of 13 numerical models for the CorT-series substructures were established. The boundary conditions and mesh size of the numerical models are shown in Fig. 14. Two edges (including the beam ends) of the substructure were fully restrained. The transverse beams and longitudinal beams have the same section dimensions. The slab has identical reinforcement in transverse and longitudinal directions. The material properties in the beam are the same to those measured in the experiment [7]. The same materials were used for the steel beams and columns. The details of the model parameters are shown in Table. 3. The central distance between the two concrete slabs is 1.8 m. The section dimension of the steel column is 200 mm (section height) \times 200 mm (section width) \times 16 mm (flange thickness) \times 12 mm (web thickness).

Table. 3

Details of the CorT-series substructures

No.	Variable	Planar Size ($L \times I$)	Slab Thickness	Reinforcement		Beam Section
				Top	Bottom	
CorT1	Baseline specimen	2000 \times 2000	100	$\Phi 12@120$	$\Phi 12@180$	200 \times 100 \times 5.5 \times 8
CorT2		2000 \times 1750	100	$\Phi 12@120$	$\Phi 12@180$	200 \times 100 \times 5.5 \times 8
CorT3	Aspect ratio	2000 \times 2250	100	$\Phi 12@120$	$\Phi 12@180$	200 \times 100 \times 5.5 \times 8
CorT4		2000 \times 2500	100	$\Phi 12@120$	$\Phi 12@180$	200 \times 100 \times 5.5 \times 8
CorT5		2000 \times 2000	75	$\Phi 12@120$	$\Phi 12@180$	200 \times 100 \times 5.5 \times 8
CorT6	Slab thickness	2000 \times 2000	125	$\Phi 12@120$	$\Phi 12@180$	200 \times 100 \times 5.5 \times 8
CorT7		2000 \times 2000	150	$\Phi 12@120$	$\Phi 12@180$	200 \times 100 \times 5.5 \times 8
CorT8		2000 \times 2000	100	$\Phi 14@120$	$\Phi 14@180$	200 \times 100 \times 5.5 \times 8
CorT9	Rebar diameter	2000 \times 2000	100	$\Phi 16@120$	$\Phi 16@180$	200 \times 100 \times 5.5 \times 8
CorT10		2000 \times 2000	100	$\Phi 10@120$	$\Phi 10@180$	200 \times 100 \times 5.5 \times 8
CorT11		2000 \times 2000	100	$\Phi 12@120$	$\Phi 12@180$	120 \times 100 \times 5.5 \times 8
CorT12	Beam section height	2000 \times 2000	100	$\Phi 12@120$	$\Phi 12@180$	160 \times 100 \times 5.5 \times 8
CorT13		2000 \times 2000	100	$\Phi 12@120$	$\Phi 12@180$	240 \times 100 \times 5.5 \times 8

Note: Dimensions in mm.

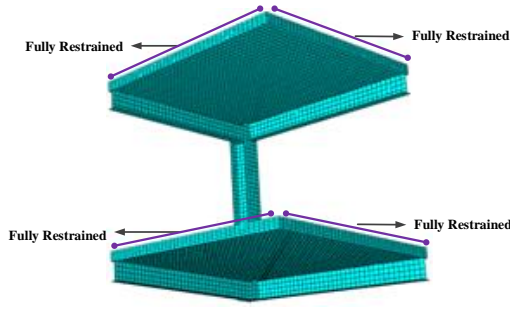


Fig. 14 Boundary conditions and mesh size of the finite element models for the CorT-series substructure

As shown in Fig. 15, the analytical method generally provided reasonable predictions on the resistance of the substructures CorT1-CorT13 at large deflections. It was concluded that the numerical resistance-displacement curves for substructures CorT1-CorT13 differed significantly from those for IntT-series substructures that they failed to apparently re-ascend at large deflections. This is because no sufficient axial restraint was provided to the cantilever steel beam in the case of EC column loss, and the catenary action was incapable of fully developing. It can be seen from Table 4 that for the substructure CorT7, the analytical ultimate bearing capacity of the substructures was larger than that for numerical analyses, with an error larger than 15%. This is because the slab thickness for the substructure CorT7 is 50% larger than that of the baseline substructure CorT1. Thus, some concrete in the

Table 4

Relative errors of the analytical ultimate bearing capacity for CorT-series substructures

No.	Numerical Ultimate Capacity (kN)	Analytical Ultimate Capacity (kN)	Relative Errors (%)
CorT1	429.4	436.8	-1.7%
CorT2	443.3	458.7	-3.5%
CorT3	410.7	420.4	-2.4%
CorT4	388.6	407.8	-4.9%
CorT5	409.9	370.8	9.5%
CorT6	453.3	502.8	-10.9%
CorT7	476.6	568.8	-19.4%
CorT8	459.5	468.3	-1.9%
CorT9	490.6	500.1	-1.9%
CorT10	402.2	405.2	-0.7%
CorT11	347.3	300.8	13.4%
CorT12	397.0	365.2	8.0%
CorT13	456.0	514.4	-12.8%

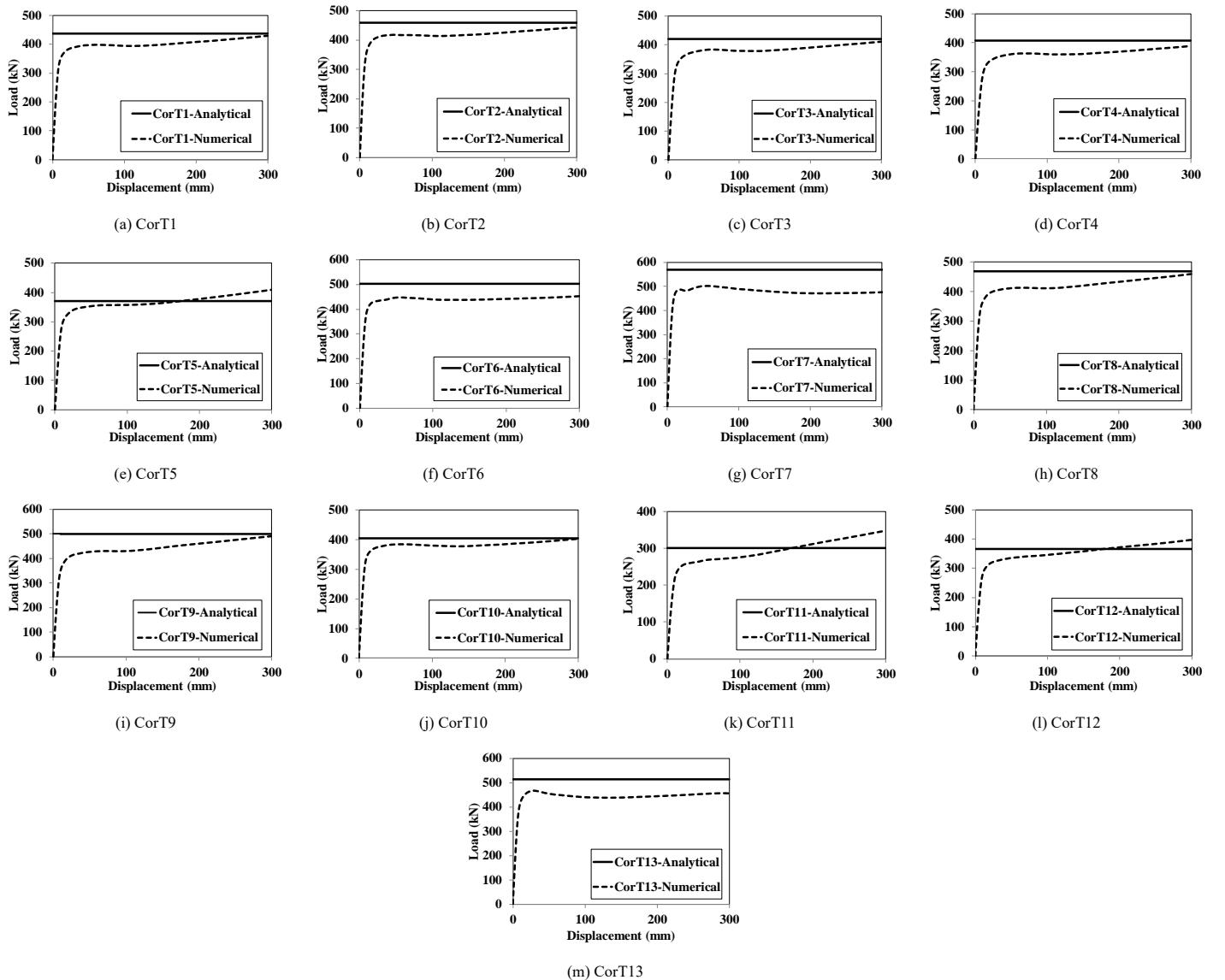


Fig. 15 Comparisons of the analytical and numerical load-displacement curves for substructures CorT1-CorT13

slab section along the yield lines crushed at the early loading stage, and the plastic bearing capacity predicted from numerical analysis was somewhat lower than that from the analytical method. However, the load-displacement curve for the substructure CorT11 re-ascended more significantly compared with that of other substructures. It is because the substructure CorT11 has a relatively small beam height, enabling the catenary action in the steel beam to develop more easily. Therefore, the analytical predictions were conservative compared with numerical predictions for the substructure CorT11.

4. Discussions

In Section 3, numerical models with various structural parameters were used to verify the accuracy of the analytical method. In this section, the contribution of vierendeel effect to the load bearing capacity of structures was discussed by a comparison of resistance-displacement curves between two-storey and single-storey framed-structures.

4.1 Edge-intermediate (EI) column removal scenario

For the IntS-series (single-storey) substructures, the details of the concrete slabs, steel beams, boundary conditions and mesh size of the numerical models were the same to those of the IntT-series (two-storey) substructures. A comparison of resistance-displacement curves for IntS-series and IntT-series substructures is shown in Fig. 16. To explicitly exhibit the potential existence of vierendeel effect in IntT-series substructures, the resistance for IntS-series substructures was doubled at the corresponding displacement. It can be seen that the resistance of the IntT-series substructures was greater than twice the resistance of the corresponding IntS-series substructures. However, the enhancement was not obvious. This is because in the case of EI column loss, the vierendeel effect merely developed in partial

portion of steel skeletons. As shown in Fig. 7, the steel skeletons ACEBDF and GCDH were firstly extracted from the structure. The bending moment distributions of the skeleton ACE for IntS-series and IntT-series substructures were the same (Fig. 17 (a) and (b)), and thus no enhancement existed in the skeleton ACEBDF. However, for the skeleton GCDH, due to the presence of the column CD, positive plastic hinges developed at the beam end C, resulting in increment in the effective bending stiffness for beams GC and HD since the point of contraflexure was shifted toward the fixed end G (Fig. 1). This yielded that the resistance for the skeleton GCDH became greater than twice that for the skeleton GC. Therefore, the vierendeel effect enhanced the resistance of two-storey substructures to a limited extent in the case of EI column loss.

4.2 Edge-corner (EC) column removal scenario

For the CorS-series (single-storey) substructures, the details of the concrete slabs, steel beams, boundary conditions and mesh size of the numerical models were the same to those of the CorT-series (two-storey) substructures. Fig. 18 shows a comparison of the resistance-displacement curves for CorS-series and CorT-series substructures. Similarly, the resistance for CorS-series substructures was doubled at the corresponding displacement. It was found that the resistance of the CorT-series substructures was remarkably greater than twice resistance of the corresponding CorS-series substructures. This is because the vierendeel effect developed in both steel skeletons RTUS and VTUW (shown in Fig. 11), which greatly enhanced the resistance of two-storey substructures (more than 60%) in the case of EC column loss. Therefore, in practical engineering design, it is over conservative to calculate the ultimate bearing capacity of two-storey structures merely based on that of single-storey structures where no vierendeel effect is considered.

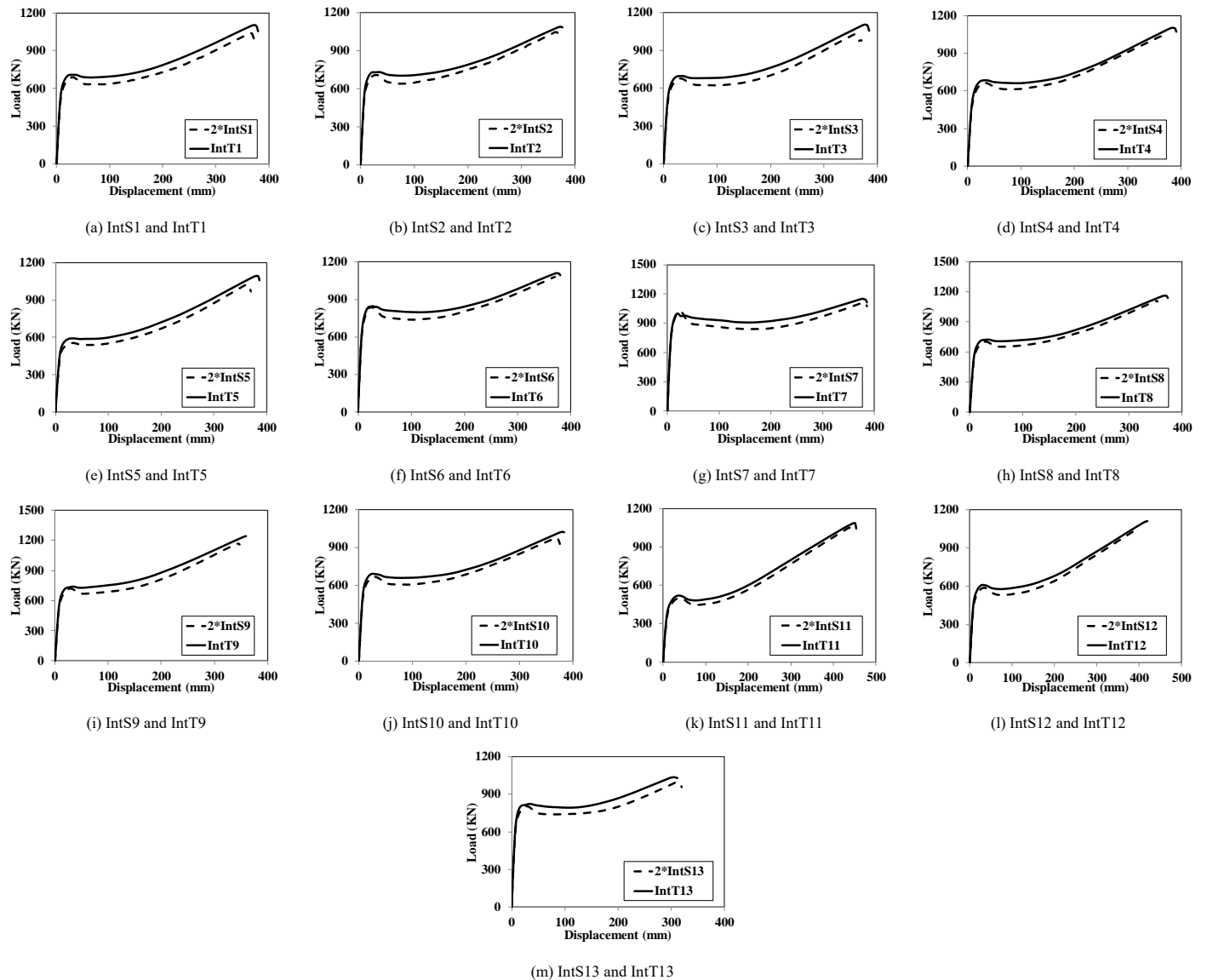


Fig. 16 Comparisons of the resistance-displacement curves for IntS-series and IntT-series substructures

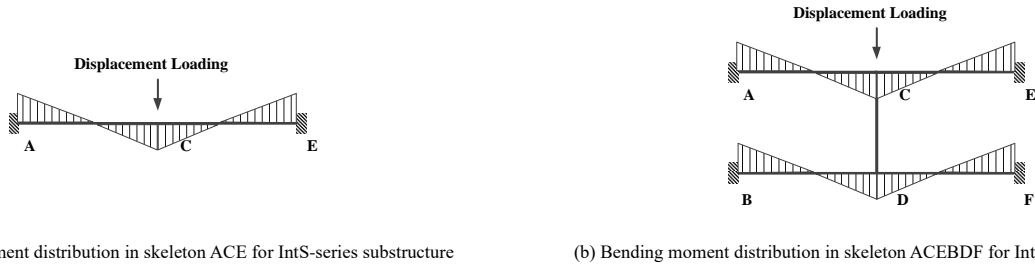


Fig. 17 Schematic of vierendeel effect in two-storey substructures subjected to EI column loss

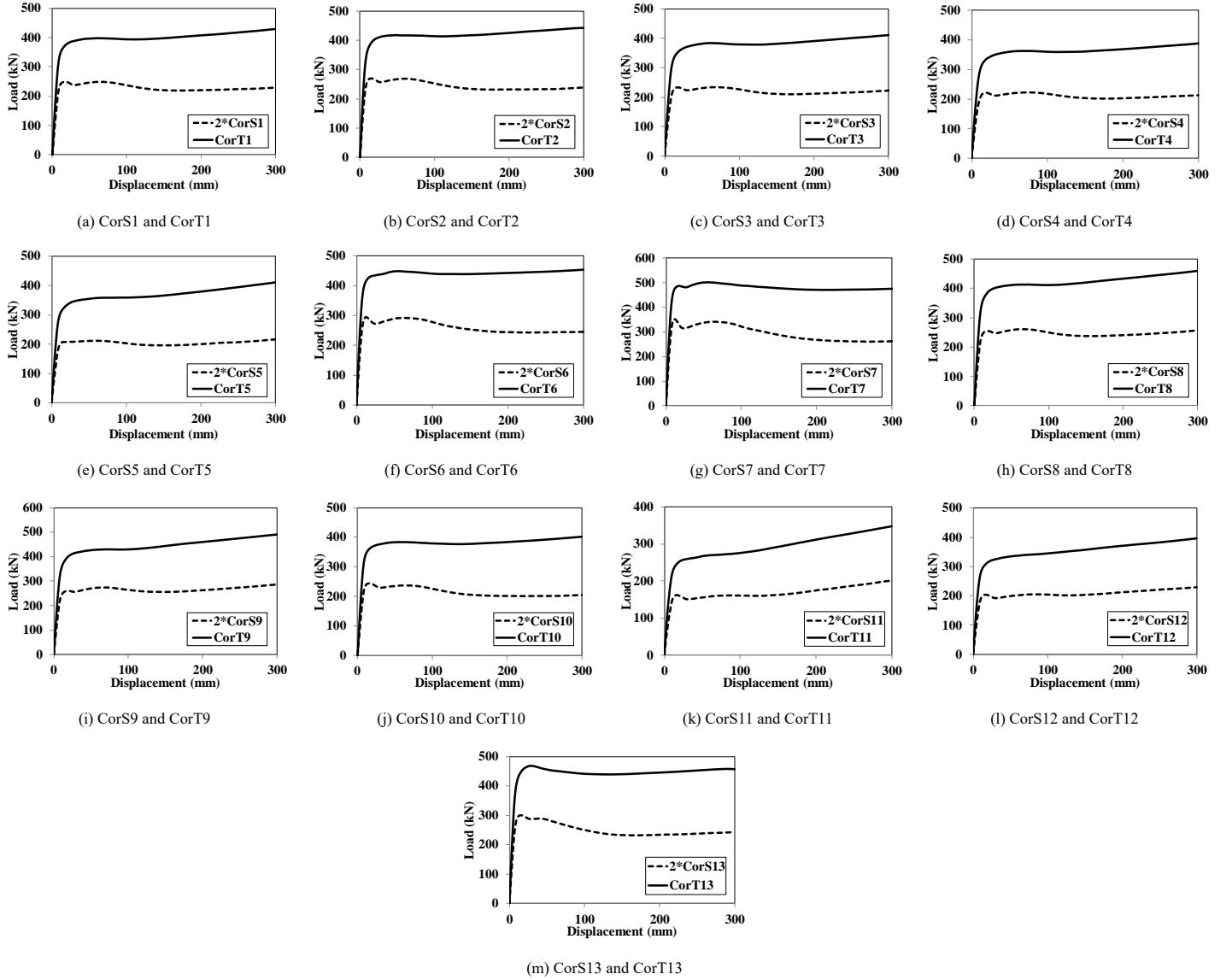


Fig. 18 Comparisons of the resistance-displacement curves for CorS-series and CorT-series substructures

5. Conclusions

This paper proposed an analytical method to quantify the progressive collapse resistance for composite multi-storey framed-structures due to an edge-column loss. Parametric studies were launched to evaluate the performance of the proposed analytical method. The contributions of vierendeel effect to the progressive collapse resistance of multi-storey structures in different edge-column loss scenarios were further analyzed. The following conclusions can be drawn from this study:

- (1) The proposed method can be used to predict the collapse resistance of the multi-storey composite structures due to an edge-column loss, with errors within 15%.
- (2) It is recommended in practical design to obtain the ultimate bearing capacity of structures due to an EC column loss based on the yield-line theory.
- (3) For EI column loss, the vierendeel effect enhances the progressive

collapse resistance of structures with limited extents. Thus, it is conservative and acceptable to obtain the progressive collapse resistance of multi-storey structures based on that of single-storey structures without considering the vierendeel effect.

- (4) For EC column loss, the vierendeel effect increases the progressive collapse resistance by more than 60%. It is thus over conservative to obtain the resistance of multi-storey structures merely from that of single-storey structures where no vierendeel effect is considered.

Acknowledgements

The work presented in this paper was supported by the Thirteen-Five Science and Technology Support Program with grant 2016YFC0701203.

References

- [1] Pearson C, Delatte N., “Ronan point apartment tower collapse and its effect on building codes”, *Journal of Performance of Constructed Facilities*, 19(2), 172-177, 2005.
- [2] Corley W.G., Sr P.F.M., Sozen M.A. and Thornton C.H., “The Oklahoma City Bombing Summary and Recommendations for Multihazard Mitigation”, *Journal of Performance of Constructed Facilities*, 12(3), 100-112, 1998.
- [3] Bazant Z.P. and Zhou Y., “Why did the World Trade Center collapse? - Simple analysis”, *Journal of Engineering Mechanics*, 128(1), 2-6, 2002.
- [4] Jiang B.H., Li G.Q., Li L.L. and Izzuddin B.A., “Experimental Studies on Progressive Collapse Resistance of Steel Moment Frames under Localized Furnace Loading”, *Journal of Structural Engineering*, 144(2), 04017190, 2018.
- [5] Johnson E.S., Meissner J.E. and Fahnestock L.A., “Experimental Behavior of a Half-Scale Steel Concrete Composite Floor System Subjected to Column Removal Scenarios”. *Journal of Structural Engineering*, 142, 040151332, 2016.
- [6] Demonceau J.F. and Jaspart J.P., “Experimental Test Simulating a Column Loss in a Composite Frame”, *Advanced Steel Construction*, 6(3), 891-913, 2011.
- [7] Guo L., Gao S., Fu F. and Wang Y., “Experimental study and numerical analysis of progressive collapse resistance of composite frames”, *Journal of Constructional Steel Research*, 89, 236-251, 2013.
- [8] Fu Q.N., Tan K.H., Zhou X.H. and Yang B., “Three-Dimensional Composite Floor Systems under Column-Removal Scenarios”, *Journal of Structural Engineering*, 144(10), 04018196, 2018.
- [9] Nethercot D.A., Stylianidis P., Izzuddin B.A. and Elghazouli A.Y., “Enhancing the Robustness of Steel and Composite Buildings”, *Advanced Steel Construction*, 7(1), 64-85(SI), 2011.
- [10] Yu H., Izzuddin B.A. and Zha X.X., “Progressive Collapse of Steel-Framed Buildings: Influence of Modelling Approach”, *Advanced Steel Construction*, 6(4), 932-948, 2010.
- [11] Alashker Y., El-Tawil S. and Sadek F., “Progressive Collapse Resistance of Steel-Concrete Composite Floors”, *Journal of Structural Engineering*, 136, 1187-1196, 2010.
- [12] Li H.H., and El-Tawil S., “Three-Dimensional Effects and Collapse Resistance Mechanisms in Steel Frame Buildings”, *Journal of Structural Engineering*, 140(8), A4014017, 2014.
- [13] Izzuddin B.A., Vlassis A.G., Elghazouli A.Y. and Nethercot D.A., “Progressive collapse of multi-storey buildings due to sudden column loss - Part I: Simplified assessment framework”, *Engineering Structures*, 30, 1308-1318, 2008.
- [14] Li G.Q., Zhang J.Z. and Jiang J., “Analytical Modeling on Collapse Resistance of Steel Beam-Concrete Slab Composite Substructures Subjected to Side Column Loss”, *Engineering Structures*, 169, 238-255, 2018.
- [15] Alashker Y. and El-Tawil S., “A design-oriented model for the collapse resistance of composite floors subjected to column loss”, *Journal of Constructional Steel Research*, 67, 84-92, 2011.
- [16] Zhang J.Z. and Li G.Q., “Collapse resistance of steel beam-concrete slab composite substructures subjected to middle column loss”, *Journal of Constructional Steel Research*, 145, 471-488, 2018.
- [17] Department of Defense (DoD). Unified facilities criteria (UFC): design of structures to resist progressive collapse, Washington (DC), 2010.
- [18] Park R. and Gamble W.L., “Reinforced concrete slabs. USA: John Wiley & Sons Inc; 2000.
- [19] Hu H.C., *Variational principles of elastic mechanics and their applications*, China, Science Press, 1981.
- [20] Yi W.J., Zhang F.Z. and Kunnath S.K., “Progressive Collapse Performance of RC Flat Plate Frame Structures”, *Journal of Structural Engineering*, 140, 040140489, 2014.
- [21] ABAQUS Analysis User's Manual Version 6.7., ABAQUS Inc, 2007.

SHEAR RESISTANCE OF NOVEL PERFORATED SHAPED STEEL-ENGINEERED CEMENTITIOUS COMPOSITE (ECC) CONNECTORS

Li-min Tian ^{1,2}, Ting Liu ¹, Tian-ji Li ^{3,*}, and Hai-liang Lin ¹

¹ Shaanxi Key Lab of Structure and Earthquake Resistance, School of Civil Engineering, Xi'an University of Architecture and Technology, Xi'an, China

² State Key Laboratory of Subtropical Building Science, South China University of Technology, Guangzhou, China

³ Shanghai Construction No.5 (Group) Co., Ltd., Shanghai, China

* (Corresponding author: E-mail: tianji.li@connect.polyu.hk)

ABSTRACT

A novel perforated shaped steel-engineered cementitious composite connector (PSSEC) is proposed in this paper based on the advantages of perforated plate connectors and engineered cementitious composite (ECC) materials. Eight short columns were designed to thoroughly investigate the mechanical mechanism, bearing capacity, and failure mode. Additionally, an equation for calculating the bearing capacity of PSSECs is presented. The results demonstrate that all eight short columns show splitting failure of the ECC or concrete. Moreover, it is determined that the cracks associated with the ECC specimens are smaller than those of the concrete specimen. Due to the effect of the perforated steel reinforcements, the PSSECs exhibit the characteristics of ductile failure. The load-slip curves of the PSSEC short columns can be divided into five stages: the no-slip, slip, yield, falling, and load residual stages. The load-slip curves of the perforated shaped steel-ECC connector without perforated steel reinforcement (PSSECW), perforated shaped steel-concrete connector (PSSCC), and shaped steel reinforced ECC (SSRE) possess no yield stage because of the absence of the perforated steel reinforcement or ECC. Except for the ultra-high-strength ECC90, the theoretical results obtained for the bearing capacity equation of the PSSECs are generally consistent with the test results.

ARTICLE HISTORY

Received: 26 July 2019
Revised: 12 September 2019
Accepted: 19 September 2019

KEYWORDS

Perforated shaped steel;
ECC;
Short column;
Push-out test;
Shear performance

Copyright © 2020 by The Hong Kong Institute of Steel Construction. All rights reserved.

1. Introduction

ECC possesses excellent characteristics, including low weight, superior ductility, and good seismic performance [1-2]. The energy dissipation capacity and the overall seismic performance of structures can be enhanced using ECC materials [3-4]. It is extremely helpful to improve the collapse resistance of structures [5-6]. Zhou et al. [7] performed uniaxial compression tests on ECC with different mix proportions and compressive strengths. Xu and Cai [8] studied the compressive performances of ultra-high toughness cementitious composites and proposed the constitutive models. In addition, the basic mechanical properties of ultra-high ductility cementitious composites were obtained [9].

In steel-concrete composite members, the effectiveness of the bonding between steel and concrete is vital for these components to work together [10-12]. Due to the low bonding strength between shaped steel and concrete (the bond strength between shaped steel and concrete is approximately 1/3 that of concrete and steel reinforcements [13]), the shear connectors (e.g., stud, steel channel, bend reinforcement, perforated plate connector, etc.) are frequently used to improve the bonding behavior. Ding et al. [14] proposed a slip-released connector and tested the slipping behaviors of the connectors.

Perforated steel plate connectors have broad application prospects because of their simple manufacturing process and good mechanical properties [15-17]. Numerous scholars have investigated perforated steel plate connectors to date, and several theories and equations have been proposed. He et al. [18] studied the force transfer mechanism of the perforated plate connector, and the influence of the position of perforated steel reinforcements on its ductility. Moreover, an equation for the perforated plate connector was derived. Cândido-Martins et al. [19] analyzed the influences of the number of hole rows and the amount of steel reinforcements on the mechanical performances of the perforated plate connector. Hosseinpour et al. [20] compared the bearing capacity as well as the failure mode of the rectangular hole perforated plate connector and those of the circular hole perforated plate connector. Zhao et al. [21] and Su et al. [22] analyzed the hole diameter of the perforated plate connector, the diameter of the perforated steel reinforcement, and the stirrup ratio. Costa-Neves et al. [23] investigated a T-type perforated plate shear connector and they performed a theoretical model. Gu et al. [24] researched a comb-type perforated plate connector and compared it with the traditional perforated plate connector to verify its superiority. Zuo et al. [25] considered a bridge panel with the perforated plate connector as an object; they analyzed the failure mode and ultimate bearing capacity of the bridge panel by changing the hole spacing and the diameter of the perforated steel reinforcements. Zhang et al. [26] studied the deformation of the perforated steel reinforcement under long-term load, as well as the relative slip between the perforated plate connector and concrete. Di et al. [27] derived a bearing capacity equation for

the perforated plate connector. However, due to the use of different analytical methods, the aforementioned equations are substantially different. In the literature [28], several equations have been compared; then, it has been determined that the maximum result obtained using these equations can be greater than 4 times the minimum result.

Based on the advantages of perforated plate connectors and ECC materials, a novel PSSEC is proposed in this paper. The novel connector is composed of H-shaped steel that is reinforced using perforated steel reinforcements, and wrapped with ECC material, as shown in Fig. 1. The integrity of a shaped steel reinforced ECC can be improved by the perforated steel reinforcements. Eight short columns were designed to thoroughly investigate the mechanical mechanism, bearing capacity, and failure mode. Additionally, a calculation method for the PSSECs is presented.

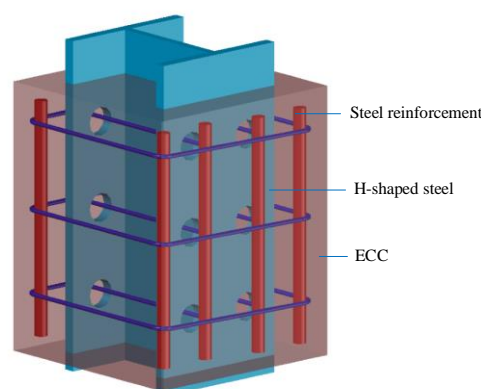


Fig. 1 The push-out test model

2. Experimental details

2.1. Test materials

The ECC was composed of common Portland cement, mineral admixture, silica sand, ultra-high-molecular-weight polyethylene fiber, silica fume, water-reducing admixture, and water preparation, as displayed in Table 1. The concrete was adopted commercial concrete with a design strength of 30 MPa. The ECC and concrete were tested for its compressive strength in the form of three cubes (100 mm × 100 mm × 100 mm), respectively. The mean values of the compressive strength are depicted in Table 2.

All H-shaped steels were constructed from Grade Q235 steel and were $H200 \times 200 \times 12 \times 16$ mm. Some penetrating holes with diameter of 40 mm were opened on the flange of shaped steel. Both the stirrups and longitudinal

reinforcements used were HRB335 grade, with diameters of 8 mm and 12 mm, respectively. Table 3 lists the measured material properties of the steel plates and steel reinforcement.

Table 1

Mixture properties of the ECC (kg/m^3)

Strength grade	Cement	Silica sand	Mineral admixture	Water	Silica fume	Water-reducing admixture	Fiber
ECC45	220.8	396.8	1104.4	380.0	6.6	8.0	15.0
ECC60	330.6	396.8	991.8	396.7	16.5	10.0	15.0
ECC90	528.9	396.8	793.4	327.0	158.7	18.0	15.0

Table 2

Measured material properties of the ECC and concrete (N/mm^2)

Strength grade	Measured strength (three trials) f_c			Mean strength f_c
C30	27.21	29.34	28.53	28.36
ECC45	44.04	47.15	46.05	45.75
ECC60	55.95	58.16	59.28	57.79
ECC90	92.25	94.37	99.48	95.37

Table 3

Measured material properties of the steel plates and steel reinforcement

Type of steel	Young's modulus (N/mm^2)	Yield strength (N/mm^2)	Ultimate strength (N/mm^2)	Elongation rate (%)
Web of H-shaped steel	2.11×10^5	336.67	470.00	28.93
Flange of H-shaped steel	2.09×10^5	278.33	441.67	30.58
Steel reinforce	2.06×10^5	324.08	453.33	31.24

2.2. Specimen design

The bonding stress between shaped steel and ECC has a non-uniform distribution. The outer flange of shaped steel bears most of the load by studying on interfacial behavior of shaped steel reinforced ECC. Considering the strength of ECC, we investigated variations of the structural characteristics of the flange of shaped steel, such as the perforations, the steel reinforcements in the holes, and the spacing of the holes, for a total of eight specimens. The specimens included five PSSEC short columns, one PSSECW short column, one PSSCC short column, and one SSRE short column. Compared with the PSSECs, PSSECW possessed no perforated steel reinforcement in the holes of shaped steel. PSSCC was composed of the shaped steel that was reinforced using perforated steel reinforcements and wrapped with concrete material. SSRE was only wrapped with ECC material outside of the non-perforated shaped steel. The specific dimensions of these specimens are manifested in Fig. 2; and the specific parameters of each specimen are shown in Table 4.

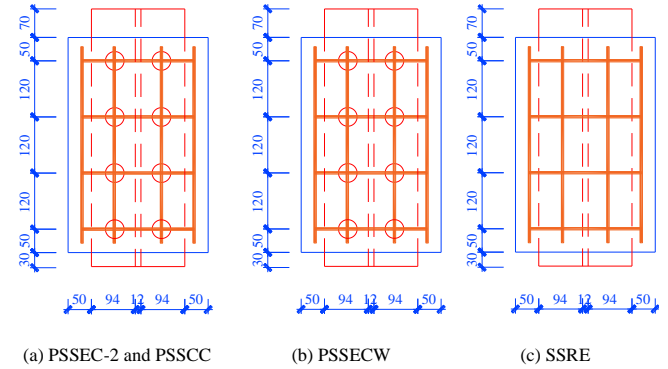
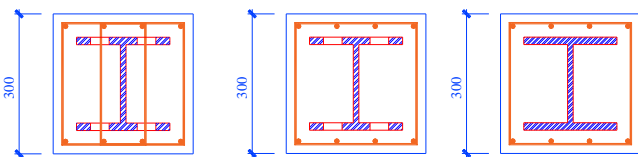


Fig. 2 Specific dimensions of the specimens (all dimensions shown are in mm)

Table 4

Design parameters of the specimens

Specimen	Material	Strength (N/mm^2)	Hole spacing (mm)	Perforated steel reinforcement
SSRE	ECC	45	/	/
PSSCC	Concrete	30	120	✓
PSSECW	ECC	60	120	/
PSSEC-1	ECC	45	120	✓
PSSEC-2	ECC	60	120	✓
PSSEC-3	ECC	60	90	✓
PSSEC-4	ECC	60	180	✓
PSSEC-5	ECC	90	120	✓

2.3. Loading and measuring method

The test was performed on a YAS-5000 kN electro-hydraulic servo pressure testing machine, as displayed in Fig. 3. The two ends of the shaped steel were the loading end and free end. The top of the shaped steel was fixed with the testing machine. The bottom of ECC/concrete was fixed with the loading platform via the special support, and the shaped steel was free. The load was performed with displacement control at a rate of 0.003 mm/s . When the displacement achieved approximately 30–40 mm or the external ECC/concrete cracked obviously, the load was terminated. The real-time load at the loading end was obtained using a pressure transducer. The displacements of the loading end and free end were measured with four linear variable differential transformers (LVDTs) that were set up at the steel plate and ECC, as depicted in Fig. 3. In addition, the strains and displacements on the surface of ECC/concrete were acquired in real-time using a Visual Image Correlation-3D (VIC-3D) non-contact full-field strain measurement system. The system can provide the data of full-field shape, displacement, and strain in three-dimensional space [28], as shown in Fig. 4.

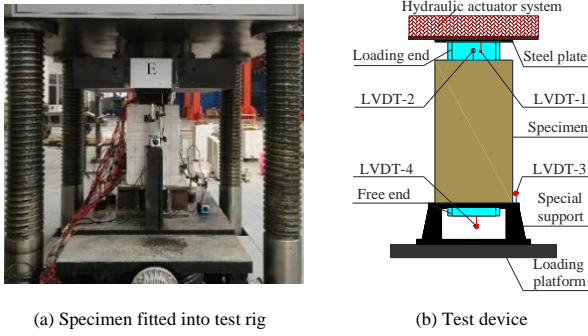


Fig. 3 The push-out test set-up

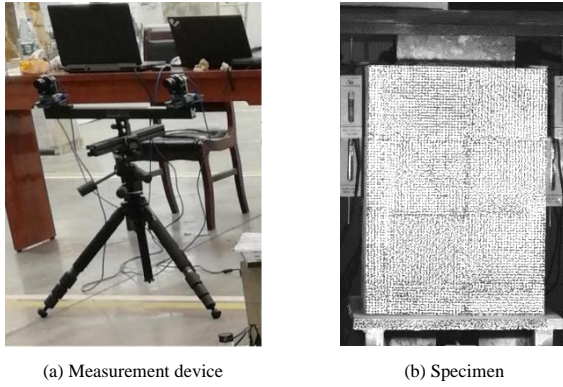


Fig. 4 The non-contact full-field measurement system

3. Test results and analysis

3.1. PSSECs and PSSECW short columns

3.1.1. Failure mode

Splitting failure of the ECC material occurred in all specimens PSSECs and PSSECW. PSSEC-2 can be used as an example (Fig. 5). When the load increased to a certain level, cracks began to appear on the surface for the first time. The cracks were small and located at the loading end on the surface of the specimen (Fig. 5a). With the increase of the load, the number of cracks increased. The cracks gradually widened and extended from the loading end to the free end (Fig. 5b). As cracks developed, the specimen reached the ultimate load. Finally, the interface between the shaped steel and ECC exhibited push-out failure (Fig. 5c).

The test results demonstrated that the surface cracks of the ECC in the outer flange of shaped steel direction were distributed in the position of or between two rows of the holes.

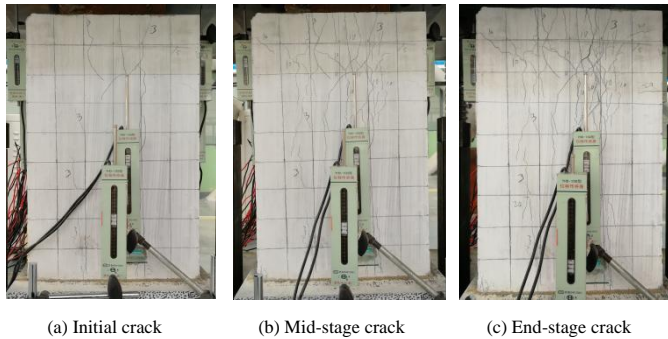


Fig. 5 Failure phenomena of PSSEC-2

The cracks of the loading end in the specimens PSSECs and PSSECW can be summarized into the following two types. The first type of cracks only appears near the limb tips of the flange of shaped steel. The second type possesses more vertical cracks in the ECC of the outer flange of shaped steel; this type of cracks occurs because the perforated steel reinforcements and ECC resist the downward load together. The first type of cracks appeared in the PSSECW because this specimen did not have the perforated steel reinforcement (Fig. 6a). The second type of cracks appeared in the PSSECs (Fig. 6b).

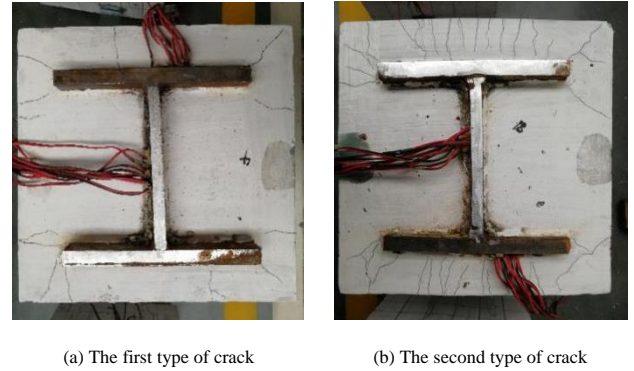


Fig. 6 Typical fracture modes

3.1.2. Z-direction displacement and strain

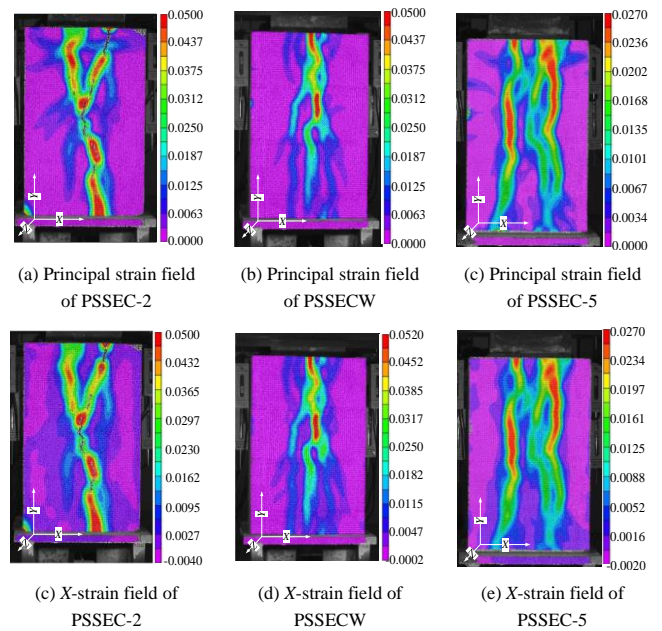
Considering the PSSEC-2, PSSEC-5, and PSSECW as examples, the strain field and displacement field on the surface of the ECC are illustrated in Fig. 7. The results indicate the following.

(1) The principal strain on the surface of ECC is distributed in the position of two rows of holes or between two rows of holes. The principal strain of ECC decreases gradually from the loading end to the free end which indicates that the shear force is transferred from the loading end to the free end.

(2) The principal strain field is approximately identical to the X-direction strain field, while the Y-direction strain field is relatively small, indicating that the principal strain is generally controlled by the X-direction strain. This is because the external ECC tends to split along the Y-direction during the loading process.

(3) The principal strain of the PSSEC-5 is smaller than that of PSSEC-2 and PSSECW, which indicates that the ductility of the latter materials is excellent, while that of the ultra-high-strength (ECC90) material is relatively unsatisfactory.

(4) The Z-displacement on the surface of ECC is generally distributed in the corresponding region of the flange of shaped steel. The maximum displacement is located in the middle and upper portions of this region, and gradually decreases to the outer ring. The Z-displacement indicates that the ECC on one side of the flange of shaped steel causes a significant restraint effect on the internal perforated shaped steel shear connectors.



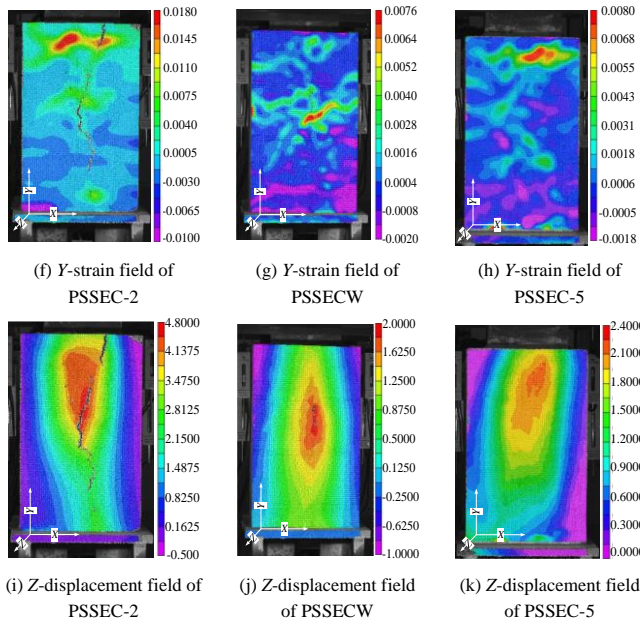


Fig. 7 Strain and displacement fields

The points with large displacement in the Z-displacement field nephogram are selected. The Z-displacement-slip curves and the principal strain-slip curves are revealed in Fig. 8. From the results, at the initial stage of loading, the Z-displacement on the surface of ECC increases for the majority of the specimens, and remains constant when the displacement increases to a certain threshold. Additionally, the non-ultra-high-strength ECC displays excellent ductility. The perforated steel reinforcements cause the PSSEC-2 to exhibit ductile failure.

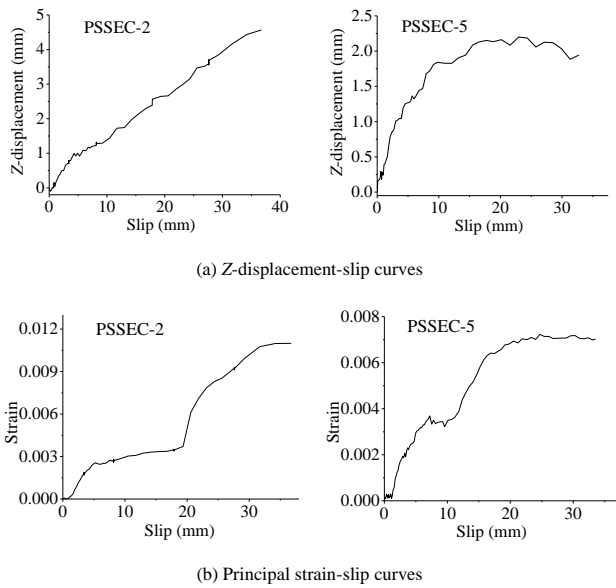


Fig. 8 Z-displacement-slip and principal strain-slip curves

3.1.3. Load-slip curves

(1) PSSECs

Fig. 9 displays the load-slip curves of the loading end and free end in the PSSECs. From the observation of Fig. 9, the trend of the load-slip curves at the loading end is approximately identical to that at the free end. Overall, there is hysteresis in the relative slip of the free end. The load-slip curves of the PSSECs can be simplified to the models shown in Fig. 10. Based on these results, the load-slip curves can be divided into the following five stages:

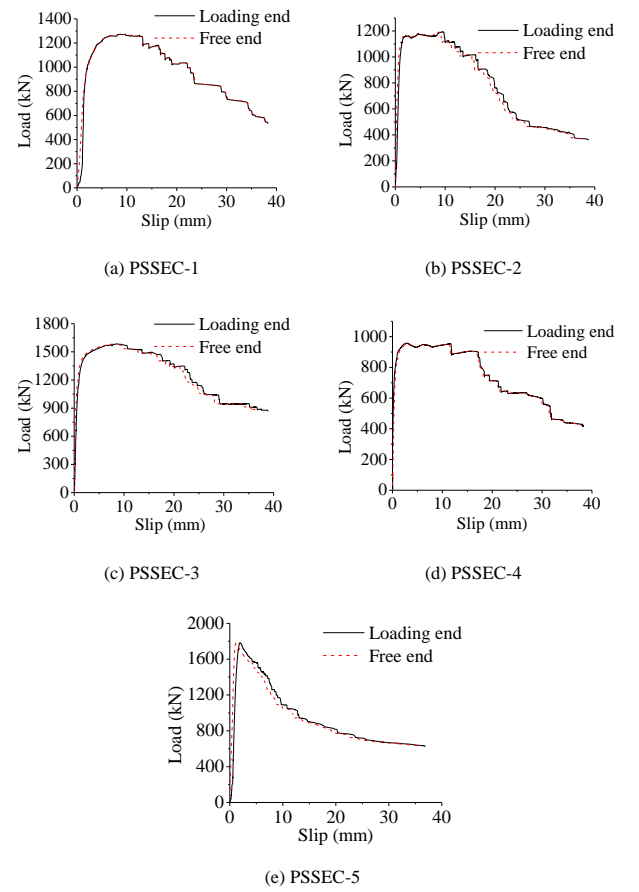


Fig. 9 Load-slip curves of PSSECs

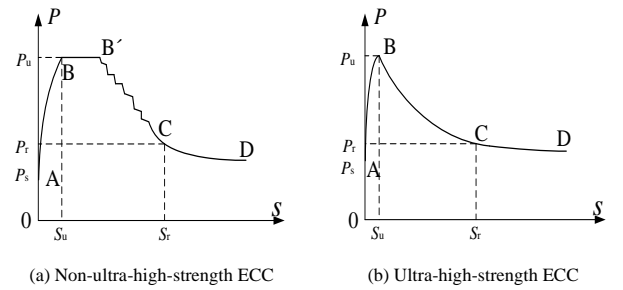


Fig. 10 Typical load-slip curves of PSSECs

1) No-slip stage (OA segment). During the initial stage of loading, the loading end and the free end of each specimen do not possess a significant relative slip. The chemical adhesion between the shaped steel and the ECC plays a major role in bonding. Moreover, the perforated shaped steel shear connector has not yet functioned at this stage.

2) Slip stage (AB segment). When the load achieves the initial slip load P_s , the loading end appears to slip firstly while the slippage of free end is not apparent. At this time, the bonding force gradually fails from the loading end to the free end. Additionally, the longitudinal load is transferred by the frictional force and the shear resistance of the perforated shaped steel shear connector. When the load exceeds 50 % of the ultimate load P_u , the slippage of the loading end develops quickly. Moreover, the slippage begins to occur at the free end.

3) Yield stage (BB' segment for Fig.10a). Except for the ultra-high-strength ECC specimen (PSSEC-5, bad ductility of ultra-high-strength ECC90), the slippage of the loading end and free end increases rapidly after the load reaches the peak and the load remains almost constant.

4) Falling stage (B'C segment for Fig.10a and BC segment for Fig.10b). After the load reaches the peak, the cracks of ECC are fully developed. Additionally, the load-slip curves are in a descending state until the load reaches the residual load P_r . For the non-ultra-high-strength ECC specimens, the load-slip curve is in a descending state with step-shaped behavior.

5) Load residual stage (CD segment). With the increase of the slip amount, the load is stabilized.

(2) PSSECW

The load-slip curves of the PSSECW are illustrated in Fig. 11. It is evident that these curves can be divided into four stages, namely, the no-slip, slip, falling, and load residual stages. Due to the absence of the perforated steel reinforcement, the ECC in the holes experiences brittle failure under the action of the shear force. Therefore, the curves possess no yield stage.

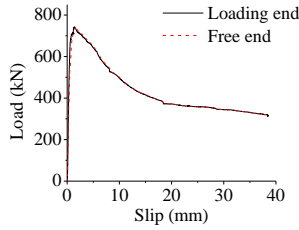


Fig. 11 Load-slip curves of PSSECW

3.1.4. Summary of test results

Table 5 shows the ultimate loads, slippages of the loading end and free end corresponding to the ultimate loads.

Table 5
Test results of PSSECs and PSSECW

Specimen	Ultimate load (kN)	Loading-end slip (mm)	Free-end slip (mm)
PSSECW	741.82	1.37	1.65
PSSEC-1	1272.23	8.68	8.72
PSSEC-2	1193.21	9.46	8.77
PSSEC-3	1584.46	8.47	7.74
PSSEC-4	957.42	2.75	2.97
PSSEC-5	1783.84	1.91	1.14

With the increase of the number of hole rows, the ultimate bearing capacity increases approximately linearly. With the increase of the strength of ECC, the ultimate bearing capacity tends to increase. The mean ultimate bearing capacity of the specimens with perforated steel reinforcements is approximately 60% higher than that of the specimen without the perforated steel reinforcement.

3.2. PSSCC and SSRE short columns

3.2.1. Failure mode

The failure mode of the PSSCC and SSRE was splitting failure of the ECC or concrete. It is noteworthy that the surface cracks of PSSCC were wider than those of the ECC specimens because of the bad ductility of concrete. In addition, the spalling and transverse cracks of the concrete appeared (Fig. 12).

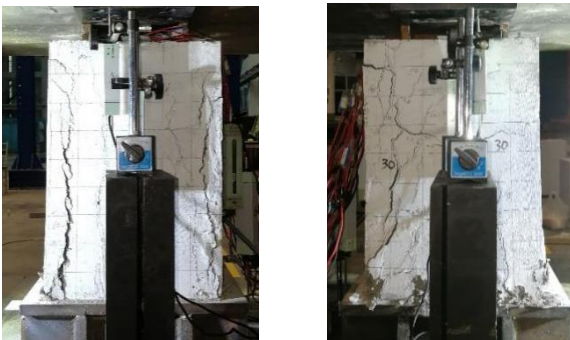


Fig. 12 The failure mode of PSSCC

After the experiment was finished, the specimen PSSCC was smashed to directly observe the failure of the perforated steel reinforcements and concrete in the holes. The failure states are described in Fig. 13. It is evident that the fractures of concrete in the holes were non-uniform. Moreover, a portion of concrete in the holes was crushed. The steel reinforcements in the holes were cut off and no longer possessed shear resistance. The steel reinforcements in the holes were shear failure along the 45° angle, accompanied by slight necking, which indicated that the steel reinforcements in the holes were subjected to

tension. Moreover, the steel reinforcements in the holes were bent.



Fig. 13 Failure states of the perforated steel reinforcements and concrete in the holes

3.2.2. Load-slip curves

The load-slip curves of the PSSCC and SSRE can be divided into four stages: the no-slip, slip, falling, and load residual stages, as manifested in Fig. 14. Compared with the load-slip curves of the PSSECs, the PSSCC and SSRE do not exhibit the yield stage. The PSSCC exhibits a slow decline with step-shaped behavior after it achieves the ultimate load, indicating that the ductility of this specimen is worse than that of the PSSECs.

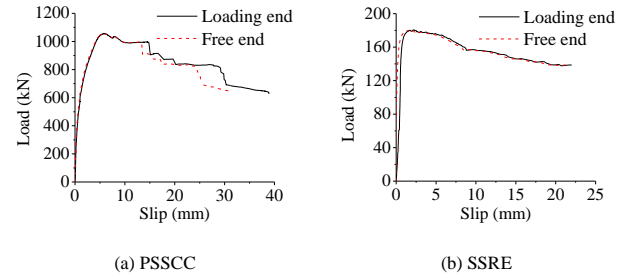


Fig. 14 Load-slip curves of PSSCC and SSRE

Table 6 shows the ultimate loads of the PSSCC and SSRE in addition to the slippages of the loading end and free end corresponding to the ultimate loads. It is evident that the slippage of PSSCC under the ultimate load is significantly less than those of the PSSECs. Moreover, the ultimate bearing capacity of the perforated shaped steel-ECC45 is approximately 7 times that of SSRE when the ECC is of identical strength.

Table 6
Test results of PSSCC and SSRE

Specimen	Ultimate load (kN)	Loading-end slip (mm)	Free-end slip (mm)
SSRE	180.21	1.74	1.42
PSSCC	1055.64	5.78	5.75

Based on these test results and analyses, it is evident that the failure mode of the PSSECW and PSSCC is brittle failure, while that of the PSSECs is ductile failure (except for the ultra-high-strength ECC90). Because of the perforated steel reinforcements, the bearing capacity of the PSSECs is improved and the brittle failure is avoided.

4. Analysis of the bearing capacity of PSSECs

Because the ultimate bearing capacity of the PSSECs increased linearly with the increase of the number of hole rows, the bearing capacity of multiple holes can be analyzed and calculated using theories of a single hole.

4.1. Analysis of bearing capacity of a single hole

The shear bearing capacity of a perforated plate connector can be divided into three parts [29]: the compressive bearing capacity of ECC/concrete at the end of a perforated steel plate, the shear bearing capacity of ECC/concrete in the hole, and the shear bearing capacity of a perforated steel reinforcement.

Fig. 15 reveals the stress of ECC in the perforated shaped steel connector. The ECC in the hole is constrained by ECC on both sides of the flange of

shaped steel. Additionally, it is subjected to the circumferential compression of the hole wall. The ECC in the hole can be regarded as existing in a three-dimensional compressive state. The compressive bearing capacity of ECC at the end of the perforated steel plate does not exist in the PSSECs. Therefore, its shear bearing capacity comprises two parts: the shear capacity of ECC in the hole and the shear capacity of a perforated steel reinforcement.

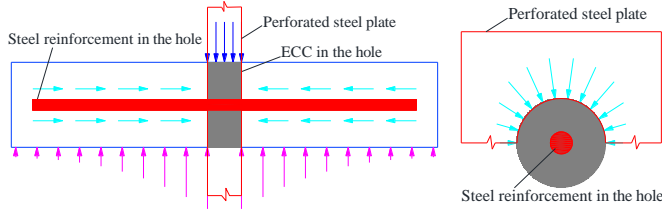


Fig. 15 The stress analysis of ECC in the hole

Because the perforated steel reinforcement is simultaneously subjected to both shear and tensile forces, its actual shear bearing capacity is larger than the pure shear bearing capacity. Therefore, it is necessary to multiply the shear bearing capacity by a magnification factor when calculating the shear strength of the steel reinforcement.

4.2. Equations of bearing capacity of a single hole

According to the literature [30], the shear bearing capacity of ECC in the hole under two shear planes (P_E) can be calculated as follows (it is assumed that the magnification factor is five):

$$P_E = 3.9A_E f_{cu}^{0.57} \quad (1)$$

where A_E is the area of ECC in the hole under a single shear plane, $A_E = \pi(d_1^2 - d_2^2)/4$; d_1 is the diameter of the hole; d_2 is the diameter of the perforated steel reinforcement; f_{cu} is the standard compressive strength of the ECC.

According to the test results of the PSSEC-2 and PSSECW, the bearing capacity can be increased by 28.2 kN for each steel reinforcement in the hole. On the other hand, the pure shear bearing capacity of steel reinforcement in the hole is 18.8 kN. Therefore, the shear magnification factor under a single shear plane is approximately 1.5. The ultimate shear bearing capacity of a single perforated steel reinforcement under two shear planes (P_s) is:

$$P_s = 3A_s \tau_u \quad (2)$$

where A_u is the cross-sectional area of a single perforated steel reinforcement and τ_u is the shear strength of the steel reinforcement.

It can be concluded that the bearing capacity of a single hole for a perforated shaped steel-ECC connector (P) is:

$$P = 3.9A_E f_{cu}^{0.57} + 3A_s \tau_u \quad (3)$$

To verify the correctness of the proposed equations, the experimental parameters are substituted into the Eq. (3) and the calculation results are compared in Table 7.

Table 7
Comparisons of the ultimate bearing capacities

Specimen	Test results (kN)	Theoretical results (kN)	Difference (%)
PSSECW	741.82	791.46	6.69
PSSEC-1	1272.23	1116.53	12.23
PSSEC-2	1193.21	1211.26	1.51
PSSEC-3	1584.46	1514.07	4.44
PSSEC-4	957.42	908.44	5.12
PSSEC-5	1783.84	1462.36	18.02

In the above comparisons, it is clear that, except for the perforated shaped steel-ECC90, the theoretical results are in good agreement with the experimental results, which indicates that the Eq. (3) is reliable for non-ultra-high-strength ECC. The ultimate bearing capacity of the perforated

shaped steel-ECC30 is 957.85 kN by using Eq. (3), which is only 9.26 % (within 10%) different from the ultimate load of the PSSCC in the experiment.

5. Conclusions

Eight short columns were designed to thoroughly investigate the mechanical mechanism, bearing capacity, and failure mode; additionally, a calculation method for PSSECs is proposed. The following conclusions are drawn.

(1) The failure mode of the PSSECs, PSSECW, PSSCC, and SSRE short columns is either ECC or concrete splitting failure. The cracks in the PSSECs, PSSECW, and SSRE are microcracks and multi-cracks. The cracks of the PSSCC are wider than those of the ECC specimens.

(2) Due to the effect of the perforated steel reinforcements, the PSSECs exhibit the characteristics of ductile failure.

(3) The load-slip curves of the PSSEC short columns can be divided into five stages: the no-slip, slip, yield, falling, and load residual stages. The load-slip curves of the PSSECW, PSSCC, and SSRE short columns possess no yield stage due to the absence of the perforated steel reinforcement or ECC.

(4) An equation for calculating the bearing capacity of PSSECs is proposed. Except for the perforated shaped steel-ECC90, the theoretical results are in good agreement with the experimental results, which should be studied in the follow-up study with special attention.

Acknowledgments

This research was supported by the National Natural Science Foundation of China (Grant No. 51608433), the Shaanxi Province Youth Science and Technology New Star Program (Grant No. 2019KJXX-040), the Shanghai Rising-Star Program (Grant No. 17QB1402300), and the State Key Laboratory of Subtropical Building Science (South China University of Technology, Grant No. 2020ZB21). These financial supports are greatly acknowledged.

References

- [1] Deng M.K., Zhang Y.X. and Li Q.Q., "Shear strengthening of RC short columns with ECC jacket: Cyclic behavior tests", *Engineering Structures*, 160, 535-545, 2018.
- [2] Said S.H. and Razak H.A., "Structural behavior of RC engineered cementitious composite (ECC) exterior beam-column joints under reversed cyclic loading", *Construction and Building Materials*, 107, 226-234, 2016.
- [3] Fischer G. and Li V.C., "Effect of matrix ductility on deformation behavior of steel reinforced ECC flexural members under reversed cyclic loading conditions", *ACI Structural Journal*, 99(6), 781-790, 2002.
- [4] Wu C., Pan Z.F., Su R.K.L., Leung C.K.Y. and Meng S.P., "Seismic behavior of steel reinforced ECC columns under constant axial loading and reversed cyclic lateral loading", *Materials and Structures*, 50, 78, 2017.
- [5] Zhang Y.X., Deng M.K. and Dong Z.F., "Seismic response and shear mechanism of engineered cementitious composite (ECC) short columns", *Engineering Structures*, 192, 296-304, 2019.
- [6] Tian L.M., Wei J.P., Hao J.P. and Wang X.T., "Method for evaluating the progressive collapse resistance of long-span single-layer spatial grid structures", *Advanced Steel Construction*, 15(1), 109-115, 2019.
- [7] Zhou J.J., Pan J.L. and Leung C.K.Y., "Mechanical behavior of fiber-reinforced engineered cementitious composites in uniaxial compression", *Journal of Materials in Civil Engineering*, 27(1), 04014111, 2015.
- [8] Xu S.L. and Cai X.R., "Experimental study and theoretical models on compressive properties of ultrahigh toughness cementitious composites", *Journal of Materials in Civil Engineering*, 22(10), 1067-1077, 2010.
- [9] Ding Y., Yu J.T., Yu K.Q. and Xu S.L., "Basic mechanical properties of ultra-high ductility cementitious composites: from 40 MPa to 120 MPa", *Composite Structures*, 185, 634-645, 2018.
- [10] Fu Z.Q., Ge H.B., Ji B.H. and Chen J.J., "Interface bond behavior between circular steel tube and lightweight aggregate concrete", *Advanced Steel Construction*, 14(3), 424-437, 2018.
- [11] Zou Y., Zhou X.H., Di J. and Qin F.J., "Partial interaction shear flow forces in simply supported composite steel-concrete beams", *Advanced Steel Construction*, 14(4), 634-650, 2018.
- [12] Zhou X.H., Gan D., Liu J. P. and Chen Y.F., "Composite effect of stub square steel tubed columns under axial compression", *Advanced Steel Construction*, 14(2), 274-290, 2018.
- [13] Ertas O., Ozden S. and Ozturan T., "Ductile connections in precast concrete moment resisting frames", *PCI Journal*, 51(3), 66-76, 2006.
- [14] Ding Y., Dai X.M. and Yan J.B., "Developments and behaviors of slip-released novel connectors in steel-concrete composite structures", *Advanced Steel Construction*, 15(1), 30-36, 2019.
- [15] Liu R.Y., Yang Y. and Zhou X.W., "Experimental study on fatigue performance of composite beam with steel-plate-concrete composite decks", *Construction and Building Materials*, 188, 833-849, 2018.
- [16] Zhang Q.H., Jia D.L., Bao Y., Cheng Z.Y., Xiao L. and Bu Y.Z., "Internal force transfer effect-based fatigue damage evaluation for PBL shear connector groups", *Journal of Constructional Steel Research*, 148, 469-478, 2018.
- [17] Tian L.M., Hao J.P., Wei J.P. and Zheng J., "Integral lifting simulation of long-span spatial steel structures during construction", *Automation in Construction*, 70, 156-166, 2016.
- [18] He S.H., Fang Z., Fang Y.W., Liu M., Liu L.Y. and Mosallam A.S., "Experimental study on perfo-bond strip connector in steel-concrete joints of hybrid bridges", *Journal of Constructional Steel Research*, 118, 169-179, 2016.

- [19] Cândido-Martins J.P.S., Costa-Neves L.F. and Vellasco P.C.G.D.S., "Experimental evaluation of the structural response of perfobond shear connectors", *Engineering Structures*, 32, 1976-1985, 2010.
- [20] Hosseinpour E., Baharom S., Badaruzzaman W.H.W. and Al Zand A.W., "Push-out test on the web opening shear connector for a slim-floor steel beam: Experimental and analytical study", *Engineering Structures*, 163, 137-152, 2018.
- [21] Zhao C.H., Li Z.X., Deng K.L. and Wang W.A., "Experimental investigation on the bearing mechanism of perfobond rib shear connectors", *Engineering Structures*, 159, 172-184, 2018.
- [22] Su Q.T., Wang W., Luan H.W. and Yang G.T., "Experimental research on bearing mechanism of perfobond rib shear connectors", *Journal of Constructional Steel Research*, 95, 22-31, 2014.
- [23] Costa-Neves L.F., Figueiredo J.P., Vellasco P.C.G.D.S. and Vianna J.D.C., "Perforated shear connectors on composite girders under monotonic loading: An experimental approach", *Engineering Structures*, 56, 721-737, 2013.
- [24] Gu J.C., Liu D., Deng W.Q. and Zhang J.D., "Experimental study on the shear resistance of a comb-type perfobond rib shear connector", *Journal of Constructional Steel Research*, 158, 279-289, 2019.
- [25] Zuo Y.Z., Mosallam A., Xin H.H., Liu Y.Q. and He J., "Flexural performance of a hybrid GFRP-concrete bridge deck with composite T-shaped perforated rib connectors", *Composite Structures*, 194, 263-278, 2018.
- [26] Zhang J., Hu X.M., Kou L.Y., Zhang B., Jiang Y.C. and Yu H.H., "Experimental study of the short-term and long-term behavior of perfobond connectors", *Journal of Constructional Steel Research*, 150, 462-474, 2018.
- [27] Di J., Zou Y., Zhou X.H., Qin F.J. and Peng X., "Push-out test of large perfobond connectors in steel-concrete joints of hybrid bridges", *Journal of Constructional Steel Research*, 150, 415-429, 2018.
- [28] Tian L.M., Wei J.P. and Hao J.P., "Optimisation of long-span single-layer spatial grid structures to resist progressive collapse", *Engineering Structures*, 188, 394-405, 2019.
- [29] Su Q.T., Xu Y.C., Wang W., "Theory model of shear transferring for perfobond rib connector", *Journal of Tongji University (Natural Science)*, 41(12), 1775-1780, 2013.
- [30] Guo Z.H. and Shi X.D., *Reinforced concrete theory and analyse*, Tsinghua University, Beijing, 2003.

INFLUENCE OF THE CORE-RESTRAINER CLEARANCE ON THE MECHANICAL PERFORMANCE OF SANDWICH BUCKLING-RESTRAINED BRACES

Lu-qi Xie¹, Jing Wu^{1,*}, Jian-hua Shi² and Yun-qing Zhu¹

¹ The Key Laboratory on Concrete and Prestressed Concrete Structures of Ministry of Education, Southeast University, Nanjing, China

² Nanjing Jiangbei New Area Center Development Co. Ltd, Nanjing, China

* (Corresponding author: E-mail: seuwj@seu.edu.cn)

ABSTRACT

The out-of-plate clearance between the core member and the restrainer is an important parameter for evaluating the hysteretic performance of a buckling-restrained brace (BRB) and may make a significant impact on its low-cycle fatigue capacity via the friction value of the core member under compression. A theoretical derivation and finite element analysis are conducted on BRBs with various clearances, in which the distribution of the friction and axial strain along the core member is obtained. The results reveal that the contact force between the core member and the restrainer under compression increases with the clearance, leading to increased friction on the contact area of the core member and a nonuniform strain distribution along the core member. Moreover, an experimental study of 8 “sandwich” BRB specimens with different clearances was conducted. The test results indicate that the compression-strength adjustment factor of the BRBs increases with the clearance; moreover, the maximum cycle number under large axial strain is significantly decreased, indicating a lower energy dissipation capacity. Additionally, a higher stiffness demand of the restrainer is needed for an excessively large clearance, which leads to a poor cost performance. In conclusion, a threshold value for the core-restrainer clearance should be proposed, and a determination method is suggested via a formula derivation at the end of this paper.

ARTICLE HISTORY

Received: 12 March 2019
Revised: 8 October 2019
Accepted: 11 October 2019

KEYWORDS

Buckling-restrained brace;
clearance;
compression-strength adjustment factor;
multi-wave buckling;
low-cycle fatigue property

Copyright © 2020 by The Hong Kong Institute of Steel Construction. All rights reserved.

1. Introduction

A buckling-restrained brace (BRB, shown in Fig. 1) is extensively employed as a lateral-resisting member and damper in newly built structures and the reconstruction of existing structures; BRBs are regarded as an effective method for performance-based seismic design (Usami et al. [1], Tsai et al. [2], Chou et al. [3], Vargas et al. [4]). BRBs can yield in tension and compression without buckling, and they exhibit stable elasto-plastic hysteretic behavior and dissipate energy during strong earthquakes (Tsai et al. [2], Chou et al. [3]). The main structural members remain elastic under strong ground motions when BRBs yield, which can ensure a stable integrity and robustness of the whole structure. The seismic rehabilitation of a structure can be achieved by replacing the BRBs, which is convenient for implementation (Usami et al. [5], Feng et al. [6]). The core member of a BRB may buckle along the weak axis under compression, while the buckling trend is prevented by the restrainer, and multi-wave buckling is sequentially formed in compression (Wu et al. [7], Takeuchi et al. [8]). The multi-wave buckling of a core member enables contact between the core member and the restrainer and produces friction between them, which does not exist in the tensile condition. The existence of friction in compression may cause a nonidentity regarding the compression and tensile strength, which can be evaluated as the compression-strength adjustment factor β , as expressed by Eq. (1):

$$\beta = \max\left(\frac{P_{\max}^i}{T_{\max}^i}\right) \quad (1)$$

where P_{\max}^i and T_{\max}^i are the amplitude of the axial compression force and the amplitude of the tensile force, respectively, in the i th cycle of the BRB. The friction may generate a nonuniform distribution of axial strain along the core member. Thus, some local parts of the core member may undergo strain concentration, which causes a decrease in the low-cycle fatigue capacity of BRBs. A larger β value indicates an amplified imbalance of the tensile and compressive capacity with a considerable strain concentration. AISC 340-10 [9] stipulates that the value of β should not exceed 1.3. A method for restricting the β value is to lay unbonded material on the surface of the core member (Uang et al. [10]), setting stoppers on the middle section of the core member (Xie et al. [11]) and controlling the clearance between the core member and the restrainer (Wu et al. [7]). Wu et al. [7] conducted a formula derivation and proposed that the variation of clearance between the core member and the restrainer will affect the magnitude and the distribution of friction force. The friction increases with the clearance, which causes an increase in the compression force and the β value. Jiang et al. [12] theoretically and numerically analyzed the stress state of the assembled buckling-restrained braces (ABRBs) under compression. The

stress state under single-wave buckling and multi-wave buckling was obtained, while the design method on the pinned ABRB with a flat core was also proposed. Wu et al. [13] theoretically and experimentally investigated the buckling mechanism of the steel cores of BRBs, in which formulas for the maximum contact force and maximum bending moment of the restrainer were proposed.



Fig. 1 BRBs in a frame

The cumulative plastic deformation (CPD) capacity is an essential performance demand criterion for evaluating the energy dissipation capacity of BRBs (FEMA450 [14]), which is expressed as

$$CPD = \sum |\Delta \varepsilon_{pi}| / \varepsilon_y \quad (2)$$

where $\Delta \varepsilon_{pi}$ is the plastic strain amplitude in the i th cycle and ε_y is the yielding strain of the core member.

Researchers have conducted a series of studies regarding the CPD capacity of BRBs. Black et al. [15] experimentally investigated the CPD regulation of BRBs with various loading histories. Wang [16], Jia [17] and Guo [18, 19] researched the BRBs manufactured using different materials and constructions via constant-amplitude and variable-amplitude cyclic loading, respectively, and simultaneously conducted intensive studies regarding the CPD capacity of BRBs on the component level. The research results reveal that the CPD capacity is closely related to the fabrication method and loading history of the BRBs. Researchers have also computationally and experimentally explored BRB frames (BRBFs) and revealed the seismic demand of the CPD capacity of BRBs during strong earthquakes. Sabelli [20] proposed a minimum demand of 185 based on time history analyses of a three-story BRBF and a six-story BRBF.

Iwata et al. [21] suggested a minimum CPD capacity of 292, while Usami et al. [22] proposed a minimum CPD capacity of 400. ANSI/AISC [9] stipulates a minimum CPD capacity of the BRB of 200 to ensure the requirement of low-cycle fatigue capacity. Lin et al. [23] proposed the seismic design method of thin profile core members. Matsui et al. [24] also studied the cumulative deformation capacity of BRBs by considering local buckling of the core plates. As the strain distribution on the axial direction of a BRB is nonuniform under compression due to the existence of friction, the strain concentration may cause a decrease in the CPD capacity of the BRB. Thus, the clearance between the core member and the restrainer is a key parameter in evaluating the CPD capacity of BRBs.

A finite element analysis and experimental study are conducted on “sandwich” BRBs to quantitatively analyze the influence of the clearance on the deformation and energy dissipation capacity of BRBs. A simplified model of “sandwich” BRBs was developed, and 6 different clearance values were chosen for the parametric analysis. Eight “sandwich” BRBs with different clearance values were manufactured for the experimental study. The friction distributions on the core member and the restrainer are obtained. The axial strain distribution and the compression-strength adjustment factor of the BRBs are also extracted via the computational and the experimental analysis, respectively. The variation in the low-cycle fatigue performance of BRBs with different clearance values and the deformation or buckling of the core members are further analyzed.

2. Theoretical and numerical analyses of brbs with different clearance values

2.1. Theoretical analysis

2.1.1 Contact force and friction between the core member and restrainer

According to Reference [7], the core member of a BRB buckles into a multi-wave shape under axial compression. The quantity of the waves increases with the axial compression load, while the “point contact situation” and “line-contact situation” alternatively appear, which causes increases in the contact point number and contact force. The contact force T_0 of one contact point in the multi-wave buckling condition is given as

$$T_0 = \frac{Py_0}{\pi} \sqrt{\frac{P}{EI}} \quad (3)$$

where P is the axial force of the core member, y_0 is the clearance between the core member and the restrainer, E is the Young's modulus, and I is the moment of inertia of the core member.

As shown in Eq. (3), the contact force T_0 is proportional to y_0 for a certain P . Once the core member yields, E should be replaced with E_t , which is the tangent modulus of the steel (Takeuchi and Wada [25]).

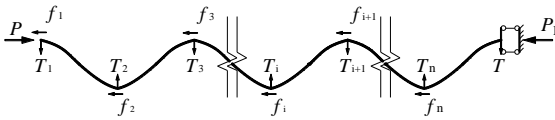


Fig. 2 Force distribution of the half core member along the length direction

With the relative movement between the core member and the restrainer, friction is produced and continuously increases with increasing axial compression load. The distribution of friction along the axial direction of the core member is also closely related to the wave shape, as shown in Fig. 2. A “relative fixed point” exists between the two members, which can balance the friction on the two sides of the core member if the point is set in the core middle. A stopper is usually set as the relative fixed point. The friction magnitude of the core member on one side of the stoppers can be expressed as

$$f = \mu \sum_{i=1}^n T_i \quad (4)$$

where f is the summary of the friction on the semistructure of the core member, μ is the friction coefficient between the core and the restrainer, and T_i is the contact force of the i^{th} wave ($i=1, 2, \dots, n$) along the core member, in which the number of waves on one side of the core member can be expressed as

$$n = \frac{1}{4} \sqrt{\frac{P}{P_E}} \quad (5)$$

where P_E is the Euler critical buckling force or the postyield critical buckling force of the core member.

As shown in Figure 2, the axial force along the core member longitude is different due to the existence of friction. The axial force decreases with the position drawing near the stopper, which can be expressed as:

$$P_1 = P - \sum_{i=1}^n f_i \quad (6)$$

The friction also increases with the amplification of the clearance and decreases with the amplification of the flexural rigidity. Furthermore, the magnitude of the axial compression load determines the quantity of the waves, the wavelength and the friction magnitude in one wave. Thus, the magnitude and distribution of friction on the core member can be obtained via the iteration method. In this paper, the lengths of the buckling waves on the core member are assumed to be equal, which indicates that the friction in each wave is equal.

2.1.2 Influence of friction on the compression-strength adjust factor

The existence of the compression-strength adjust factor β may cause the yielding force to exceed the expected range, which may produce an uncertainty in the design. However, the friction is an important factor that affects the β value, although it is not a unique factor.

According to Eq. (3) and (4), the friction between the core member and the restrainer members also increases with the clearance, which may cause a larger β value. AISC 340-10 [9] stipulates that the β value should not exceed 1.3; the threshold value range of the clearance should be limited to a certain BRB. In this paper, the index β of the test specimens can be obtained by the hysteretic curves that are gathered from the force transducer on the test machines and the linear variable differential transducers (LVDTs).

2.1.3 Influence of friction on the core member axial strain

The existence of friction will cause a nonuniform axial force and strain distribution along the length of the core member according to Eq. (4) and (6), while the axial strain decreases from the end of the core member to the middle of the core member due to the force distribution. Furthermore, as the BRB commonly functions the under cyclic load of tension and compression during strong earthquakes, the strain distribution of a core member in tension should also be considered. When the core member develops into tension from compression, the contact between the core member and the restrainer is relieved because the buckling of the core member is rehabilitated. The friction is also relieved, while the axial force along the core member is equal. Because the section area along the core member length in compression is different and the area of the core member at the end is larger than that in the middle, the axial stress in the core member in the middle is larger than that at the end, which indicates that the strain distribution along the core member is not uniform, even if a further nonuniform level is attained. This phenomenon reveals that the no uniform distribution of the strain along the length direction of the core member will become increasingly important during the cyclic load of tension and compression. After the core member yields, the stiffness will significantly decrease, and even a slight increase in the stress will cause a large strain variation. In this case, the nonuniform distribution of the strain in a core member is substantially more serious, as shown in Fig. 3. Once the core member yields and the stiffness decreases, the quantity of the buckling waves increases, which indicates that the quantity of the contact points and the friction significantly increase, and the strain concentration will become even

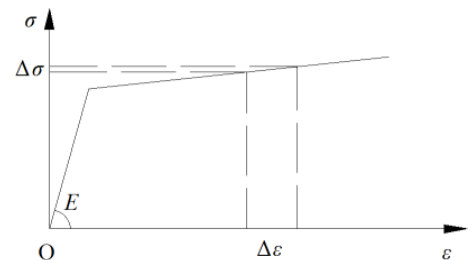


Fig. 3 Stress-strain relationship of the core member material

more important. As the low-cycle fatigue performance of a BRB decreases with increasing strain amplitude, the strain concentration of a core member should be avoided. As shown in Eq. (3) and (4), controlling the clearance between the core member and the restrainer can be an effective method.

2.2. Numerical model verification

The theoretical analysis of the influence of clearance listed in Section 2.1 is verified in this section by a finite element method. A simplified analytical model of BRBs is established in ABAQUS/Explicit, in which the restrainer is regarded as rigid, while the material nonlinearity, geometric nonlinearity and contact nonlinearity are comprehensively considered. The core member of a BRB is simplified as a steel plate, which disregards the influence of the connection details between the BRB and the structural members. Both the core member and the restrainer are modeled with S4R elements. An axial load is applied to both ends of the core member, while a fixed constraint is applied to the middle. Additionally, the fixed constraints are also applied to the restrainers for simulating the rigid plates. The clearance is the key parameter that is varied; values of 0.5 mm, 1 mm, 1.5 mm, 2 mm, 2.5 mm and 3 mm are selected in this paper. To determine the effect of the out-of-plane clearance on BRBs, the in-plane deformation is disregarded when establishing the model. Because the stoppers settling in the middle of the core member may affect the friction distribution of the BRB, the load is applied to both ends of the core member, while the middle is restrained. A bilinear kinematic hardening model is selected as the constitutive relationship, in which the yielding strength (σ_s) is 296 MPa, as obtained from material property tests. The Young's modulus is 2.037×10^5 N/mm², while the tangent modulus is 4840 N/mm². The Poisson's ratio is 0.3. The parameters of the models are listed in Table 1 below.

Table 1
Model parameters

Model No.	CL (mm)	CW (mm)	RL (mm)	RW (mm)	CR(y_0) (mm)	LA (mm)
1	1075	100	1150	200	0.5	32.25
2	1075	100	1150	200	1	32.25
3	1075	100	1150	200	1.5	32.25
4	1075	100	1150	200	2	32.25
5	1075	100	1150	200	2.5	32.25
6	1075	100	1150	200	3	32.25

Note: CL stands for the core member length; CW stands for the core member width; RL stands for the restrainer length; RW stands for the restrainer width; CR stands for the clearance between the core member and restrainer; LA is the loading amplitude of the model.

Finite element analyses are conducted on all six models listed in Table 1, in which the loading protocol is one cyclic loading on a 3% nominal strain amplitude in tension and compression. The conditions of considering friction and not considering friction are applied. Analyses that disregard the influence of friction are used to verify the multi-wave buckling theory mentioned in Section 2.1, while analyses that consider the friction coefficient are conducted to analyze the nonuniform distribution extent of strain along the core member for different clearance magnitudes.

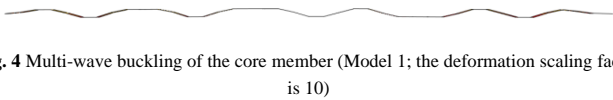


Fig. 4 Multi-wave buckling of the core member (Model 1; the deformation scaling factor is 10)

First, friction is disregarded. The buckling characteristic of Model 1 under the maximum compression load is shown in Fig. 4. The core member is settled in the line-contact condition. The shapes of the buckling segments are similar, while the distribution of the line-contact length is nonuniform. The distribution of the line-contact length is random, which does not have an effect on the validity of the theory mentioned in Section 2.1.

The contact force T of the six BRB core members can be obtained using Eq. (3), while the finite element analysis results of the contact force T are also obtained. The results of the ratio between the finite element analysis results and the theoretical values are listed in Fig. 5, in which the horizontal axial represents the theoretical values, while the vertical axial represents the finite element analyses results. The results reveal that the ratio values primarily distribute around the 45° line, which indicates that the results obtained from the two methods coincide. The increase in the contact force T with increasing clearance, which coincides with the theory mentioned in Section 2.1, is confirmed.

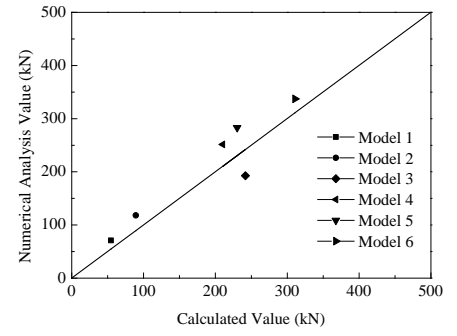


Fig. 5 Contact force of models

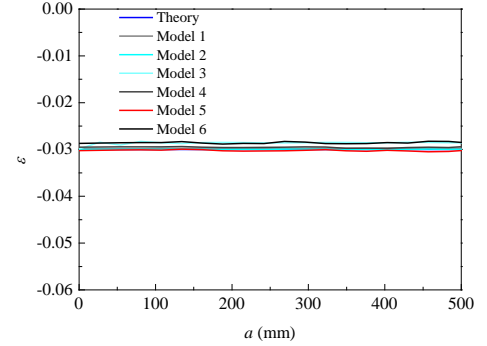


Fig. 6 Strain distribution of 6 models without friction under maximum deformation (semi-structure on the left)

Fig. 6 lists the axial strain distribution of the core member in the models, which disregards the effect of friction. The strain distribution along the axial direction is consistent, which is a nearly 3% constant amplitude under the maximum deformation.

Second, to consider friction, a friction factor of 0.3 is added to the models. The results reveal that the friction distribution is contrary between the left part of the core member and the right part of the core member, in which the middle of the core member is restrained while the load is symmetrically applied to both ends. The direction of the friction on the restrainer is opposite that on the core member, which is consistent with the interaction principle of forces.

The sum of the absolute values of friction along the core member length direction is chosen as the index for evaluating the effect of friction on the core member performance. The relationship between the friction value and the loading history of the six models is shown in Fig. 7. No contact occurs between the core member and the restrainer when the specimens are in tension, which causes zero friction. Once the BRB is under compression and the load exceeds the critical buckling force, the core member starts to buckle and make contact with the restrainer. The friction increases from the initial contact to the largest compression deformation amplitude and then maintains the maximum value. The friction decreases with the unloading of the compression load, while a reverse friction appears, which is due to the relative movement trend between the core member and the restrainer in the unloading stage contrary to the loading stage. The core member will be separated from the restrainer with further unloading, which indicates that the friction decreases to zero.

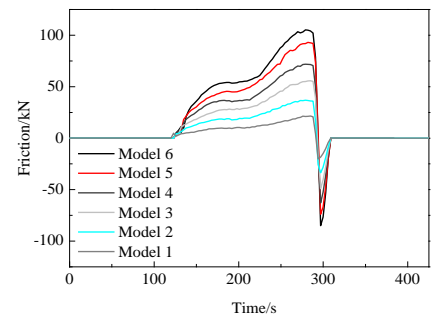


Fig. 7 Friction history

The nonuniform axial strain distribution is shown in Fig. 8, which is consistent with the previously mentioned theoretical derivation. The axial

force of the ends of the core member is greater than that in the middle, with a continuous decreasing trend along the length direction that is symmetric with the intermediate boundary, which can verify the accuracy of Eq. (6).

A comparison of Fig. 8 with Fig. 6 indicates that the friction is an immediate factor of the nonuniform strain distribution. The strain distributions also indicate that strain near the end of the core member with a nominal amplitude of 3% is considerably greater than 3%, which may cause a decrease in the low-cycle fatigue performance. This conclusion is consistent with the theoretical analysis in Section 2.1.3. Furthermore, fracture of the BRB is predicted to occur on one end of the core member.

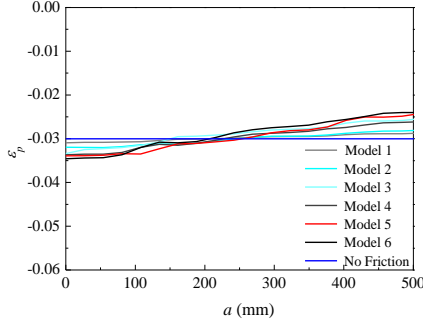


Fig. 8 Strain distribution of 6 models under a deformation amplitude of 3% (semi-structure on the left)

3. Experimental study of BRBs with various clearance values

3.1. Main sections

3.1.1 Axial tension test

The BRBs should be manufactured of steel with a high ductility performance, which can undergo a large deformation amplitude and a reverse loading test without fracturing. In this paper, Q235 steel is selected, and the mechanical properties are obtained from the axial tension test, including the yield strength, yield ratio, and percentage elongation, as reported in Table 2.

Table 2

Test results of axial tension test

No.	σ_y (MPa)	σ_p (MPa)	σ_y/σ_p (%)	E_s (N/mm ²)	μ (%)
1	276.0	420.0	65.7	205000	38.7
2	282.0	423.0	66.7	204000	39.6
3	283.0	432.0	65.5	205000	41.9
Average	280.3	425.0	66.0	204700	40.1

Note: σ_y stands for the yielding strength; σ_p stands for the limit strength; σ_y/σ_p is the yield ratio of the specimen; E_s is the Young's modulus; μ stands for the percentage elongation.

3.1.2 Low-cycle fatigue performance of Q235 steel

The low-cycle fatigue property of the BRBs substantially depends on the fatigue capacity of the steel, which is commonly related to its elasto-plastic performance. In this paper, the low-cycle fatigue properties of the selected Q235 steel are chosen based on the test results presented in Reference [11], as listed in Table 3.

Table 3

Test results of material experiments

No.	ε_a	N_f	N_{fave}
1	0.01	276	378
2	0.01	481	
3	0.02	104	104
4	0.02	104	
5	0.03	19	19
6	0.03	19	

Note: ε_a is the strain amplitude of the specimen; N_f is the number of failure cycles; N_{fave} is the average value of N_f .

Table 3 indicates that the low-cycle fatigue property of the specimens significantly decreases with increasing strain amplitude. Once the strain amplitude exceeds 2%, the low-cycle fatigue property decreases even more rapidly. However, the strain amplitude of the BRBs usually exceeds 2% during rare earthquakes. Thus, the study of the low-cycle fatigue property of BRBs is essential, especially when considering the clearance.

3.2. Design of the BRB specimens

In this paper, a type of all-steel sandwich BRB is chosen for experimental study of the influence of clearance on the mechanical property and low-cycle fatigue performance of BRBs. The clearance of the sandwich BRBs can be easily controlled, and the construction of the BRBs is convenient (Usami et al. [5]).

A sandwich BRB is composed of a core plate, a restrainer and unbonded material, as shown in Fig. 9. The core plate is a steel plate with an expanded section segment on the ends, while stiffening ribs are welded to the end of the core member, forming a cross-section. The restrainer is composed of two restraining plates and two filler strips that are connected by high-strength bolts to form a square socket, which can effectively restrain the buckling of the core member. Grooves are set on the end of the restraining plates to avoid contact between the restraining plates and the stiffening ribs when the specimen is under compression. The restraining plates should remain elastic and enable a sufficient amount of out-of-plane stiffness to resist the contact force between the core member and the restrainer without overall buckling of the BRB. This demand can be obtained by thickening the restraining plate or welding stiffening ribs on the back of the restraining plate.

The key factor in this study is the clearance in the out-of-plane direction, which can be adjusted by changing the thickness of the filler strips or adding some thin steel slices between the restraining plate and the filler strip. The dimensions of the core plate, restraining plates and filler strips are listed in Fig. 10. The clearance value d is selected to be 1.0 mm, 1.5 mm and 2.0 mm. In this paper, a total of 8 specimens were analyzed. The factors chosen for research are the key factor clearance and the thickness of the restraining plate. The main geometric factors of the specimens are listed in Table 4. The specimens are named "BRB-clearance-strain amplitude", and BRB-1-2 indicates that the specimen is set with a clearance of 1 mm and a loading strain amplitude of 2%.

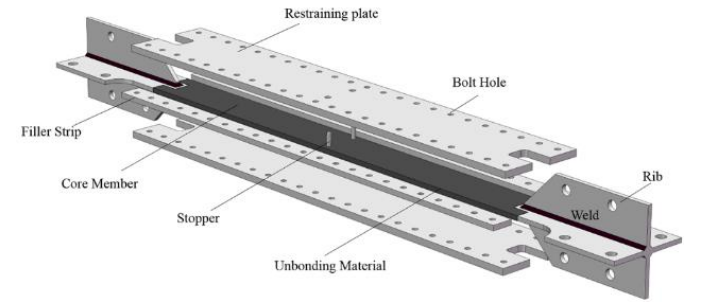


Fig. 9 Construction of a sandwich BRB

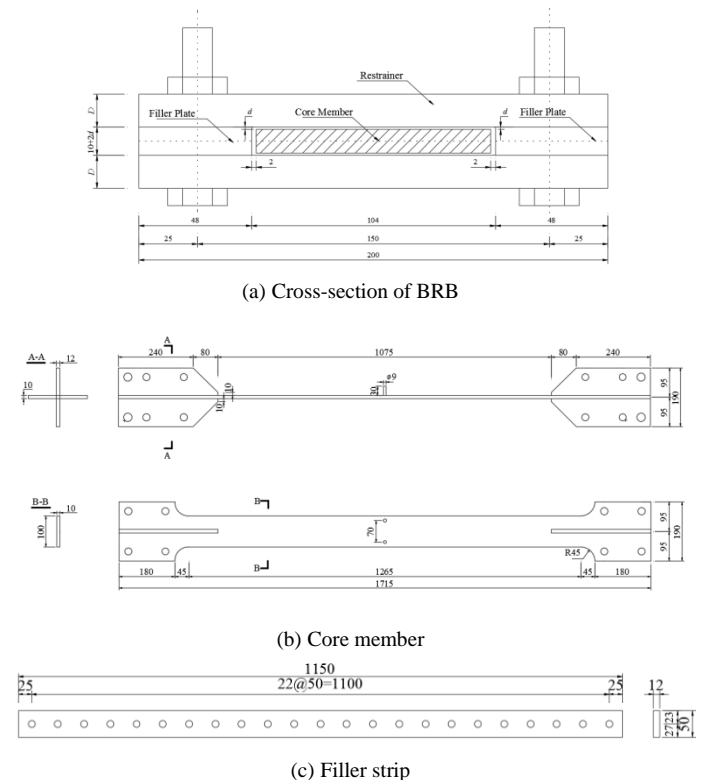




Fig. 10 Dimensions of the BRB specimens

Table 4
Factors of the BRB specimens

	D (mm)	d (mm)	ε_{nom}	v_l (mm/s)
BRB1-3	14	1	3%	0.1
BRB1-2	14	1	2%	0.1
BRB-2-3-A	14	2	3%	0.3
BRB-2-2-A	14	2	2%	0.6
BRB1.5-3	30	1.5	3%	0.3
BRB1.5-2	30	1.5	2%	0.3
BRB2-3	30	2	3%	0.3
BRB2-2	30	2	2%	0.3

Note: D is the thickness of the restraining plate; d is the clearance between the core member and the restraining plate; ε_{nom} is the nominal strain amplitude; v_l is the loading velocity of the test.

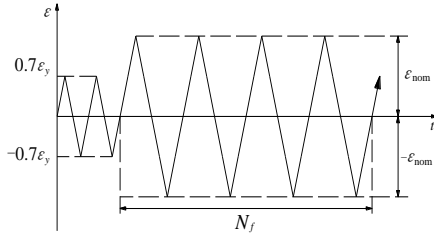


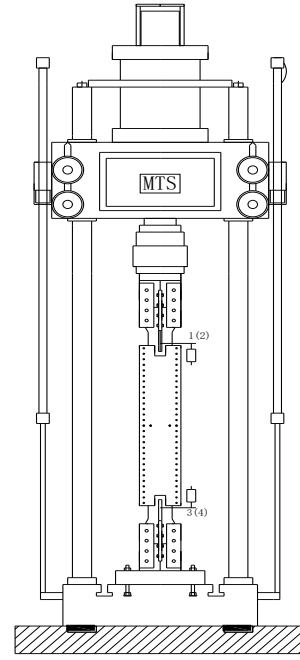
Fig. 11 Loading protocol

3.3 Testing setup

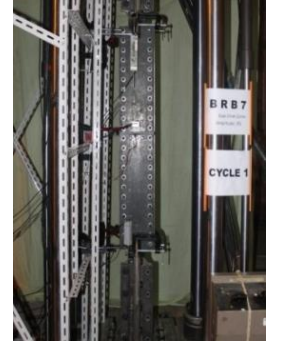
The specimens were tested in a quasi-static reversed loading test on the material testing system (MTS) shown in Fig. 12. The MTS is an electrohydraulic testing machine, whose load resisting capacity is ± 1000 kN. The load value of the MTS actuator was collected using a force transducer embedded in the system. However, the displacement of the actuator is composed of the specimen deformation and the actuator elastic deformation. The specimen deformation includes not only the deformation of the yield segment but also the deformation of the connection and transition segment, which may cause the displacement value collected by the operating device of the MTS to exceed the actual deformation of the core member yield segment. To obtain the actual deformation of the core plate, four 100 mm-capacity LVDTs were vertically placed on the specimens, which were placed on the two ends of the core member, as shown in Fig. 12(a). A 50 mm-capacity LVDT was horizontally placed on the middle of a restraining plate to monitor the out-of-plane deformations of the BRB specimens. The axial force values and the displacement values were collected by the LVDTs and a TDS-530 data acquisition instrument. The ends of the BRB specimens were connected with the MTS by the connection plates and high-strength bolts, in which a pretension torsional moment of the high-strength bolts of 500 N.m is preloaded to minimize the probable slippage of the connections between the specimens and the MTS. The arrangement of the LVDTs and the connections between the specimens and the MTS are shown in Fig. 12(b) and Fig. 12(c), respectively.

The loading protocol of the experiment was divided into two stages: preloading stage and low-cycle reversed loading stage. In the preloading stage, two elastic deformation cycles with a strain amplitude of $0.7\varepsilon_y$ (ε_y is the yielding strain) were imposed on the specimens to assess the effectiveness of the loading system and TDS-530. The low-cycle reversed loading stage was conducted with a constant strain amplitude, in which the loading velocity ranged from 0.1–0.3 mm/s. The average strain amplitudes are listed in Table 4, and the loading protocol is shown in Fig. 11. The deformation of the core

member yield segment is obtained using the LVDTs installed on the ends of the specimen, which are also used to control the MTS actuator.



(a) Test machine



(b) LVDT arrangement



(c) Connection between the specimen and MTS

Fig. 12 Test setup

3.4 Testing results

First, the reversed loading tests on specimens BRB-1-3 and BRB-1-2 were conducted with a clearance value of 1 mm, with the thickness of the restraining plates equal to 14 mm. As mentioned in Section 3.3, two elastic deformation cycles were conducted to evaluate the validity of the MTS actuator. The two specimens were tested under nominal axial strain amplitudes of 3% and 2%, with the displacements of the actuator equal to 32.04 mm and 21.40 mm, respectively. The loading velocity was 0.1 mm/s. The test results revealed that the specimen BRB-1-3 fractured at the 16th cycle, while the failure position was at the middle of the core member, which was close to the stoppers (shown in Fig. 13(a)). Specimen BRB-1-2 fractured at the 27th cycle, and the failure position was one end of the yield segment, which is close to the stiffening rib weld, as shown in Fig. 13(b). As shown in Fig. 14(a) and (b), the specimens can perform stable hysteretic properties, although no buckling occurred on the restrainer (Fig. 13(a) and (b)). However, the cyclic number of specimen BRB-1-2 was considerably less than the reversed capacity of the Q235 steel material compared with the value in Table 2, which may be attributed to the existence of the weld on the core plate end, whose heat-affected zone can decrease its low-cycle fatigue capacity.

Second, specimens BRB-2-3A and BRB-2-2A were tested with a clearance value of 2 mm, and the thickness of the restraining plates was 14 mm. The constant strain amplitudes of the two specimens were 3% and 2%, respectively, while the loading velocity was 0.3 mm/s. The specimen BRB-2-3A fractured at the 9th cycle with significant global buckling, as shown in Fig. 13(c). The specimen BRB-2-2A fractured at the 20th cycle, with global buckling in some of the last cycles, as shown in Fig. 13(d). The low-cycle fatigue capacity of the two specimens significantly decreased compared with those of BRB-1-3 and BRB-1-2, while a significant tremble phenomenon was observed in the hysteretic curves shown in Fig. 14(c) and (d). According to the theoretical analysis in Section 2.1, the value of the contact force under compression exceeded the critical buckling load, which increased with the clearance. For the two specimens, the 14 mm-thick



(a) BRB1-3

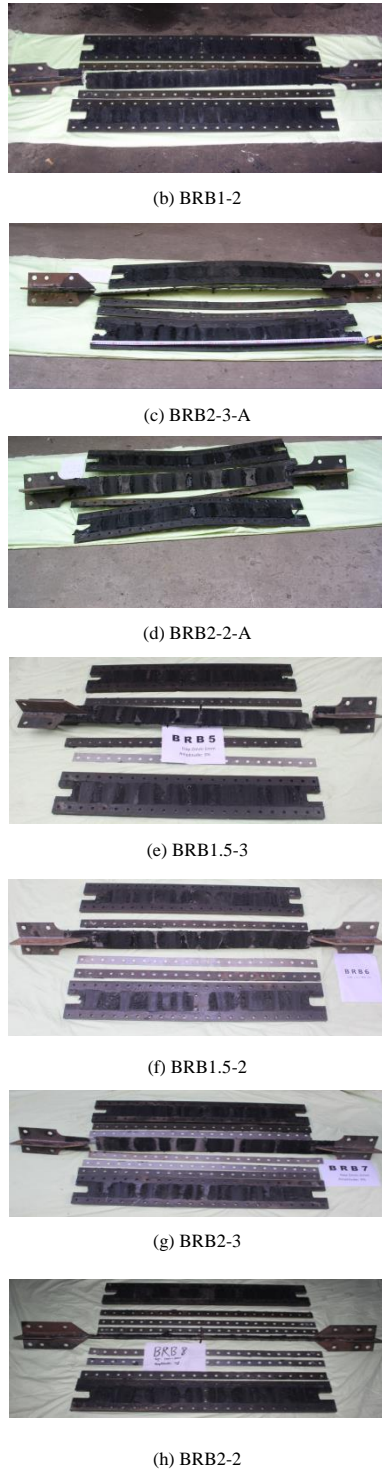


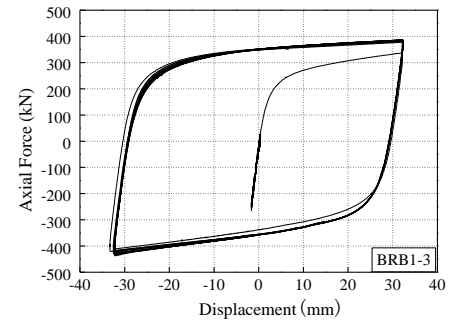
Fig. 13 Fracture mode of specimens

plates could not provide a sufficient amount of out-of-plane stiffness, which led to the global buckling. The tangent modulus of the specimen sharply decreased after the steel yielded, which further decreased the out-of-plane stiffness. The fracture occurred during the compression loading stage, while the fracture positions were on the end of the yield segment very close to the weld position, as shown in Fig. 14 (c) and (d).

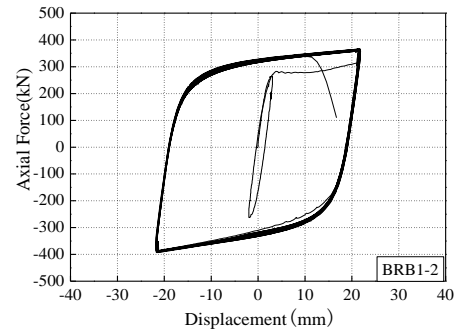
As the amplification of the clearance may improve the out-of-plane stiffness demand of the restraining plates, the thickness of the restraining plate was increased to 30 mm, in which specimens BRB-1.5-3, BRB-1.5-2, BRB-2-3 and BRB-2-2 were tested. Specimens BRB-1.5-3 and BRB-1.5-2, whose clearance was 1.5 mm, were tested under strain amplitudes of 3% and 2%, respectively. Specimen BRB-1.5-3 fractured at the 10th cycle, while BRB-1.5-2 fractured at the 25th cycle. Specimens BRB-2-3 and BRB-2-2 were also tested with clearance values of 2.0 mm. BRB-2-3 fractured at the 7th cycle, while BRB-2-2 fractured at the 27th cycle. The fracture mode and hysteretic curves of the specimens are shown in Fig. 13(e-h) and Fig. 14(e-h). No global buckling occurred, which confirmed that the thickened restraining

plates could provide a sufficient amount of out-of-plane stiffness. However, this finding also indicated that the cost of the specimens was increased, which decreased the cost performance in return. The low-cycle fatigue performance of these four specimens was also decreased compared with those of BRB-1-3 and BRB-1-2, which was similar to the specimens BRB-2-3A and BRB-2-2A, although the stiffness of the restrainer had been strengthened. These test results indicated that a large clearance cannot ensure the low-cycle fatigue performance.

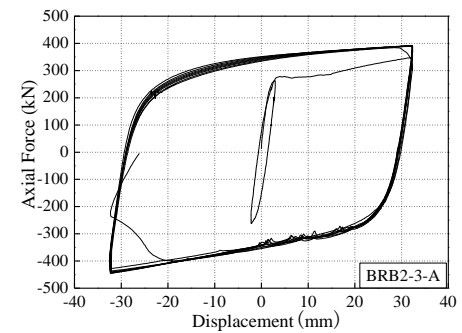
The hysteretic curves shown in Figure 14 indicate that the 8 specimens can perform stable energy dissipation capacity, while their CPD capacities can substantially exceed the CPD demand stipulated by AISC2010 ($200\Delta_y$), as shown in Table 6. The unbonded material on the yield segment was worn at the contact position, which indicates that the unbonded material can be used to ascertain the crest and trough of the buckling wave. All specimens experienced multi-wave buckling, as shown in Fig. 13, while the analysis of the multi-wave buckling will be further conducted in Section 4.3.



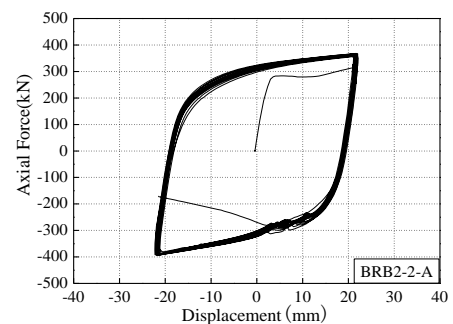
(a)



(b)



(c)



(d)

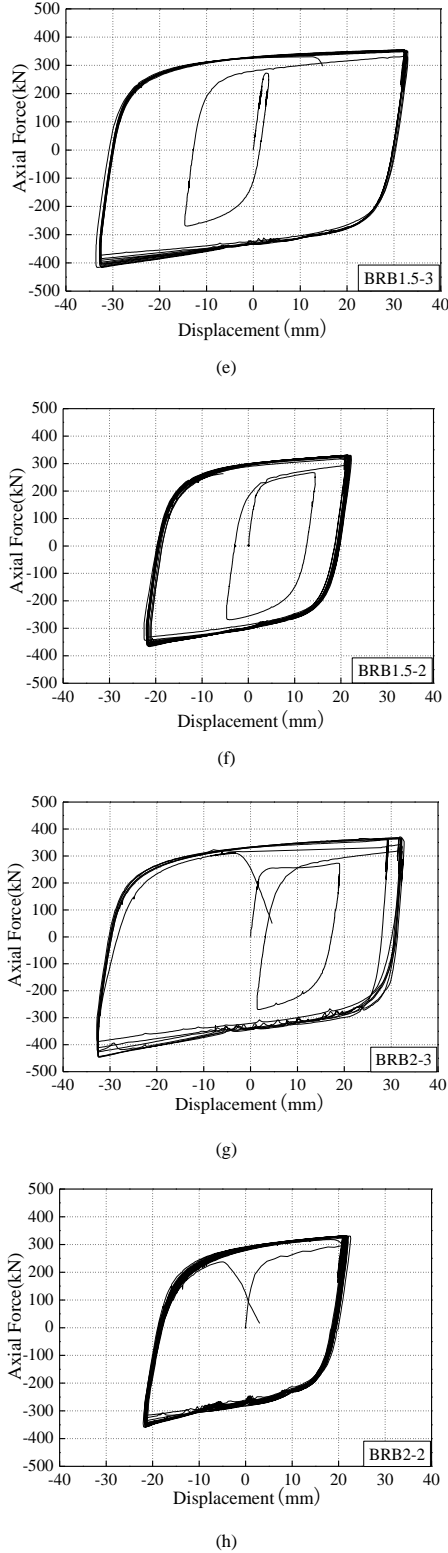


Fig. 14 Hysteretic curves of specimens

4. Influence of clearance on the performance of BRBs

4.1 Compression-strength adjustment factor

The compression-strength adjustment factor (β) of the specimens, which was obtained from the hysteretic curves, is listed in Table 5. Simultaneously, the numerical models of the BRB specimens were conducted using the method mentioned in Section 2.2; their compression-strength adjustment factors obtained via finite element analysis are also listed in Table 5. The variation trend of the compression-strength adjustment factor of the specimens is depicted in Fig. 15.

As shown in Table 5 and Fig. 15, the experimental values of the compression-strength adjustment factor are consistent with the finite element analysis values because the ratio between the two values is almost distributed around the 45° line. The conclusion that the friction increases with the

clearance can also be confirmed.

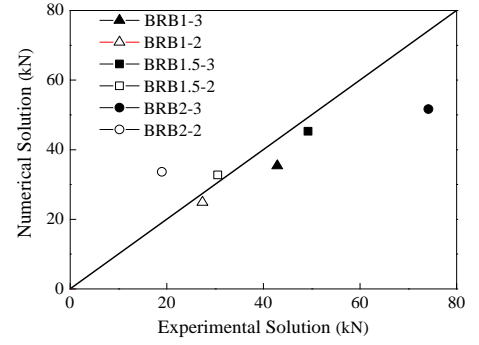


Fig. 15 Relationship of the compression-strength adjustment factor

Table 5

Compression-strength adjustment factor of specimens

	ε_{nom} (%)	d (mm)	EV (kN)	FV (kN)	β_E	β_F	β_C
BRB1-3	3	1	50.55	35.35	1.13	1.101	1.122
BRB1-2	2	1	25.75	24.86	1.07	1.072	1.105
BRB1.5-3	3	1.5	61.05	45.28	1.172	1.146	1.195
BRB1.5-2	2	1.5	35.85	32.74	1.108	1.109	1.150
BRB2-3	3	2	74.18	51.61	1.202	1.164	1.275
BRB2-2	2	2	26.10	33.63	1.078	1.112	1.200

Note: ε_{nom} is the nominal strain amplitude; d is the clearance between the core member and the restraining plate; EV is the experimental difference value of the compression force and tensile force, while FV is the finite element analysis difference value; β_E is the compression-strength adjustment factor obtained via experiment, while β_E and β_C are the factors obtained via numerical analysis and theoretical calculation, respectively.

4.2 Fracture of the specimens

The test phenomenon shown in Figure 14 indicates that only specimen BRB-1-3 fractured at the middle of the core member, while the other specimens fractured at the end of the yield segment. One important reason for these results is the influence of the weld, which causes a stress concentration and a decrease in the low-cycle fatigue performance due to the existence of a heat-affected zone. The influence of friction on this phenomenon should not be disregarded.

According to Section 2.1.2, the strain distribution of the sandwich BRBs with stoppers settled in the middle of the core member is not uniform, and the strain in the middle of the core member is less than the nominal strain amplitude, while the strain on the end of the yield segment is greater than the nominal strain amplitude. This trend is more significant with increasing clearance. When the clearance is relatively small, the friction is also small, and the distribution of the strain along the core member is relatively uniform. The fracture of the core member can occur at a random position. However, with increasing clearance, the strain of the yielding segment end is significantly greater than that in the middle, which shows that the low-cycle fatigue capacity of the member end is less than that in the middle and the low-cycle fatigue fracture is most likely occur at the end of the core member. The numerical result of specimen BRB-1-2 reveals that the strain on the core member end is 2.18%, while that on the middle is only 1.80%. This result indicates that the friction is a key factor that leads to a nonuniform strain distribution.

4.3 Low-cycle fatigue performance

The cycle number and CPD of the specimens (with the exception of BRB-2-3A and BRB-2-2A) are listed in Table 6. A comparison between the fatigue performance of the BRB specimens and the material specimens mentioned in Section 3.1 is also presented in the table.

It can be observed from Table 6 that the cycle number of specimens tested under a strain amplitude of 3% is less than that under a strain amplitude of 2%. This phenomenon is consistent with the conclusion of Section 3.1.2, which indicates that the low-cycle fatigue property of the specimens will decrease significantly with increasing strain amplitude.

As indicated in Table 6, the cycle number of specimen BRB-1-3 is 16, while that of the material 3% specimen is 19. The cycle numbers of the two tests are relatively consistent, while the BRB cycle number is slightly less than that of the material test specimen. First, the length of the BRB specimen is

substantially greater than that of the material test specimen, which may produce a larger amount of friction on the BRB. The nonuniform strain distribution is more substantial, which may cause a larger strain amplitude on the end. Furthermore, the ratio of the clearance to the core thickness in the BRB specimen (1/9.3) is relatively greater than that in the material specimen (1/20). The larger clearance-thickness ratio can cause a larger flexural moment and stress, which may decrease the low-cycle fatigue performance. However, the cycle number of specimen BRB-1-2 (27) is only 1/5 of that of the material 2% specimen (104), in which the low-cycle fatigue capacity failed to fulfill the requirement. Specimens BRB-1.5-2 and BRB-2-2 also remained within the range of 25-27 cycles, which was not less than that of BRB-1-2. The low-cycle fatigue capacity was not affected by the clearance due to the influence on the weld, which is responsible for the low-amplitude specimens (Usami et al. [26]). The heat-affected zone caused by the weld on the end of the core member may be a key factor that limits the low-cycle fatigue capacity, which indicates that the weld should be reduced or avoided if possible. Wang et al. [27, 28] proposed a type of partly welded BRB and obtained a larger cycle number. Xie et al. [11, 31] proposed a weld-free sandwich BRB, which can eliminate the effect on the weld, and obtained 147 reverse cycles of the core member under a strain amplitude of 2%.

Table 6
Fatigue performance of specimens

	d (mm)	ε_{nom} (%)	N_f	CPD	N_{fm}
BRB2-3	2	3	7	$641\Delta_y$	19
BRB1.5-3	1.5	3	10	$916\Delta_y$	19
BRB1-3	1	3	16	$1325\Delta_y$	19
BRB1.5-2	2	2	25	$1527\Delta_y$	104
BRB2-2	2	2	27	$1649\Delta_y$	104
BRB1-2	1	2	27	$1491\Delta_y$	104

Note: d is the clearance between the core member and restraining plate; ε_{nom} is the nominal strain amplitude; N_f is the cycle number of the BRB specimen; N_{fm} is the cycle number of material specimens.

A comparison of specimens BRB-1-3, BRB-1.5-3 and BRB-2-3 reveals that the low-cycle fatigue property decreases with the clearance, which causes a decrease in the cycle number. This finding is attributed to the notion that the flexural stress due to the buckling deformation of the specimen increases as the clearance increases. As mentioned in Section 3.4, the excessively low tangent modulus of the material may cause a further increase in the strain amplitude of the specimens and reduces the low-cycle fatigue capacity.

4.4 Fracture mechanism of sandwich BRBs

As indicated by the entire process of the reversed loading test, the BRB specimens primarily fractured on the yield segment end due to the weld and the friction. The weld on the end of the yielding segment cracked. Although the fracture did not immediately occur during the cycling, the cracks closed during the compression stage but extended when the specimens were under tension. The fracture therefore occurred after a certain number of cycles after the appearance of cracks.

The cracks of the weld on the core member end were caused by the stress concentration at the heat-affected zone of the weld, while the nonuniform strain distribution aggravated the development of cracks during the cyclic loading test. The actual effective area of the cross-section is smaller than the theoretical results due to cracks, which caused an increased stress and larger strain on the end of yielding segment. The cracks developed with the continued cycle loading, which aggravated the cross-section area, decreased and triggered brittle fracture in the weld heat-affected zone of the core member end.

Table 7
Buckling condition of BRB specimens

	P_E (kN)	P (kN)	P/P_E	n_e	n_f
BRB1-3	1.107	437.45	395.2	10	9
BRB1-2		393	355	9	9
BRB1.5-3		416.35	421	10	11
BRB1.5-2	0.989	366.45	370.5	10	10
BRB2-3		423.3	428	10	11
BRB2-2		356	360	9	9

Note: P_E is the critical buckling load of the specimens; P is the maximum load of the specimen; n_e is the quantity of buckling waves obtained via theoretical derivation, while n_f represents the test results.

Butyl rubber was used as unbonded material around the whole yielding segment to reduce the friction between the core member and the restrainer. The abrasion of the butyl rubber on the contact positions of the core member surface indicates the peaks and troughs of the buckling waves, as shown in Figure 14. Furthermore, the quantity of the buckling waves on the core member can be obtained by the number of abrasion positions. Note that this quantity only reflects the buckling in the last cycle of the tests.

The quantities of the buckling waves in the last cycle of the tests obtained by the experiment and the theoretical results are listed in Table 7. In Table 7, P_E represents the critical buckling load of the specimens, which was obtained via Euler's formula, while the modulus is chosen as the tangent modulus. The test results are consistent with the theoretical results.

5. Clearance demand of the BRB

As mentioned in Section 2, the nonidentity of the value of the compression and tensile strength is an important factor that affects the strain distribution and the low-cycle fatigue performance of the core member, in which the friction is the main inducement. In this section, the analytic formula of the β value of the BRB is proposed; Poisson's effect is disregarded. The tensile force of the BRB can be expressed as

$$F_T = \sigma_e \cdot A_e \quad (7)$$

where F_T is the tensile force of the BRB, σ_e is the axial stress of the core member under strain ε , and A_e is the cross-section area of the core member. Only the core member bears an axial force, while the restrainer is free when the BRB is under tension.

The compression force of the BRB can be expressed as the sum of the compression force of the core member and the friction between the core member and the restrainer:

$$P = \sigma_e \cdot A_e + f \quad (8)$$

where P is the axial force of the core member, σ_e is the axial stress of the core member under strain ε , A_e is the cross-section area of the core member, and f is the friction between the core member and the restrainer, which can be obtained using Eq. (3) and (4).

Integrating Eq. (3), (7) and (8) into Eq. (1), the β value of the BRB can be expressed as

$$\beta = \frac{\sigma_e A_e + \mu \cdot (2n)^2 \cdot \frac{Py_0}{\pi} \cdot \sqrt{\frac{P}{EI}}}{\sigma_e A_e} \quad (9)$$

where n is the number of waves on one side of the core member, while the other symbols are identical to those in Eq. (1)-(8). The β value is proportional to the clearance between the core member and the restrainer, while the friction coefficient μ and the number of waves can also affect the β value. The β value is relative to the strain amplitude experienced by the core member, in which different strain amplitudes can directly cause different β values. The other factors are disregarded, and only friction is considered. The β values for the experimental specimens obtained via Eq. (9) are listed in Table 5. Comparing these calculated values β_c with the experimental values β_E and the numerical values β_F , Eq. (9) can be used to evaluate the β value.

As stipulated in AISC341-10, the β value should satisfy

$$\beta \leq 1.3 \quad (10)$$

The clearance demand can be expressed by combining Eq. (9) and (10):

$$y_0 \leq \frac{0.3F_T \cdot \pi \sqrt{EI}}{2n\mu P \sqrt{P}} = \frac{0.3\pi \sqrt{EI}}{2n\mu \sqrt{F_T} \cdot \beta^2} \quad (11)$$

where EI is the inertia moment of the core member, and the other symbols are listed in Eq. (7)-(10).

Considering that the core member predominantly yielded under compression, the tangent modulus E_t of the material is used for E in Eq. (11).

The clearance (y_0) demand between the core member and the restrainers of a certain BRB under a certain nominal axial strain amplitude and axial force can be obtained, where the friction coefficient μ is inversely proportional to the clearance demand. The unbonded material can release the β value, which is attributed to a decrease in the friction coefficient between the core member and the restrainer caused by the unbonded material.

Once a stricter β value limit is expected, Eq. (10) can be generalized as

$$\beta \leq 1 + x \quad (12)$$

in which $0 \leq x \leq 0.3$.

Eq. (11) can also be generalized as

$$y_0 \leq \frac{(\beta - 1)F_T \cdot \pi \sqrt{EI}}{2n\mu P \sqrt{P}} = \frac{(\beta - 1)\pi \sqrt{EI}}{2n\mu \sqrt{F_T} \cdot \beta^2} \quad (13)$$

The y_0 value upper limit of the BRB specimens in this paper is obtained using Eq. (11) and (13), in which the nominal strain amplitude is chosen to be 3% and 2%. The upper limit of the β value is chosen to be 1.3, 1.2 and 1.1. Simultaneously, the laying of the unbonded material is regarded as a variable in this analysis, in which the contribution of the unbonded material to the β value is verified. The friction coefficient between the core member and the restrainer is 0.3 without laying the unbonded material, while 0.1 is selected when the unbonded material is laid according to GB50017-2017 [29] and Jia et al. [30].

Table 8
 y_0 demand of BRB specimens

β	Unbonding material	Friction coefficient	$\varepsilon_{nom}=3\%$	$\varepsilon_{nom}=2\%$
1.3	no	0.3	0.727	0.829
	lay	0.1	2.42	2.49
1.2	no	0.3	0.547	0.622
	lay	0.1	1.64	1.868
1.1	no	0.3	0.311	0.353
	lay	0.1	0.934	1.06

Note: ε_{nom} is the nominal strain amplitude of test specimens; “no” means no unbonding material laid on the specimen, while “lay” means that unbonding material is laid on the specimen.

Table 8 reveals that laying the unbonded material can effectively release the limit of y_0 between the core member and the restrainer. Considering the condition in which the nominal strain amplitude is 3% and the β value upper limit is 1.3 as an example, the y_0 upper limit is 0.727 mm if no unbonded material is laid, whereas 2.42 mm can be allowed when laying the unbonded material. Achieving a clearance demand less than 1 mm is difficult, while laying the unbonded material during the design of a BRB is feasible. The upper limit of y_0 is released with decreasing nominal strain amplitude, which can be observed from Table 8. Furthermore, a stricter β upper limit will cause a considerably stricter y_0 upper limit. Note that the upper limit of the y_0 value can make the β value satisfy the stipulation of AISC341-10, while a trend of the hysteretic curves in the compression stage is observed in the test specimens whose y_0 value is 2 mm, as shown in Figure 13(c), (d), (g) and (h). A similar phenomenon is also observed in Reference [28]. This phenomenon reveals that the clearance should be limited by the β value upper limit, and the hysteretic performance of the actual specimens should also be considered.

Poisson's effect of the core member should not be disregarded in the design because the cross-sectional area increases under compression and may fill the clearance. Once the reserved clearance is too thin, the restrainer may form a hoop effect on the core member, which can significantly improve the compressive strength of the BRB specimen. The specimen may not yield first, and the elastic strain of the main members may not be ensured in this condition, which may decrease the ductility of the whole structure. Furthermore, the restrainer may bear a large force, which may cause fracture. Thus, a minimum value for the clearance between the core member and the restrainer should be reserved.

Poisson's ratio is chosen to be 0.5 for the plastic condition, while the transverse strain can be obtained as

$$\varepsilon_t = \nu \varepsilon_v = 0.5 \varepsilon_v \quad (14)$$

where ε_v is the axial strain of the core member, ε_h is the transverse strain, and ν is Poisson's ratio.

The minimum clearance value of the in-plane direction can be defined as $d_{0,min}$:

$$d_{0,min} = 0.5B\varepsilon_t = 0.25B\varepsilon_v \quad (15)$$

where B is the width of the core member.

Similarly, the minimum clearance value of the out-of-plane direction is defined as d_{min} :

$$d_{min} = 0.25t\varepsilon_v \quad (16)$$

where t is the thickness of the core member.

The minimum clearance can be obtained from Eq. (14)-(16). The minimum clearance of the in-plane direction and out-of-plane direction of the specimens in this paper is 0.15 mm. In conclusion, the contribution of the unbonded material in limiting the β value should be considered, in which an upper limit of the clearance should be obtained by Eq. (11) or (13). Simultaneously, the clearance value should not be less than the minimum value obtained using Eq. (15) and (16). Furthermore, the stability of the hysteretic property of the specimens should also be considered. It is essential to mention that the analytical solution of this paper could be applied as a standard for sandwich BRBs, while it could also be used for BRBs whose yielding segments of the core member are manufactured from steel plates.

6. Conclusion

The influence of the clearance between the core member and the restrainer on the mechanical performance of BRBs is analyzed in this paper via experimental and numerical studies.

Six finite element models of BRBs with various clearances were conducted, and the multi-wave buckling of the BRB core members was analyzed. The strain distribution along the core member was not uniform due to the clearance effect. The results indicated that the core member buckles under compression when the load exceeds the critical buckling load and the core member is in contact with the restrainer due to the contact force between them. Additionally, the relative movement trend causes friction between them, which leads to a nonuniform strain distribution along the core member. This phenomenon causes the strain on the core member end to exceed the nominal value, while it is lower in the middle of the core member, which hinders expression of the low-cycle fatigue property of the specimen. When the friction increases with the amplification of the clearance, it causes an increase in the compression-strength adjustment factor (β) and aggravates the nonuniformity of the strain distribution on the core member. The low-cycle fatigue property of the specimen is significantly decreased.

Eight sandwich BRB specimens that were manufactured with different clearances were tested under reversed loading, in which the compression-strength adjustment factors, the CPDs, the energy dissipation capacity and the buckling characteristic were analyzed. The experimental results revealed a stable hysteretic property and energy dissipation capacity, which can satisfy the stipulated value of AISC2010. However, the compression-strength adjustment factor increased with the clearance, and the cycle number under the same strain amplitude decreased. Specimen BRB-1-3, whose nominal strain amplitude is 3% with a clearance value of 1 mm, can achieve a full low-cycle fatigue capacity. However, the low-cycle fatigue capacity of specimens with a clearance of 1.5 mm and 2 mm significantly decreased, which is in agreement with the theoretical derivation and numerical analysis. Conversely, the specimens with a nominal strain amplitude of 2% performed a relatively stable cycle number, which seemed to prevent the influence on the clearance. However, the cycle numbers of the BRB specimens were significantly less than those of the material specimens. The fracture positions were mostly concentrated on the end of the yielding segment of the core member because the weld heat-affected zone cracked during the reversed loading tests, which caused brittle failure of the specimens, while the low-cycle fatigue capacity of the material could not be fully displayed. Furthermore, the larger clearance signifies a higher restrainer stiffness demand, which may decrease the cost performance of the BRBs.

A formula for evaluating the compression-strength adjustment factor is deduced, which confirms that the calculated value is consistent with that of the experimental value and the numerical analysis results. The upper limit of the clearance is also proposed by considering the β value limit, while the lower limit can be restricted by considering Poisson's effect. The results also confirmed that the clearance between the core member and the restrainer

should be strictly limited in the design of the BRB for assuring the low-cycle fatigue performance, which should be limited according to the formula derivation and experimental results. The influence of the weld should be solved by reducing or eliminating the weld on the specimens, which can help the specimens achieve a low-cycle fatigue performance under minimal nominal strain amplitude. The analytical solution of this paper could be used in BRBs whose yielding segments of the core member are manufactured from steel plates.

References

- [1] Usami T., Wang C. L. and Funayama J., "Developing high-performance aluminum alloy buckling-restrained braces based on series of low-cycle fatigue tests", *Earthquake Engineering & Structural Dynamics*, 41(4), 643-661, 2012.
- [2] Tsai K.C., Hsiao P.C., Wang K.J., Weng Y.T., Lin M.L., Lin K.C., Chen C.H., Lai J.W. and Lin S.L., "Pseudo-dynamic tests of a full-scale CFT/BRB frame—Part I: Specimen design, experiment and analysis", *Earthquake Engineering & Structural Dynamics*, 37(7), 1081-1098, 2008.
- [3] Chou C.C. and Chen S.Y., "Subassemblage tests and finite element analyses of sandwich buckling-restrained braces", *Engineering Structures*, 32(8), 2108-2121, 2010.
- [4] Vargas R. and Bruneau M., "Experimental response of buildings designed with metallic structural fuses. II", *Journal of structural engineering*, 135(4), 394-403, 2009.
- [5] Usami T., Wang C. and Funayama J., "Low-cycle fatigue tests of a type of buckling restrained braces", *Procedia Engineering*, 14, 956-964, 2011.
- [6] Feng Y.L., Wu J. and Meng S.P., "Elastic displacement spectrum-based design approach for buckling-restrained braced frames", *Journal of Earthquake Engineering*, 20(6), 841-860, 2016.
- [7] Wu J., Liang R.J., Wang C.L. and Ge H.B., "Restrained buckling behavior of core component in buckling-restrained braces" *International Journal of Advanced Steel Construction*, 8(3), 212-225, 2012.
- [8] Takeuchi T., Hajjar J.F., Matsui R., Nishimoto K. and Aiken I.D., "Effect of local buckling core plate restraint in buckling restrained braces", *Engineering Structures*, 44, 304-311, 2012.
- [9] AISC A. "AISC 341-10, Seismic Provisions for Structural Steel Buildings", Chicago, IL: American Institute of Steel Construction, 2010.
- [10] Ung C.M., Nakashima M. and Tsai K.C., "Research and application of buckling-restrained braced frames", *International Journal of Steel Structures*, 4(4), 301-313, 2004.
- [11] Xie L.Q., Wu J. and Huang Q., "Experimental Study on Low-Cycle Fatigue Performance of Weld-Free Buckling-Restrained Braces", *Journal of Earthquake Engineering*, 22(8), 1392-1414, 2018.
- [12] Jiang Z.Q., Dou C., Guo Y.L. and Zhang A.L., "Theoretical study on design methods for pinned assembled BRB with flat core", *Engineering Structures*, 133, 1-13, 2017.
- [13] Wu B. and Mei Y., "Buckling mechanism of steel core of buckling-restrained braces", *Journal of Constructional Steel Research*, 107, 61-69, 2015.
- [14] FEMA450 F. "NEHRP recommended provisions for seismic regulations for new buildings and other structures, Part 1: Provisions", Washington (DC, USA), BSSC, 2003.
- [15] Black C.J., Makris N. and Aiken I.D., "Component testing, seismic evaluation and characterization of buckling-restrained braces", *Journal of Structural Engineering*, 130(6), 880-894, 2004.
- [16] Wang C.L., Usami T., Funayama J. Imase F., "Low-cycle fatigue testing of extruded aluminium alloy buckling-restrained braces", *Engineering Structures*, 46, 294-301, 2013.
- [17] Jia M.M., Yu X.H., Lu D.G. and Lu B.B. "Experimental research of assembled buckling-restrained braces wrapped with carbon or basalt fiber", *Journal of Constructional Steel Research*, 131, 144-161, 2017.
- [18] Guo Y.L., Fu P.P., Zhou P. and Tong J.Z. "Elastic buckling and load resistance of a single cross-arm pre-tensioned cable stayed buckling-restrained brace", *Engineering Structures*, 126, 516-530, 2016.
- [19] Guo Y.L., Zhou P., Bradford M.A., Pi Y.L., Tong J.Z. and Fu P.P., "Theoretical and numerical studies of elastic buckling and load resistance of double cross-arm pre-tensioned cable stayed buckling-restrained braces", *Engineering Structures*, 153, 674-699, 2017.
- [20] Sabelli R., "Research on improving the design and analysis of earthquake-resistant steel-braced frames", EERI, 2001.
- [21] Iwata M., Kato T. and Wada A., "Performance evaluation of buckling-restrained braces in damage-controlled structures", *Behavior of steel structures in seismic areas: STESSA*, 37-43, 2003.
- [22] Usami T., Kasai A. and Kato M., "Behavior of buckling-restrained brace members", *Behavior of Steel Structures in Seismic Areas, Proc., 4th Int. Conf. STESSA 2003*, Naples, Italy, 211-216, 2003.
- [23] Lin P.C., Tsai K.C., Chang C.A., Hsiao Y.Y. and Wu A.C., "Seismic design and testing of buckling-restrained braces with a thin profile", *Earthquake Engineering and Structural Dynamics*, 45(3), 339-358, 2016.
- [24] Matsui R. and Takeuchi T., "Cumulative Deformation Capacity of Buckling Restrained Braces Taking Local Buckling of Core Plates into Account", *Proc. 15th World Conference on Earthquake Engineering (Lisbon)*, 2012.
- [25] Takeuchi T. and Wada A., "Buckling-Restrained Braces and Applications", JSSI, 2017
- [26] Usami T., Sato T. and Kasai A., "Developing high-performance buckling-restrained braces", *Journal of Structural Engineering*, 55, 719-729, 2009.
- [27] Wang C.L., Usami T. and Funayama J., "Evaluating the influence of stoppers on the low-cycle fatigue properties of high-performance buckling-restrained braces", *Engineering Structures*, 41, 167-176, 2012.
- [28] Wang C.L., Li T., Chen Q. and Wu J., "Experimental and theoretical studies on plastic torsional buckling of steel buckling-restrained braces", *Advances in Structural Engineering*, 17(6), 871-880, 2014.
- [29] GB 50017-2017, Code for design of steel structure, Ministry of Housing and Urban-Rural Development of the People's Republic of China, Beijing, 2017. (in Chinese)
- [30] Jia M.M., Zhang S.M. and Lu D.G., "Stability behavior and ductility performance analysis of buckling restrained braces", *Journal of Building Structures (Supplementary Issue 2)*, 76-81, 2010. (in Chinese)
- [31] Xie L.Q., Wu J., Huang Q. and Tong C., "Analysis of the Seismic Demand of High-Performance Buckling-Restrained Braces under a Strong Earthquake and its Aftershocks", *Advances in Civil Engineering*, 1482736, 2019.

Acknowledgments

The authors would like to acknowledge financial support from the National Natural Science Foundation of China (51978165), the China National Key Research and Development Program (2016YFC0701403) and the Priority Academic Program Development of Jiangsu Higher Education Institutions (PAPD).

LATERAL TORSIONAL BUCKLING STRENGTH OF STEEL I-BEAMS WITHIN PREFLEXED BEAMS IN PRE-BENDING STAGE

Lin-jie Tian¹, Zhe Li², Ming Yang^{1,*}, Shan Chang¹ and Jian-qi Qian¹

¹ School of Transportation, Southeast University, Nanjing, China

² Tongji Architectural Design(Group) Co., Ltd, Shanghai, China

* (Corresponding author: E-mail: mingyang@seu.edu.cn)

ABSTRACT

Attention should be paid to the lateral torsional buckling (LTB) of steel I-beams in pre-bending stage for the usage of preflexed beams. This paper develops analytical and numerical models for predicting LTB strength of steel I-beams arranged with different numbers of lateral braces and subjected to two movable concentrated loads in pre-bending stage. The different out-of-plane deformations of beam segments under assumed and actual conditions caused by bending moment distribution were considered, and the modified Rayleigh-Ritz method was proposed based on the constraint effect of adjacent beam segments. ABAQUS 2017 program was used for finite element analysis (FEA), and then have a comparison with the theoretical analysis. Additionally, LTB strength of steel I-beams with different parameters were investigated, and the effect of every selected parameter was described. The comparison results show that the modified Rayleigh-Ritz method has better applicability and accuracy under different parameters than the traditional Rayleigh-Ritz method, which can be used for selecting parameters and predicting LTB strength of steel I-beams in pre-bending stage.

ARTICLE HISTORY

Received: 25 April 2019
Revised: 20 October 2019
Accepted: 24 October 2019

KEYWORDS

Preflexed beam;
Lateral torsional buckling;
Modified Rayleigh-Ritz method;
Lateral brace;
LTB critical moment

Copyright © 2020 by The Hong Kong Institute of Steel Construction. All rights reserved.

1. Introduction

Preflexed beam was first proposed by Belgian bridge engineer A.Lipski around 1940s, which is widely used in South Korea, United States and other countries due to the advantages of convenient construction, light lifting, and low beam height. These beams are composed of steel I-beams, generally with symmetric or monosymmetric cross sections [1]. As shown in Fig.1, in order to make the concrete bottom flange prestressed, the steel I-beam is firstly preflexed by two concentrated loads, then concrete is cast around the bottom flange of the steel I-beam, after it has sufficiently hardened, the steel I-beam is unloaded with the concrete flange becomes prestressed subsequently.

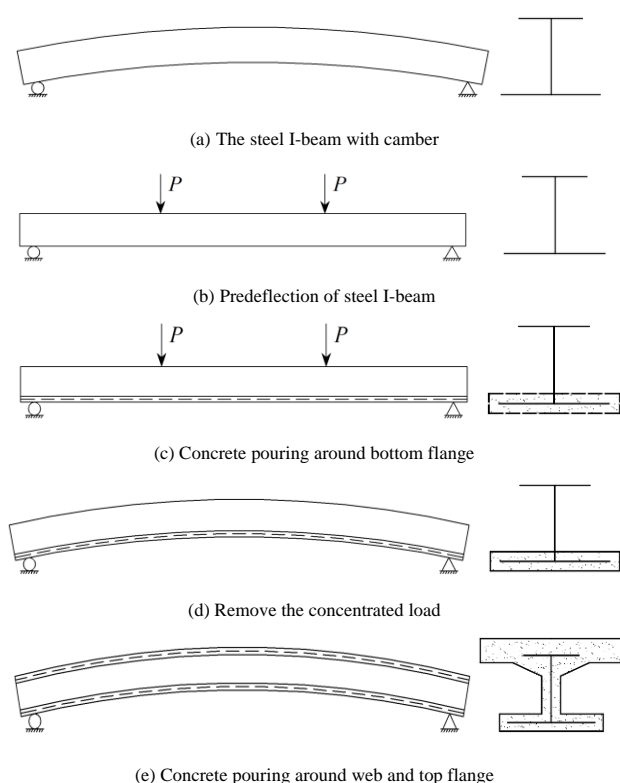


Fig.1 Construction process of preflexed beam

As preflexed beam employed in more and more buildings and large span bridges, the concrete in compression area needs more compressive stress to improve its bearing capacity, which requires large concentrated loads in pre-bending stage [2]. However, lateral torsional buckling (LTB) usually occurs especially when the steel I-beam is slender enough (shown as Fig. 2). As one of the most effective ways, the longitudinal direction of the steel I-beams is usually set with discrete lateral braces to prevent this phenomenon (shown as Fig. 3).

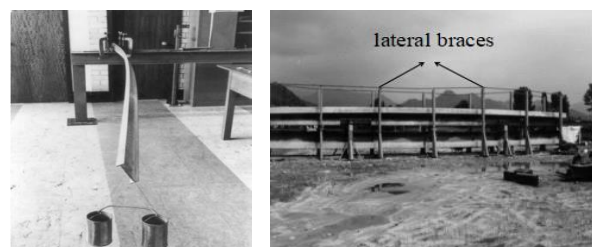


Fig. 2 LTB of the steel I-beam Fig. 3 Lateral braces of the steel I-beam

Considerable attention has been paid by researchers to study the LTB strength of steel I-beams. Some research on this issue are as follows: Taylor and Ojalvo [3] derived the exact solution for LTB strength of steel I-beams under uniform pressure, mid-span concentrated load and pure bending, respectively. Mutton et al. [4] studied the LTB strength of a simply supported steel I-beam under a central concentrated load arranged with a single brace at mid-span. Kitipornchai and Wang [5] investigated the LTB strength of simply supported steel I-beams with monosymmetric sections under moment gradient. Wang et al. [6] presented an automated Rayleigh-Ritz method for elastic buckling analysis of symmetric steel I-beams subjected to arbitrary loading condition. Nguyen et al. [7] studied the LTB strength of steel I-beams with discrete braces and then had a further study [8] on steel I-beams under various loading conditions. Gelera [9] analyzed the LTB strength of a steeped I-beam with singly symmetric cross sections. Ozbasaran et al. [10] proposed a closed-form equation to determine the LTB load, and an alternative design procedure was presented for predicting LTB strength of steel I-beams. Mohammadi et al. [11] investigated the LTB strength of steel I-beams with different degree of monosymmetry and web heights.

Few articles exist on steel I-beams subjected to two movable concentrated loads. In this study, steel I-beams arranged with different lateral bracing numbers and subjected to two movable concentrated loads were analyzed using traditional Rayleigh-Ritz method, and the modified Rayleigh-Ritz method was proposed based on the constraint effect of adjacent beam segments. Theory analysis and finite element analysis (FEA) were compared

under the most commonly used parameters for preflexed beams, and the effect of every selected parameter was investigated. The comparison results show that the finite element analysis results are in good agreement with the theoretical analysis results. In addition, the study of parameters can provide reference value for parameter selection of steel I-beams in pre-bending stage.

2. Theoretical Solution Based on Rayleigh-Ritz Method

Fig. 4(a) and Fig. 4(b) show two simply supported steel I-beams subjected to two movable concentrated loads without brace and with n lateral braces, respectively. The location of both of the concentrated loads are assumed at the distance of l/m from the beam ends, where l is the whole length of the steel I-beam, and the value of loading location parameter m can be optional, which denotes the loading location of concentrated loads.

It is assumed in Fig. 5(a) that x , y and z axes denote strong axis, weak axis, and longitudinal axis of the steel I-beam, respectively. The u , v , and w are designated for corresponding deformation of x , y and z , respectively. The letter R in Fig. 4(b) represents the stiffness of lateral braces and the symbol φ in Fig. 5(b) represents the rotation angle of cross section. The point O and S in Fig. 5(b) stand for the centroid and the shear center of cross section, respectively.

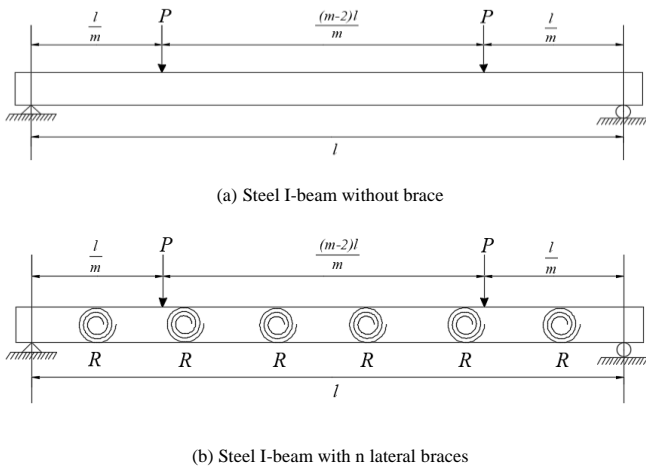


Fig.4 Theoretical calculation models of steel I-beams

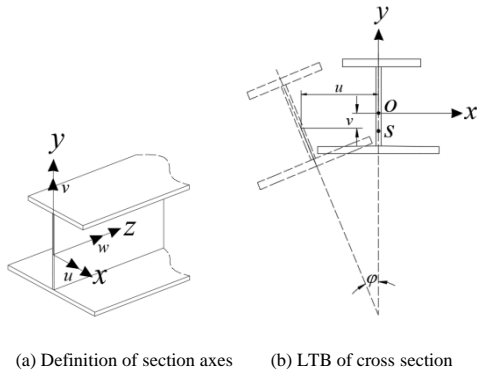


Fig. 5 Cross section of the steel I-beam

of steel I-beams. The solution is derived based on the following assumptions: (a) the deformation in-plane can be ignored; (b) the material of the structure follows Hook' law; (c) the deformation of the member is small; (d) the contour of the cross section is rigid; (e) the elastic torsional braces are all set to centroidal axis; (f) the stiffness of the lateral braces R are all larger than or equal to bracing stiffness requirement R_T .

According to the above assumptions, the potential energy stored in steel I-beams without brace and with n lateral braces shown in Fig. 4(a) and Fig. 4(b) can be written as follows, respectively:

$$\begin{cases} U_0 = \frac{1}{2} \int_0^l [EI_y u''^2 + EI_w \varphi''^2 + (GI_t + 2\beta_y M_x) \varphi'^2 + 2M_x u' \varphi] dz \\ U_n = \frac{1}{2} \int_0^l [EI_y u''^2 + EI_w \varphi''^2 + (GI_t + 2\beta_y M_x) \varphi'^2 + 2M_x u' \varphi] dz + \frac{1}{2} R \sum_{i=1}^n \varphi_i^2 \end{cases} \quad (1)$$

Where E denotes the Young's modulus; I_y denotes the moment of inertia about weak axis; I_w denotes the warping constant; G denotes the shear modulus; I_t denotes the torsional constant; β_y denotes the monosymmetric property; M_x denotes the moment about strong axis of steel I-beams induced by concentrated load; φ_i ($i=1,2,3,\dots,n$) denotes the twisting angle of cross section at lateral bracing points.

The energy increased by concentrated loads is:

$$\Omega = -\frac{1}{2} Pa [\varphi(l/m)]^2 - \frac{1}{2} Pa \left[\varphi \left(\frac{m-1}{m} l \right) \right]^2 \quad (2)$$

Where P denotes the movable concentrated load; a denotes the distance of loading point above shear center.

Thus the total energy equations are obtained as follows from the sum of the above energy Eqs. (1) and (2):

$$\begin{cases} \Pi_0 = U_0 + \Omega \\ \Pi_n = U_n + \Omega \end{cases} \quad (3)$$

Where Π_0 and Π_n are the total energy of steel I-beams without brace and with n lateral braces, respectively.

Based on the theory of material mechanics [12], the following equilibrium differential equation about the steel I-beam is obtained:

$$EI_y u'' = -M_x \varphi \quad (4)$$

For I-beams subjected to concentrated loads shown as Fig. 4(a) and Fig. 4(b), the functions about M_x are expressed as:

$$M_x = \begin{cases} Pz & 0 \leq z \leq \frac{l}{m} \\ \frac{Pl}{m} & \frac{l}{m} \leq z \leq \frac{(m-1)l}{m} \\ P(l-z) & \frac{(m-1)l}{m} \leq z \leq l \end{cases} \quad (5)$$

For a simply supported steel I-beam, there exists no torque, deflection, and bending moment at both beam ends. As a result, the boundary conditions are considered as follows:

$$u(0) = v(0) = w(0) = \varphi(0) = u'(0) = v'(0) = w'(0) = \varphi(l) = 0 \quad (6)$$

When no brace exists, the buckling model is a symmetric half-sine-wave, when the bracing stiffness is larger than the bracing stiffness requirement R_T , it will buckle in $n+1$ model [13], so the twisting angle φ is assumed as follows which satisfies the above boundary conditions:

$$\begin{cases} \varphi_0(z) = C \sin\left(\frac{\pi z}{l}\right) & 0 \leq z \leq l \\ \varphi_n(z) = C \sin\left(\frac{(n+1)\pi z}{l}\right) & 0 \leq z \leq l, R \geq R_T \end{cases} \quad (7)$$

In this study, the Rayleigh-Ritz method was used to analyse LTB strength

Where $\varphi_0(z)$ and $\varphi_n(z)$ denote twisting angle of the steel I-beam without brace and with n lateral braces, respectively; C is the deformation coefficient of the steel I-beam deformed as the sine half-wave curve.

Substituting Eqs. (1), (2), (4), (5) and (7) into Eq. (3) yields the following equations:

$$\left\{ \begin{aligned} \Pi_0 &= \frac{1}{2} \int_0^l \left(\frac{\pi^4 E I_w}{l^4} C^2 \sin^2 \frac{\pi z}{l} + \frac{\pi^2 G I_t}{l^2} C^2 \cos^2 \frac{\pi z}{l} \right) dz \\ &+ \frac{1}{2} \int_0^l \left(\frac{2\pi^2 \beta_y M_x}{l^2} C^2 \cos^2 \frac{\pi z}{l} - \frac{M_x^2 C^2}{E I_y} \sin^2 \frac{\pi z}{l} \right) dz - P a k_0^2 C^2 \\ \Pi_n &= \frac{1}{2} \int_0^l \left(\frac{(n+1)^4 \pi^4 E I_w}{l^4} C^2 \sin^2 \frac{(n+1)\pi z}{l} + \frac{(n+1)^2 \pi^2 G I_t}{l^2} C^2 \cos^2 \frac{(n+1)\pi z}{l} \right) dz \\ &+ \frac{1}{2} \int_0^l \left(\frac{2(n+1)^2 \pi^2 \beta_y M_x}{l^2} C^2 \cos^2 \frac{(n+1)\pi z}{l} - \frac{M_x^2 C^2}{E I_y} \sin^2 \frac{(n+1)\pi z}{l} \right) dz - P a k_n^2 C^2 \end{aligned} \right. \quad (8)$$

Where $k_0 = \sin(\pi/m)$, $k_n = \sin[(n+1)\pi/m]$.

According to the potential energy principle and the elastic stability theory of structure [13], the following equation is given as:

$$\frac{\partial \Pi_l}{\partial C} = 0 \quad (9)$$

Substituting Eq. (8) and $P = mM/l$ into Eq. (9) leads to:

$$\left\{ \begin{aligned} M_{cr,0} &= \beta_1 \frac{\pi^2 E I_y}{l^2} \left\{ \left[-\beta_2 a + \beta_3 \beta_y \right] + \sqrt{\frac{[-\beta_2 a + \beta_3 \beta_y]^2 + \frac{I_w}{I_y} \left(1 + \frac{l^2 G I_t}{\pi^2 E I_w} \right)}{2}} \right\} \\ M_{cr,n} &= \chi_1 \frac{\pi^2 E I_y}{l^2 (n+1)^2} \left\{ \left[-\chi_2 a + \chi_3 \beta_y \right] + \sqrt{\frac{[-\chi_2 a + \chi_3 \beta_y]^2 + \frac{I_w}{I_y} \left(1 + \frac{l^2 (n+1)^2 G I_t}{\pi^2 E I_w} \right)}{2}} \right\} \end{aligned} \right. \quad (10a, b)$$

Where $M_{cr,0}$ and $M_{cr,n}$ represent the LTB critical moment of steel I-beams subjected to two movable concentrated loads without brace and with n lateral braces, respectively. And the functions of the parameters are expressed as follows:

$$\begin{aligned} \beta_1 &= \sqrt{\frac{6\pi t^2}{-8t^3 + 3\sin(2t) + 6\pi t^2 - 6t \cos 2t}}, \quad \beta_2 = \frac{2k^2}{\pi t} \beta_1, \\ \beta_3 &= \frac{\pi t - t^2 - \sin^2 t}{\pi t} \beta_1, \quad \chi_1 = \sqrt{\frac{6(n+1)\pi t_1^2}{-8t_1^3 + 3\sin(2t_1) + 6\pi t_1^2 - 6t_1 \cos 2t_1}}, \\ \chi_2 &= \frac{2k_n^2}{\pi t_1} \chi_1, \quad \chi_3 = \frac{\pi t_1 - t_1^2 - \sin^2 t_1}{\pi t_1} \chi_1, \quad k = \sin t, \\ t &= \frac{\pi}{m}, \quad k_1 = \sin t_1, \quad t_1 = \frac{(n+1)\pi}{m}. \end{aligned}$$

3. Modification of Rayleigh-Ritz Method

It should be noted that the derivation of the above equations of the steel I-beam with lateral braces are based on the assumption that the out-of-plane deformation distributes as the equal amplitude between the length of every brace [13]. However, for the steel I-beam subjected to two concentrated loads in pre-bending stage, the distribution of the out-of-plane deformation is unequal due to the influence of bending moment distribution, which is shown in Table 1.

In Table 1, u_n and u_{nj} represent the out-of-plane deformation of each steel I-beam segment distributed by n lateral braces under assumed and actual condition, respectively. Under actual condition, it is obvious that the out-of-plane deformation in the area of mid-span is larger than that of the beam ends. The larger the out-of-plane deformation of the adjacent beam segments is, the greater the constraint effects, which results that the LTB

critical moment $M_{cr,n}$ (Eq. 10b) derived as the assumed condition is larger than the actual LTB critical moment of steel I-beams in pre-bending stage, and this result is disadvantageous to the stability of steel I-beams in pre-bending stage.

Table 1

Comparison of out-of-plane deformation between assumed and actual condition

The number of lateral braces	Out-of-plane deformation	
	Assumed condition	Actual condition
$n = 1$		
$n = 2$		
$n = 3$		
$n = 4$		

It is known that for a simply supported steel I-beam subjected to pure bending moment without brace, the LTB critical moment of the steel I-beam segment is provided as [14]:

$$M_{cr} = \beta_b \frac{\pi^2}{l_b^2} E I_y \left[\beta_y + \sqrt{\beta_y^2 + \frac{I_w}{I_y} \left(1 + \frac{l_b^2 G I_t}{\pi^2 E I_w} \right)} \right] \quad (11)$$

Where β_b is recommended by SSRC [15] as the following equation:

$$\beta_b = \frac{12.5 M_{\max}}{2.5 M_{\max} + 3 M_A + 4 M_B + 3 M_C} \quad (12)$$

Where M_{\max} is the maximum absolute moment value of the unbraced beam segment; M_A , M_B , M_C are the absolute values of moment at quarter, center, and three-quarter point, respectively.

As for Eq. (11), l_b is the length of unbraced beam segment; M_{cr} is the LTB critical moment of the unbraced beam segment which only considers the effect of pure bending, but ignores the constraint effect of adjacent beam segments due to the reason that there exists no lateral brace for the steel I-beam in the process of calculation. As a result, the provided LTB critical moment M_{cr} (Eq. 11) is smaller than the actual LTB critical moment of steel I-beams in pre-bending stage.

Compared with the actual LTB critical moment in pre-bending stage, the proposed LTB critical moment $M_{cr,n}$ derived from Eq. (10b) is larger, while the provided LTB moment M_{cr} derived from Eq. (11) is smaller. In order to obtain the LTB critical moment of steel I-beams in pre-bending stage accurately, the modified combination coefficient $\alpha = p\chi_1 + q\beta_b$ was proposed, and five different combinations of modified coefficients about p and q were analyzed based on seven cross section types shown in Table 2, and the relative errors of LTB critical moment between the results of theoretical calculation and FEA are shown in Tables 3(a), 3(b) and 3(c).

As shown in Table 2, Q345 was selected for all steel I-beams, the length of the steel I-beams were selected based on the specification that the maximum span of a single preflexed beam should not exceed 50m [16], and the other dimensions of cross sections were all selected according to the AISC

specification to prevent local buckling [14].

It is evident in Tables 3(a), 3(b) and 3(c) that when the number of lateral brace is constant, the relative errors produced by different combinations of modified coefficients show an increasing or decreasing trend. According to the comprehensive relative errors of all cross section types from A to G, when the coefficient combination is $0.6\chi_1 + 0.4\beta_b$, the standard deviation is 1.184, which is the smallest of all the modified coefficient combinations. Additionally, the relative errors of $0.6\chi_1 + 0.4\beta_b$ are all less than 5%, which meet the calculation requirement of steel I-beams for the usage of preflexed beams (CJJ/T 276-2018, 2018). Therefore, the $0.6\chi_1 + 0.4\beta_b$ is chose as the optimal modified coefficient combination in this study.

Table 2

Cross section types of steel I-beams

Cross	l (m)	h	$b_{f1} = b_{f2}$ (mm)	t_w (mm)	$t_{f1} = t_{f2}$ (mm)
A	20	600	350	15	20
B	25	700	400	18	22
C	30	900	560	22	28
D	35	1000	630	25	32
E	40	1200	750	30	38
F	45	1500	950	38	50
G	50	1700	1000	48	60

Table 3(c)

Relative errors of LTB critical moment (%)

Combination of modified coefficients	Cross section type E			Cross section type F			Cross section type G		
	$n = 1$	$n = 2$	$n = 3$	$n = 1$	$n = 2$	$n = 3$	$n = 1$	$n = 2$	$n = 3$
$0.3\chi_1 + 0.7\beta_b$	0.96	-8.74	-3.45	1.36	-8.37	-2.58	1.24	-8.56	-3.34
$0.4\chi_1 + 0.6\beta_b$	1.01	-6.75	-1.21	1.4	-6.37	-0.32	1.28	-6.56	-1.1
$0.5\chi_1 + 0.5\beta_b$	1.05	-4.76	1.02	1.45	-4.37	1.93	1.32	-4.56	1.14
$0.6\chi_1 + 0.4\beta_b$	1.09	-2.77	3.26	1.49	-2.37	4.18	1.34	-2.03	3.37
$0.7\chi_1 + 0.3\beta_b$	1.13	-0.78	5.49	1.53	-0.37	6.44	1.41	-1.27	5.61

As a result, the optimal combination coefficient α , shown as Eq. (13), is proposed to describe the constraint effect of beam segments, which can minimize the relative errors of LTB critical moments of steel I-beams between assumed and actual condition to the greatest extent:

$$\alpha = 0.6\chi_1 + 0.4\beta_b \quad (13)$$

Replacing χ_1 with α for the LTB critical moment $M_{cr,n}$, then Eq. (10b) is amended as:

$$M'_{cr,n} = \alpha \frac{\pi^2 E I_y}{l^2 / (n+1)^2} \left\{ \left[-\chi_2 a + \chi_3 \beta_y \right] + \sqrt{\left[-\chi_2 a + \chi_3 \beta_y \right]^2 + \frac{I_w}{I_y} \left(1 + \frac{l^2 / (n+1)^2 G I_t}{\pi^2 E I_w} \right)} \right\} \quad (14)$$

Where $M'_{cr,n}$ represents the modified LTB critical moment of steel I-beam with n lateral braces, and subjected to two movable concentrated loads in pre-bending stage.

Thus, the bracing stiffness requirement R_T is presented by:

$$R_T = \frac{(M_{cr,n}^2 - M_{cr,0}^2) l}{\beta_b^2 n E I_y} \quad (15)$$

4. Parameter analysis

4.1. FEA parameters

In this study, a plenty of three-dimensional finite element models were created using ABAQUS 2017 program based on different steel I-beam cross sections to verify the proposed modified Rayleigh-Ritz method. Shell element was used as the part of steel I-beams, and S4R element type was adopted for mesh generation. As shown in Fig. 6, reference points RP1 and RP2 were coupling constrained to the surfaces cut from the upper flange of the steel

Table 3(a)

Relative errors of LTB critical moment (%)

Combination of modified coefficients	Cross section type A			Cross section type B		
	$n = 1$	$n = 2$	$n = 3$	$n = 1$	$n = 2$	$n = 3$
$0.3\chi_1 + 0.7\beta_b$	0.17	-8.28	-2.51	-0.01	-8.67	-3.25
$0.4\chi_1 + 0.6\beta_b$	0.21	-6.27	-0.26	0.04	-6.67	-1.01
$0.5\chi_1 + 0.5\beta_b$	0.26	-4.27	2.00	0.08	-4.68	1.23
$0.6\chi_1 + 0.4\beta_b$	0.29	-2.27	4.26	0.12	-2.68	3.47
$0.7\chi_1 + 0.3\beta_b$	0.34	-0.26	6.52	0.16	-0.69	5.70

Table 3(b)

Relative errors of LTB critical moment (%)

Combination of modified coefficients	Cross section type C			Cross section type D		
	$n = 1$	$n = 2$	$n = 3$	$n = 1$	$n = 2$	$n = 3$
$0.3\chi_1 + 0.7\beta_b$	0.47	-8.75	-3.20	0.54	-8.86	-3.51
$0.4\chi_1 + 0.6\beta_b$	0.51	-6.76	-0.96	0.59	-6.87	-1.28
$0.5\chi_1 + 0.5\beta_b$	0.55	-4.77	1.28	0.63	-4.87	0.96
$0.6\chi_1 + 0.4\beta_b$	0.60	-2.78	3.53	0.67	-2.89	3.19
$0.7\chi_1 + 0.3\beta_b$	0.64	-0.79	5.76	0.71	-0.90	5.42

I-beam to avoid local stress concentration. Reference points RP3, RP4 and RP5 were created using “connect points to ground” type in ABAQUS 2017 Interaction module as lateral braces.

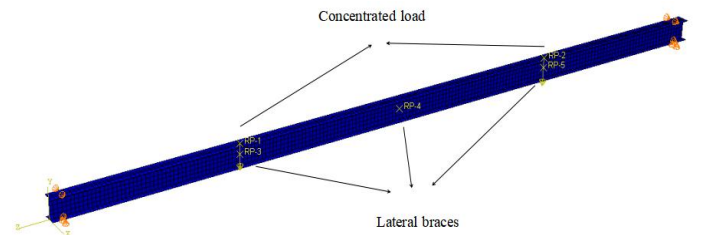


Fig. 6 Finite element model of the steel I-beam

The boundary condition used for FEA was simply supported at both beam ends as shown in Fig.6. According to the principle that the error of finite element model calculation results of different density grids are less than 2% [17,18], the FEA models have been debugged repeatedly, and the seed spacing of 0.05m was selected to divide the grids, which can not only ensure the accuracy of simulation results but also save the calculation cost.

4.2. Case parameters

In this study, steel I-beams with symmetric and monosymmetric cross sections were selected to analyse and verify the proposed solution.








The dimensions of steel I-beams with symmetric sections are shown in Table 2. The length of steel I-beams with monosymmetric cross sections are 25m, the thickness of the top and bottom flange are 35mm, the thickness of web is 18mm, and the width of bottom flange is fixed at 400mm. The monosymmetric cross sections are vary with the value of the degree of monosymmetry ρ , which is calculated by:

$$\rho = \frac{I_{top}}{I_x} \quad (16)$$

Where I_{top} and I_x represent the moment of inertia of the top flange and the whole cross section of steel I-beams about strong axis, respectively. The shape of cross sections changed with ρ are shown in Table 4.

Table 4

The shape of cross sections change with ρ

The value of ρ	0.2	0.3	0.4	0.5	0.6	0.7	0.8
The shape of cross sections							

In order to verify the applicability of the proposed solution under different parameters, some research parameters commonly used for preflexed beams were selected according to CJJ/T 276-2018. The number of lateral braces n was set to 0,1,2, and 3, the high-span ratio of the steel I-beam λ was set to 0.02, 0.03, and 0.04, and the loading location parameter m was set to 3,4, and 5.

5. Verification and parameter study

5.1. Verification of proposed solution

5.1.1. LTB critical moments of steel I-beams with symmetric cross sections

In this section, a comparative analysis between the traditional and modified Rayleigh-Ritz method was conducted in order to verify the proposed solution, the number of lateral braces was set varied from 0 to 3, the most commonly used and studied high-span ratio $\lambda=0.03$ and loading location parameter $m=4$ was selected.

Table 5 shows the LTB critical moment values of steel I-beams with symmetric cross sections under different parameters in pre-bending stage. For all selected cross section types from A to G in Table 2, it can be seen that the relative errors between theoretical calculation and FEA are less than 2% when there exists no lateral brace or only one lateral brace is arranged. However, with the increase of lateral bracing number, the theoretical results calculated by traditional Rayleigh-Ritz method (Eq. 10b) become larger than the results of FEA, especially for $n=3$, the relative errors of all cross section types are larger than 10%. As a contrast, the results of modified Rayleigh-Ritz method (Eq. 14) are close to that simulated by FEA no matter how many lateral braces exist, when $n=3$, the relative errors are reduced by about 9% for all cross section types.

It is evident that the relative errors of modified Rayleigh-Ritz method are all less than 5%, which meet the calculation requirement of the standard (CJJ/T 276-2018, 2018), and it is accurate for predicting LTB strength of steel I-beams with symmetric cross sections in pre-bending stage.

5.1.2. LTB critical moments of steel I-beams with monosymmetric cross sections

As shown in Fig. 7(a), Fig. 7(b), Fig. 7(c), and Fig. 7(d), the LTB critical moments of steel I-beams with monosymmetric cross sections were analyzed to verify the modified Rayleigh-Ritz method.

The results shown in Fig. 7(a) demonstrate that when no lateral brace exists, the traditional Rayleigh-Ritz method (Eq. 10a) and the FEA are in good agreement as ρ varied from 0.2 to 0.8. When there exists only one lateral brace, it can be seen from the detailed structure diagram of Fig. 7(b) that the results of Rayleigh-Ritz method after modification (Eq. 14) are closer to FEA than that before modification (Eq. 10b). As can be seen from Fig. 7(c) and Fig. 7(d), when there exist more than two lateral braces, the relative errors between Eq. (10b) and FEA become large with the increase of the value of ρ and the lateral bracing number, when $n=3$ and $\rho=0.8$, the relative error is about 11.97%.

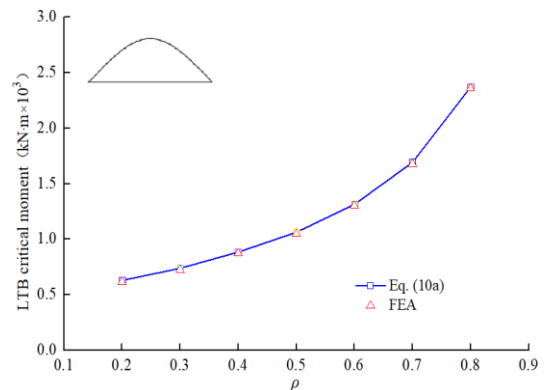
As is shown, the modified Eq.(14) is always well matched with the FEA as ρ varied from 0.2 to 0.8 and n varied from 0 to 3. When $n=3$ and $\rho=0.8$, the relative error is reduced by 10.53%, about 1.44%. As a result, the modified Rayleigh-Ritz method has better accuracy than the traditional Rayleigh-Ritz method for predicting LTB strength of steel I-beams in pre-bending stage.

Table 5

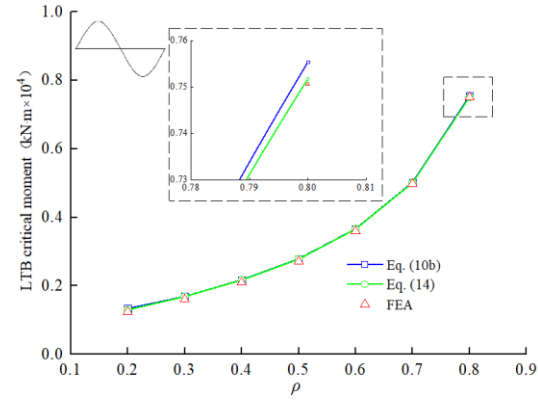
LTB critical moments of steel I-beams with symmetric cross sections

Cross section types	n	Eq. (10a,b) (kN·m)	Eq. (14) (kN·m)	FEA (kN·m)	Relative error between Eq. (10a, b) and FEA (%)	Relative error after modification(%)
A	0	368.2	-	375.4	-1.92	-
A	1	1091.0	1089.1	1085.9	0.47	0.29
A	2	2603.0	2405.8	2461.6	5.74	-2.27
A	3	4619.8	4251.7	4078.1	13.28	4.26
B	0	482.3	-	490.7	-1.71	-
B	1	1391.4	1389.1	1387.4	0.29	0.12
B	2	3263.1	3015.9	3099.1	5.29	-2.68
B	3	5746.5	5288.7	5111.5	12.72	3.47
C	0	1260.9	-	1271.2	-0.81	-
C	1	3931.0	3924.5	3901.0	0.77	0.60
C	2	9683.9	8929.4	9184.5	5.44	-2.78
C	3	17365.3	15981.9	15437.2	12.79	3.53
D	0	1766.6	-	1755.0	0.66	-
D	1	5370.0	5361.1	5325.4	0.84	0.67
D	2	13082.1	12026.5	12383.8	5.64	-2.89
D	3	23249.5	21397.3	20735.3	12.13	3.19
E	0	3122.1	-	3122.5	-0.01	-
E	1	9673.0	9656.9	9552.8	1.26	1.09
E	2	23742.6	21897.8	22521.1	5.42	-2.77
E	3	42525.4	39137.6	37903.0	12.20	3.26
F	0	7666.7	-	7615.0	0.68	-
F	1	24591.6	24550.7	24191.1	1.66	1.49
F	2	61340.0	56693.5	58069.7	5.63	-2.37
F	3	110919.3	102082.7	97982.8	13.20	4.18
G	0	11142.3	-	11073.8	0.62	-
G	1	33677.4	33621.1	33168.9	1.53	1.34
G	2	81334.2	75173.9	77153.1	5.42	-2.03
G	3	145118.0	133556.6	129201.5	12.32	3.37

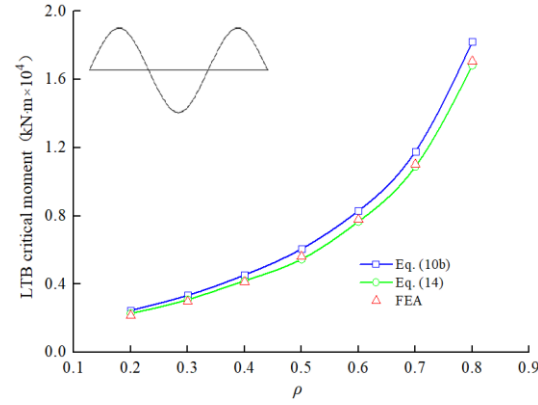
It can also be seen from Fig. 7 that with the increase of the value of ρ , LTB critical moments increase in concave parabola. Additionally, for the average value of LTB critical moments with all cross sections of ρ varied from 0.2 to 0.8, when the number of lateral braces changes from 0 to 1, the increase extent of LTB critical moments is the largest, about 2.77 times, followed by 2.08 times from 1 to 2, and the smallest from 2 to 3, about 1.87 times.



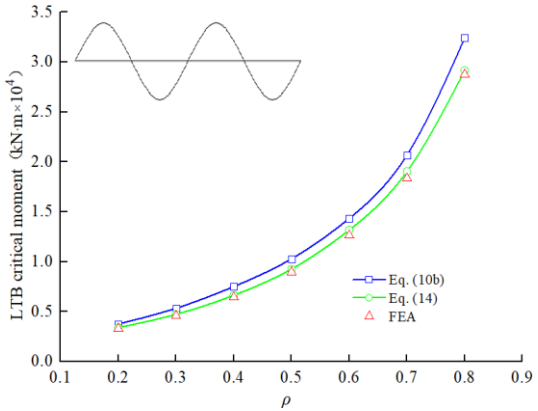
(a) LTB critical moments of steel I-beams without lateral brace



(b) LTB critical moments of steel I-beams with one lateral brace



(c) LTB critical moments of steel I-beams with two lateral braces



(d) LTB critical moments of steel I-beams with three lateral braces

Fig. 7 Comparison of LTB critical moments with different numbers of lateral braces

Therefore, the effect of increasing the LTB critical moment is not obvious with the increase of lateral bracing number, and it is necessary to arrange lateral braces rationally and economically according to reasonable calculation theory.

5.2. Effects of loading location parameter

In this section, a numerical study was done to analyse the LTB critical moment of steel I-beams under different loading location parameters as lateral bracing number varied from 1 to 3, and the high-span ratio λ was set to 0.03.

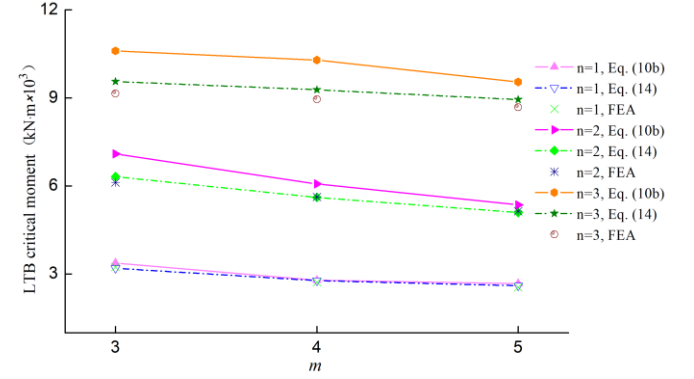
It is found according to the analysis results that the variation of LTB critical moments with different loading location parameters were similar for different values of ρ . As a result, LTB critical moments with the cross section of $\rho = 0.5$ were selected as shown in Fig. 8.

Fig. 8 indicates that when $n=1$, the relative errors between traditional Rayleigh-Ritz method (Eq. 10b) and FEA are small, and the curves in Fig. 8 basically coincide.

When $n=2$, the relative errors are larger than that of $n=1$, as $m=3$, the relative error is 15.95%, and as $m=5$, the relative error is 4.18%, while the

relative errors between modified Rayleigh-Ritz method (Eq. 14) and FEA are 3.26% and -0.91%, respectively, the maximum relative error is reduced by 12.69%.

When $n=3$, the relative error before modification is the largest as $m=3$, about 15.84%, and the smallest as $m=5$, about 9.91%, while the relative errors after modification are 4.46% and 3.01% as $m=3$ and $m=5$, respectively. As a result, the maximum relative error is reduced by 11.38%.

**Fig. 8** Effects of different loading location parameters on LTB critical moment

It can be learned from Fig. 8 that the LTB critical moments of steel I-beams decrease with the increase of the value of m , and as the value of m decreases, the relative errors from the traditional Rayleigh-Ritz method increase, while the modified Rayleigh-Ritz method has good accuracy under different loading location parameters.

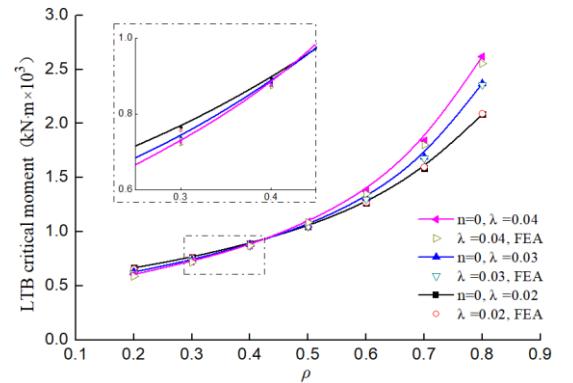
5.3. Effects of high-span ratio

In order to analyse the effects of different high-span ratios on LTB critical moments of steel I-beams in pre-bending stage, the high-span ratio λ in this section was set to 0.02, 0.03, and 0.04, the loading location parameter m was set to 4, and the proposed modified Rayleigh-Ritz method (Eq. 14) was used to compare with the FEA.

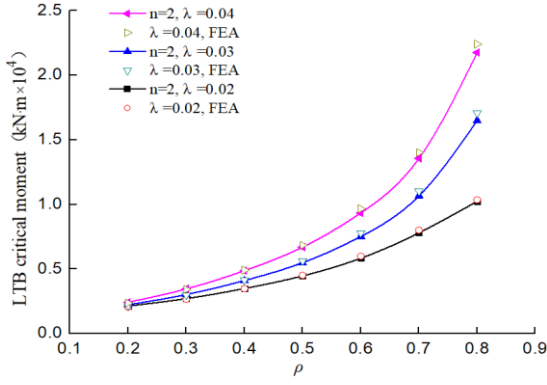
According to the theoretical calculation and FEA, it is concluded that the curves law of LTB critical moments change with λ as $n=1$, $n=2$ and $n=3$ were similar. As a result, LTB critical moments change with different values of λ as $n=0$ and $n=2$ were selected for analysis as shown in Fig. 9(a) and Fig. 9(b).

It is found from the detailed structural diagram of Fig. 9(a) that when there is no lateral brace, for the cross section with the same value of ρ , when $\rho < 0.5$, LTB critical moment is larger as λ is smaller, however, when $\rho \geq 0.5$, LTB critical moment is larger as λ is larger. When $\rho = 0.8$, LTB critical moment is most affected by the value of λ , and as λ changes from 0.02 to 0.04, the LTB critical moment of the latter is 1.29 times of the former.

As a contrast, for steel I-beams with lateral braces, LTB critical moments increase with the increase of λ for all cross sections of ρ varied from 0.2 to 0.8, and LTB critical moments change significantly affected by different values of λ with the increase of ρ . As can be seen from Fig. 9(b), when $n=2$, $\rho=0.8$, as λ changes from 0.02 to 0.04, the LTB critical moment of the latter is 2.12 times of the former, which is much larger than that of $n=0$, $\rho=0.8$.



(a) LTB critical moments of steel I-beams without lateral brace



(b) LTB critical moments of steel I-beams with two lateral braces

Fig. 9 Effects of different high-span ratios on LTB critical moments

Therefore, it is necessary to select high-span ratio reasonably according to the value of ρ as well as whether the steel I-beam is arranged with lateral brace or not, so as to prevent the occurrence of LTB in pre-bending stage.

As can be seen from Fig. 9 that the results of modified Rayleigh-Ritz method are close to that of FEA for different high-span ratios as ρ varied from 0.2 to 0.8, which proves that the modified Rayleigh-Ritz method has good accuracy and applicability.

5.4. Effects of stability coefficient

5.4.1. The definition of stability coefficient of steel I-beams

This section aims to investigate the effects of stability coefficient of steel I-beams in pre-bending stage. For this purpose, the loading location parameter was set to 4, and the high-span ratio was set to 0.03. The stability coefficient ϕ is defined as the ratio of $M'_{cr,n}$ (Eq. 14) to the design moment of the mid-span cross section M_d :

$$\phi = \frac{M'_{cr,n}}{M_d} \quad (17)$$

Where M_d is provided as:

$$M_d = \frac{P_0 l}{4} \quad (18)$$

Where P_0 is the preflexed force with the loading location parameter $m=4$, which can be written as:

$$P_0 = \frac{4(\sigma_{con} - \sigma_z) I_s}{l_{ysu}} \quad (19)$$

Where σ_z is the maximum stress of mid-span cross section caused by gravity of steel I-beams; I_s is the moment of inertia of steel I-beam around its center of gravity axis; l_{ysu} is the distance between the neutral axis and the upper flange edge of steel I-beam; σ_{con} is the control stress of mid-span cross section of steel I-beam, which is given as:

$$\sigma_{con} \leq 0.75 f_y \quad (20)$$

5.4.2. Effects of stability coefficient of steel I-beams

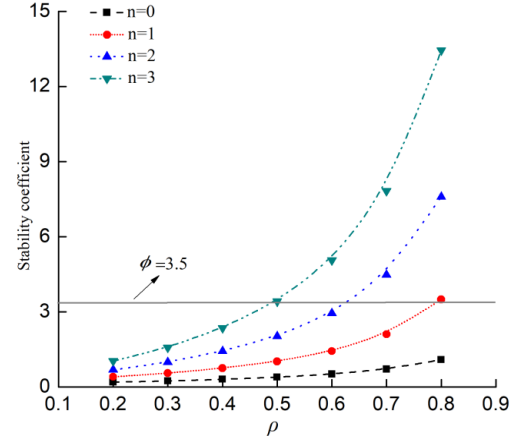
In this section, the modified Rayleigh-Ritz method was used to analyse the stability coefficients of steel I-beams with different numbers of lateral braces in pre-bending stage, and the results were shown in Fig. 10.

It can be observed from Fig. 10 that the variation of stability coefficients with different lateral bracing numbers are small when $\rho=0.2$, while there is a big increase when $\rho=0.8$. It is evident that the stability coefficients increase as the number of lateral brace increases, while as $\rho < 0.5$, this increasing trend is not obvious. Therefore, the stability coefficient is greatly affected by the number of lateral braces when the value of ρ is large enough.

It is recommended that the stability coefficient of steel I-beams should be

larger than 3.5 [2]. As shown in Fig. 10, for the steel I-beams selected in this paper, when, the steel I-beams with more than three lateral braces satisfy the requirement.

Therefore, it is important to set lateral braces reasonably for different types of steel I-beams according to theoretical calculation in pre-bending stage, and the modified Rayleigh-Ritz method with good accuracy and applicability verified above can provide reference value for theoretical calculation in pre-bending stage.

**Fig. 10** Effects of stability coefficient

6. Summary and conclusions

In this research, in order to investigate the LTB strength of steel I-beams within preflexed beams in pre-bending stage, the steel I-beams subjected to two movable concentrated loads were analyzed. Due to the distribution of bending moment caused by concentrated loads, different combinations of modified coefficients were compared and analyzed, and the modified Rayleigh-Ritz method was proposed and verified under different parameters.

The LTB strength of steel I-beams with symmetric and monosymmetric cross sections show that the relative errors of traditional Rayleigh-Ritz method increase with the increase of the lateral bracing number, the degree of monosymmetry of the cross section, and the decrease of the value of loading location parameter. It is proved that the modified Rayleigh-Ritz method has good applicability and accuracy, which can provide theoretical calculation reference value for predicting LTB strength of steel I-beams in pre-bending stage.

Additionally, the parameter study in this paper can provide reference value for parameter selection of steel I-beams within preflexed beams in pre-bending stage.

Acknowledgement

The financial support of Chinese National Natural Science Foundation (Grant No. 51078078) is gratefully acknowledged.

References

- [1] Salvatore G. M. and Claudio M., "Preflex Beams: A method of calculation of creep and shrinkage effects", Journal of bridge engineering, 11(1), 48-58, 2006.
- [2] Huang Q., Design principle of bridge steel-concrete composite structure, China Communication Press, Beijing, China, 190-197, 2017. (in Chinese).
- [3] Taylor A.C. and Ojalvo M., "Torsional restraint of lateral buckling", Journal of the Structural Division, 92(2), 115-130, 1966.
- [4] Mutton B.C. and Trahair N.S., "Stiffness requirements for lateral bracing", Journal of the Structural Division, 99(10), 2167-2182, 1973.
- [5] Kitipornchai S. and Wang C.M., "Lateral buckling of tee beams under moment gradient", Computers & Structures, 23(1), 69-76, 1986.
- [6] Wang C.M., Wang L. and Ang K.K., "Beam-buckling analysis via Automated Rayleigh-Ritz method", Journal of Structural Engineering, 120(1), 200-211, 1994.
- [7] Nguyen C.T., Joo H.S., Moon J. and Lee H.E., "Flexural-torsional buckling strength of I-girders with discrete torsional braces under various loading conditions", Engineering Structures, 36(12), 337-350, 2012.
- [8] Nguyen C.T., Moon J., Le V.N. and Lee H.E., "Lateral-torsional buckling of I-girders with discrete torsional bracings", Journal of Constructional Steel Research, 66(2), 170-177, 2010.
- [9] Geleka K.M. and Park J.S., "Elastic lateral torsional buckling strength of monosymmetric stepped I-beams", KSCE Journal of Civil Engineering, 16(5), 785-793, 2012.
- [10] Ozbasaran H., Aydin R. and Dogan M., "An alternative design procedure for lateral torsional buckling of cantilever I-beams", Thin-Walled Structures, 90(1), 235-242, 2015.
- [11] Mohammadi E., Hosseini S.S. and Rohanimanesh M.S., "Elastic lateral-torsional buckling

- strength and torsional bracing stiffness requirement for monosymmetric I-beams”, Thin-Walled Structures, 104(3), 116-125, 2016.
- [12] Sun X.F., Fang X.S. and Guan L.T., Mechanics of materials(I), Higher Education Press, Beijing, China, 157-175, 2008. (in Chinese).
- [13] Chen J., Stability and steel structures theory and design, Science Press, Beijing, China, 323-344, 2011. (in Chinese).
- [14] American Institute of Steel Construction, Steel construction manual, 14th Edition, Vol. 2, AISC, USA, 2011.
- [15] Structural Stability Research Council (SSRC), Guide to stability design criteria for metal structures, 5th Edition, Galambos. T.V., Wiley, New York, 1998.
- [16] CJJ/T 276-2018, Technical standard for preflexed composite beam bridges, Ministry of Housing and Urban-Rural Construction of the Republic of China, 2018. (in Chinese).
- [17] Cao J.F. and Shi Y.P., FAQ Answers for ABAQUS Finite Element Analysis, China Machine Press, Beijing, China, 130-156, 2008. (in Chinese).
- [18] ABAQUS (2017). “Standard user’s manual”, Version 6.17, Dassault Systemes, Paris.

IN-PLANE NONLINEAR ANALYSIS AND BUCKLING OF SHEAR-DEFORMABLE CIRCULAR ARCHES

Gen-shu Tong^{1,*}, Yong-lin Pi² and Wei Gao²

¹Department of Civil Engineering, Zhejiang University, Hangzhou 310058, China,

²Department of Civil & Environmental Engineering, The University of New South Wales, NSW 2052, Australia

*(corresponding author, tonggs@zju.edu.cn)

ABSTRACT

A new theory for nonlinear analysis of shear-deformable circular arches is derived, in which Timoshenko's assumption on the deformation of cross-section and the Green strains are adopted. In the variational equation, the nonlinear energy of the shear and the transverse normal stresses is included. Substituting the internal forces from linear analysis, a set of linearized equations is derived for buckling analysis of shear deformable arches. These equations are then used to solve the buckling of circular arches and rings under three types of radial pressures to compare the various results appeared in the literature.

Linear analysis is carried out on hinged arches under uniform radial pressure to check the changes of displacements and internal forces after the shear deformation is considered. It is found that the axial force is more uniform along the arch length when shear deformation is considered, and the bending moment and shear force are smaller, but the displacements are always larger.

Buckling of arches under radial pressure under various boundary conditions are studied, buckling factors for symmetrical and anti-symmetrical buckling are tabulated, and approximate formulas for the critical loads are proposed.

ARTICLE HISTORY

Received: 22 February 2019
Revised: 15 January 2020
Accepted: 20 January 2020

KEYWORDS

Circular arch;
Buckling;
Nonlinear analysis;
Shear deformation;
Linear analysis

Copyright © 2020 by The Hong Kong Institute of Steel Construction. All rights reserved.

1. Introduction

In-plane buckling of arches is a classic problem [1,2,3]. The early literature review on arches with Bernoulli's assumption was presented in Ref. [4]. This paper will address the buckling of circular arches whose shear deformation cannot be neglected. Such a situation occurs when the arch is a trussed arch, or the web of the arch has openings with regular intervals. Early studies on shear-deformable arches were mainly focused on their vibration [5,6].

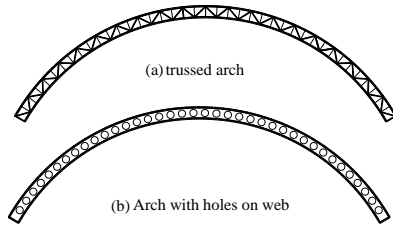


Fig.1 Shear deformable arches

Study on buckling of arches incorporating shear deformation of their cross-sections may date back to the early Russian literature [7]. Dinnik [7], without any introduction to the theoretical development, presented Eq. (1) as the critical force of hinged arches under water pressure:

$$(qR)_{cr} = \frac{1}{1 + \Phi_s} \left(1 - \frac{\alpha^2}{\pi^2} \right) \frac{\pi^2 EI}{(\alpha R)^2}, \quad \Phi_s = \frac{\pi^2}{\alpha^2} \Phi, \quad \Phi = \frac{EI}{GA_s R^2} \quad (1)$$

Where E, G are Young's and shear moduli of steel respectively, I the second moment of the cross-section, A_s the effective shear area, R the centroidal radius of the arch, α half of the subtended angle of the arch. Based on Ref. [7], Eq. (1) was obtained by Bovin in 1937, but no further information is available because of the language limitation and the long history.

Smith and Simitses [8] investigated also the effect of transverse shear deformation on buckling of rings and developed the following equation for the fundamental mode of buckling ($n = 1$):

$$pR = \frac{1}{1 + 4\Phi} \cdot \frac{3EI}{R^2} \quad (2)$$

Guo and Huang [9], Dou et al. [10] studied the buckling of arches with I-section with regular web openings numerically, and used the following equation to define the slenderness of arches.

$$(qR)_{cr} = \frac{1}{1 + (1 - \alpha^2/\pi^2)\Phi_s} \left(1 - \frac{\alpha^2}{\pi^2} \right) \frac{\pi^2 EI}{(\alpha R)^2} \quad (3)$$

Guo et al. [11] investigated the buckling and load-carrying capacity of 3D-trussed arches, Guo et al. [12] studied the arches with corrugated webs. Attard, Zhu and Kellermann [13] carried out a new study on the effect of shear deformation, using finite strain formulation, the following critical load was obtained:

$$(pR)_{cr} = \left[\frac{1}{2} \left(1 + \frac{1}{\Phi} \right) + \sqrt{\frac{1}{4} \left(1 + \frac{1}{\Phi} \right)^2 + \left(\frac{\pi^2}{\alpha^2} - 1 \right) \frac{1}{\Phi}} \right] \frac{EI}{R^2} \quad (4)$$

Zhu, Attard and Kellermann [14] investigated the nonlinear buckling of shallow shear-deformable arches, Attard, Zhu and Kellermann [15] studied the buckling of funicular (parabolic and catenary) shear-deformable arches.

There exist great differences among Eqs. (1,3,4). This paper presents a new study on the buckling of shear-deformable circular rings and arches under radial pressure. The theoretical derivation is an extension of the authors' early study on arches based on Bernoulli's assumption [4].

2. A nonlinear theory of arches incorporating shear deformation

2.1 Assumptions and coordinate systems

Fig.2 illustrates the following right-handed coordinate systems:

(1) $r - \varphi - y$ is a cylindrical coordinate system located at the curvature center of the arch, it is fixed in space and used to measure the deformations of the arch;

(2) $x - y - z$ is a Cartesian coordinate system located at the centroid of the cross-section, it is fixed on the cross-section and changes its direction as the arch deforms. The original x -axis has the same direction as the r -axis, the z -axis points in the direction of increasing φ .

The cross-section of the arch is bi-symmetrical, the radius of the centroidal axis is R . The displacements of any point $P(x, y)$ on the cross-section are denoted by \bar{u} and \bar{w} in the x - and z -directions, respectively. Following assumptions are adopted in the derivation:

- (1) The cross section has dimensions far less than the radius of the arch;
- (2) The cross-section remains plane but not perpendicular to the deformed axis;
- (3) The displacements may be finite, but the strain is small.

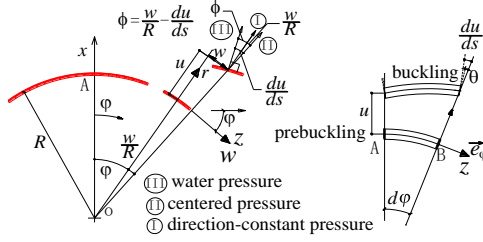


Fig.2 Coordinate systems, deformation of the cross-section

2.2 The strain-displacement relations

Referring to Fig.2, \bar{u} and \bar{w} of Point P (x, y) on the middle surface of the cross-section in the x and z directions can be written out

$$\bar{u} = u, \quad \bar{w} = \frac{r}{R} w - x\theta \quad (5a, b)$$

in which u and w are the displacements of the centroid of the cross section in the x and z directions respectively, θ is the rotation of the cross-section due to pure flexural deformation. $(\cdot)' = \partial(\cdot)/\partial\phi$, r is the radius of Point P (x, y). There are three independent strain components, each of them is composed of linear and nonlinear parts.

$$\varepsilon_z = \varepsilon_z^L + \varepsilon_z^N, \quad \varepsilon_{zx} = \varepsilon_{zx}^L + \varepsilon_{zx}^N, \quad \varepsilon_x = \varepsilon_x^L + \varepsilon_x^N \quad (6a, b, c)$$

Strain-displacement relations are expressed as [16]:

$$\varepsilon_x^L = \frac{\partial \bar{u}}{\partial x} = \frac{\partial u}{\partial x} = 0 \quad (\text{web}) \quad (7a)$$

$$\varepsilon_z^L = \frac{\partial \bar{w}}{r \partial \phi} + \frac{\bar{u}}{r} = \frac{u}{r} + \frac{1}{R} w' - \frac{x}{r} \theta' \quad (7b)$$

$$\varepsilon_{xz}^L = \frac{\partial \bar{u}}{r \partial \phi} - \frac{\bar{w}}{r} + \frac{\partial \bar{w}}{\partial x} = \frac{u' - R\theta}{r} = \frac{R}{r} \left(\frac{u'}{R} - \theta \right) \quad (7c)$$

$$\varepsilon_x^N = \frac{1}{2} \left[\left(\frac{\partial \bar{u}}{\partial x} \right)^2 + \left(\frac{\partial \bar{w}}{\partial x} \right)^2 \right] = \frac{1}{2} \left(\frac{\partial \bar{w}}{\partial x} \right)^2 \quad (7d)$$

$$\varepsilon_z^N = \frac{1}{2} \left[\left(\frac{\partial \bar{u}}{r \partial \phi} - \frac{\bar{w}}{r} \right)^2 + \left(\frac{\partial \bar{w}}{r \partial \phi} + \frac{\bar{u}}{r} \right)^2 \right] \quad (7e)$$

$$\varepsilon_{zx}^N = \frac{\partial \bar{u}}{\partial x} \left(\frac{\partial \bar{u}}{r \partial \phi} - \frac{\bar{w}}{r} \right) + \frac{\partial \bar{w}}{\partial x} \left(\frac{\partial \bar{w}}{r \partial \phi} + \frac{\bar{u}}{r} \right) = \frac{\partial \bar{w}}{\partial x} \left(\frac{\partial \bar{w}}{r \partial \phi} + \frac{\bar{u}}{r} \right) \quad (7f)$$

$$\varepsilon_y^L = 0, \quad \varepsilon_y^N = \frac{1}{2} \left(\frac{\partial \bar{u}}{\partial y} \right)^2 + \frac{1}{2} \left(\frac{\partial \bar{v}}{\partial y} \right)^2 + \frac{1}{2} \left(\frac{\partial \bar{w}}{\partial y} \right)^2 = 0 \quad (\text{flanges}) \quad (7g)$$

Substituting Eqs. (5a, 5b) into Eqs. (7a-5f), one obtains

$$\varepsilon_z^L = \varepsilon_m - \frac{x}{r} \kappa, \quad \varepsilon_z^N = \frac{1}{2} \left[\left(\frac{R}{r} \gamma + \beta \right)^2 + \left(\varepsilon_m - \frac{x}{r} \kappa \right)^2 \right] \quad (8a, b)$$

$$\varepsilon_x^L = 0, \quad \varepsilon_x^N = \frac{1}{2} \beta^2 \quad (\text{web}) \quad (8c, d)$$

$$\varepsilon_{xz}^L = \frac{R}{r} \gamma, \quad \varepsilon_{xz}^N = -\beta \left(\varepsilon_m - \frac{x}{r} \kappa \right) \quad (8e, f)$$

Where

$$\varepsilon_m = \frac{w' + u}{R}, \quad \kappa = \frac{u}{R} + \theta', \quad \beta = \theta - \frac{w}{R}, \quad \gamma = \frac{u'}{R} - \theta \quad (9a, b, c, d)$$

γ is the shear angle of the cross-section. There are following relations between these quantities

$$\varepsilon_m - \kappa = -\beta', \quad \beta + \gamma = \frac{u' - w}{R}, \quad \kappa + \gamma' = \frac{u + u''}{R} \quad (10a, b, c)$$

Stresses on the cross-sections are σ_z , τ_{xz} and σ_x (in the web) and σ_y (in the flanges). The external loads are balanced by the longitudinal normal stress σ_z and the shear stress τ_{xz} , the transverse normal stress σ_x (σ_y) are produced to keep equilibrium of the infinitesimal sectorial plate elements(web) or cylindrical elements(flange). σ_z is related to the normal strain, τ_{xz} is found based on the equilibrium of infinitesimal elements, it is also related to the shear deformation in an averaged sense because Timoshenko's assumption is only concerned with cross-sectional average shear deformation. σ_x (σ_y) can only be determined by equilibrium condition of the infinitesimal element.

Based on Hooke's law, the stresses σ_z and τ_{xz} are

$$\sigma_z = E(\varepsilon_z^L + \varepsilon_z^N) = E \left\{ \varepsilon_m - \frac{x}{r} \kappa + \frac{1}{2} \left[\left(\frac{R}{r} \gamma + \beta \right)^2 + \left(\varepsilon_m - \frac{x}{r} \kappa \right)^2 \right] \right\} \quad (11a)$$

$$\tau_{xz} = G(\varepsilon_{xz}^L + \varepsilon_{xz}^N) = E \left[\frac{R}{r} \gamma - \beta \left(\varepsilon_m - \frac{x}{r} \kappa \right) \right] \quad (11b)$$

The axial force N , bending moment M and shear force Q_x on the cross section are:

$$N = \int_A \sigma_z dA = E \int_A \left(\varepsilon_m - \frac{x}{r} \kappa \right) dA = EA \varepsilon_m + \frac{EI}{R^2} \kappa \quad (12a)$$

$$M = - \int_A \sigma_z x dA = -E \int_A \left(\varepsilon_m - \frac{x}{r} \kappa \right) x dA = \frac{EI}{R} \kappa \quad (12b)$$

$$Q_x = \int_A \tau_{xz} dA = GR \gamma \int_A \frac{1}{r} t_w dr = G t_w R \gamma \ln \frac{R + 0.5h}{R - 0.5h} \approx GA_s \gamma \quad (12c)$$

The axial force is positive when it is tensile, the bending moment is positive when the inner side of the arch is in tension, the shear force is positive when it points in the positive x direction on the positive cross-section.

2.2 Principle of virtual work and equilibrium equation

For arches, the virtual work equation is

$$\int_V (\sigma_z \delta \varepsilon_z^L + \tau_{xz} \delta \varepsilon_{xz}^L + \sigma_z \delta \varepsilon_z^N + \tau_{xz} \delta \varepsilon_{xz}^N + \sigma_x \delta \varepsilon_x^N) dV = \int_\phi (q_z \delta w + q_x \delta u) R d\phi \quad (13)$$

where $dV = r dA d\phi$ and

$$\delta \varepsilon_z^L = \delta \varepsilon_m - \frac{x}{r} \delta \kappa, \quad \delta \varepsilon_x^N = \beta \delta \beta \quad (14a, b)$$

$$\delta \varepsilon_z^N = \left(\frac{R}{r} \gamma + \beta \right) \left(\frac{R}{r} \delta \gamma + \delta \beta \right) + \left(\varepsilon_m - \frac{x}{r} \kappa \right) \left(\delta \varepsilon_m - \frac{x}{r} \delta \kappa \right) \quad (14c)$$

$$\delta \varepsilon_{xz}^L = \frac{R}{r} \delta \gamma, \quad \delta \varepsilon_{xz}^N = -\delta \beta \left(\varepsilon_m - \frac{x}{r} \kappa \right) - \beta \left(\delta \varepsilon_m - \frac{x}{r} \delta \kappa \right) \quad (14d, e)$$

$$\delta \varepsilon_m = \frac{\delta w' + \delta u}{R}, \quad \delta \kappa = \frac{\delta u}{R} + \delta \theta', \quad \delta \beta = \delta \theta - \frac{\delta w}{R}, \quad \delta \gamma = \frac{\delta u'}{R} - \delta \theta \quad (15)$$

(1) The first part of the virtual work is related to the linear longitudinal strain:

$$\int_V \sigma_z \delta \varepsilon_z^L dV = \int_\phi \int_A \sigma_z \left(\delta \varepsilon_m - \frac{x}{r} \delta \kappa \right) r dA d\phi = \int_\phi [(RN - M) \delta \varepsilon_m + M \delta \kappa] d\phi \quad (16a)$$

in which

$$\int_A \sigma_z r dA = RN - M, \quad N = \int_A \sigma_z dA, \quad M = - \int_A \sigma_z x dA \quad (16b, c, d)$$

(2) The second part is related to the nonlinear longitudinal strain:

$$\int_V \sigma_z \delta \varepsilon_z^N dV = \int_\varphi [(RN - M + W) \cdot \gamma \delta \gamma + NR \beta \delta \gamma + NR \gamma \delta \beta] d\varphi \\ + \int_\varphi [(RN - M) \beta \delta \beta + (RN - M) \varepsilon_m \delta \varepsilon_m + M \varepsilon_m \delta \kappa + M \kappa \delta \varepsilon_m + W \kappa \delta \kappa] d\varphi \quad (17)$$

Where

$$\int_A \sigma_z \frac{R^2}{r} dA = RN - M + W, \quad W = \int_A \sigma_z \frac{x^2}{r} dA \quad (18a, b)$$

(3) The linear part of the virtual work of the shear stress τ_{zx} is

$$\int_V \tau_{zx} \delta \varepsilon_{zx}^L dV = \int_\varphi \int_A \tau_{zx} \frac{R}{r} \delta \gamma r dA d\varphi = R \int_\varphi \int_A \tau_{zx} \delta \gamma dA d\varphi = R \int_\varphi Q_x \delta \gamma d\varphi \quad (19)$$

The nonlinear part of the virtual work of the shear stress τ_{zx}

$$\int_V \tau_{zx} \delta \varepsilon_{zx}^N dV = \int_\varphi [(RQ_x + T)(-\beta \delta \varepsilon_m - \varepsilon_m \delta \beta) + T(\kappa \delta \beta + \beta \delta \kappa)] d\varphi \quad (20)$$

where

$$\int_A \tau_{zx} r dA = RQ_x + T, \quad T = \int_A \tau_{zx} x dA \quad (21a, b)$$

(4) the nonlinear virtual work of the transverse normal stress σ_x is

$$\int_V \sigma_x \delta \varepsilon_x^N dV = \int_\varphi \int_A \sigma_x \beta \delta \beta r dA d\varphi = \int_\varphi \left[\int_A \sigma_x r dA \right] \beta \delta \beta d\varphi \quad (22)$$

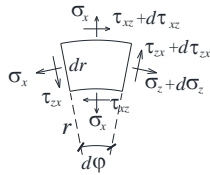


Fig.3 Balance of infinitesimal sectorial element

Fig.3 shows an infinitesimal element, its equilibrium equation in the radial direction is:

$$\frac{\partial \sigma_x r}{\partial x} + \frac{\partial \tau_{zx}}{r \partial \varphi} - \frac{\sigma_z r - \sigma_x r}{r} = 0$$

from which

$$\frac{\partial (\sigma_x r t)}{\partial r} = \sigma_z t - \frac{\partial \tau_{zx} t}{\partial \varphi}$$

Multiplying both sides by x , integration along the height of the cross section, one has

$$\int_{-0.5h}^{0.5h} \frac{\partial (\sigma_x r t)}{\partial x} dx = \int_{-0.5h}^{0.5h} \sigma_z t dx - \int_{-0.5h}^{0.5h} \frac{\partial (\tau_{zx} t)}{\partial \varphi} dx = -M - \frac{\partial T}{\partial \varphi}$$

on the other hand

$$\int_{-0.5h}^{0.5h} \frac{\partial (\sigma_x r t)}{\partial x} dx = \sigma_x r t \cdot x \Big|_{-0.5h}^{0.5h} - \int_{-0.5h}^{0.5h} \sigma_x r t dx = -M - \frac{\partial T}{\partial \varphi}$$

Therefore

$$\int_{-0.5h}^{0.5h} \sigma_x r dA = M + T' + \sigma_x r t \cdot x \Big|_{-0.5h}^{0.5h}$$

If the radial load q_x is on the centroid, then $\sigma_x|_{x=-0.5h} = 0, \sigma_x|_{x=0.5h} = 0$, $\sigma_x|_{x=-0.5h} + q_x = \sigma_x|_{x=0.5h}$, one has $\sigma_x r t \cdot x \Big|_{-0.5h}^{0.5h} = \sigma_x r t \cdot x \Big|_{-0.5h}^{0.5h} + \sigma_x r t \cdot x \Big|_{0}^{0.5h} = 0$, $\int_A \sigma_x r dA = M + T'$. Similarly, if the radial load is on the outer surface: $\int_A \sigma_x r dA = M + T' + 0.5q_x(R + 0.5h)h$, and if the radial load is on the inner

surface: $\int_A \sigma_x r dA = M + T' - 0.5q_x(R - 0.5h)h$, so for the radial loads at any position on the cross-section, one obtains

$$\int_A \sigma_x r dA = M + T' + q_x(R + x_q)x_q = M + T' + q_x R_q x_q$$

where R_q is the radius on which the radial load acts, x_q is the coordinate.

$$\int_V \sigma_x \delta \varepsilon_x^N dV = \int_\varphi (M + T' + q_x R_q x_q) \beta \delta \beta d\varphi \quad (23)$$

The final virtual work equation is:

$$\int_\varphi [(RN - M)(\delta \varepsilon_m + \beta \delta \beta + \varepsilon_m \delta \varepsilon_m) + M \delta \kappa + RQ_x \delta \gamma + M \delta (\varepsilon_m \kappa) \\ + W \kappa \delta \kappa + (M + T' + q_x R_q x_q) \beta \delta \beta + (RQ_x + T)(-\beta \delta \varepsilon_m - \varepsilon_m \delta \beta) \\ + T(\kappa \delta \beta + \beta \delta \kappa)] d\varphi + \int_\varphi [(RN - M + W) \cdot \gamma \delta \gamma + NR \beta \delta \gamma + NR \gamma \delta \beta] d\varphi \\ - \int_\varphi (q_x \delta u + q_z \delta w) R d\varphi = 0 \quad (24)$$

Substituting Eqs. (15a-d) into Eqs. (24), and combining like terms

$$\int_\varphi \left\{ \left[N - \frac{M}{R} + (N - \frac{M}{R}) \varepsilon_m + \frac{M}{R} \kappa - (Q_x + \frac{T}{R}) \beta \right] \delta w' \right. \\ + \left[(Q_x + \frac{T}{R}) \varepsilon_m - (N + \frac{T' + q_x R_q x_q}{R}) \beta - \frac{T}{R} \kappa - N \gamma \right] \delta w \\ + [M + M \varepsilon_m + W \kappa + T \beta] \delta \theta' + \left[N + N \varepsilon_m + \frac{M + W}{R} \kappa - Q_x \beta \right] \delta u \\ + [(T' + q_x R_q x_q) \beta - RQ_x + T \kappa + (M - W) \cdot \gamma - (RQ_x + T) \varepsilon_m] \delta \theta \\ \left. + \left[Q_x + (N + \frac{W - M}{R}) \cdot \gamma + N \beta \right] \delta u \right\} d\varphi - \int_\varphi (q_x \delta u + q_z \delta w) R d\varphi = 0 \quad (25)$$

Carrying out partial integration and introducing $\varepsilon_m - \kappa = -\beta'$:

$$\int_{-\alpha}^{\alpha} \left\{ \left[-N' + \frac{M'}{R} - \frac{M \beta''}{R} + \left(Q_x' - N - \frac{q_x R_q x_q}{R} \right) \beta + (Q_x - \frac{M'}{R}) \beta' - N \varepsilon_m' - N \gamma \right. \right. \\ + (Q_x - N') \varepsilon_m - q_z R \delta w + [-M' - RQ_x - (M \varepsilon_m)' - (W \kappa)' - RQ_x \varepsilon_m - W \cdot \gamma \\ + M \gamma + q_x R_q x_q \beta] \delta \theta + \left[N - Q_x' - q_x R + N(\varepsilon_m - \beta') - (Q_x + N') \beta + \frac{M \kappa + W \kappa}{R} \right. \\ \left. - [(N + \frac{W - M}{R}) \gamma]' \right] \delta u \Big\} d\varphi + \left[N - \frac{M}{R} (1 + \varepsilon_m - \kappa) + N \varepsilon_m - (Q_x + \frac{T}{R}) \beta \right] \delta w \Big|_{-\alpha}^{\alpha} \\ + (M + M \varepsilon_m + W \kappa + T \beta) \frac{\delta \theta}{R} \Big|_{-\alpha}^{\alpha} + \left(Q_x + (N + \frac{W - M}{R}) \cdot \gamma + N \beta \right) \delta u \Big|_{-\alpha}^{\alpha} = 0 \quad (26)$$

one obtains the following equilibrium equations for infinitesimal segment of the cross-section:

(1) the axial equilibrium

$$-N' + \frac{M'}{R} - \frac{M \beta''}{R} + \left(Q_x' - N - \frac{q_x R_q x_q}{R} \right) \beta + \left(Q_x - \frac{M'}{R} \right) \beta' \\ - N \varepsilon_m' + (Q_x - N') \varepsilon_m - N \gamma - q_z R = 0 \quad (27a)$$

(2) the bending moment equilibrium

$$-M' - RQ_x - (M \varepsilon_m)' - (W \kappa)' - RQ_x \varepsilon_m - W \cdot \gamma + M \gamma + q_x R_q x_q \beta = 0 \quad (27b)$$

(3) the radial balance:

$$N - Q_x' + N(\varepsilon_m - \beta') + \frac{M \kappa + W \kappa}{R} - \left[(N + \frac{W - M}{R}) \gamma \right] \\ - (Q_x + N') \beta - q_x R = 0 \quad (27c)$$

Eqs. (27a-c) are derived without any simplification, they are used for buckling or nonlinear analysis with moderate displacements, the quantity T , defined in Eq. (21b) and appearing in Eqs. (20,23), disappears in Eqs. (27a,b,c). This is because the second order effects of different stresses cancel each other partly. If one neglects the effect of the transverse stress σ_x (σ_y), some

quantities will be left in the equilibrium equations and probably lead to unexpected solutions[4].

The boundary conditions are given in Table 1

Table 1

Boundary conditions

Displacement	The corresponding generalized force
δw	$(N - \frac{M}{R})(1 + \varepsilon_m) + \frac{M}{R}\kappa - (Q_x + \frac{T}{R})\beta$
δu	$Q_x + (N + \frac{W - M}{R}) \cdot \gamma + N\beta = N\beta - \frac{M'}{R}$ $-\frac{M\varepsilon'_m}{R} - \frac{(W\kappa)'}{R} - \left(Q_x + \frac{M'}{R}\right)\varepsilon_m + N \cdot \gamma$
$\delta\theta / R$	$M(1 + \varepsilon_m) + W\kappa + T\beta$

From Eq. (27b) ($x_q = 0$ is introduced for simplicity) :

$$Q_x = -\frac{M'}{R} - Q_x \varepsilon_m - \frac{(M\varepsilon_m + W\kappa)'}{R} + \frac{(M - W)\gamma}{R} \quad (28)$$

Substituting Q_x into Eq. (27c), one obtains

$$N + \frac{M''}{R} + N(\varepsilon_m - \beta') + \frac{M}{R}(\varepsilon_m'' + \kappa) + \left(\frac{2M'}{R} + Q_x\right)\varepsilon'_m + \left(\frac{M''}{R} + Q'_x\right)\varepsilon_m - (Q_x + N')\beta + \frac{W\kappa}{R} + \left(\frac{W\kappa}{R}\right)' - (N\gamma)' - Rq_x = 0 \quad (29)$$

2.3 Differential equations for linear analysis

Equilibrium equations for linear analysis are (Fig.4)

$$Q'_x - N + q_x R = 0, \quad N' + Q_x + q_z R = 0, \quad M' + Q_x R = 0 \quad (30a, b, c)$$

Eliminating Q_x from the above equations

$$NR + M'' - q_x R^2 = 0 \quad (31a)$$

$$N'R - M' + q_z R^2 = 0 \quad (31b)$$

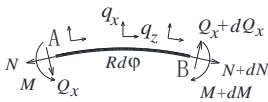


Fig.4 Balance of an infinitesimal segment

Substituting Eq. (8a) into Eqs. (16a, b, c), using Eq. (30c), the following relations are obtained for linear analysis

$$N = EA\varepsilon_m + \frac{EI\kappa}{R^2} = \frac{EA}{R}(w' + u) + \frac{EI}{R^3}(u + R\theta') \quad (32a)$$

$$M = -\int_A \sigma_z x dA = \frac{EI}{R^2}(R\theta' + u), \quad Q_x = GA_s \left(\frac{u'}{R} - \theta \right) \quad (32b, c)$$

$$W = \int_A \sigma_z \frac{x^2}{r} dA = \int_A E(\varepsilon_m - \frac{x}{r}\kappa) \frac{(r-R)^2}{r} dA \approx \frac{EI}{R^2}(w' + u) \quad (32d)$$

Equilibrium differential equations in terms of displacements for linear analysis are:

$$EA(w'' + u') + q_z R^2 = 0 \quad (33a)$$

$$EA(w' + u) + \frac{EI}{R^2}(u + u'' + R\theta' + R\theta'') - q_x R^2 = 0 \quad (33b)$$

$$u' = \frac{R}{1 + \Phi}(\theta - \Phi\theta') \quad (33c)$$

Differentiating Eq. (33b) once, and subtracting Eq.(33a) from it, one has

$$\frac{EI}{R^4}(u' + u''' + R\theta'' + R\theta^{(4)}) = q'_x + q_z \quad (34)$$

Substituting Eq. (33c) into Eq. (34), the basic differential equation for linear analysis of Timoshenko's circular arch is obtained:

$$\frac{EI}{(1 + \Phi)R^5}(\theta^{(4)} + 2\theta'' + \theta) = q'_x + q_z \quad (35)$$

Solving Eq. (35) for θ , and then finding u by Eq. (33c), and w by Eq. (33a) or Eq. (33b), introducing boundary conditions, one may obtain the full linear solution of Timoshenko's circular arch.

2.4 Differential Equations for Linearized Buckling Analysis

Equations for linearized buckling analysis of circular arches are derived from Eqs. (27a,b,c), based on the static criterion for buckling.

An arch satisfying Eqs. (27a,b,c) is in a state of equilibrium. Introducing a small perturbation into the arch, letting it drift from this equilibrium state. When the perturbation is removed, if the arch is still in a state of equilibrium (still satisfying Eqs. (27a,b,c)), the equilibrium of the original system is neutral, the corresponding load is the critical load. The terms after perturbation are

$$u + \dot{u}, \quad w + \dot{w}, \quad \beta + \dot{\beta}, \quad \kappa + \dot{\kappa}, \quad \varepsilon_m + \dot{\varepsilon}_m, \quad \theta + \dot{\theta}, \quad \gamma + \dot{\gamma} \quad (36a)$$

$$q_x + \dot{q}_x, \quad q_z + \dot{q}_z, \quad N + \dot{N}, \quad M + \dot{M}, \quad Q_x + \dot{Q}_x, \quad W + \dot{W} \quad (36b)$$

It is usually required that the loads are kept unchanged during the perturbation, here load increments are produced due to the change of loading direction as explained by Dinnik[7] and Simitses[3].

Substituting Eqs. (36a,b) into Eq. (27a) and Eq.(29), neglecting higher order terms, and noting that the system is in a state of equilibrium before the perturbation, the following equations for buckling analysis are obtained

$$-\dot{N}' + \frac{\dot{M}'}{R} - N\dot{\varepsilon}'_m - \dot{N}\varepsilon'_m - \frac{M\dot{\beta}''}{R} - \frac{\dot{M}\beta''}{R} + (Q'_x - N)\dot{\beta} + (\dot{Q}'_x - \dot{N})\beta + \left(Q_x - \frac{M'}{R}\right)\dot{\beta}' + \left(\dot{Q}_x - \frac{\dot{M}'}{R}\right)\beta' + (Q_x - N')\dot{\varepsilon}_m + (\dot{Q}_x - \dot{N}')\varepsilon_m - N\dot{\gamma} - \dot{N}\gamma - R\dot{q}_z = 0 \quad (37a)$$

$$\dot{N} + \frac{\dot{M}''}{R} + N(\dot{\varepsilon}_m - \dot{\beta}') + \dot{N}(\varepsilon_m - \beta') + \frac{M}{R}(\varepsilon_m'' + \kappa) + \frac{\dot{M}}{R}(\varepsilon_m'' + \kappa) + \left(\frac{2\dot{M}'}{R} + \dot{Q}_x\right)\dot{\varepsilon}'_m + \left(\frac{2\dot{M}'}{R} + \dot{Q}_x\right)\varepsilon'_m + \left(\frac{M''}{R} + \dot{Q}'_x\right)\dot{\varepsilon}_m + \left(\frac{\dot{M}''}{R} + \dot{Q}'_x\right)\varepsilon_m - (Q_x + N')\dot{\beta} - (\dot{Q}_x + \dot{N}')\beta + \frac{W\dot{\kappa} + \dot{W}\kappa}{R} + \left(\frac{\dot{W}\kappa + W\dot{\kappa}}{R}\right)' - (N\dot{\gamma} + \dot{N}\gamma)' - R\dot{q}_z = 0 \quad (37b)$$

$$R\dot{Q}_x = -\dot{M}' - (M\dot{\varepsilon}_m + \dot{M}\varepsilon_m)' - (\dot{W}\kappa + W\dot{\kappa})' - R\dot{Q}_x\varepsilon_m - RQ_x\dot{\varepsilon}_m + (M - W)\dot{\gamma} + (\dot{M} - \dot{W})\gamma \quad (37c)$$

If one neglects the effect of the prebuckling deformation, then

$$-\dot{N}' + \frac{\dot{M}'}{R} - N\dot{\varepsilon}'_m - \frac{M\dot{\beta}''}{R} + (Q'_x - N)\dot{\beta} + \left(Q_x - \frac{M'}{R}\right)\dot{\beta}' + (Q_x - N')\dot{\varepsilon}_m - N\dot{\gamma} - R\dot{q}_z = 0 \quad (38a)$$

$$\dot{N} + \frac{\dot{M}''}{R} + N(\dot{\varepsilon}_m - \dot{\beta}') + \frac{M}{R}(\varepsilon_m'' + \kappa) + \left(\frac{2\dot{M}'}{R} + \dot{Q}_x\right)\dot{\varepsilon}'_m + \left(\frac{M''}{R} + \dot{Q}'_x\right)\dot{\varepsilon}_m - (Q_x + N')\dot{\beta} + \frac{1}{R}W\dot{\kappa} + \frac{1}{R}(W\dot{\kappa})' - (N\dot{\gamma})' - R\dot{q}_z = 0 \quad (38b)$$

$$R\dot{Q}_x = -\dot{M}' - (M\dot{\epsilon}_m)' - (W\dot{\kappa})' - RQ_x\dot{\epsilon}_m - W \cdot \dot{\gamma} + M\dot{\gamma} \quad (38c)$$

If the prebuckling internal forces are computed by linear analysis, then these forces satisfy Eqs. (30a, b, c). Eqs. (38a, b, c) are further simplified into

$$-\dot{N}' + \frac{\dot{M}'}{R} - N\dot{\epsilon}_m' - \frac{M\dot{\beta}'}{R} - q_x R\dot{\beta} - \frac{2M'}{R}\dot{\beta}' + (Q_x - N')\dot{\epsilon}_m - N\dot{\gamma} - R\dot{q}_x = 0 \quad (39a)$$

$$\begin{aligned} \dot{N} + \frac{\dot{M}''}{R} + N(\dot{\epsilon}_m - \dot{\beta}') + \frac{M}{R}(\dot{\epsilon}_m'' + \dot{\kappa}') + \frac{M'}{R}\dot{\epsilon}_m' + q_x R\dot{\beta} + \frac{W\dot{\kappa}}{R} \\ + \left(\frac{W\dot{\kappa}}{R}\right)'' - (N\dot{\gamma})' - R\dot{q}_x = 0 \end{aligned} \quad (39b)$$

$$R\dot{Q}_x = -\dot{M}' - M\dot{\epsilon}_m' - (W\dot{\kappa})' - W \cdot \dot{\gamma} + M\dot{\gamma} \quad (39c)$$

Because the incremental quantities are small, the increments of internal forces are given by

$$\dot{N} = \frac{EA}{R}(\dot{w}' + \dot{u}) + \frac{EI}{R^3}(R\dot{\theta}' + \dot{u}), \quad \dot{M} = \frac{EI}{R^2}(R\dot{\theta}' + \dot{u}) \quad (40a, b)$$

$$\dot{Q}_x = -\frac{EI}{R^3}(R\dot{\theta}'' + \dot{u}') = GA_s\left(\frac{\dot{u}'}{R} - \dot{\theta}\right), \quad \dot{W} = \frac{EI}{R^2}(\dot{w}' + \dot{u}), \quad (40c, d)$$

$$\dot{\epsilon}_m = \frac{\dot{w}' + \dot{u}}{R}, \quad \dot{\kappa} = \frac{\dot{u}}{R} + \dot{\theta}', \quad \dot{\beta} = \dot{\theta} - \frac{\dot{w}}{R}, \quad \dot{\gamma} = \frac{\dot{u}'}{R} - \dot{\theta}, \quad \dot{\epsilon}_m - \dot{\kappa} = -\dot{\beta}' \quad (41a-e)$$

Substituting Eqs. (42a-d) and Eqs. (43a-e) into Eqs. (41a-c), one has

$$\begin{aligned} -\frac{EA}{R}(\dot{w}'' + \dot{u}') - N\frac{\dot{w}'' + \dot{u}'}{R} - \frac{M}{R^2}(R\dot{\theta}'' - \dot{w}'') - q_x(R\dot{\theta} - \dot{w}) - \frac{2M'}{R^2} \times \\ (R\dot{\theta}' - \dot{w}') + (Q_x - N')\frac{\dot{w}' + \dot{u}}{R} - N\left(\frac{\dot{u}'}{R} - \dot{\theta}\right) - R\dot{q}_x = 0 \end{aligned} \quad (42a)$$

$$\begin{aligned} \frac{EA}{R}(\dot{w}' + \dot{u}) + \frac{EI}{R^3}(R\dot{\theta}'' + R\dot{\theta}' + \dot{u}'' + \dot{u}) + \frac{N}{R}(2\dot{w}' + \dot{u} - R\dot{\theta}') \\ + \frac{M}{R^2}(\dot{w}'' + \dot{u}'' + R\dot{\theta}' + \dot{u}) + \frac{M'}{R^2}(\dot{w}'' + \dot{u}') + q_x(R\dot{\theta} - \dot{w}) \\ + \frac{W(\dot{u} + R\dot{\theta}')}{R^2} + \left(\frac{W(\dot{u} + R\dot{\theta}')}{R^2}\right)'' - \left[N\left(\frac{\dot{u}'}{R} - \dot{\theta}\right)\right]' - R\dot{q}_x = 0 \end{aligned} \quad (42b)$$

$$\begin{aligned} GA_s(\dot{u}' - R\dot{\theta}) = -\frac{EI}{R^2}(R\dot{\theta}'' + \dot{u}') - \frac{M}{R}(R\dot{\theta} + \dot{w}'') \\ - W'\left(\frac{\dot{u}}{R} + \dot{\theta}'\right) - \frac{W}{R}(2\dot{u}' + R\dot{\theta}'' - R\dot{\theta}) \end{aligned} \quad (42c)$$

Eqs. (42a, b, c) are the linearized differential equations for buckling analysis of Timoshenko's arches, in which the effect of the prebuckling deformation has been neglected, but all prebuckling internal forces are retained.

3. Buckling of rings under radial pressure

3.1 Prebuckling deformations

The ring is acted on by the uniform radial pressure p (along the centroid line), $q_x = -p$, $q_z = 0$. The deformation is a uniform contraction, no shear deformation occurs. The linear solution is

$$\begin{aligned} q_x^p = -p, \quad q_z^p = 0, \quad N^p = -pR, \quad w^p = 0, \quad \theta^p = 0, \quad \beta^p = 0, \quad Q_x^p = 0 \\ \gamma^p = 0, \quad \chi = \frac{EI}{EAR^2}, \quad u^p = -\frac{pR^2}{(1+\chi)EA}, \quad \epsilon_m^p = \frac{u^p}{R}, \quad \kappa^p = \frac{u^p}{R} \\ M^p = \frac{EI}{R^2}u^p = -\frac{\chi}{1+\chi}pR^2, \quad W^p \approx \frac{EI}{R^2}(w^p + u^p) = M^p \end{aligned} \quad (43)$$

3.2 Buckling Equations

In this example Eqs. (42a, b, c) simplify to

$$\frac{EA}{R}(\dot{w}'' + \dot{u}') + N^p\left(\frac{\dot{w}'' + 2\dot{u}'}{R} - \dot{\theta}\right) + \frac{M^p}{R^2}(R\dot{\theta}'' - \dot{w}'') + q_x(R\dot{\theta} - \dot{w}) = R\dot{q}_x \quad (44a)$$

$$\begin{aligned} \frac{EA}{R}(\dot{w}' + \dot{u}) + \frac{EI}{R^3}(R\dot{\theta}'' + R\dot{\theta}' + \dot{u}'' + \dot{u}) + \frac{N^p}{R}(2\dot{w}' + \dot{u} - R\dot{\theta}') \\ + \frac{M^p}{R^2}(\dot{w}'' + R\dot{\theta}'' + 2\dot{u}'' + 2R\dot{\theta}' + 2\dot{u}) - N^p\left(\frac{\dot{u}'}{R} - \dot{\theta}\right) - R\dot{q}_x = 0 \end{aligned} \quad (44b)$$

$$GA_s(\dot{u}' - R\dot{\theta}) = -\frac{EI}{R^2}(R\dot{\theta}'' + \dot{u}') - \frac{M^p}{R}(\dot{w}'' + 2\dot{u}' + R\dot{\theta}'') \quad (44c)$$

The effect of pre-buckling bending moment is further neglected, Eq. (44c) simplifies to

$$\dot{u}' = \frac{R}{1+\Phi}(\dot{\theta} - \Phi\dot{\theta}'') \quad (45a)$$

and Eqs. (44a, b) simplify to

$$EA(\dot{w}'' + \dot{u}') - pR(\dot{w}'' - \dot{w}' + 2\dot{u}') + R^2\dot{q}_x = 0 \quad (45b)$$

$$EA(\dot{w}'' + \dot{u}') + \frac{EI}{(1+\Phi)R}(\dot{\theta}^{(4)} + 2\dot{\theta}'' + \dot{\theta}) + N(2\dot{w}'' + \dot{u}' - \dot{u}''') - R^2\dot{q}_x' = 0 \quad (45c)$$

Considering three types of radial pressure (Fig.2):

Pressure 1: the direction of the pressure is unchanged during buckling, $\dot{q}_x = 0$, $\dot{q}_z = 0$;

Pressure 2: the pressure is directed toward the center of the arch, $\dot{q}_x = 0$, $\dot{q}_z = -p\dot{w}/R$;

Pressure 3: the pressure is perpendicular to the tangent of the deformed centroid axis of the arch (static water pressure), $\dot{q}_x = 0$, $\dot{q}_z = -p(\dot{w} - \dot{u}')/R$

$$\dot{q}_x = \begin{cases} 0 \\ 0 \end{cases}, \quad \dot{q}_z = -\frac{p}{R} \begin{cases} 0 \\ \dot{w} \\ \dot{w} - \dot{u}' \end{cases} \quad (46)$$

Assuming that the buckling deformations are

$$\dot{w} = B_n \cos n\phi, \quad \dot{\theta} = C_n \cos n\phi, \quad \dot{u}' = \eta_n RC_n \cos n\phi \quad (47a, b, c)$$

where $\eta_n = \frac{1+n^2\Phi}{1+\Phi}$. Introduction of Eqs. (47a,b,c) into Eqs. (45b, c),

$$\left[pR(n^2 + 1) - n^2 EA \right] B_n + (EA - 2pR)\eta_n RC_n - pR \begin{Bmatrix} 0 \\ B_n \\ B_n - \eta_n RC_n \end{Bmatrix} = 0 \quad (48a)$$

$$(2pR - EA)n^2 B_n + \left[EA\eta_n + \frac{(n^2 - 1)^2 EI}{(1+\Phi)R^2} - pR(1+n^2)\eta_n \right] RC_n = 0 \quad (48b)$$

Let the determinant of coefficients of Eqs. (48a, b) vanish, one obtains the critical loads for three types of pressures ($n = 2$)

$$(pR)_{cr1} = \frac{4EI}{(1+4\Phi)R^2} \left(1 - \frac{pR}{4(EA - pR)} \right) \quad (49a)$$

$$(pR)_{cr2} = \frac{4.5EI}{(1+4\Phi)R^2} \left(1 - \frac{pR}{2EA - pR} \right) \quad (49b)$$

$$(pR)_{cr3} = \frac{3EI}{(1+4\Phi)R^2} \quad (49c)$$

Eq.(49c) is the same as that by Smith and Simitses [8].

Considering that the shear stiffness and the axial stiffness may be in the same order of magnitudes, exact buckling loads may be found from Eq.(49a) and Eq.(49b) as follows

$$(pR)_{cr1} = \frac{1}{2} \left[\frac{AR^2}{I} + \frac{5}{1+4\Phi} - \sqrt{\left(\frac{AR^2}{I} + \frac{5}{1+4\Phi} \right)^2 - \frac{16}{1+4\Phi} \cdot \frac{AR^2}{I}} \right] \frac{EI}{R^2} \quad (50a)$$

$$= \eta_1 \frac{4EI}{(1+4\Phi)R^2} \approx \frac{4EI}{(1+4\Phi)R^2}$$

$$(pR)_{cr2} = \frac{1}{2} \left[\frac{2AR^2}{I} + \frac{9}{1+4\Phi} - \sqrt{\left(\frac{2AR^2}{I} + \frac{9}{1+4\Phi} \right)^2 - \frac{36}{1+4\Phi} \cdot \frac{AR^2}{I}} \right] \frac{EI}{R^2} \quad (50b)$$

$$= \eta_2 \frac{4.5EI}{(1+4\Phi)R^2} \approx \frac{4.5EI}{(1+4\Phi)R^2}$$

Table 2 presents values of η_1 and η_2 for $R/i = 5 \sim 100$ and $A/A_s = 1.2 \sim 20$, both are close to 1.0.

Table 2
Factors η_1 and η_2

$\frac{A}{A_s}$	$\eta_1, R/i =$				$\eta_2, R/i =$			
	5	10	50	100	5	10	50	100
1.2	0.971	0.991	1.00	1.00	0.940	0.980	0.999	1.000
2	0.977	0.992	1.00	1.00	0.951	0.981	0.999	1.000
5	0.987	0.993	1.00	1.00	0.971	0.985	0.999	1.000
10	0.992	0.995	1.00	1.00	0.983	0.989	0.999	1.000
20	0.996	0.997	1.00	1.00	0.990	0.993	0.999	1.000

3.3 Solution under the assumption of inextensible arches

Inextensibility is frequently used to simplify solution of arch buckling. In the case of rings, if one adopts this assumption, $\dot{\epsilon}_m = 0$, then

$$\dot{w}' = -\dot{u} \quad (51)$$

Substituting Eq.(51) into Eq.(45c) leads to

$$EI(\dot{\theta}^{(4)} + 2\dot{\theta}'' + \dot{\theta}) + pR^3[\dot{\theta} + \dot{\theta}'' - \Phi(\dot{\theta}'' + \dot{\theta}^{(4)})] = 0 \quad (52)$$

from which one obtains $(pR)_{cr} = (pR)_{cr3}$. Eq. (45b) becomes

$$pR(\dot{w}'' + \dot{w}) - pR \begin{Bmatrix} 0 \\ \dot{w} \\ \dot{w} + \dot{w}'' \end{Bmatrix} = 0 \quad (53)$$

So, the axial equilibrium is satisfied only in the case of Pressure 3 (static water pressure). For Pressure 1 and 2, the axial equilibrium equation is not satisfied, so the inextensibility assumption should not be used for these two types of pressures, Eqs. (49a, b) indicate that the buckling loads are affected by the axial stiffness of the arch for both Pressure 1 and Pressure 2.

4. Linear analysis of circular arches under radial pressure

First we derive the prebuckling internal forces N , M , Q_x , using Eq. (35) and Eqs. (33a, c). In the case of radial pressure, Eq. (35) is

$$\theta^{(4)} + 2\theta'' + \theta = \frac{(q'_x + q_z)(1+\Phi)R^3}{EI} = 0 \quad (54)$$

The general solution is

$$\theta = C_1 \cos \varphi + C_2 \varphi \cos \varphi + C_3 \sin \varphi + C_4 \varphi \sin \varphi \quad (55a)$$

$$u = R[C_1 \sin \varphi + C_2(\varphi \sin \varphi + \cos \varphi) - C_3 \cos \varphi + C_4(\sin \varphi - \varphi \cos \varphi)] - \frac{2R\Phi}{1+\Phi}(C_2 \cos \varphi + C_4 \sin \varphi) + C_5 \quad (55b)$$

Eq. (33b) becomes $w' = \frac{q_x R^2}{EA} - \frac{EI}{EAR^2} C_5 - u$, integrating once:

$$w = R[C_1 \cos \varphi + C_2(\varphi \cos \varphi - 2 \sin \varphi) + C_3 \sin \varphi + C_4(\varphi \sin \varphi + 2 \cos \varphi)] + \frac{2R\Phi}{1+\Phi}(C_2 \sin \varphi - C_4 \cos \varphi) - \left(1 + \frac{1}{\rho^2}\right) C_5 \varphi + C_6 + \frac{q_x R^2}{EA} \varphi \quad (55c)$$

where $\rho = R/i$. Because of the symmetry, u is an even function, and w is an odd function, ϕ starts at the arch top, $C_1 = C_4 = C_6 = 0$. Eq. (33a) becomes $EA(w'' + u') = 0$, so $EA(w' + u)/R = \text{constant}$, and Eq. (33b) is:

$$u + u'' + R\theta' + R\theta'' = K = C_5 \quad (56)$$

$$K = \frac{R^3}{EI} \left(Rq_x - EA \frac{w' + u}{R} \right) \quad (57)$$

The boundary conditions are: $\theta = \pm \alpha : u = w = 0, \theta' = 0$, 3 constants are

$$C_2 = C_{20} \frac{q_x R}{EA}, \quad C_3 = C_{30} \frac{q_x R}{EA}, \quad C_5 = C_{50} \frac{q_x R^2}{EA} \quad (58)$$

$$C_{20} = -\frac{2\alpha(1+\Phi)\cos\alpha}{2\alpha[1+\Phi+2(1+1/\rho^2)\cos^2\alpha] - (3+\Phi)\sin 2\alpha}$$

$$C_{30} = (\alpha \tan \alpha - 1)C_{20}, \quad C_{50} = -\frac{2R\cos\alpha}{1+\Phi}C_{20}$$

Thus, we obtain the linear exact solution of hinged shear-deformable arches under uniform radial pressure:

$$u = \left[C_{20} \left(\varphi \sin \varphi + \frac{1-\Phi}{1+\Phi} \cos \varphi \right) - C_{30} \cos \varphi + C_{50} \right] \frac{q_x R^2}{EA} \quad (59a)$$

$$w = \left[\varphi + \left(\phi \cos \phi - \frac{2}{1+\Phi} \sin \varphi \right) C_{20} + C_{30} \sin \varphi - \left(1 + \frac{1}{\rho^2} \right) C_{50} \varphi \right] \frac{q_x R^2}{EA} \quad (59b)$$

$$\theta = (C_{20} \varphi \cos \varphi + C_{30} \sin \varphi) \frac{q_x R}{EA} \quad (59c)$$

$$u' = \left(C_{20} \varphi \cos \varphi + C_{30} \sin \varphi + \frac{2\Phi}{1+\Phi} C_{20} \sin \varphi \right) \frac{q_x R^2}{EA} \quad (59d)$$

$$\gamma = \frac{u'}{R} - \theta = \frac{2\Phi}{1+\Phi} \cdot \frac{q_x R}{EA} \cdot C_{20} \sin \varphi \quad (59e)$$

The internal forces are

$$N = q_x R + \frac{2EI}{(1+\Phi)R^2} C_2 \cos \varphi = q_x R \left(1 + \frac{2}{(1+\Phi)\rho^2} C_{20} \cos \varphi \right) \quad (60a)$$

$$M = \frac{1}{8} q_x \alpha^2 R^2 \frac{2}{1+\Phi} \frac{8}{\alpha^2 \rho^2} C_{20} (\cos \varphi - \cos \alpha) \quad (60b)$$

$$Q_x = GA_s \gamma = -\frac{M'}{R} = \frac{1}{2} q_x (\alpha R) \left(\frac{4}{1+\Phi} \cdot \frac{1}{\alpha \rho^2} \right) C_{20} \sin \varphi \quad (60c)$$

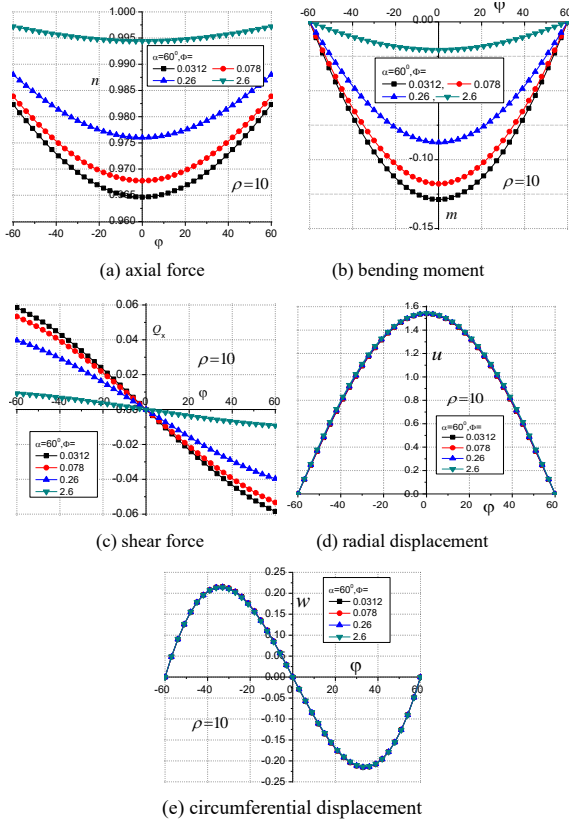
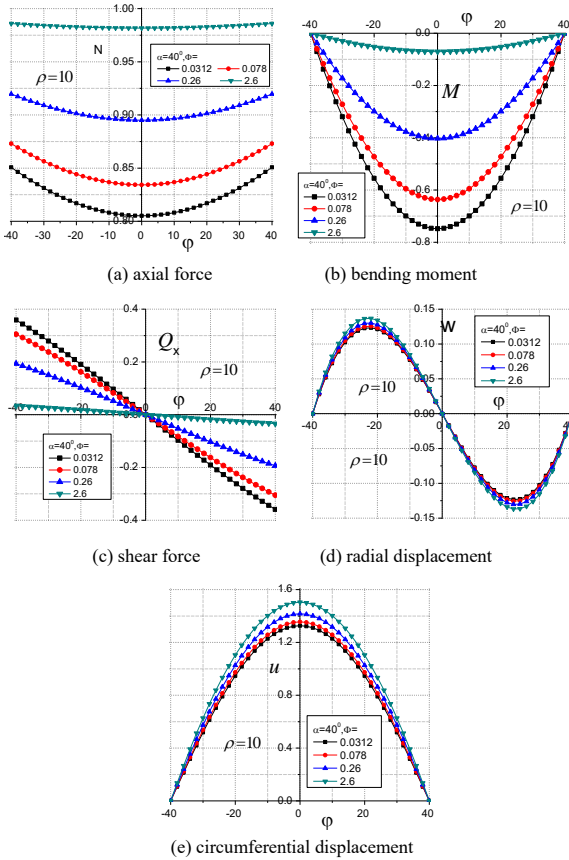
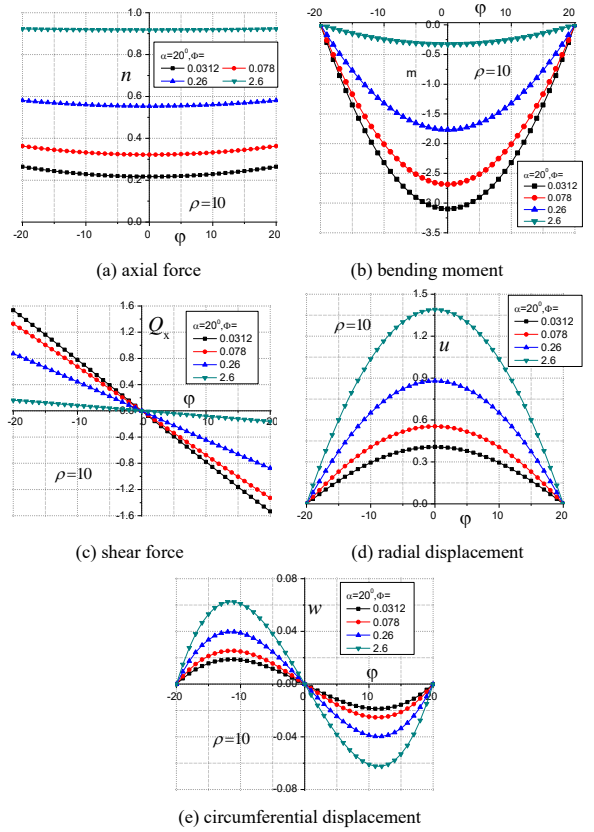
$$W \approx \frac{EI}{R^2} (w' + u) \approx \frac{1}{\rho^2} q_x R^2 \left(1 - \frac{1}{\rho^2} C_{50} \right) \quad (60d)$$

The linear solutions are illustrated in Fig.5, Fig.6 and Fig.7, where

$$n = \frac{N}{pR}, m = \frac{M}{M_0}, M_0 = \frac{q_x (\alpha R)^2}{8}, Q = \frac{Q_x}{0.5 q_x \alpha R}, U = u / \frac{q_x R^2}{EA}, W = w / \frac{q_x R^2}{EA}$$

To highlight the effect of shear deformation, we take $\rho = 10$ and $\Phi = 0.0312, 0.078, 0.26, 2.6$, corresponding to $A/A_s = 1.2, 3, 10, 100$, respectively. It can be seen in Fig. 5, Fig. 6 and Fig. 7 that

(1) displacements become larger when shear deformation is included, but for the arch with $\alpha = 60^\circ$, the increase is very small; and

Fig.5 Linear solutions for $\rho=10$, $\alpha=60^\circ$ Fig.6 Linear solution for $\rho=10$, $\alpha=40^\circ$ Fig.7 Linear solutions for $\rho=10$, $\alpha=20^\circ$

(2) the axial force is more uniform along the arch axis when shear deformation is included, and the bending moment and shear force are smaller. Such results are somewhat beyond expectation.

5. Buckling of hinged circular arches

This section addresses the buckling of shear-deformable hinged arches under three types of radial pressures

(1) Assuming that there is only the uniform axial force $N = q_x R = -pR$. Assuming

$$\dot{\theta} = D_1 \cos \frac{\pi\varphi}{\alpha}, \quad \dot{w} = D_2 \left(\cos \frac{\pi\varphi}{\alpha} + 1 \right) \quad (61a, b)$$

from Eq. (45a)

$$u' = \frac{1 + \Phi_s}{1 + \Phi} \cdot D_1 R \cos \frac{\pi\varphi}{\alpha}, \quad \ddot{u} = \frac{1 + \Phi_s}{1 + \Phi} \cdot \frac{\alpha R}{\pi} D_1 \sin \frac{\pi\varphi}{\alpha} \quad (61c, d)$$

Using Galerkin's method to Eqs. (45b, c), one obtains the critical loads for three types of radial pressures p .

For Pressure 1 (constant-direction):

$$(pR)_{cr1} = \frac{(\pi^2 / \alpha^2 - 1)^2}{(1 + \Phi_s) \left[\left(\frac{\pi^2}{\alpha^2} - 1 \right)^2 + 2 \right]} \cdot \frac{EI}{R^2} \cdot \frac{EA - (1 + 3\alpha^2 / \pi^2) pR}{EA - pR + 2pR \left/ \left(\frac{\pi^2}{\alpha^2} + 3 \frac{\alpha^2}{\pi^2} - 2 \right) \right.} \quad (62)$$

from which

$$(pR)_{cr1} \approx \frac{\psi_1}{1 + \Phi_s} \cdot \frac{(\pi^2 / \alpha^2 - 1)^2}{(\pi^2 / \alpha^2 - 1)^2 + 2} \cdot \frac{\pi^2 EI}{(\alpha R)^2} \quad (63a)$$

$$\psi_1 = 1 - \frac{1}{1 + 0.2\rho^2(1 + \Phi_s)} \quad (63b)$$

For Pressure 2 (centered pressure):

$$(pR)_{cr2} = \frac{(\pi^2 / \alpha^2 - 1)^2}{(1 + \Phi_s)(\pi^2 / \alpha^2 - 2)} \cdot \frac{EI}{R^2} \cdot \frac{EA - pR}{EA - pR + pR / (\pi^2 / \alpha^2 - 2)} \quad (64)$$

From which

$$(pR)_{cr2} \approx \frac{\psi_2}{1+\Phi_s} \cdot \frac{(\pi^2/\alpha^2-1)^2}{(\pi^2/\alpha^2-1)^2-1} \cdot \frac{\pi^2 EI}{(\alpha R)^2} \quad (65a)$$

$$\psi_2 = 1 - \frac{1}{1+0.6\rho^2(1+\Phi_s)} \quad (65b)$$

The parameters ψ_1, ψ_2 are solved for from Eq. (62) and Eq. (64), respectively, the expressions are complicated, exact values are compared with Eq. (63b) and Eq. (65b) in Fig.8, excellent agreements are found.

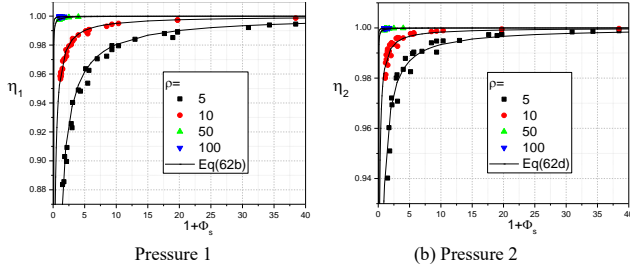


Fig.8 Coefficients ψ_1, ψ_2

and for Pressure 3 (water pressure):

$$(pR)_{cr3} = \frac{1}{1+\Phi_s} \cdot \left(\frac{\pi^2}{\alpha^2} - 1 \right) \frac{EI}{R^2} \quad (66)$$

$(pR)_{cr3}$ is identical to Eq. (1) introduced by Dinnik [7].

When the shear stiffness of the cross-section is infinite, $\Phi_s = 0$, the critical loads are denoted by $(pR)_{cr,f}$, they are

$$(pR)_{cr1,f} = \frac{1}{1+0.2\rho^2} \cdot \frac{(\pi^2/\alpha^2-1)^2}{(\pi^2/\alpha^2-1)^2+2} \cdot \frac{\pi^2 EI}{\alpha^2 R^2} \quad (67a)$$

$$(pR)_{cr2,f} = \frac{1}{1+0.6\rho^2} \cdot \frac{(\pi^2/\alpha^2-1)^2}{(\pi^2/\alpha^2-1)^2-1} \cdot \frac{\pi^2 EI}{\alpha^2 R^2} \quad (67b)$$

$$(pR)_{cr3,f} = \left(1 - \frac{\alpha^2}{\pi^2} \right) \cdot \frac{\pi^2 EI}{\alpha^2 R^2} \quad (67c)$$

On the other hand, if the bending stiffness is very large, and the shear stiffness is small, shear buckling of the arch will occur, the critical loads are denoted by $(pR)_{cr,s}$, they are obtained from Eqs. (62, 64, 66) by setting $EI = \infty$

$$(pR)_{cr1,s} = \left(1 - \frac{2}{(\pi^2/\alpha^2-1)^2+2} \right) \frac{GA_s}{\eta_{s1}}, \quad \eta_{s1} = 1 + 5.2 \frac{\alpha^2 GA_s}{\pi^2 EA} \quad (68a)$$

$$(pR)_{cr2,s} = \left(1 + \frac{1}{(\pi^2/\alpha^2-1)^2-1} \right) \frac{GA_s}{\eta_{s2}}, \quad \eta_{s2} = 1 + 2.6 \frac{\alpha^2 GA_s}{\pi^2 EA} \quad (68b)$$

$$(pR)_{cr3,s} = \left(1 - \frac{\alpha^2}{\pi^2} \right) GA_s \quad (68c)$$

So Eqs. (63a, 64a, 66) may be expressed in form of interactive buckling

$$\frac{1}{(pR)_{cr,i}} = \frac{1}{(pR)_{cr1,f}} + \frac{1}{(pR)_{cr1,s}} \quad i = 1, 2, 3 \quad (69)$$

Eq. (69) is also valid for ring, and for ring

$$(pR)_{cr1,f} = \frac{\pi^2 EI}{(0.5\pi R)^2}, (pR)_{cr2,f} = \frac{9}{8} \frac{\pi^2 EI}{(0.5\pi R)^2}, (pR)_{cr3,f} = \frac{3}{4} \frac{\pi^2 EI}{(0.5\pi R)^2} \quad (70)$$

$$(pR)_{cr1,s} = \frac{9}{11} GA_s, (pR)_{cr2,s} = \frac{9}{8} GA_s, (pR)_{cr3,s} = \frac{3}{4} GA_s \quad (71)$$

6. Buckling loads under other boundary conditions

Assuming that the arches are uniformly compressed, and no other forces and deformations are considered. The buckling of such arches may be solved based on Eqs. (46a, b, c). Only water pressure (Pressure 3) is considered. In this particular pressure, the inextensible assumption is exactly satisfied, the differential equations for buckling of shear deformable circular arches under uniform compression are Eqs. (45a) and Eqs. (51, 52). The general solutions valid for any boundary conditions are

$$\theta = C \sin \varphi + D \cos \varphi + \frac{1}{1-k^2} (A \sin k\varphi + B \cos k\varphi) \quad (72a)$$

$$u = -CR \cos \varphi + DR \sin \varphi + \frac{(1+\Phi k^2)R}{(1+\Phi)(1-k^2)k} (B \sin k\varphi - A \cos k\varphi) + F \quad (72b)$$

$$w = R(C \sin \varphi + D \cos \varphi) + \frac{(1+\Phi k^2)R(A \sin k\varphi + B \cos k\varphi)}{(1+\Phi)(1-k^2)k^2} - F\varphi + J \quad (72c)$$

$$M = \frac{EI}{R^2} \left[F - \frac{R}{(1+\Phi)k} (A \cos k\varphi - B \sin k\varphi) \right] \quad (72d)$$

$$Q_x = -\frac{EI}{(1+\Phi)R^2} (A \sin k\varphi + B \cos k\varphi) \quad (72e)$$

where A, B, C, D, F, J are unknown constants, and

$$k = \sqrt{\frac{1+pR^3/EI}{1-\Phi pR^3/EI}} \quad (73)$$

6.1 Fixed arch

(1) Antisymmetrical buckling

In this case, u is an odd function, w and θ are even functions. The boundary conditions are: at $\varphi = \alpha$: $u = w = 0, \theta = 0$. The final critical equation is

$$\tan k\alpha - \frac{(1+\Phi)k}{1+\Phi k^2} \tan \alpha = 0 \quad (74)$$

The solutions are given in Table 3 in terms of buckling factors K , and the approximate expression is

$$(pR)_{cr} = \frac{K\pi^2 EI}{(\alpha R)^2} = \frac{1}{(1+2.247\Phi_s)} \left(2.045 - \frac{\alpha}{10\pi} \right) \frac{\pi^2 EI}{(\alpha R)^2} \quad (75)$$

Table 3

Buckling factors of fixed arches: anti-symmetrical buckling

α	Φ_s						
	0	0.05	0.1	0.2	0.3	0.4	0.5
15°	2.0435	1.8370	1.6685	1.4100	1.2211	1.0770	0.9635
30°	2.0369	1.8310	1.6630	1.4052	1.2168	1.0731	0.9599
45°	2.0269	1.8220	1.6548	1.3981	1.2104	1.0673	0.9546
60°	2.0153	1.8116	1.6451	1.3899	1.2032	1.0608	0.9486
75°	2.0049	1.8021	1.6366	1.3826	1.1969	1.0550	0.9434
90°	2.0000	1.7978	1.6328	1.3793	1.1940	1.0528	0.9413

(2) Symmetrical buckling: The critical equation is

$$\frac{(1+\Phi k^2)}{(1+\Phi)k^2} (\alpha k \cot k\alpha - 1) = \alpha \cot \alpha - 1 \quad (76)$$

The solutions are given in Table 4 in terms of buckling factors K , and the approximate expression is

$$(pR)_{cr} = \frac{K\pi^2 EI}{(\alpha R)^2} = \frac{1}{(1+3.96\Phi_s)} \left(3.366 - \frac{9\alpha^2}{16\pi^2} \right) \frac{\pi^2 EI}{(\alpha R)^2} \quad (77)$$

Table 4
Buckling factors of fixed arches: symmetrical buckling

α	Φ_s						
	0	0.05	0.1	0.2	0.3	0.4	0.5
15°	3.3615	2.8059	2.4107	1.8861	1.5537	1.3239	1.1553
30°	3.3491	2.7952	2.4011	1.8780	1.5464	1.3173	1.1492
45°	3.3288	2.7777	2.3855	1.8648	1.5347	1.3066	1.1393
60°	3.3009	2.7537	2.3641	1.8468	1.5187	1.2920	1.1257
75°	3.2663	2.7240	2.3377	1.8245	1.4990	1.2741	1.1092
90°	3.2258	2.6895	2.3073	1.7990	1.4765	1.2535	1.0903

6.2 Symmetrical buckling of hinged arches

The critical equation is

$$\frac{(1 + \Phi k^2) \tan k\alpha - k\alpha}{k^3} = (1 + \Phi) \tan \alpha - \alpha \quad (78)$$

The buckling factors K are listed in Table 5, and the approximate expression is

$$(pR)_{cr} = K \frac{\pi^2 EI}{(\alpha R)^2} = \frac{1}{(1 + 2.245\Phi_s)} \left(2.225 - \frac{8\alpha^2}{9\pi^2} \right) \frac{\pi^2 EI}{(\alpha R)^2} \quad (79)$$

Table 5
Buckling factors K of hinged arches: symmetrical buckling

α	Φ_s						
	0	0.05	0.1	0.2	0.3	0.4	0.5
15°	2.2192	1.9951	1.8121	1.5313	1.3259	1.1691	1.0455
30°	2.2002	1.9779	1.7965	1.5180	1.3144	1.1589	1.0364
45°	2.1686	1.9495	1.7706	1.4961	1.2953	1.1421	1.0213
60°	2.1246	1.9098	1.7344	1.4654	1.2687	1.1186	1.0002
75°	2.0682	1.8592	1.6884	1.4264	1.2349	1.0887	0.9734
90°	2.0000	1.7978	1.6328	1.3793	1.1940	1.0528	0.9413

6.3 Symmetrical buckling of arches with three hinges

The anti-symmetrical buckling load is the same as the antisymmetrical buckling of hinged arches. In the case of symmetrical buckling, 5 boundary conditions are

$$\varphi = \alpha: u = w = 0, M = 0; \quad \varphi = 0: w = 0, M = 0 \quad (80)$$

The sixth boundary condition comes from Table 1. Because $u \neq 0$ at the apex of the arch, the force must vanish, $Q_s - p \cdot (u' - w) = 0$. Introducing Eqs. (72a-e) into these boundary conditions, it obtains

$$\frac{(1 + \Phi k^2) \tan 0.5k\alpha - 0.5k\alpha}{(0.5k\alpha)^3} = \frac{4[(1 + \Phi) \tan \alpha - \alpha]}{\alpha^3} \quad (81)$$

The buckling factors K are given in Table 6, and the approximate expression is

$$(pR)_{cr} = K \frac{\pi^2 EI}{(\alpha R)^2} = \frac{3}{4} \frac{\pi^2 EI}{(1 + \Phi_s)(\alpha R)^2} \quad (82)$$

Table 6
Buckling factors of arches with 3 hinges: symmetrical buckling

α	Φ_s						
	0	0.05	0.1	0.2	0.3	0.4	0.5
15°	0.7525	0.7166	0.6840	0.6270	0.5787	0.5373	0.5015
30°	0.7521	0.7163	0.6837	0.6267	0.5784	0.5371	0.5013
45°	0.7516	0.7158	0.6832	0.6263	0.5780	0.5367	0.5009
60°	0.7509	0.7151	0.6826	0.6257	0.5776	0.5363	0.5006
75°	0.7503	0.7146	0.6821	0.6252	0.5771	0.5359	0.5002
90°	0.7500	0.7143	0.6818	0.6250	0.5770	0.5358	0.5000

6.4 Fixed arches with a hinge at the apex of the arch

The buckling load of anti-symmetrical buckling is the same as that of fixed arches. The critical equation for symmetrical buckling is

$$\left\{ (1 - k^2) \cos k\alpha + \left[\frac{(1 + \Phi k^2)}{(1 - k^2)} \cos k\alpha + k\alpha \sin k\alpha - 2 \right] (1 + \Phi k^2) \right\} \frac{\tan \alpha}{(1 + \Phi)k} + k\alpha \cos k\alpha - \frac{(1 + \Phi k^2)}{(1 - k^2)} \sin k\alpha = 0 \quad (83)$$

The buckling factors K are presented in Table 7, and the approximate expression is

$$(pR)_{cr} = K \frac{\pi^2 EI}{(\alpha R)^2} = \frac{1}{(1 + 2.245\Phi_s)} \left(1.112 + \frac{\alpha^2}{6\pi^2} \right) \frac{\pi^2 EI}{(\alpha R)^2} \quad (84)$$

Table 7
Buckling factors of arches with one hinge: symmetrical buckling

α	Φ_s						
	0	0.05	0.1	0.2	0.3	0.4	0.5
15°	1.114	0.999	0.907	0.770	0.672	0.599	0.543
30°	1.117	1.002	0.910	0.772	0.674	0.601	0.544
45°	1.122	1.007	0.914	0.776	0.677	0.604	0.546
60°	1.129	1.014	0.921	0.782	0.682	0.608	0.549
75°	1.140	1.024	0.930	0.790	0.689	0.613	0.554
90°	1.154	1.037	0.943	0.800	0.698	0.621	0.561

6.5 Comparison between proposed formulas and FE buckling analysis

Table 8 gives some comparison between proposed formulas and FE buckling analysis for the arch $\alpha = 45^\circ, R = 13.56\text{m}$ under various boundary conditions, the cross-section is $H500 \times 300 \times 10 \times 16$, and $\Phi_s = 0.2669$. Comparison shows that the proposed formulas are on the safe side. The largest difference is 5.9% occurring in fixed arch for which the actual uniformity of the axial force in the arch is slightly larger.

Table 8
Comparison of N_{cr}/R between proposed formulas and FE buckling analysis

	Anti-symmetrical buckling			Symmetrical buckling		
	FEM	Eqn	FEM/Eqn	FEM	Eqn	FEM/Eqn
Hinged arch	597.6	594.3	0.995	1073.2	1031.5	0.961
Fixed arch	1040.6	979.8	0.942	1312.2	1257.5	0.958
Three hinges	594.7	591.3	0.994	458.9	447.4	0.975
One hinge	1028.9	968.1	0.941	549.9	538.1	0.979

7. Conclusions

This paper derived a new theory for nonlinear and buckling analysis of shear-deformable circular arches. The derivation is based on the well-accepted Timoshenko's assumption on the deformation of the cross-section, the Green strains are used. Based on the virtual work principle, the paper derived a new set of equilibrium equations for buckling analysis and nonlinear analysis with moderate displacements considering the shear deformation of the cross-section of the arches. Compared with others, the present paper included not only the nonlinear effect of longitudinal and shear stresses in the arch, but also the nonlinear effect of the transverse normal stresses in the arch. This was included because the authors believed that the second order effects of all the stresses necessary to keep equilibrium of the plate or shell element will cancel each other partly, and neglect of any one of them will probably lead to incorrect solutions.

Linearization was carried out to obtain a set of differential equations suitable for buckling analysis. These equations are then used to solve the buckling of shear-deformable circular arches and rings under radial pressures to compare the various results appeared in the literature.

Linear analysis is carried out on hinged arches under uniform radial pressure to see the changes of displacements and internal forces after the shear deformation is included. It is found that the displacements become larger when shear deformation is included, but for the arch with $\alpha = 60^\circ$, the increase is very

small. The axial force is more uniform along the arch when shear deformation is considered, and the bending moment and shear force are smaller.

The buckling factors for symmetrical and anti-symmetrical buckling under

various boundary conditions are tabulated, and approximate formulas for the critical loads are proposed.

References

- [1] Timoshenko, S. P. Gere, J. M., Theory of elastic stability, McGrawHill-Kogakusha Ltd, Tokyo, 109, 1961.
- [2] Pi Y.L., Bradford M.A. and Uy B., "In-plane stability of arches", International Journal of Solids and Structures, 39(1), 105-125, 2002.
- [3] Simitses G.J., An introduction to the elastic stability of structures, Prentice Hall Inc, Englewood Cliffs, 1976.
- [4] Tong G.S., Pi Y.L., Bradford M.A. and Tin-Loi F., "In-plane nonlinear buckling analysis of deep circular arches incorporating transverse stresses", Journal of engineering mechanics, 134(5), 362-373, 2008.
- [5] Friedman Z. and Kosmatka Z.B., "An Accurate two-node finite element for shear deformable curved beams", International Journal for Numerical Methods in Engineering, 41, 473-498, 1998.
- [6] Huang C.S, Nieh K.Y. and Yang M.C., "In-plane free vibration and stability of loaded and shear-deformable circular arches", International Journal of Solids and Structures, 40, 5865-5886, 2003
- [7] Dinnik A.N., "Stability of arches", OGIS, Gostechizdat (in Russian, Chinese translation in 1958), 1946.
- [8] Smith C.V. and Simitses G.J., "Effect of shear and load behavior on ring stability", Journal of the Engineering Mechanics Division, 95(3), 559-570, 1969.
- [9] Guo Y.L. and Huang L., "Design theory and method for in-plane ultimate strength of arches with web openings", Journal of Building Structures, 3, 003, 2007.
- [10] Dou C., Guo Y.F., Jiang Z.Q., Gao W. and Pi Y.L., "In-plane buckling and design of steel tubular truss arches", Thin-Walled Structures, 130, 613-621, 2018
- [11] Guo Y.L., Guo Y.F. and Dou C., "In-plane buckling and design of two-hinged steel tube circular truss-arches under pure compression", Journal of Building Structures, 31(8), 45-53, 2010.
- [12] Guo Y.L., Chen H., Pi Y.L. and Bradford M.A., "In-plane strength of steel arches with a sinusoidal corrugated web under a full-span uniform vertical load: Experimental and numerical investigations", Engineering Structures, 110, 105-115, 2016.
- [13] Attard M.M., Zhu J.B. and Kellermann D.C., "In-plane buckling of circular arches and rings with shear deformations", Archive of Applied Mechanics, 83(8), 1145-1169, 2013.
- [14] Zhu J.B., Attard M.M. and Kellermann D.C., "In-plane nonlinear buckling of circular arches including shear deformation", Archive of Applied Mechanics, 84, 1841-1860, 2014.
- [15] Attard M.M., Zhu J.B. and Kellermann D.C., "In-plane buckling of prismatic funicular arches with shear deformations", Archive of Applied Mechanics, 84, 693-713, 2014.
- [16] Washizu K., Variational methods in elasticity and plasticity, Pergamon press, 1975.

EXPERIMENTAL STUDY ON BEARING CAPACITY OF AUSTENITIC STAINLESS STEEL LIPPED CHANNEL COLUMNS

Sheng-gang Fan ^{1,*}, Run-min Ding ¹, Yun-long Han ², Mei-he Chen ¹, Cheng-liang Liu ³ and Yue-lin Tao ³

¹ Key Laboratory of Concrete and Prestressed Concrete Structures of Ministry of Education, School of Civil Engineering, Southeast University, Nanjing, China

² Architectural Design and Research Institute Co. Ltd. of Southeast University, Nanjing, China

³ East China Architectural Design & Research Institute Co. Ltd., Shanghai, China

* (Corresponding author: E-mail: 101010393@seu.edu.cn)

ABSTRACT

An experimental program was conducted to study the bearing capacity of austenitic stainless steel lipped channel columns subjected to axial and eccentric compression in this paper. 14 tensile austenitic AISI304 stainless steel tensile coupons were tested to obtain the material properties of the flat and the corner zones of the specimens. The tensile test results show nonlinear stress-strain behaviour with low proportionality limit, anisotropy and strength enhancement because of cold working. To supplement the experimental data on stainless steel lipped channel members, 24 specimens in all were carried out, including 6 axially compressed columns and 18 eccentrically compressed columns. The test specimens were carried out using a specially designed set-up. The test phenomena, stress-strain curves in cross section, load-displacement curves, rotation-displacement curves, and bearing capacity of the columns were obtained. The results were applied to validate the accuracy of the Direct Strength Method (DSM) in current specifications, as well as to evaluate the Effective Width Method (EWM).

ARTICLE HISTORY

Received: 13 August 2019
Revised: 22 January 2020
Accepted: 23 January 2020

KEYWORDS

Bearing capacity;
Lipped channel columns;
Mechanical properties;
Stainless steel;
Direct Strength Method

Copyright © 2020 by The Hong Kong Institute of Steel Construction. All rights reserved.

1. Introduction

Stainless steel materials have several advantages, such as attractive appearance, easy maintenance, and strong corrosion resistance [1]. In recent years, stainless steel has shown great prospects in a wide variety of structural applications and becomes a new favorite of many structural engineers and architects. However, the design methods and specifications for stainless steel structures are not perfect, and the section shape and size of a member has not been fully normalized. Moreover, the stress-strain curve of stainless steel is non-linear, which greatly differs from carbon steel. The design methods and rules for carbon steel cannot directly be applied to stainless steel. Therefore, the design methods of stainless steel columns require further study.

The cold-formed thin-walled members with open section (such as lipped channel section) are highly prone to several buckling modes, namely local, overall and distortional buckling, and interactions involving the three buckling modes. At present, a considerable amount of research effort was devoted to stainless steel columns experiencing local and global buckling, but the available literature on distortional buckling is much scarcer [2, 3]. Kwon and Hancock [4, 5] conducted extensive experiments on cold-formed columns with different sections, and the results show that distortional buckling tends to happen to the singly symmetric open section columns and is the controlling factor of bearing capacity. Tang and Young [6, 7] performed the column tests of cold-formed steel channels with complex stiffeners and inclined simple edge stiffeners, and the results show that the columns failing in distortional buckling presented the post-buckling strength and the interactions involving different buckling modes occurred in the columns. Many tests of lipped C- and Z- section beams experiencing distortional buckling were performed and the DSM was proposed [8-11]. Becque and Rasmussen [12-15] studied the local and overall buckling of lipped C- and I- section stainless steel columns. The experimental research on the ultimate strength of lipped channel stainless steel stub columns under axial and eccentric compression is detailed in [16-19], in

which comparisons of the test results with the predictions of the codes were analysed. Some experimental as well as numerical researches on stainless steel lipped channel members experiencing distortional and overall flexural-torsional interaction are reported in [20, 21]. For the stainless steel lipped channel columns, DSM was proposed by Lecce and Rasmussen [22-24], but limited test results are available.

In this paper, material properties were obtained according to 14 flat and corner tensile coupon tests. Totally, 6 axially compressed lipped channel stainless steel columns and 18 eccentrically compressed columns were tested. The structural behavior and ultimate strength of stainless steel lipped channel members under eccentric and concentric compression was investigated in the experiments, which can provide test phenomena, stress-strain curves, load-displacement curves, rotation-displacement curves, and bearing capacity of the columns. The experimental results were compared with the prediction results of four design specifications, ASCE [25], EC3 [26], AISI [27] and AS/NZS [28].

2. Material properties

Material tensile tests were conducted to determine the mechanical properties of austenitic AISI304 (EN1.4301) stainless steel in the flat and corner regions. The flat and corner coupons were cut from the lipped channel stainless steel column, with the thickness of 2.0 mm (0.079 in.) and 3.0 mm (0.118 in.), respectively. The flat and corner tensile coupons were tested in direction of rolling.

2.1. Tests of flat coupons

The flat coupons were divided into two groups according to the thickness of the coupons, and each group included 3 coupons, as shown in Table 1. The flat tensile coupons were tested at a strain rate of 0.5 mm/min (0.020 in./min.).

Table 1
Number and dimensions of flat tensile coupons

Group	Number	Thickness (mm)	Measured Dimensions (mm)		Group	Number	Thickness (mm)	Measured Dimensions (mm)	
			Thickness	Width				Thickness	Width
1	CT-2-1	2.0	1.84	12.52	2	CT-3-1	3.0	2.78	12.54
	CT-2-2	2.0	1.84	12.53		CT-3-2	3.0	2.79	12.53
	CT-2-3	2.0	1.84	12.54		CT-3-3	3.0	2.78	12.53

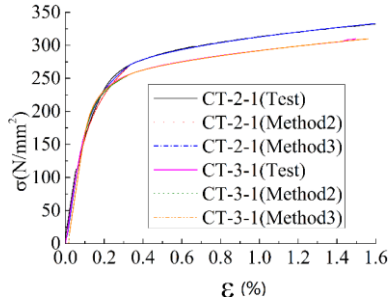
The tensile tests indicate that the stainless steel has a high elongation and smooth fracture surface. Table 2 gives the results of the flat tensile coupons. For coupon CT-3-3, the stress and tension were not collected

synchronously. Thus, the mechanical property could not be obtained. The stress-strain curves obtained from the flat tensile coupons are given in Fig. 1. For each flat coupon, there are three σ - ϵ curves in Fig. 1, obtained from the

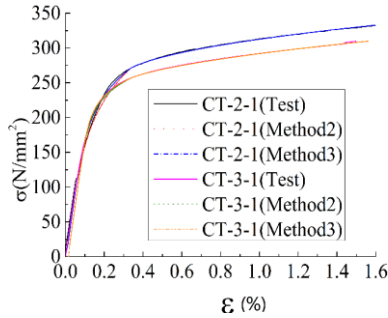
following methods: (1) Method 1: fitting the curves depending on the test data; (2) Method 2: drawing the σ - ε curves on the basis of the 2-stage model (Eq. (1)) [29]; (3) Method 3: drawing the σ - ε curves on the basis of the 2-stage model, but replacing index n with n_f (according to the tensile results). The comparison of the curves in Fig. 1 indicates that the curves from Method 3 are consistent with the test results.

$$\varepsilon = \begin{cases} \frac{\sigma}{E_0} + 0.002 \left(\frac{\sigma}{\sigma_{0.2}} \right)^n & \sigma \in [0, \sigma_{0.2}] \\ \frac{\sigma - \sigma_{0.2}}{E_0} + \left(\varepsilon_{1.0} - \varepsilon_{0.2} - \frac{\sigma_{1.0} - \sigma_{0.2}}{E_{0.2}} \right) \left(\frac{\sigma - \sigma_{0.2}}{\sigma_{1.0} - \sigma_{0.2}} \right)^{n_{0.2,1.0}} + \varepsilon_{0.2} & \sigma \in (\sigma_{0.2}, \sigma_u] \end{cases} \quad (1)$$

where $\sigma_{0.2}$ is the 0.2% proof stress, $\varepsilon_{0.2}$ is the total strain at the 0.2% proof stress, $\sigma_{1.0}$ is the 1.0% proof stress, $\varepsilon_{1.0}$ is the total strain at the 1.0% proof stress, E is the Young's modulus, $n_{0.2,1.0} = 12.255(E_{0.2}/E_0)(\sigma_{1.0}/\sigma_{0.2}) + 1.037$ [29] is the second strain hardening exponent, $E_{0.2}$ is the tangent modulus at the 0.2% proof stress, n is the strain hardening exponent.



(a) Coupons CT-2-1 and CT-3-1



(b) Coupons CT-2-2 and CT-3-2

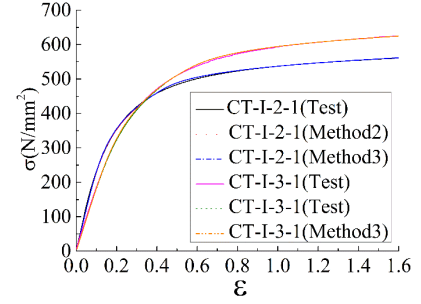
Fig. 1 σ - ε curves of flat coupon tests

2.2. Tests of corner coupons

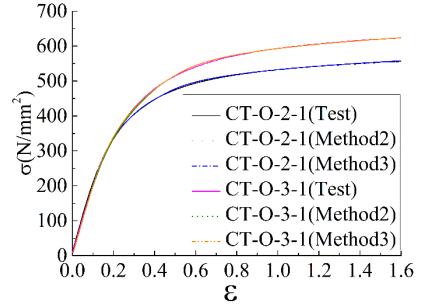
The corner coupons were divided into two groups according to the coupon thickness, and each group includes 4 coupons, as shown in Table 3. These corner coupons were tested in pairs (Part A and Part B shown in Table 3) to avoid eccentric loading. Table 4 gives the results of the flat tensile coupons, and the test data shows that the elongations of corner coupons are more than 20% but lower than those of flat coupons.

By comparing Tables 2 and 4, it shows that the cold-working significantly

enhance the strength of the corner coupons. The σ - ε curves of corner coupons were obtained in the same way as flat coupons. The measured σ - ε curves of the corner coupons are shown in Fig. 2, which indicates that the σ - ε curves from Method 2 and 3 coincide with the measured curves.



(a) Coupons CT-I-2-1 and CT-I-3-1



(b) coupons CT-O-2-1 and CT-O-3-1

Fig. 2 σ - ε curves of corner coupon tests

3. Distortional buckling tests

3.1. Section design

The failure modes of lipped channel columns are substantially determined by the elastic buckling load, which is related to the section size, length and boundary condition. The CUFSM software [30] was adopted to select cross sections failing in distortional buckling, and elastic buckling curve for a particular section was obtained, as presented in Fig. 3.

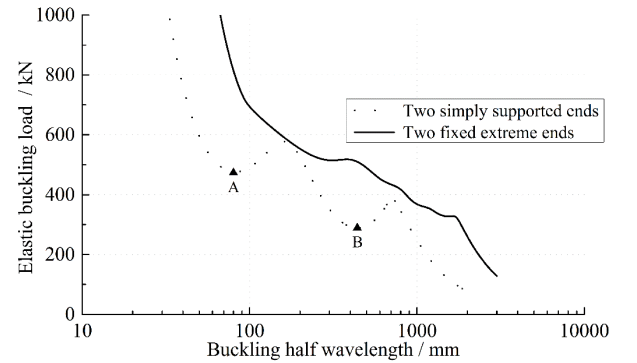


Fig. 3 The relationship curve of elastic buckling load and half-wave length

Table 2

Mechanical properties of stainless steel in the flat regions

Group	Number	E_0 (N/mm ²)	$\sigma_{0.01}$ (N/mm ²)	$\sigma_{0.2}$ (N/mm ²)	n	n_f	$\sigma_{1.0}$ (N/mm ²)	$n_{0.2}$	$\varepsilon_{0.2}$	$\varepsilon_{1.0}$	σ_u (N/mm ²)
1	CT-2-1	199581	141.32	271.80	4.58	5.71	318.98	2.02	0.00338	0.01164	793.11
	CT-2-2	206830	162.18	267.98	5.97	6.98	314.39	1.95	0.00328	0.01151	757.74
	CT-2-3	188981	160.01	267.04	5.85	6.62	314.03	2.18	0.00341	0.01163	751.37
	Average	198464	154.50	268.94	5.47	6.44	315.80	2.05	0.00336	0.01159	767.41
2	CT-3-1	193693	184.59	257.71	8.98	9.94	297.69	1.83	0.00334	0.01153	743.70
	CT-3-2	199254	163.38	254.61	6.75	7.77	298.02	1.87	0.00328	0.01149	757.18
	CT-3-3	-	-	-	-	-	-	-	-	-	-
	Average	196473	173.98	256.16	7.86	8.86	297.86	1.85	0.00331	0.01151	750.44

E_0 is the initial elastic modulus; σ_u is the ultimate strength; $\sigma_{0.01}$ is the strength with a residual deformation of 0.01%; $\sigma_{0.2}$ is the strength with a residual deformation of 0.2%; $\sigma_{1.0}$ is the strength with a residual deformation of 1.0%; $\varepsilon_{0.2}$ is the strain with the stress of $\sigma_{0.2}$; $\varepsilon_{1.0}$ is the strain with the stress of $\sigma_{1.0}$; n is the hardening index ($n = \ln(20)/\ln(\sigma_{0.2}/\sigma_{0.01})$), and n_f is the fitted hardening index by the method of least squares.

The continuous curve is for the fixed-ended columns and the dotted curve is for pinned-ended columns. The plot clearly shows two distinct minima to represent local buckling and distortional buckling (i.e., Point A and Point B) and finally an asymptotic portion representing overall buckling. However, the continuous curve does not show such distinct minima. Point A on the dotted curve represents the elastic local buckling load P_{cr1} , corresponding to a smaller half wavelength, and Point B represents the elastic distortional buckling load P_{crd} , which is lower than the elastic local buckling load P_{cr1} for the columns. Thus, when the column length is appropriately selected, the overall buckling

will be avoided and the distortional buckling primarily determines the bearing capacity of the columns.

The elastic buckling analysis of lipped channel columns was carried out, including 21 sections in Chinese Code (GB50018-2002) [31], and 108 sections in Steel Framing Industry Association (SFIA), which was compiled according to AISI. Six sections were finally selected for the specimens, as presented in Table 5. The length of specimens was twice the distortional half-wavelength of the specimens.

Table 3

Number and dimensions of corner tensile coupons

Group	Corner coupons		Thickness (mm)	Weight (g)	Length (mm)	Section area (mm ²)	Density (kg/cm ³)
	Number	Compositions					
1	CT-I-2-1	Part A	2.0	31.66	200	20.02	7.92
		Part B	2.0	31.76	200	20.09	
	CT-I-2-2	Part A	2.0	31.89	200	20.14	
		Part B	2.0	31.53	200	19.91	
	CT-O-2-1	Part A	2.0	32.60	200	20.61	
		Part B	2.0	31.91	200	20.20	
	CT-O-2-2	Part A	2.0	32.12	200	20.26	
		Part B	2.0	33.07	200	20.88	
2	CT-I-3-1	Part A	3.0	52.56	200	33.33	7.90
		Part B	3.0	52.41	200	33.20	
	CT-I-3-2	Part A	3.0	51.55	200	32.60	
		Part B	3.0	52.33	200	33.10	
	CT-O-3-1	Part A	3.0	53.38	200	33.86	
		Part B	3.0	55.32	200	35.10	
	CT-O-3-2	Part A	3.0	53.06	200	33.56	
		Part B	3.0	53.84	200	34.08	

Part A and Part B represents two compositions cut from the symmetric corner regions of lipped C-section column.

Table 4

Mechanical properties of stainless steel in the corner regions

Group	Number	E_0 (N/mm ²)	$\sigma_{0.01}$ (N/mm ²)	$\sigma_{0.2}$ (N/mm ²)	n	n_f	$\sigma_{1.0}$ (N/mm ²)	$n_{0.2}$	$\epsilon_{t0.2}$	$\epsilon_{t1.0}$	σ_u (N/mm ²)
1	CT-I-2-1	244672	251.49	454.07	5.07	5.25	547.83	3.31	0.00386	0.01224	850.93
	CT-I-2-2	225135	254.78	440.86	5.46	5.55	533.42	2.92	0.00395	0.01238	835.42
	CT-O-2-1	206656	266.84	453.71	5.64	5.67	545.74	3.35	0.00420	0.01266	867.67
	CT-O-2-2	207870	249.24	435.33	5.37	5.48	526.66	3.34	0.00410	0.01255	-
	Average	221083	255.58	445.99	5.39	5.49	538.41	3.23	0.00402	0.01246	851.34
2	CT-I-3-1	185155	264.31	499.77	4.70	5.00	613.47	3.91	0.00470	0.01331	880.03
	CT-I-3-2	-	-	-	-	-	-	-	-	-	-
	CT-O-3-1	207971	242.38	493.04	4.22	4.58	610.68	3.75	0.00437	0.01294	895.74
	CT-O-3-2	-	-	-	-	-	-	-	-	-	-
	Average	196563	253.34	496.40	4.46	4.79	612.08	3.83	0.00453	0.01312	887.89

Table 5

Selected section and analysis results for specimens of column tests

Group	Section	Dimensions (mm)					P_{crd} (kN)	P_{crd} (kN)	l_{crd} (kN)	P_{cr1}/P_{crd}	P_y (kN)	λ_d
		h	b	a	t	r						
1	C100x76x16x2	100	76	16	2	6	213.23	175.03	520	1.218	211.54	1.099
2	C100 x76x16x3	100	76	16	3	6	704.62	419.49	410	1.68	309.53	0.859
3	C92x64x16x2	92	64	16	2	6	230.43	202.7	450	1.137	184.15	0.953
4	C92x64x16x3	92	64	16	3	6	761.17	487.38	360	1.562	268.44	0.742
5	C64x42x13x2	64	42	13	2	6	340.66	244.31	270	1.394	117.38	0.693
6	C64x42x13x3	64	42	13	3	6	-	599.31	210	-	168.29	0.530

P_{crd} is the elastic distortional buckling load, l_{crd} is the half wavelength of elastic distortional buckling, P_y is the elastic yield load, and λ_d is the slenderness ratio of distortional buckling.

3.2. Test specimens

A total of 24 columns, including 6 axially compressed columns and 18 eccentrically compressed columns, were tested. The columns are presented in Fig. 4, the number and dimensions are detailed in Table 6. The symbolic meanings in Table 6 are shown in Fig. 5. To ensure uniform compression and prevented the top and bottom edges from localized failure, a 20 mm end plate was welded at both ends. The end plate material is Q235 steel.

The specimens were split into two groups according to the direction of eccentric load, that is negative or positive eccentricity, as shown in Fig. 6. The

eccentricity e takes a positive sign when the load is toward the lip; the eccentricity e takes a negative sign when the load is toward the web. Fig. 7 shows six types of stress distribution states, corresponding to the Code A-F specimens in Table 6: (1) Code A, the stress distribution is $\sigma_1 = 0.5\sigma_2$, as shown in Fig. 7 (a), where σ_1 represents the compressive stress at web-flange junction and σ_2 represents the compressive stress at the flange-lip junction; (2) Code B, the stress distribution is $\sigma_2 = 0.5\sigma_1$, as given in Fig. 7 (b); (3) Code C, the stress distribution is $\sigma_1 = 0$, as shown in Fig. 7 (c); σ_2 is the compressive stress; (4) Code D, the stress distribution is $\sigma_2 = 0$, as shown in Fig. 7 (d); σ_1 is the compressive stress; (5) Code E, the stress distribution is

$\sigma_1 = -0.125\sigma_2$, as shown in Fig. 7 (e); σ_1 is the tensile stress and σ_2 is the compressive stress; (6) Code F, the stress distribution is $\sigma_2 = -0.125\sigma_1$, as shown in Fig. 7 (f); σ_1 is the compressive stress and σ_2 is the tensile stress. Code A, C and E specimens represent the positive eccentric compression specimens, and Code B, D, and F represent the negative eccentric compression specimens.

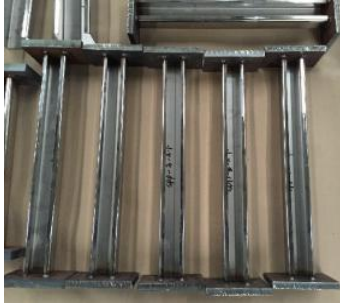


Fig. 4 Processed specimens

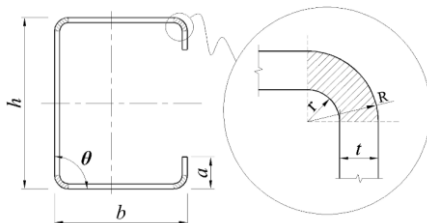


Fig. 5 Geometric parameters of lipped C section

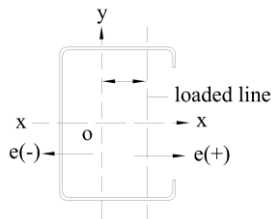


Fig. 6 Eccentric positions and directions of test load

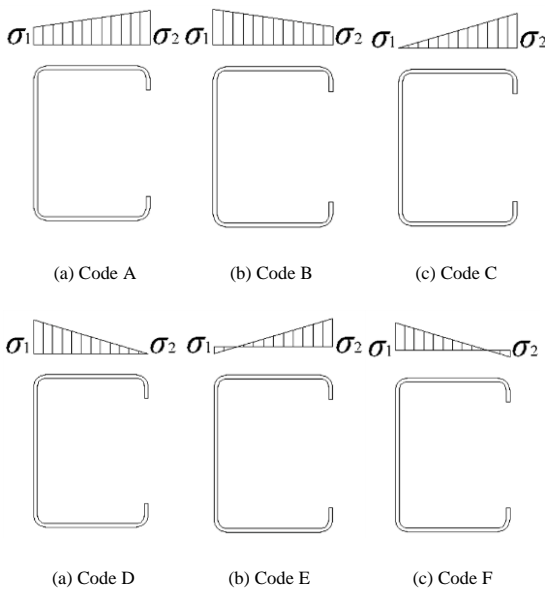


Fig. 7 Stress distribution of cross section under different eccentric loads

3.3. Initial imperfection

The initial imperfections have a noticeable impact on the ultimate

strength of stainless steel lipped channel columns. Therefore, the initial imperfections were measured along 9 parallel lines for each cross-section. 3 lines on the upper flange (points A-1, A-2 and A-3), 3 lines on the web (points A-4, A-5 and A-6), and 3 lines on the lower flange (points A-7, A-8 and A-9), as shown in Fig. 8.

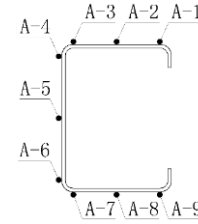


Fig. 8 Layout of measuring point for initial imperfection

The initial imperfections at the ends of the specimens are fairly higher than that in other regions because of the thermal properties and the effects of welding. They are not widely representative. Fan et al. [16] suggested deleting the data of two points close to the ends of the members. The initial imperfection curves of the specimens are presented in Fig. 9. The maximum amplitudes of the recorded initial imperfections are detailed in Table 7.

3.4. Test setups and measuring point distribution

The test setups include displacement meters, an RSA-600 electronic universal testing machine, and a TDS303 data logger, etc. All columns adopted pin-ended boundary conditions at the minor axis. The RSA-600 electronic universal testing machine is equipped with a servo control system, which can realize the infinitely variable speed movement of the beam in the range of 0.1~200mm/min. To accurately simulate the pin-ended boundary conditions, an improved loading system was designed, which primarily consisted of the hinged supports and holding devices, as given in Fig. 10 (a)-(c).

22 strain gauges were arranged at mid-height section of each specimen, which allowed the determination of the variation of stresses in the cross section, and the layout is shown in Fig. 11. The numbers of brackets in Fig. 11 represent the codes of strain gauges on the inner surface of the cross section. The axial displacement and end rotation were measured by eight displacement meters located at the corners of end plates to measure, as shown in Fig. 12 (a), and five displacement gauges were positioned at mid-height of the specimens, as given in Figs. 12 (b) and (c). Three displacement gauges were arranged at the web to measure the deformation of web and the overall lateral displacement. The other two were respectively positioned at the left and right flanges near the flange-lip junction for measuring the deformation of the flange.

Loaded with force control during the initial loading period, the loading rate is 0.5mm/min. After the load reaches 60% of the estimated strength of the columns, displacement control was adopted. If the load drops to 80% of the ultimate bearing capacity, the test terminated.

3.5. Test phenomena

3.5.1. Axially loaded columns

During the tests of columns under axial compression, two buckling modes were observed. One is distortional buckling (specimens SPZ-1 to SPZ-4), and the other is distortional-overall interaction (specimens SPZ-5 and SPZ-6). Specimens SPZ-2 and SPZ-6 were taken as examples.

For specimen SPZ-2, the phenomena and failure process are summarized as follows: For relatively small loads, there was only small axial compression deformation and no other obvious phenomena occurred in the specimen, as shown in Fig. 13 (a). As the load climbed, the both side flanges of the specimens began to rotate around the web-flange junction and the support end plates rotated. When the load was close to its bearing capacity, the flange involved outward flange-lip motions at the top end and the flange involved inward flange-lip motions at the bottom end, respectively, as given in Fig. 13 (b). Eventually, when the load passed its bearing capacity, the deformation of flanges and the rotation angle of two end plates increased rapidly with the decrease of load. The phenomenon and failure process of specimen SPZ-2 under different loads are given in Fig. 13 (a)-(c). The distortional buckling of specimen SPZ-2 before and after unloading is respectively illustrated in Figs. 13 (d) and (e). As can be seen in Fig. 13, (1) there was distinct distortional buckling when the specimen SPZ-2 failed; (2) two distortional half-waves

occurred in the specimen SPZ-2; (3) after unloading, distortional buckling

presented an apparent rebound deformation.

Table 6

Number and measured dimensions of specimens

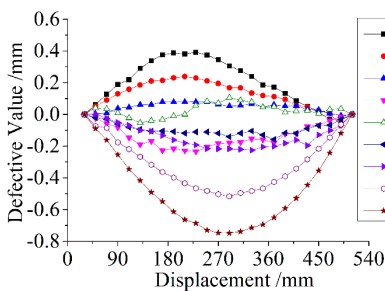
Group	Number	Section type	h (mm)	b_1 (mm)	b_2 (mm)	a_1 (mm)	a_2 (mm)	t (mm)	l (mm)	r (mm)	θ_1	θ_2	A (mm ²)
Axially compressed columns	SPZ-1	C100×76×16×2	100.18	75.98	75.86	15.90	16.01	2.78	1039.27	6	89.1	88.3	723.14
	SPZ-2	C100×76×16×3	100.17	76.93	76.43	15.45	15.85	2.78	818.63	6	89.6	89.4	725.64
	SPZ-3	C92×64×16×2	92.38	65.07	64.81	15.34	15.91	2.78	898.73	6	88.9	88.1	638.57
	SPZ-4	C92×64×16×3	92.15	64.69	64.40	15.88	16.00	2.78	718.73	6	91.4	87.2	637.49
	SPZ-5	C64×42×13×2	63.85	42.45	42.90	13.10	13.00	2.78	538.67	6	88.6	90.1	421.15
	SPZ-6	C64×42×13×3	64.24	42.54	42.36	13.16	12.97	2.78	420.23	6	88.4	90.8	421.07
Eccentrically compressed columns	SPP-1-A	C100×76×16×2	100.64	76.94	76.99	16.62	16.3	1.84	1039.40	6	88.6	88.5	493.58
	SPP-1-B		100.17	76.45	77.23	15.85	15.91	1.84	1038.97	6	87.9	89.1	490.12
	SPP-1-C		100.13	76.69	76.84	15.95	15.99	1.84	1038.33	6	90.0	88.2	490.10
	SPP-1-D		100.59	77.04	76.66	16	16.33	1.84	1039.07	6	89.4	88.3	491.98
	SPP-1-E		100.49	76.43	76.40	15.71	16.12	1.84	1039.03	6	89.4	88.8	489.27
	SPP-1-F		100.44	76.83	76.09	15.78	15.96	1.84	1038.67	6	89.7	88.1	489.18
	SPP-2-A	C92×64×16×2	92.35	64.67	65.20	16.01	15.77	1.84	898.53	6	88.3	89	431.96
	SPP-2-B		92.05	64.47	65.22	16.03	15.93	1.84	899.00	6	90.2	89.4	431.41
	SPP-2-C		92.48	64.8	64.15	16.29	15.72	1.84	899.57	6	88.0	87.8	430.93
	SPP-2-D		92.22	64.91	64.54	16.14	15.91	1.84	898.57	6	89.0	89.4	431.44
	SPP-2-E		92.18	64.28	64.98	15.88	15.97	1.84	898.17	6	88.1	90.2	430.65
	SPP-2-F		92.08	64.36	64.89	15.8	16.09	1.84	898.33	6	86.6	92.1	430.52
	SPP-3-A	C64×42×13×2	64.06	42.61	42.40	13.21	12.92	1.84	539.03	6	89.7	89.9	286.97
	SPP-3-B		63.65	42.56	42.58	13.11	12.82	1.84	538.60	6	89.9	89.4	286.08
	SPP-3-C		64.06	42.48	42.52	13.28	13.26	1.84	538.07	6	87.8	88.8	287.70
	SPP-3-D		64.05	42.46	42.45	13.31	13.27	1.84	538.73	6	88.6	88.9	287.59
	SPP-3-E		63.69	42.47	42.55	13.25	13.31	1.84	537.83	6	88.3	91.4	287.09
	SPP-3-F		63.98	42.59	32.46	12.88	12.99	1.84	538.60	6	89.4	88.7	268.01

h is height of lipped C section; b_1 and b_2 are separately upper and lower flange widths; a_1 and a_2 are separately upper and lower lips widths; t is thickness of lipped C section; l is length of specimen; r is the internal radius of corner region on cross section; θ_1 and θ_2 are separately the angle between the web and upper and lower flange; A is the section area.

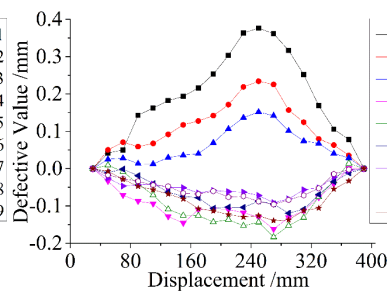
Table 7

Measured initial imperfection values of specimens

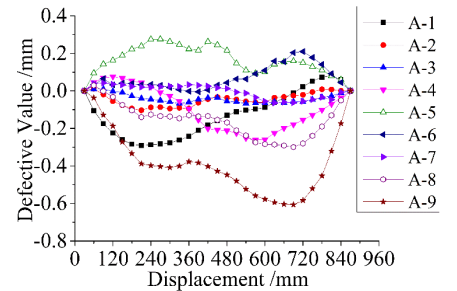
Number	Section	Imperfection position	Measured value (mm)	Number	Section	Imperfection position	Measured value (mm)
SPZ-5, SPP-3-A (B/C/D/E/F)	C64×42×13×2	Center of the web	0.1059	SPZ-6	C64×42×13×3	Center of the web	0.1830
		Flange-lip junction	0.7485			Flange-lip junction	0.3766
SPZ-3, SPP-2-A (B/C/D/E/F)	C92×64×16×2	Center of the web	0.2626	SPZ-4	C92×64×16×3	Center of the web	0.3230
		Flange-lip junction	0.6066			Flange-lip junction	0.8445
SPZ-1, SPP-1-A (B/C/D/E/F)	C100×76×16×2	Center of the web	0.2417	SPZ-2	C100×76×16×3	Center of the web	0.9477
		Flange-lip junction	1.0826			Flange-lip junction	0.7056



(a) C64×42×13×2



(b) C64×42×13×3



(c) C92×64×16×2

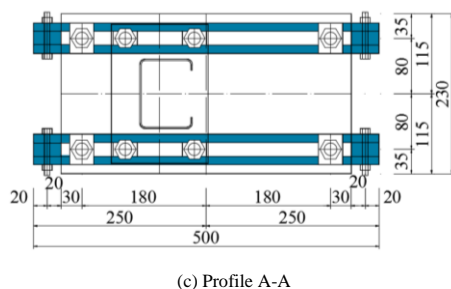
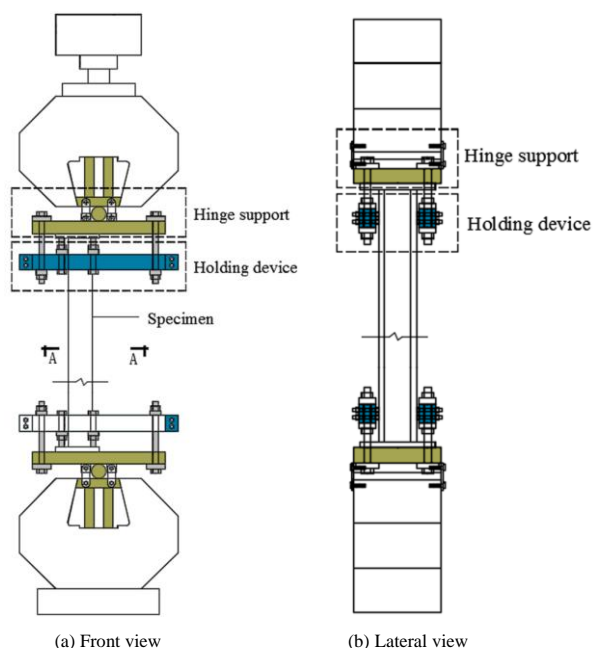
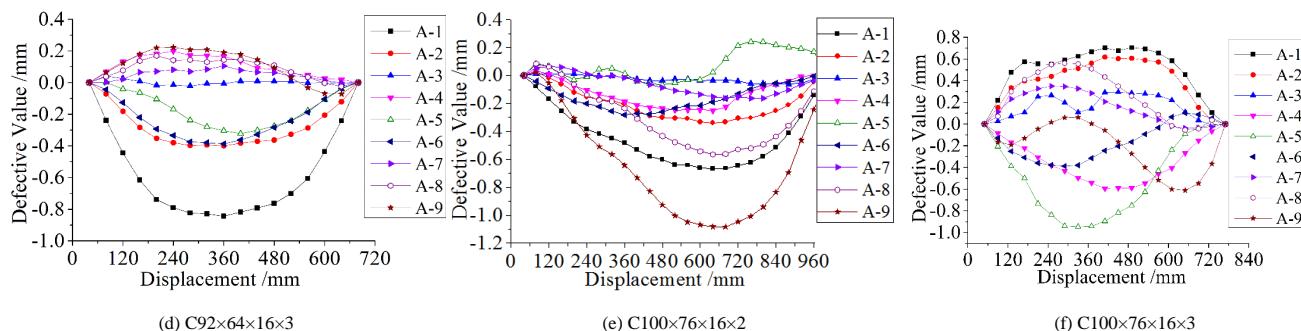


Fig. 10 Improved loading system

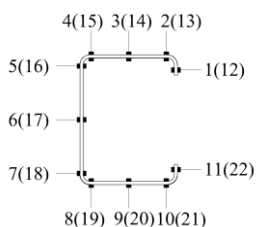


Fig. 11 Layout of strain gauges

For specimen SPZ-6, the failure procedure was summarized as follows: when the load is small, there was only slight axial deformation and no other obvious phenomena occurred in the specimen, as shown in Fig. 14 (a). As the load climbed, two end plates began to rotate, and overall buckling occurred in the specimen. Then a relatively large lateral displacement appeared at the mid-height of the specimen. When the load reached its ultimate bearing capacity, the flange involved outward flange-lip motions at the mid-height of

the column, and a large rotation occurred at the bottom end plate, as shown in Figs. 14 (b). Subsequently, with the rapid decrease of the test load, the distortional-overall interaction became rather apparent until the failure of the column, as pictured in Fig. 14(c). The distortional-overall interaction of SPZ-6 is respectively illustrated in Fig. 14 (d) and (e). The Fig. 14 shows that: (1) distortional-overall interaction occurred in the specimen SPZ-6; (2) the flange involved outward flange-lip motions at the mid-height of the column; and (3) a distortional half-wave was observed in the specimen.

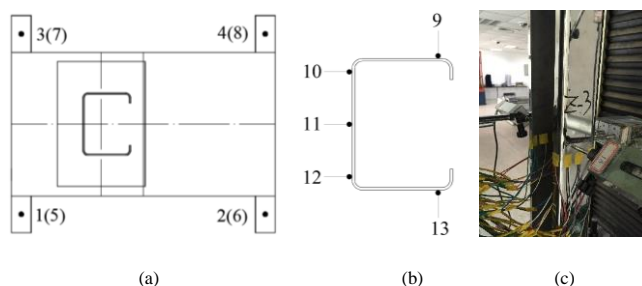


Fig. 12 Layouts of displacement gauges: (a) axial displacement (b) lateral displacement (c) lateral displacement at the mid-height of the specimen

3.5.2. Positive eccentrically loaded specimens

For the positive eccentrically loaded specimens SPP-1-A/C/E, SPP-2-A/C/E and SPP-3-A/C/E, the failure process and phenomena are like those of columns under axial compression. The failure modes of the columns under positive eccentric compression are given in Fig. 15 (a)-(c). Fig. 15 shows: (1) distortional buckling occurred in the specimens under positive eccentric compression, and at least a half-wave of distortional buckling was observed; (2) there were differences between the wave shapes of different specimens; for specimens SPP-1-C/E and SPP-2-A/C, there are two distortional half-waves, and the flange involved outward flange-lip motions at top end the flange involved inward flange-lip motions at bottom end; whereas the wave shapes of buckling are just the opposite for specimens SPP-1-A, SPP-2-E and SPP-3-A; and (3) for the specimen SPP-3-C/E, a half-wave of distortional buckling observed at mid-height of the specimen, and the flange involved outward flange-lip motions.

3.5.3. Negative eccentrically loaded specimens

For the negative eccentrically loaded specimens SPP-1-B/D/F, SPP-2-B/D/F and SPP-3-B/D/F, the failure process and phenomena are different from those of the columns under positive eccentric compression. The specimen SPP-1-B was chosen as an example.

For relatively small loads, there was only the slight axial deformation, and no other observable phenomena occurred in the specimen, as shown in Fig. 16 (a). With the increase of the load, local buckling began to appear in the web and flanges, as given in Fig. 16 (b). When the load was up to the bearing capacity, apparent local buckling was observed in the flanges and web, as given in Fig. 16 (c). Finally, when the load passed its bearing capacity, observable local buckling at mid-height of the specimens developed rapidly, which led to the damage of the columns, as given in Fig. 16 (d). The buckling modes of the members SPP-1-B before and after unloading are illustrated in Figs. 16 (e) and (f), respectively.

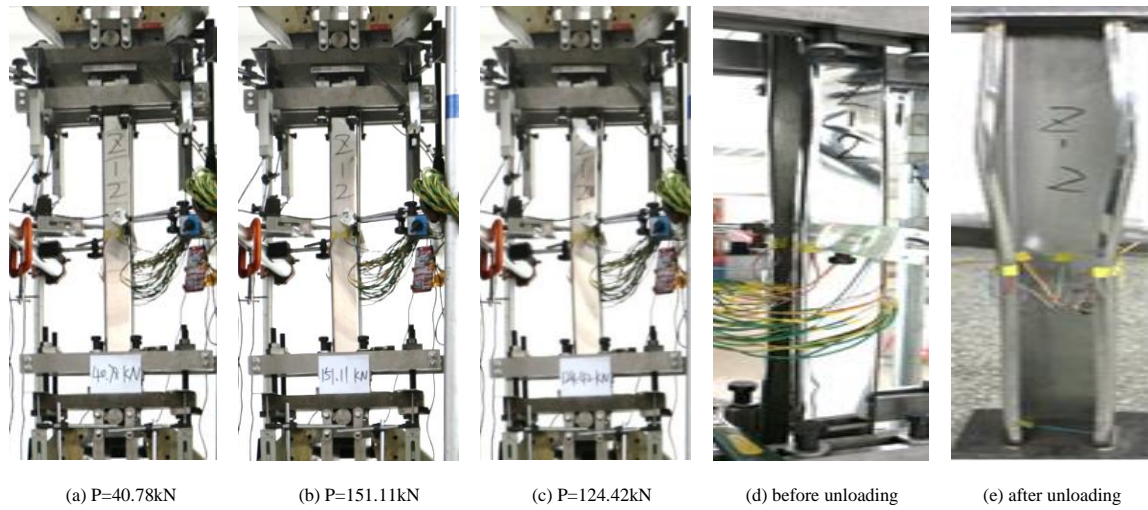


Fig. 13 Failure process of axially loaded specimen SPZ-2

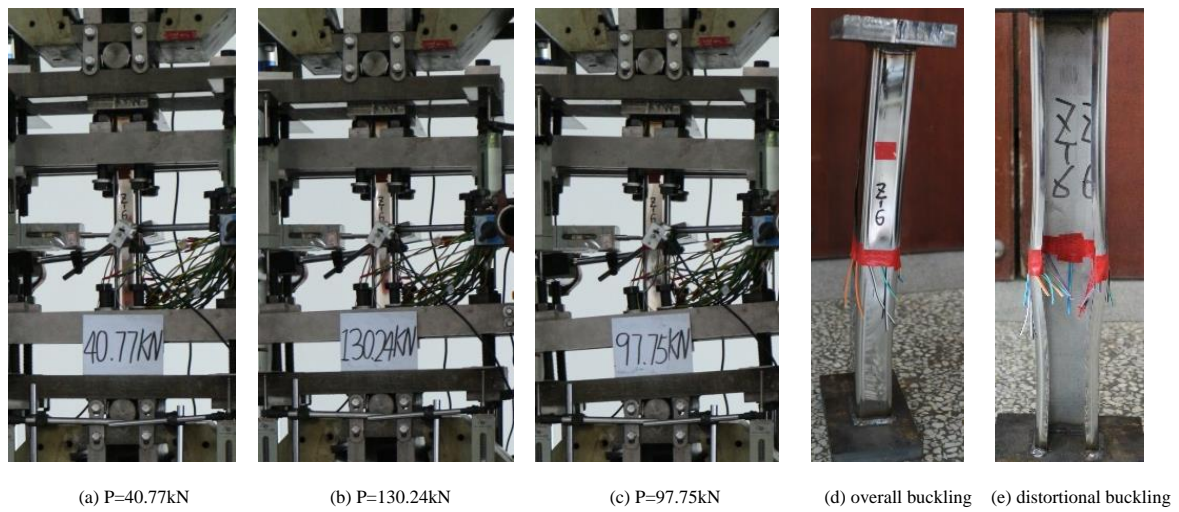


Fig. 14 Failure process of axially loaded specimen SPZ-6



Fig. 15 Failure of positive eccentrically loaded specimens

3.6. Experimental results

3.6.1. Load-axial displacement curves

The load-axial displacement curves of the column under axial and eccentric compression are shown in Fig. 17, which indicates that: (1) the load-axial displacement curves of the columns have a similar pattern, and the axial displacement of the column grows linearly with the increase of load at initial stage; (2) For the specimens under eccentric compression, the ultimate

bearing capacities of the specimen reduce gradually with the increase of eccentricity; and (3) its ductility is related to the eccentric direction and the eccentricity; for specimens with same eccentric direction (such as SPP-1-A/C/E or SPP-1-B/D/F), the ductility is enhanced with the increase of eccentricity; for the specimens with different eccentric directions (such as SPP-1-A and SPP-1-B), the ductility of the specimens with positive load eccentricity is larger than that of the specimens with negative load eccentricity.

3.6.2. Load-lateral displacement curves

Fig. 18 shows the load-lateral displacement curves of the columns subjected to concentric and eccentric compression. The conclusions according to Fig. 18 are as follows: (1) for the specimens SPZ-1, the deformation of flange firstly appeared, and then the overall buckling was observed in the specimen, as given in Fig. 18 (a); for the specimens SPZ-6, the overall buckling firstly figured, and then the deformation of flange appeared, as shown in Fig. 18 (c); for other specimens under axial compression, the deformation of the flange as well as overall buckling were simultaneously observed at the initial stage, as given in Fig. 18 (b); and (2) the deformation of flanges is outward, and the web is inward, as shown by specimens SPZ-6 and SPP-3-A; and vice versa, as shown by specimens SPZ-1, SPZ-3, SPP-1-E, and SPP-3-E.

3.6.3. Strain distribution on the cross-section

The layout of strain gauges at the mid-height of the specimen are shown in Fig. 11. The strain distribution of the members under axial compression is shown in Fig. 19 (a)-(c), and the strain distribution of the members under eccentric compression is presented in Fig. 19 (d)-(i).

For the specimens subjected to axial compression, it can be seen from Fig. 19 (a)-(c): (1) for specimen SPZ-1, the strain distribution showed an M shape before the load is up to its ultimate value, which is similar to the strain

distribution of specimens SPZ-2~SPZ-4 when the load reached its limit load, as shown in Fig. 19 (a); (2) for specimens SPZ-2, SPZ-3 and SPZ-4, before the load up to its limit load, the strain increased as the increase of the load, and the increasing rate of strain in the flanges is larger than that in the web or lip; the strain distribution shown a W shape, as shown in Fig. 19 (b); when the load up to its limit load, the strain value in web and lip was rarely enhanced, but strain value in the flanges was increased further; (3) for the specimens SPZ-5 and SPZ-6, before the test load reached the ultimate value, the compressive strain on the cross section remains substantially linear, indicating that the global buckling occurred and the distortional buckling was not obviously observed; when the load reached its limit load, the strain in the lip was increased rapidly, showing that the distortional buckling was gradually observed in the specimen, as shown in Fig. 19 (c).

It can be seen from Fig. 19 (d)-(i): (1) for the specimens under positive eccentric compression, the strain distribution of the cross section is similar to that of the specimens subjected to axial compression with the same section, and the strain in the web is always tensile strain; (2) for the specimens under negative eccentric compression, the strain distribution of cross section is basically consistent, such as the specimens SPP-1-F, SPP-2-F and SPP-3-F; and (3) the tensile strain in the lips of the specimen SPP-3-F is larger than that of the specimens SPP-1-F and SPP-2-F, indicating the specimen SPP-3-F failing in overall buckling is more obvious.

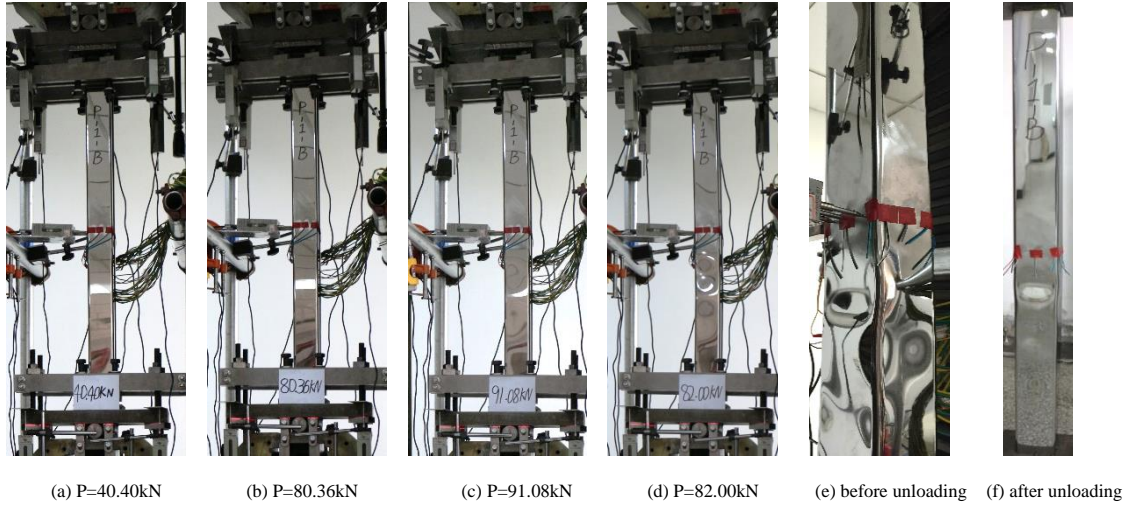


Fig. 16 Failure process of negative eccentrically loaded specimen SPP-1-B

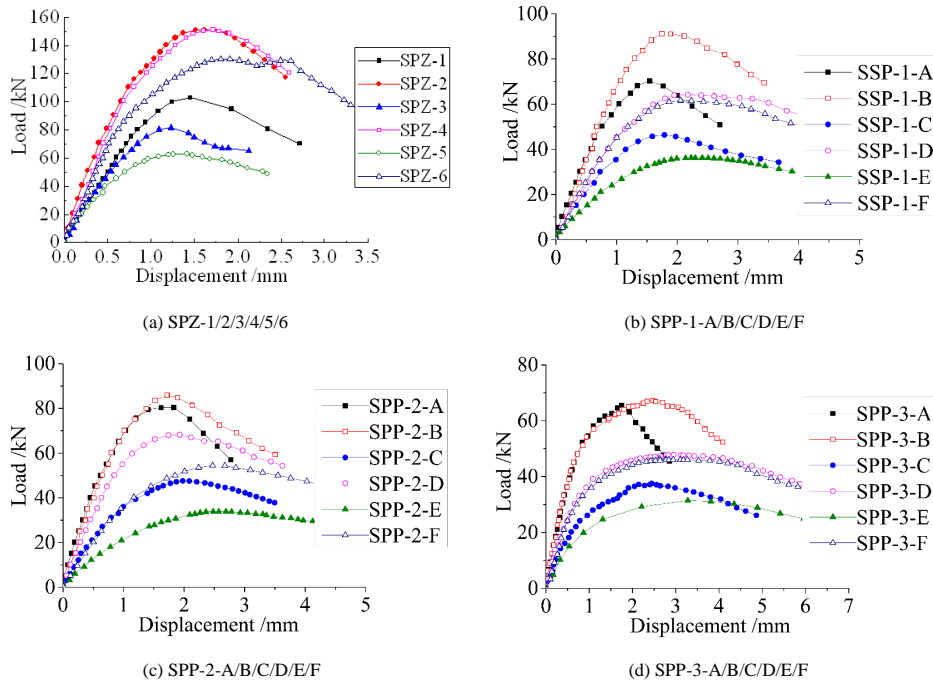


Fig. 17 Load-axial displacement curves of specimens

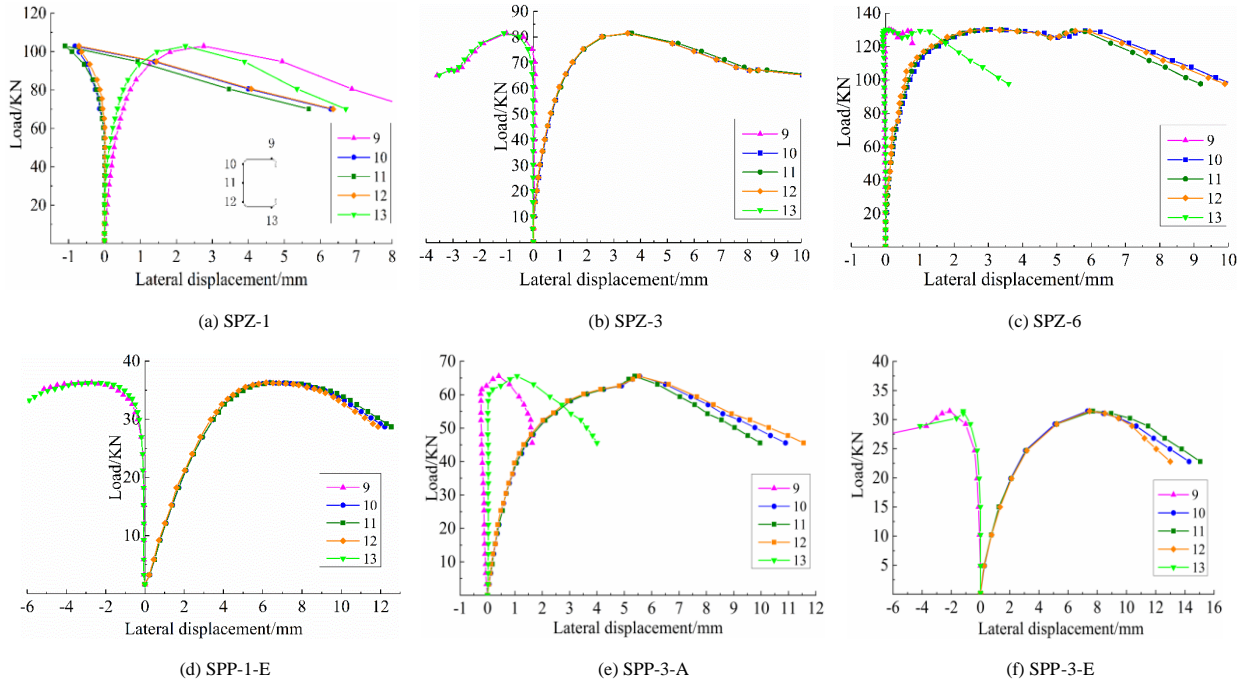


Fig. 18 Load-lateral displacement curves of specimens

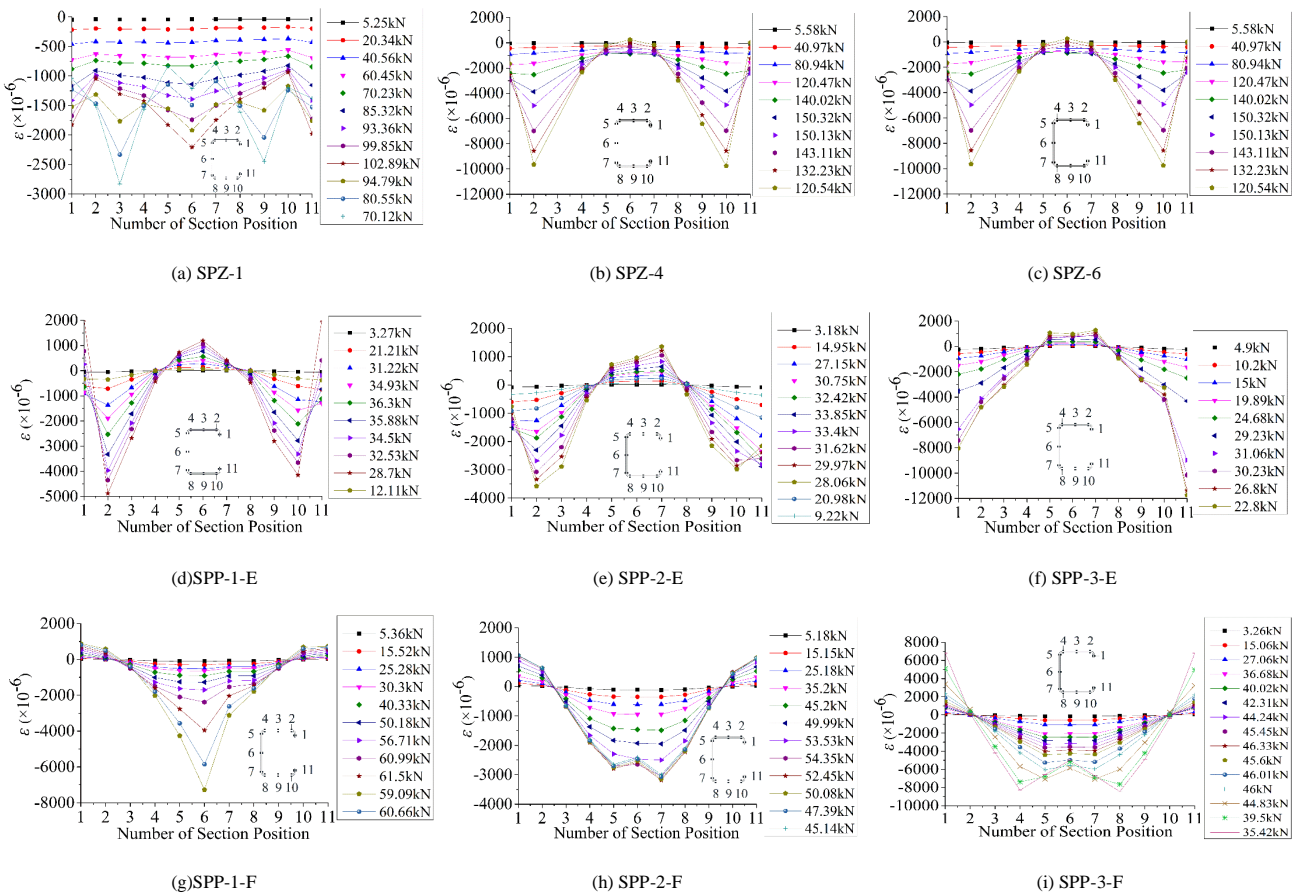


Fig. 19 Strain distribution at the mid-height of specimens

3.6.4. Bearing capacity and failure modes

The test results and the failure modes of the members are detailed in Table 8. The difference between the theoretical and the practical value of eccentricity was generated due to the installation of the test setup and the manufacturing of the specimens. The practical value of eccentricity was deduced from the stress distribution at the mid-height section of each specimen.

As presented in Table 8, for the specimens subjected to axial compression, the distortional-overall interaction occurred in the specimens SPZ-5 and

SPZ-6, and there is only distortional buckling in other specimens; the distortional buckling and distortional-overall interaction were observed in the specimens under positive eccentric compression; the local buckling and local-global interaction were presented in the specimens under negative eccentric compression.

4. Comparisons of test results and code results

For stainless steel columns, to determine the bearing capacity of

distortional buckling, two methods were adopted, including effective width method (EWM) and DSM. In the EWM, the distortional buckling is treated as a special local buckling, and the influence of distortional buckling on the bearing strength of the columns is considered by decreasing the buckling coefficient of plate or reducing the section thickness. The calculation will be very complicated when the section form of component becomes more and more complex. In the DSM, the ultimate bearing capacity is determined according to the relationship between the elastic critical buckling load and the ultimate strength. Comparisons between the experimental values and the predictions by above two methods were performed.

4.1. Comparisons of test results with EWM results

EWM is available in current design codes including the EC3 and ASCE. For the axially loaded specimens SPZ-1~SPZ-6, the distortional buckling bearing capacities can be obtained by the EWM in the two design codes. The calculation results were compared with the test results, as shown in Table 9. P_T is the experimental value; P_{EC3} is the calculated value obtained from EC3; P_{ASCE} is the calculated value obtained from ASCE; DEV_T is the deviation

between test results and calculation results; and λ_d is the distortional buckling slenderness, determined by Eqs. (2) and (3).

$$\lambda_d = \sqrt{P_y / P_{crd}} \quad (2)$$

$$P_y = Af_y \quad (3)$$

where, P_{crd} is the elastic critical buckling strength; P_y is the yield bearing capacity; A is the section area of columns; and f_y is the yield strength.

The ratios of the calculation results obtained by EWM with the test results under different slenderness ratios λ_d are drawn in Fig. 20 (a). Table 9 and Fig. 20 (a) indicate that: (1) except for the specimen SPZ-1, the calculation results obtained from the two design codes are higher than the experimental values; (2) the ratios of the calculation results to the experimental values are greater than 1.0, and it indicates that the EWM is unsafe to calculate the distortional buckling strength for lipped channel members; and (3) the calculation results obtained from ASCE are greater than those from EC3.

Table 8

Bearing capacity and buckling modes of specimens

Number	Eccentricity (mm)		Buckling mode	Number of half-wave of distortional buckling	P_T (kN)
	Theoretical value	Practical value			
SPZ-1	0	0.41	D	2	102.89
SPZ-2	0	0.82	D	2	151.11
SPZ-3	0	2.47	D	2	81.53
SPZ-4	0	1.64	D	2	151.02
SPZ-5	0	2.01	D+F	2	62.76
SPZ-6	0	0.49	D+F	1	130.24
SPP-1-A	7.35	6.77	D	2	70.28
SPP-1-B	6.21	-5.49	L	—	91.08
SPP-1-C	26.43	26.71	D	2	46.40
SPP-1-D	-16.31	-18.98	L	—	64.20
SPP-1-E	37.29	36.52	D	2	36.30
SPP-1-F	-19.65	-20.48	L	—	61.66
SPP-2-A	6.26	5.09	D	2	80.38
SPP-2-B	-5.34	-5.02	L	—	85.90
SPP-2-C	22.60	22.16	D	2	47.60
SPP-2-D	-13.96	-13.71	L	—	68.22
SPP-2-E	31.92	35.50	D	2	33.85
SPP-2-F	-16.97	-19.51	L	—	54.44
SPP-3-A	4.02	4.56	D+F	2	65.56
SPP-3-B	-3.48	-3.29	L+F	—	67.21
SPP-3-C	14.31	16.56	D+F	1	37.50
SPP-3-D	-9.27	-9.45	L+F	—	47.82
SPP-3-E	19.90	21.31	D+F	1	30.13
SPP-3-F	-11.23	-11.70	L+F	—	46.04

D means distortional buckling, L means the local buckling, and F means overall buckling; P_T is the test result of ultimate bearing capacity of specimen.

4.2. Comparisons of test results with DSM results

Currently, DSM is available in AS/NZS and AISI. For the axially loaded specimens SPZ-1~SPZ-6 and the positive eccentrically loaded specimens SPP-1-A/C/E, SPP-2-A/C/E and SPP-3-A/C/E, the capacities in distortional buckling and distortional-overall interaction were obtained by the DSM in design codes, and comparison between the predictions and the experimental values was performed. The ultimate bearing capacity of stainless steel columns could be calculated by the DSM including in AISI (Eq. (4)) [27] and AS/NZS (Eq. (5)) [28], and the DSM equation (Eq. (6)) proposed by Lecce and Rasmussen [23, 24]. The comparisons of test results from this paper and calculation values obtained by the DSM are shown in Table 10. P_{AISI} , P_{AS} , and P_{LR} are the design strengths for AISI, AS/NZS, and DSM proposed by Rasmussen and Lecce.

$$\begin{cases} P_{nd} = P_y & \text{For } \lambda_d \leq 0.561 \\ P_{nd} = \left[1 - 0.25 \left(\frac{P_{crd}}{P_y} \right)^{0.6} \right] \left(\frac{P_{crd}}{P_y} \right)^{0.6} P_y & \text{For } \lambda_d > 0.561 \end{cases} \quad (4)$$

$$\begin{cases} P_{nd} = Af_y \left(1 - \frac{f_y}{4f_{od}} \right) & \text{For } f_{od} > \frac{f_y}{2} \\ P_{nd} = Af_y \left[0.055 \left(\sqrt{\frac{f_y}{f_{od}}} - 3.6 \right)^2 + 0.237 \right] & \text{For } \frac{f_y}{13} \leq f_{od} \leq \frac{f_y}{2} \end{cases} \quad (5)$$

$$\begin{cases} P_{nd} = P_y & \text{For } \lambda_d \leq 0.533 \\ P_{nd} = \left(\frac{0.8}{\lambda_d^{1.1}} - \frac{0.15}{\lambda_d^{2.2}} \right) P_y & \text{For } \lambda_d > 0.533 \end{cases} \quad (6)$$

where f_{od} is the elastic critical buckling stress, P_{nd} is the distortional buckling strength.

The ratios of the calculation results obtained by DSM with the test results under different slenderness ratios λ_d are drawn in Fig. 20 (b). The conclusions based on Table 10 and Fig. 20 (b) are as follows: (1) the calculation results obtained by the DSM are greater than the experimental values; (2) the DSM detailed in AS/NZS and AISI is primarily applied for calculating the strength of carbon steel or low yield point steel columns, and is inapplicable to the distortional buckling strength of stainless steel members in

compression; there are significant deviations between the test values and the DSM calculation results of design codes; (3) the load eccentricity has distinct influences on the distortional buckling bearing capacity of the columns under eccentric compression; and (4) for the stainless steel lipped channel members,

the DSM can predict the distortional buckling strength more accurately than the EWM.

Table 9

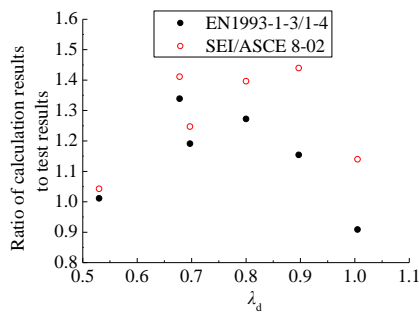
Comparisons of test results from this paper and calculation results obtained from effective width method

Number	λ_d	Test		European Code			American Specification		
		Eccentricity (mm)	P_T (kN)	P_{EC3} (kN)	DEV_T (%)	P_{EC3}/P_T	P_{ASCE} (kN)	DEV_T (%)	P_{ASCE}/P_T
SPZ-1	1.005	0.41	102.89	100.28	-2.54	0.97	117.29	14.00	1.14
SPZ-2	0.800	0.82	150.81	199.94	32.58	1.33	210.56	39.62	1.40
SPZ-3	0.897	2.47	81.53	102.09	25.22	1.25	117.35	43.94	1.44
SPZ-4	0.697	1.64	151.02	186.63	23.58	1.24	188.37	24.73	1.25
SPZ-5	0.678	2.01	62.76	87.26	39.03	1.39	88.57	41.12	1.41
SPZ-6	0.530	0.49	130.24	135.82	4.28	1.04	135.82	4.28	1.04
Average					20.36	1.20	Average	27.95	1.28

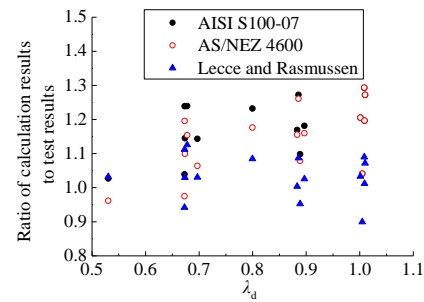
Table 10

Comparisons of test results from this paper and calculation results obtained from direct strength method

Number	λ_d	Test		North American Specification			Australia Specification			Lecce and Rasmussen's method		
		Eccentricity (mm)	P_T (kN)	P_{AISI} (kN)	P_{AISI}/P_T	DEV_T (%)	P_{AS} (kN)	P_{AS}/P_T	DEV_T (%)	P_{LR} (kN)	P_{LR}/P_T	DEV_T (%)
SPZ-1	1.005	0.41	102.89	107.08	1.04	4.07	107.11	1.04	4.10	92.53	0.90	-10.07
SPZ-2	0.800	0.82	150.81	185.81	1.23	23.21	177.43	1.18	17.65	163.60	1.08	8.48
SPZ-3	0.897	2.47	81.53	96.34	1.18	18.17	94.57	1.16	15.99	83.62	1.03	2.56
SPZ-4	0.697	1.64	151.02	172.64	1.14	14.32	160.69	1.06	6.40	155.62	1.03	3.04
SPZ-5	0.678	2.01	62.76	77.77	1.24	23.91	72.41	1.15	15.38	70.64	1.13	12.55
SPZ-6	0.530	0.49	130.24	133.74	1.03	2.69	125.23	0.96	-3.85	134.39	1.03	3.19
SPP-1-A	1.001	6.77	70.28	84.72	1.21	20.54	84.73	1.21	20.56	72.62	1.03	3.33
SPP-1-C	1.009	26.71	46.40	55.51	1.20	19.62	55.54	1.20	19.69	46.96	1.01	1.20
SPP-1-E	1.009	36.52	36.30	46.93	1.29	29.29	46.95	1.29	29.35	39.56	1.09	8.97
SPP-2-A	0.889	5.09	80.38	88.25	1.10	9.79	86.67	1.08	7.83	76.57	0.95	-4.75
SPP-2-C	0.883	22.16	47.60	55.67	1.17	16.95	54.99	1.16	15.53	47.78	1.00	0.37
SPP-2-E	0.886	35.50	33.85	43.07	1.27	27.25	42.68	1.26	26.09	36.80	1.09	8.71
SPP-3-A	0.673	4.56	65.56	68.12	1.04	3.91	63.93	0.98	-2.48	61.75	0.94	-5.81
SPP-3-C	0.674	16.56	37.50	42.93	1.14	14.48	41.23	1.10	9.93	38.61	1.03	2.95
SPP-3-E	0.673	21.31	30.13	37.32	1.24	23.88	36.02	1.20	19.56	33.50	1.11	11.21
Average				1.168	17.80	Average	1.135	14.66	Average	1.03	3.63	



(a) Effective width method



(b) Direct strength method

Fig. 20 Ratios of calculation results to test results under different slenderness ratios

5. Conclusions

Experimental studies were performed on the lipped channel stainless steel columns under eccentric and concentric compression, and the test results were compared with the calculation results obtained by different design codes. It can be concluded as follows:

(1) The distortional buckling and distortional-overall interaction were observed in the members subjected to pure axial and positive eccentric compression, and the local buckling and local-overall interaction occurred in the columns under negative eccentric compression.

(2) For the specimens subjected to axial compression, the strain

distribution is uniform and almost horizontal at the initial loading period. With the increase of the test load, the strain in the middle web became lower while the strain at lip became higher.

(3) The strength of the specimens subjected to eccentric compression is gradually decreased with the increase of eccentricity, and the ductility of the specimens subjected to eccentric compression in the same direction is enhanced with the increase of eccentricity. For the eccentrically loaded columns in different directions, the ductility of the columns with positive load eccentricity is larger than that of the columns with negative load eccentricity.

(4) The calculation results obtained from EWM and DSM are higher than the experimental values. For lipped channel stainless steel columns, the DSM

can accurately predict the distortional buckling strength.

Acknowledgments

The writers are thankful to Prof. Benjamin W. Schafer and Dr. Shahabeddin Torabian at the Johns Hopkins University for offering ideas with

test rig. The research was sponsored by National Natural Science Foundation of China (No. 51878146 and No. 51378105), and National Key Research and Development Program of China (No. 2017YFC0703802). The authors also appreciate the financial supports from High level talents of "six talent peaks" in Jiangsu Province (No. JZ-001) and Qing Lan Project of Jiangsu Province (2016).

References

- [1] Waller G. and Cochrane D.J., "Stainless steel for durability, fire-resistance and safety", *Architecture Technique*, 9, 254-257, 2011.
- [2] Rasmussen K.J.R. and Hancock G.J., "Design of cold-formed stainless steel tubular members. I: Column", *Journal of Structural Engineering*, 119(8), 2349-2367, 1993.
- [3] Van den Berg G.J., "The effect of the non-linear stress-strain behaviour of stainless steel on member capacity", *Journal of Constructional Steel Research*, 54(1), 135-160, 2000.
- [4] Kwon Y.B. and Hancock G.J., "Tests of cold-formed channels with local and distortional buckling", *Journal of Structural Engineering*, 118(7), 1786-1803, 1992.
- [5] Yang D. and Hancock G.J., "Compression tests of high strength steel channel columns with interaction between local and distortional buckling", *American Society of Civil Engineers*, 130(12), 1954-1963, 2004.
- [6] Tang J. and Young B., "Column tests of cold-formed steel channels with complex stiffeners", *Journal of Structural Engineering*, 128(6), 737-745, 2002.
- [7] Tang J. and Young B., "Compression tests of channels with inclined simple edge stiffeners", *Journal of Structural Engineering*, 129(10), 1403-1411, 2002.
- [8] Schafer B.W., "Distortional buckling of cold-formed steel columns", Final Report to the American Iron and Steel Institute, Washington (DC), 2000.
- [9] Schafer B.W., "Local, distortional, and Euler buckling of thin-walled columns", *Journal of Structural Engineering*, 128(3), 289-299, 2002.
- [10] Yu C. and Schafer B.W., "Distortional buckling tests on cold-formed steel beams", *Journal of Structural Engineering*, ASCE, 132(4), 515-528, 2006.
- [11] Moen C.D. and Schafer B.W., "Experiments on cold-formed steel columns with holes", *Thin-Walled Structures*, 46(3), 1164-1182, 2008.
- [12] Becque J. and Rasmussen K.J.R., "Experimental investigation of local-overall interaction buckling of stainless steel lipped channel columns", *Journal of Constructional Steel Research*, 65(8-9), 1677-1684, 2009.
- [13] Becque J. and Rasmussen K.J.R., "Numerical investigation of local-overall interaction buckling of stainless steel lipped channel columns", *Journal of Constructional Steel Research*, 65(8-9), 1685-1693, 2009.
- [14] Becque J. and Rasmussen K.J.R., "Experimental investigation of the interaction of local and overall buckling of stainless steel I-columns", *Journal of Structural Engineering*, ASCE, 135(11), 1340-1348, 2009.
- [15] Becque J. and Rasmussen K.J.R., "Numerical investigation of the interaction of local and overall buckling of stainless steel I-columns", *Journal of Structural Engineering*, ASCE, 135(11), 1349-1356, 2009.
- [16] Fan S.G., Liu F., Zheng B.F., Shu G.P. and Tao Y.L., "Experimental study on bearing capacity of stainless steel lipped C section stub columns", *Thin-Walled Structures*, 83, 70-84, 2014.
- [17] Fan S.G., Tao Y.L., Zheng B.F. and Liu F., "Capacity of stainless steel lipped Channel stub column under axial compression", *Journal of Constructional Steel Research*, 103(12), 251-263, 2014.
- [18] Fan S.G., Zheng B.F., Liu M.J., Liu F. and Tao Y.L., "Direct strength method of capacity of stainless steel lipped C section stub columns", *Journal of Southeast University (Natural Science Edition)*, 44(6), 1246-1253, 2014.
- [19] Liu F., Theoretical and experimental investigations on the method of effective section of stainless steel lipped C stub columns, Master Thesis, School of Civil Engineering, Southeast University, 2012.
- [20] Rossi B., Jaspart J.P. and Rasmussen K.J.R., "Combined distortional and overall flexural-torsional buckling of cold-formed stainless steel sections: Experimental investigations", *Journal of Structural Engineering*, ASCE, 136(4), 354-360, 2010.
- [21] Rossi B., Jaspart J.P. and Rasmussen K.J.R., "Combined distortional and overall flexural-torsional buckling of cold-formed stainless steel sections: Design", *Journal of Structural Engineering*, ASCE, 136(4), 361-369, 2010.
- [22] Lecce M., Distortional buckling of stainless steel sections, PhD Thesis, University of Sydney, 2006.
- [23] Lecce M. and Rasmussen K.J.R., "Distortional buckling of cold-formed stainless steel sections: Experimental investigation", *Journal of Structural Engineering*, ASCE, 132(4), 497-504, 2006.
- [24] Lecce M. and Rasmussen K.J.R., "Distortional buckling of cold-formed stainless steel sections: Finite element modeling and design", *Journal of Structural Engineering*, ASCE, 132(4), 505-514, 2006.
- [25] ASCE, Specification for the Design of Cold-formed Stainless Steel Structural Members, American Society of Civil Engineers, SEI/ASCE8-90, Reston, Virginia, 2002.
- [26] EC3, Eurocode 3: Design of steel structures Part 1.4: General rules—supplementary rules for stainless steels, European Committee for Standardization, EN 1993-1-4, CEN, Brussels, 2006.
- [27] AISI, North American Specification for the design of cold formed steel structures: Appendix 1: Design of cold-formed steel structural members using the direct strength method, American Iron and Steel Institute, Washington (DC), 2004.
- [28] Australian/New Zealand Standard, Cold-formed steel structures, AS/NZS4600, Sydney, 2005.
- [29] Gardner L., A new approach to stainless steel structural design, PhD Thesis, Department of Civil and Environmental Engineering, Imperial College, London, 2002.
- [30] Li Z. and Schafer B.W., "Buckling analysis of cold-formed steel members with general boundary conditions using CUFSM: conventional and constrained finite strip methods", *Proceedings of the 20th International conference: Special Conference on Cold-Formed Steel Structures*, St. Louis, 2010.
- [31] National Standard of the People's Republic of China, Technical code of cold-formed thin-wall steel structures, GB50018-2002, Beijing, China planning press, 2002.

EXPERIMENTAL EVALUATION OF THE FULL-RANGE BEHAVIOUR OF STEEL BEAM-TO-COLUMN CONNECTIONS

Shen Yan ^{1*}, Kim J.R. Rasmussen ¹, Lu-li Jiang ¹, Chen Zhu ¹ and Hao Zhang ¹

¹ The University of Sydney, Sydney, Australia

* (Corresponding author: E-mail: shen.yan@sydney.edu.au)

ABSTRACT

The paper summarises recent experimental research undertaken at the University of Sydney on determining the full-range behaviour of steel beam-to-column connections. Three series of tests were conducted on three different types of connections including bolted extended end-plate connections, top-and-seat angle connections and double web angle connections. The tests were continued well into the post-ultimate range until complete failure of the connection, obtaining the connection's full-range behaviour comprising the initial linear response, non-linear behaviour resulting from gradual yielding of connection components, ultimate state, and post-ultimate softening and fracture behaviour. The failure modes were observed and analysed for the tested connection types. Moreover, for the top-and-seat angle connections and double web angle connections, multiple tests were conducted on nominally identical connections to examine the variability of the connection behaviour, which stems from the random variation in geometric and material properties.

ARTICLE HISTORY

Received: 8 November 2019
Revised: 1 February 2020
Accepted: 1 February 2020

KEYWORDS

Bolted end-plate connection;
Top-and-seat angle connection;
Web angle connection;
Experiments;
Statistical data;
Full-range behaviour

Copyright © 2020 by The Hong Kong Institute of Steel Construction. All rights reserved.

1. Introduction

Seeing the semi-rigidity of joints affects the strength and serviceability of unbraced steel frames, a large number of studies have been carried out to investigate the semi-rigid behaviour of different types of beam-to-column joints, including bolted end-plate connections [1-3], top-and-seat angle connections [4-6], web angle connections [7-9], and other connection types [10-12]. Based on these studies, connection models have been proposed aimed at predicting the connection behaviour [13-15], notably the Component Method now implemented in Eurocode 3 [16].

The above many studies, especially the experimental studies, primarily focused on the initial stiffness and inelastic behaviour under small joint rotation, with little attention paid to the ultimate limit state, failure mode and post-ultimate response. The post-ultimate response may be of less interest in structural design against ordinary loads, where the structural members and connections primarily undergo elastic deformation, but is very important in structural design against loads induced by extreme events such as terrorist attacks. Moreover, advances in computing power and analysis software over the last decade have made it possible to perform structural design by Geometric and Material Nonlinear Analysis with Imperfections (GMNIA), or “advanced” analysis, and the understanding of the full-range performance of joints is indispensable in such structural designs.

Therefore, research programs were undertaken recently at the University of Sydney aiming at determining the full-range behaviour of various types of steel beam-to-column joints [17-20]. This paper summarises the experimental studies. Three types of steel connections were tested, including bolted extended end-plate (EP) connections, top-and-seat angle (TSA) connections and double web angle (WA) connections. The connections were tested well into the post-ultimate range until their complete failure, and thus the failure modes and full-range connection behaviour could be examined. The connections were subjected to a variety of load combinations, including major-axis bending, combined bending and axial force and bi-axial bending. Moreover, for the TSA and WA connections, multiple tests were conducted on nominally identical connections so as to investigate the variability of joint properties, e.g. stiffness, resistance and ductility, due to the variable geometric and material properties and the random variations in fabrication.

2. Experimental program

2.1. General

Table 1 summarises the experimental program which comprised 49 tests, including tests on 13 EP connections (Nos. 1–13 in Table 1), 18 TSA connections (Nos. 14–31) and 18 WA connections (Nos. 32–49).

The EP connections featured two different geometric configurations, differing in the thickness of the end-plate, which was 10 mm for the EP10 series

connections (Nos. 1–7 in Table 1) and 20 mm for the EP20 series connections (Nos. 8–13 in Table 1). All EP20 connections had backing plates to strengthen

Table 1
Summary of connections^a.

No.	Designation	Connection [*]	Loading [#]
1	EP10	10-EP, no BP	B
2	EP10BP	10-EP, BP	B
3	EP10_TS	10-EP, no BP	B & small T
4	EP10_TL	10-EP, no BP	B & large T
5	EP10_BS	10-EP, no BP	B & small MB
6	EP10_BL	10-EP, no BP	B & large MB
7	EP10_M	10-EP, no BP	MB
8	EP20BP	20-EP, BP	B
9	EP20BP_CS	20-EP, BP	B & small C
10	EP20BP_CL	20-EP, BP	B & large C
11	EP20BP_BS	20-EP, BP	B & small MB
12	EP20BP_BL	20-EP, BP	B & large MB
13	EP20BP_M	20-EP, BP	MB
14–18	TSA360-1~5	360UB 56.7	B
19–20	TSA360_T-1~2	360UB 56.7	B & T
21–22	TSA360_C-1~2	360UB 56.7	B & C
23–27	TSA530-1~5	530UB 92.4	B
28–29	TSA530_T-1~2	530UB 92.4	B & T
30–31	TSA530_C-1~2	530UB 92.4	B & C
32–36	WA360-1~5	360UB 56.7	B
37–38	WA360_T-1~2	360UB 56.7	B & T
39–40	WA360_C-1~2	360UB 56.7	B & C
41–45	WA460_1~5	460UB 82.1	B
46–47	WA460_T-1~2	460UB 82.1	B & T
48–49	WA460_C-1~2	460UB 82.1	B & C

^a More details of specimens and results refer to [18–20] (EP – [18], TSA – [19], WA – [20]);

^{*} 10-EP = 10-mm end-plate, 20-EP = 20-mm end-plate, BP = backing plate;

[#] B = major-axis bending, T = tension, C = compression, MB = minor-axis bending;

the end-plate, while all EP10 connections had no backing plates except for one, i.e. EP10BP, which investigated the effect of backing plates on the end-plate bending behaviour. For each connection series, four different load combinations were applied, including major-axis bending, combined bending and axial force, bi-axial bending and minor-axis bending, as shown in Table 1.

The TSA connections featured two different geometric configurations with the difference being the beam section, which was 360UB 56.7 for the TSA360 series connections (Nos. 14–22 in Table 1) and 530UB 92.4 for the TSA530 series connections (Nos. 23–31 in Table 1). Multiple tests were carried out on nominally identical specimens, and three load combinations were considered. For each connection series, five nominally identical specimens were subjected to bending, two were subjected to combined bending and axial tension, and two were subjected to combined bending and axial compression, as shown in Table 1.

The WA connections had two different geometric configurations, featuring difference in the beam section, which was 360UB 56.7 for the TSA360 series connections (Nos. 32–40 in Table 1) and 530UB 92.4 for the TSA 530 series connections (Nos. 41–49 in Table 1). As a result of the different beam sections, different numbers of bolt rows were used to connect the double web angle cleats to the beam web and column flange. The TSA360 and TSA530 connections had three and five bolt rows, respectively. The WA connection tests were similar to the TSA connection tests in terms of load combinations and the number of tests for each load combination, as shown in Table 1.

2.2. Specimen details

Figure 1 shows the dimensions of the tested connections. It is noted that the TSA530 connections had larger beam size than the TSA360 connections, which led to longer flange cleats in the TSA530 connections, as shown in Fig. 1(b). Similarly, the larger beam size in the WA460 connections compared to the WA360 connections resulted in longer web angle cleats and more bolt rows, as depicted in Fig. 1(c).

All EP connections were manufactured from Grade 350 steel to AS/NZS 3679.1 [21], while all TSA and WA connections were manufactured from Grade 300 steel. The material properties of the sections, including the end-plates, the angle cleats, as well as the beams and columns, were obtained from coupon tests and are summarised in Table 2. In the EP connections, the end-plate was welded to the beam end with full strength 45° continuous fillet welds, using manual metal arc welding with E48/W50X welding rods.

Table 2
Mechanical properties of materials.

Section	Young's Modulus (GPa)	Yield stress (MPa)	Ultimate strength (MPa)	Uniform elongation [#]	Total elongation
310UB 46.2	207	353	505	0.18	0.26
310UC 96.8	207	382	498	0.20	0.31
250UC 89.5 flange	210	276	448	0.23	0.40
250UC 89.5 web	209	335	476	0.21	0.33
360UB 56.7 flange	201	306	479	0.21	0.35
360UB 56.7 web	210	336	476	0.21	0.33
530UB92.4 flange	203	294	452	0.22	0.37
460 UB 82.1 web	200	347	477	0.20	0.34
10-mm end-plate	205	425	567	0.17	0.25
20-mm end-plate	204	355	503	0.18	0.26
125x125x8EA	205	322	483	0.19	0.28
100x100x8EA	209	308	444	0.21	0.31

[#] Uniform elongation = elongation corresponding to the ultimate strength

2.3. Test setup

All connection types were tested using essentially the same test set-up which was constructed with several movable rig parts in order to accommodate a variety of load combinations, as shown in Fig. 2. The column ends were connected to the supports using pins, with one end fixed against displacements while the other end capable of moving in the direction of the column centreline, ensuring a simply supported condition for the column. The beam was loaded through a loading arm using a hydraulic jack installed on a stiff reaction frame.

For bending tests, the supports had the same height, and thus the beam was in the vertical direction and perpendicular to the loading arm, as depicted in Fig.

2(a). For combined bending and axial force tests, the heights of the supports were altered, introducing an angle (θ_1) between the loading arm and the direction perpendicular to the axis of the beam, as depicted in Fig. 2(b). This set-up generated an axial load in the beam in addition to the bending moment. By adjusting the heights of the supports and thereby changing the angle θ_1 , connections subjected to same bending moment could have different axial loads applied simultaneously. For bi-axial bending tests, the specimen was rotated about the centerline of the beam to create an angle (θ_2) between the loading arm and the major axis bending plane of the beam, as shown in Fig. 2(c). Similarly, different ratios between the major-axis and minor-axis bending moments were achievable by adjusting the angle θ_2 . When θ_2 equaled 90°, the loading direction was along the minor-axis of the beam and the connection was subjected to minor-axis bending.

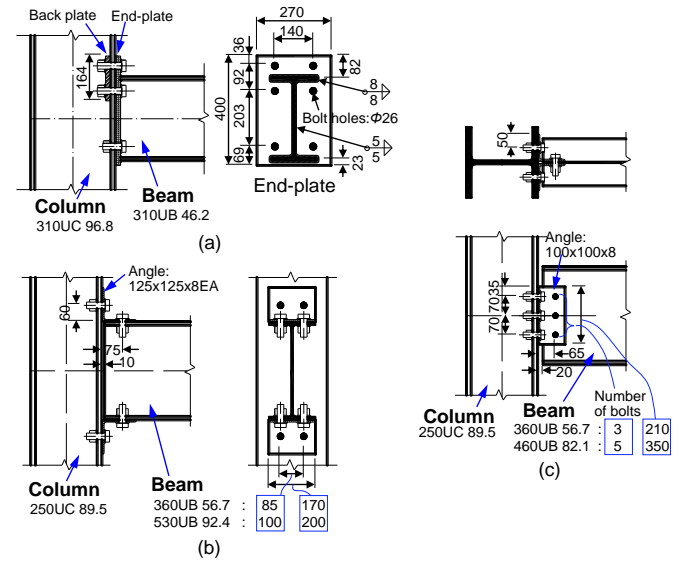


Fig. 1 Geometry of specimens (all dimensions in mm). (a) Bolted extended end-plate connections; (b) top-and-seat angle connections; (c) double web angle connections.

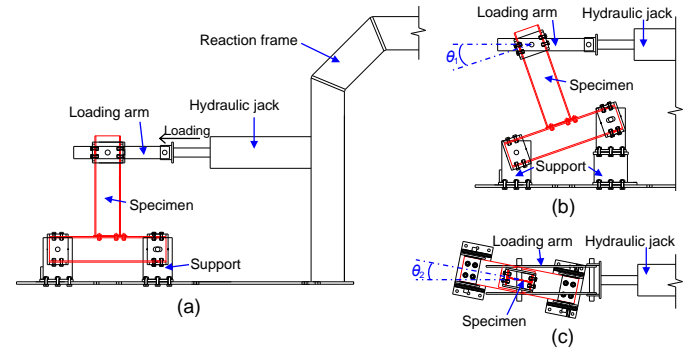


Fig. 2 Test setup. (a) Bending tests; (b) combined bending and axial force tests; (c) bi-axial bending tests, and minor-axis bending tests.

2.4. Instrumentation and test procedure

All tests were instrumented with displacement transducers and inclinometers. All specimens were loaded using a servo-controlled hydraulic jack with a displacement rate set at 1 mm/min, and all data were recorded at 1 sec intervals. Using the measurements from the load cell, transducers and inclinometers, the bending moment and axial force applied to the connection were calculated, as was the rotation of the connection, which is defined as the relative rotation between the centerlines of the column and the beam. The detailed arrangement of the instrumentation and the equations used for calculating the moment, force and rotation can be found in [18–20].

Although load was applied slowly, the effect of strain rate on material strength is non-negligible and needs to be eliminated. Therefore, during the tests, the loading was paused for 2 mins every 10–20 mins in order to acquire the static resistance. The raw data were processed to obtain smooth continuous curves through the static resistance loading points. An example of the data processing can be found in [18].

3. Experimental results for bolted end-plate connections

3.1. EP10 series tests

Figure 3 presents the bending moment versus joint rotation curves of all EP10 series connections, in which the bending moment refers to the minor-axis bending moment for EP10_M, and to the major-axis bending moment for all other connections. Table 3 summarises the experimental results.

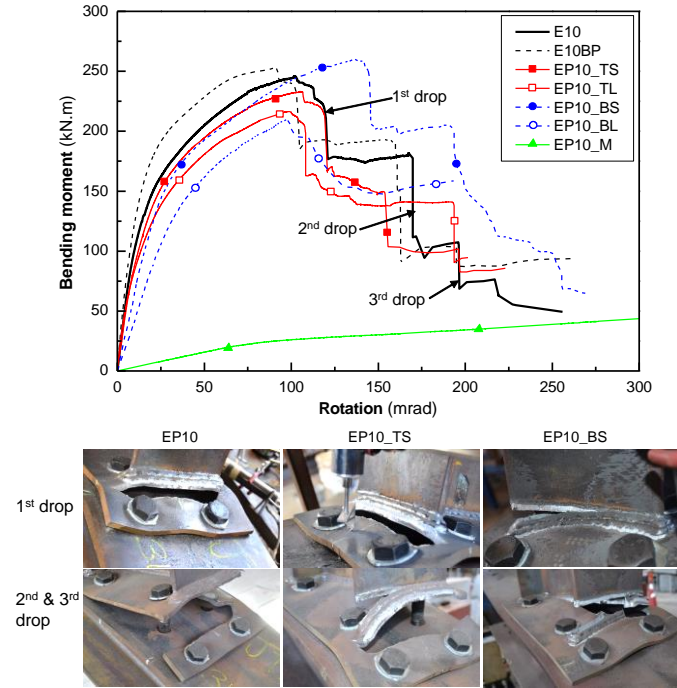


Fig. 3 Test results for EP10 series connections.

In EP10_M, which was subjected to minor-axis bending, the major source of deformation was observed to be the column flange twisting. The corresponding deformation capacity was extensive, and the connection performed essentially linearly under large joint rotation, as shown in Fig. 3. The connection did not reach its ultimate resistance under a rotation up to 0.45 rad, at which the test was terminated.

For the other connections, the main applied action was the major-axis bending moment. These connections had the same failure mode, i.e. the end-plate fracture (EPF) failure mode, which featured crack initiation and propagation in the end-plate. Connection EP10 was the baseline specimen, so its behaviour is described in detail herein.

Connection EP10 had an initial linear response followed by a nonlinear response caused by the gradual yielding of the connection components, the

end-plate in particular, as shown in Fig. 3. Before reaching the ultimate resistance, two cracks initiated in the heat affected zone of the weld connecting the beam flange to the end-plate. The crack initiation locations were aligned with the two bolts in the extended part of the end-plate. The two cracks progressively grew wider and merged, causing the connection to reach its ultimate resistance and the subsequent first drop in bending resistance, as shown in Fig. 3. The merged crack grew around the tip of the beam flange on one side, and towards the edge of the end-plate on the other side. Eventually the propagated crack caused the extended part of the end-plate to tear off the connection, resulting in the second drop in resistance. The crack propagation continued along the weld of the inside edge of the tension flange and eventually along the weld of the web plate, leading to unloading of the inner bolt on this side. This increased the tensile force in the inner bolt on the other side, thereby causing the bolt to fracture. This marked the third abrupt drop in resistance on the moment-rotation curve and the complete failure of the connection, as shown in Fig. 3.

Connections EP10_TS and EP10_TL received additional axial tensile force, which led to smaller resistance in the gradual yielding range and smaller ultimate resistance in comparison with EP10. The additional tensile load, however, did not change the failure mode of the connections, which was characterised by a three-stage post-ultimate failure process, as shown in Fig. 3.

Connections EP10_BS and EP10BL were subjected to bi-axial bending. The additional minor-axis bending reduced both the initial stiffness and the major-axis strength over the gradual yielding range. The ultimate major-axis bending resistance of EP10_BL was 14.7% smaller than that of EP10, while the bending resistance of EP10_BS was unexpectedly increased by 5.7%. The increase in strength may be caused by random variations introduced during fabrication, including better-than-expected welding quality in this case.

Connection EP10BP used backing plates to strengthen the column flange. The backing plates increased the stiffness and the strength of the connection, but resulted in a reduction in the rotation capacity, as shown in Fig. 3. In the post-ultimate range, EP10BP experienced sequential abrupt reductions in strength similar to EP10 due to the initiation and propagation of cracks.

3.2. EP20 series tests

Figure 4 presents the bending moment versus joint rotation curves of all EP20 series connections, in which the bending moment refers to the minor-axis bending moment for EP20BP_M, and to the major-axis bending moment for all other connections. Table 4 summarises the experimental results.

The minor-axis bending connection, EP20BP_M, behaved similarly to EP10_M, with the major deformation arising from column flange twisting. The connection had an essentially linear response under large joint rotations, as shown in Fig. 4, and did not reach its ultimate resistance under a rotation up to 0.45 rad, at which the test was terminated.

For the other connections, the main action applied was the major-axis bending moment. These connections had the same failure mode, i.e. the column web buckling (CWB) failure mode. Connection EP20BP was the baseline specimen, so its behaviour is described in detail herein.

EP20BP had a 20-mm thick end-plate as well as backing plates, which greatly strengthened its performance in the tension zone. Consequently, S20BP failed in the compression zone due to inelastic buckling of the column web,

Table 3

Summary of EP10 series test results. [18]

Designation	Initial stiffness (kN·m/rad)	Ultimate resistance			Joint rotation at ultimate resistance (rad)	Joint ductility (rad)	Failure mode*
		Major-axis moment (kN·m)	Minor-axis moment (kN·m)	Axial force# (kN)			
EP10	11706	245	–	–	0.103	0.256	EPF
EP10BP	14890	252	–	–	0.092	0.258	EPF
EP10_TS	9976	233	–	88	0.106	0.223	EPF
EP10_TL	10816	216	–	140	0.099	0.201	EPF
EP10_BS	6452	259	50	–	0.138	0.270	EPF
EP10_BL	4050	209	93	–	0.098	0.192##	EPF
EP10_M	316	–	–	–	–	0.45##	EPF

* EPF = End-plate fracture

Positive values indicate tension

Loading was terminated before complete failure of the connection; this value of the last recorded value

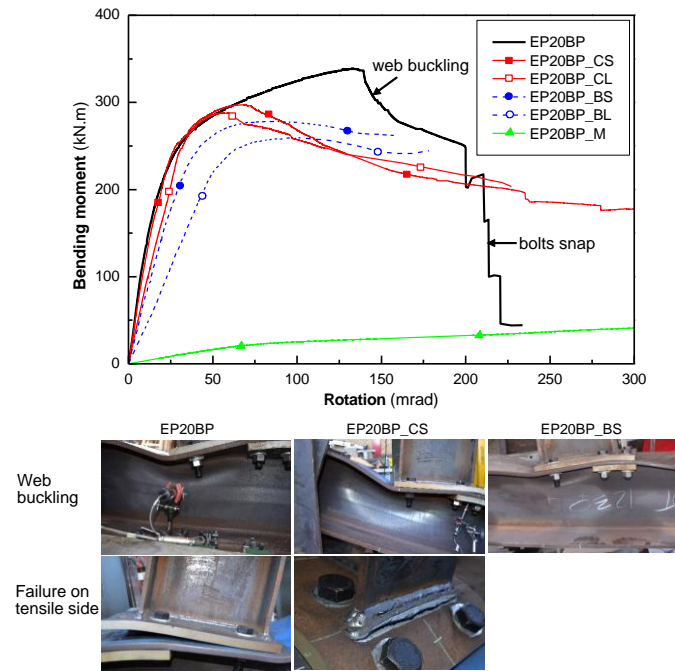


Fig. 4 Test results for EP20 series connections.

instead of in the tension zone as occurred in the EP10 series connections. The web buckling appeared when the connection approached its ultimate resistance, and triggered rapidly growing web out-of-plane deflections associated with a gradual reduction in resistance. The complete failure of the connection was caused by the fracture of the tensile bolts on the tension side, as shown in Fig. 4. The ultimate strength and corresponding rotation were significantly higher than those of the EP10 series connections.

Connections EP20BP_CS and EP20BP_CL received additional axial compression, and failed in the same CWB failure mode as EP20BP. The compressive axial load precipitated the column web buckling, and therefore both connections reached their ultimate bending resistance significantly earlier than that of EP20BP. The complete failure of EP20BP_CS was due to the formation of a crack in the HAZ along the tension flange, while no component failed on the tension side in the EP20BP_CL test.

Connections EP20BP_BS and EP20BP_BL were subjected to bi-axial bending, and failed in the CWB failure mode as the other EP20 series connections did. The additional minor-axis bending reduced the initial stiffness, the ultimate strength as well as the rotation corresponding to the ultimate major-axis bending moment, as shown in Fig. 4. For both tests, no component failure was observed on the tensile side of the connections.

3.3. Failure mechanism

The test results of the EP10 series connections showed that the end-plate connections with relatively thin end-plates were prone to failing in an end-plate fracture (EPF) failure mode when subjected to major-axis bending, whether or

not additional axial load or additional minor-axis bending moment was applied.

Figure 5 shows a typical example of the failure process, which can be described by four stages, with the last three stages giving rise to the three drops observed on the moment-rotation curve. After the first, second and third drops, the connection preserved around 75%, around 43%, and below 40% of its ultimate bending strength, respectively.

The end-plate connections with a relatively thick end-plate failed as a result of column web buckling (CWB), as observed in the tests of the EP20 series connections. This failure mode featured a gradual resistance reduction in the post-ultimate range. Load combinations affected the resistance reduction rate, but all connections preserved over 70% of their ultimate strengths under large rotations up to 0.20 rad. The complete failure of the connections was caused by the fracture on the tension side, either tensile bolt fracture or crack propagation in the heat affected zone along the welds.

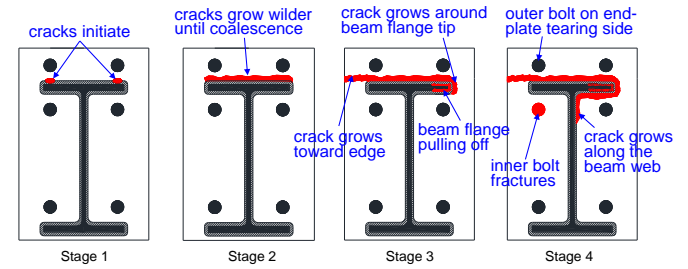


Fig. 5 End-plate fracture failure mode.

4. Experimental results for top-and-seat angle connections

4.1. TSA360 series tests

Figure 6 presents the bending moment versus joint rotation curves of all TSA360 series connections and pictures showing the connection failure mode. All connections behaved similarly and had the same failure mode, i.e. top angle fracture (TAF), but the applied axial force in addition to the major-axis bending moment affected the ultimate bending resistance and the corresponding joint rotation. Table 5 summarises the experimental results.

For TSA360-1, the initial moment-rotation response was stiff and largely linear, followed by a nonlinear response due to the gradual yielding of the joint components, the top flange cleat in particular. The bolts connecting the angle cleats slipped during the transition from the linear to the nonlinear range, forming a plateau on the moment-rotation curve, as shown in Fig. 6. Gradually, plastic hinges formed on the top flange cleat at multiple cross-sections, including the two cross-sections where the bolts connected the column leg and the beam leg, as well as the two cross-sections near the root of the cleat where its thickness changed. This constituted a major difference from the deformation pattern specified in Eurocode 3, in which the top flange cleat is modelled as an equivalent T-stub, implying that the top flange cleat undergoes a purely horizontal displacement without rotation of the beam leg and thus does not develop plastic hinges in the beam leg. As the load approached the ultimate strength of the connection, on the top flange cleat, two cracks initiated at the surface of the column leg near the root of the cleat where the plastic hinge formed. The occurrence of the two cracks marked the ultimate bending

Table 4

Summary of EP20 series test results. [18]

Designation	Initial stiffness (kN·m/rad)	Ultimate resistance			Joint rotation at ultimate resistance (rad)	Joint ductility (rad)	Failure mode [*]
		Major-axis moment (kN·m)	Minor-axis moment (kN·m)	Axial force [#] (kN)			
EP20BP	13983	338	—	—	0.133	0.235	CWB
EP20BP_CS	12372	297	—	-66	0.067	0.487	CWB
EP20BP_CL	8652	288	—	-138	0.056	0.302	CWB
EP20BP_BS	7581	278	54	—	0.081	0.156 ^{##}	CWB
EP20BP_BL	4150	259	115	—	0.098	0.178 ^{##}	CWB
EP20BP_M	348	—	—	—	—	0.45 ^{##}	CWB

* CWB = Column web buckling

Negative values indicate tension

Loading was terminated before complete failure of the connection; this value of the last recorded value

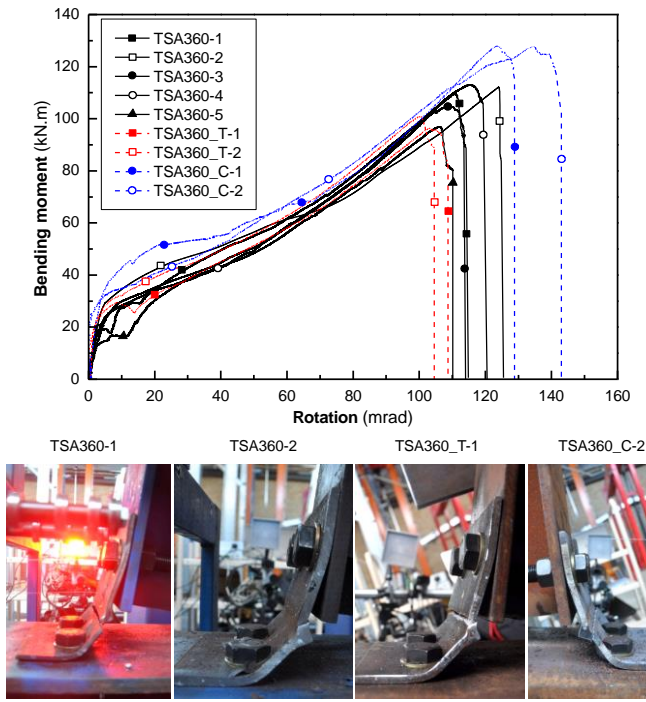


Fig. 6 Test results for TSA360 series connections.

resistance of the connection. The cracks were initially aligned with the two bolt lines, and subsequently propagated quickly to the edges of the angle cleat, as well as towards to each other. The propagation of the cracks led to a very quick reduction in the bending resistance of the connection. When the two cracks merged to form a single continuous crack, the connection failed with the load dropping instantly to zero, as shown in Fig. 6.

The other nominally identical bending connections had the same deformation pattern and failure mode as TSA360-1, but showed certain variabilities in response, demonstrating the effect of inherent variations in geometric and material properties. The CoVs of the initial stiffness, ultimate bending resistance, joint rotation corresponding to the ultimate bending resistance, and ductility of joint were 0.173, 0.061, 0.062 and 0.053, respectively. The crack that occurred in the top flange cleat could form either in the beam leg or in the column leg, as shown in Fig. 6.

Applying an axial load in addition to the bending moment did not change the failure mode, but altered the ultimate strength and the corresponding rotation. The additional tensile force accelerated the failure of the top angle cleat, thereby reducing the ultimate bending resistance, the corresponding rotation, and the joint ductility, as shown in Fig. 6. On the other hand, the additional compressive force postponed the connection failure, thereby increasing the ultimate bending resistance, the corresponding rotation, and the joint ductility.

Table 5
Summary of TSA360 series test results. [19]

Designation	Initial stiffness (kN·m/rad)	Ultimate resistance		Joint rotation at ultimate resistance (rad)	Joint ductility (rad)	Failure mode*
		Bending moment (kN·m)	Axial force [#] (kN)			
TSA360-1	8670	109	11.5	0.111	0.115	TAF
TSA360-2	8390	112	13.0	0.124	0.126	TAF
TSA360-3	5390	105	11.7	0.109	0.114	TAF
TSA360-4	7320	113	13.5	0.116	0.120	TAF
TSA360-5	7850	96.9	10.3	0.106	0.110	TAF
TSA360_T-1	19300	96.4	31.9	0.103	0.109	TAF
TSA360_T-2	25000	101	34.1	0.101	0.104	TAF
TSA360_C-1	8150	128	-33.4	0.123	0.129	TAF
TSA360_C-2	21700	128	-32.5	0.135	0.143	TAF

* TAF = Top angle fracture

Positive values indicate tension; negative values indicate compression

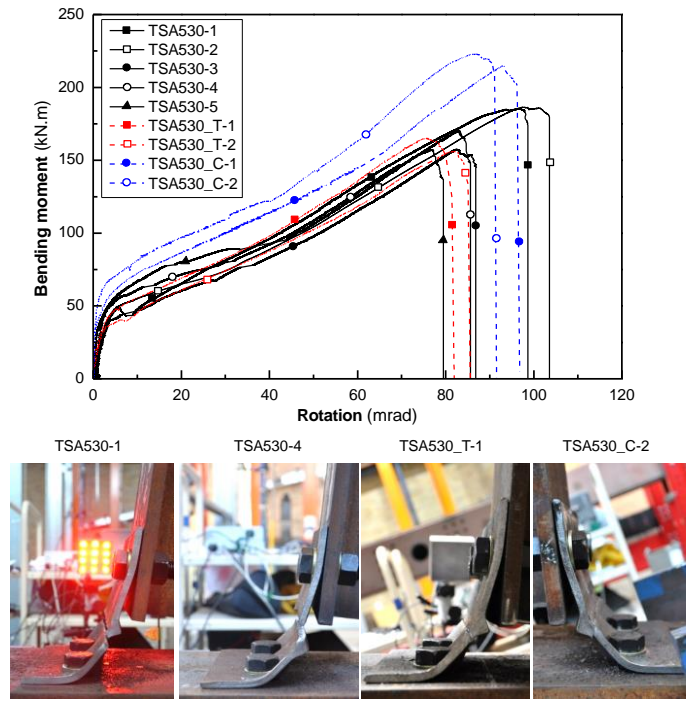


Fig. 7 Test results for TSA530 series connections.

4.2. TSA530 series tests

Figure 7 presents the bending moment versus joint rotation curves of all TSA530 series connections and pictures showing the connection failure mode. In general, the connections behaved similarly to the TSA360 series connections over the full loading range, and had the same failure mode, i.e. top angle fracture (TAF). Table 6 summarises the experimental results.

Each of the TSA530 bending connections showed an initial linear response, followed by a transient stage of bolt slip, which was more pronounced for some connections than others, and a stage featuring a nonlinear increase in bending resistance, as shown in Fig. 7. During the nonlinear stage, four plastic hinges formed in the top flange cleat, two in the column leg and two in the beam leg. All connections failed in the TAF mode. Similar to the TSA360 tests, the connection failure was caused by the initiation and propagation of a crack formed at one of the two plastic hinges near the root of the top flange cleat. The joint properties were also variable. The CoVs of the initial stiffness, ultimate strength and corresponding joint rotation, and joint ductility were 0.537, 0.087, 0.109 and 0.107, respectively. These CoVs were consistently larger than those for the TSA360 connections, indicating greater variation in the joint properties of the TSA530 connections.

The additional axial force in the beam affected the connection behaviour in the same way as it affected the TSA360 series connections. That is, the tensile

force accelerated the failure of the top angle cleat, thereby reducing the ultimate bending resistance, the corresponding joint rotation, and the joint ductility, while the compressive force was beneficial in terms of increasing the strength and ductility of the joints. The additional axial force did not change the failure mode. Hence, the connections subjected to combined bending and axial force also failed in the TAF mode, with the crack forming either in the column or beam leg of the top flange cleat.

4.3. Failure mechanism

Figure 8 schematically illustrates the typical process of the crack initiation and propagation in the top angle fracture (TAF) failure mode. As shown in the figure, the cracks formed in the column leg of the top flange cleat near the root of the cleat where the plastic hinge developed, and propagated to the edges. It is noted that the cracks could also form in the beam leg, as observed in some of the tests.

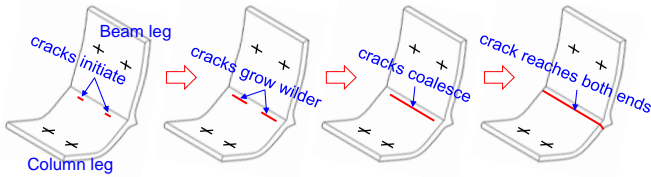


Fig. 8 Top angle fracture failure mode.

5. Experimental results for double web angle connections

5.1. WA360 series tests

Figure 9 presents the bending moment versus joint rotation curves of all WA360 series connections and pictures showing the two failure modes observed in the tests. Table 7 summarises the experimental results.

The WA360-1 connection had a linear moment-rotation response with a relatively large stiffness in the initial stage, followed by a bolt slip stage which led to a plateau on the moment-rotation curve, as shown in Fig. 9. Henceforth, the top and bottom parts of the angle cleats transmitted tensile and compressive loads, respectively, through bearing of bolts, and the moment resistance of the joint increased significantly. Due to the yielding of the joint components, the joint stiffness gradually decreased until the joint rotation brought the compressive flange of the beam into contact with the face of the column flange. The contact made the beam bottom flange the new centre of compression, leading to an increase in the lever arm between the parts of the connection transferring compression and tension. After contact was established, the moment resistance and joint stiffness increased dramatically. As the joint approached its ultimate strength, a crack initiated near the root of each web angle cleat aligning with the top bolt row, and progressively propagated towards both edges of the cleat, causing a significant reduction in the moment resistance. This mode of failure is referred to as the web angle fracture (WAF) mode.

The other nominally identical bending connections behaved similarly to WA360-1, as demonstrated by the similar moment versus rotation curves,

featuring slip of bolts, contact between the beam bottom flange and the column flange, and the WAF failure mode. However, noticeable variations were observed in the joint properties. The CoVs of the initial stiffness, ultimate bending resistance, joint rotation corresponding to the ultimate resistance, and joint ductility were 0.194, 0.062, 0.082 and 0.152, respectively.

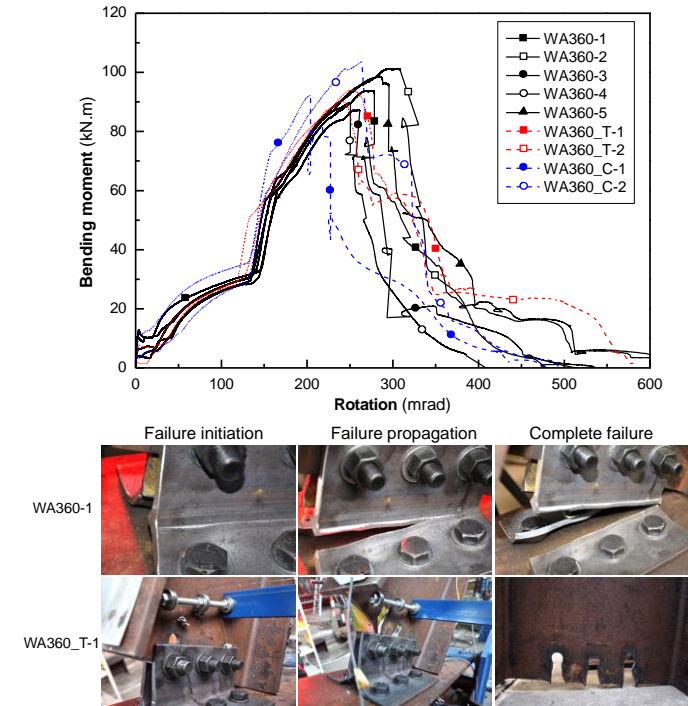


Fig. 9 Test results for WA360 series connections.

The combined bending and axial compression connections, i.e. WA360_C-1 and WA360_C-2, had full-range behaviour similar to that of the bending connections, and failed in the same WAF mode. The additional compressive force delayed the failure of connection on the tensile side, thereby increasing the ultimate bending resistance, as shown in Fig. 9.

The combined bending and axial tension connections, i.e. WA360_T-1 and WA360_T-2, also behaved similarly to the bending connections except for the failure mode. Instead of having fracture initiation and propagation in the web angle cleats, the connections failed as a result of the significant plastic bearing deformation of the beam web at the bolt rows, and the subsequent shear-out of the bolts. The bolt at the top bolt row sheared-out first, marking the ultimate resistance of the joint. This was followed by the consecutive shear-out of the bolts at the remaining bolt rows, which generated a series of drops of bending resistance in the moment-rotation curve, as shown in Fig. 9. This failure mode is referred to as the bolt shear-out (BSO) mode. The additional tensile force reduced the ultimate bending resistance and the corresponding joint rotation.

Table 6

Summary of TSA530 series test results. [19]

Designation	Initial stiffness (kN·m/rad)	Ultimate resistance		Joint rotation at ultimate resistance (rad)	Joint ductility (rad)	Failure mode*
		Bending moment (kN·m)	Axial force [#] (kN)			
TSA530-1	13300	185	20.9	0.0969	0.0987	TAF
TSA530-2	14900	187	21.5	0.0981	0.103	TAF
TSA530-3	15100	157	15.2	0.0822	0.0869	TAF
TSA530-4	37100	170	16.0	0.0828	0.0857	TAF
TSA530-5	38100	157	12.6	0.0768	0.0795	TAF
TSA530_T-1	13200	165	55.6	0.0754	0.0819	TAF
TSA530_T-2	13200	156	53.8	0.0820	0.0856	TAF
TSA530_C-1	66700	215	-61.1	0.0932	0.0968	TAF
TSA530_C-2	70200	223	-59.9	0.0867	0.0915	TAF

* TAF = Top angle fracture

[#] Positive values indicate tension; negative values indicate compression

5.2. WA460 series tests

Figure 10 presents the bending moment versus joint rotation curves of all WA460 series connections and pictures showing the connection failure process. There was only one failure mode for the WA460 series connections, i.e. the WAF mode. Table 8 summarises the experimental results.

In general, the bending connections WA460-1 to WA460-5 behaved similarly to the WA360 bending connections over the full loading range. The moment-rotation curves had an initial linear range, a near-plateau caused by the slip of bolts, a nonlinear range primarily associated with the gradual yielding of the web angle cleats, a hardening range after the beam bottom flange came into contact with the column flange, and a resistance reduction range due to the initiation and propagation of cracks in the angle cleats, as shown in Fig. 10. As a result of the greater number of bolt rows and the longer web angle cleats, the WA460 connections had significantly larger resistances than the WA360 connections. Variabilities in connection behaviour were observed in the nominally identical connections. The CoVs of the initial stiffness, ultimate bending resistance, joint rotation corresponding to the ultimate resistance, and joint ductility were 0.081, 0.033, 0.070 and 0.082, respectively. It is noted that the above CoVs were consistently smaller than those for the WA360 bending connections, implying comparatively smaller variation in the moment-rotation behaviour of the WA460 connections.

The combined bending and axial force connections, i.e., WA460_T-1 and WA460_T-2 subjected to combined bending and tension, and, WA460_C-1 and WA460_C-2 subjected to combined bending and compression, all behaved similarly to the bending connections, having moment-rotation curves with similar shapes as shown in Figs. 10, and sharing the same WAF failure mode. The additional compressive force in the WA460_C-1 and WA460_C-2 connections delayed the failure of the connection on the tensile side, thereby

increasing the ultimate bending resistance in comparison with the bending connections, as shown in Fig. 10. In the tests of the WA460_T-1 and WA460_T-

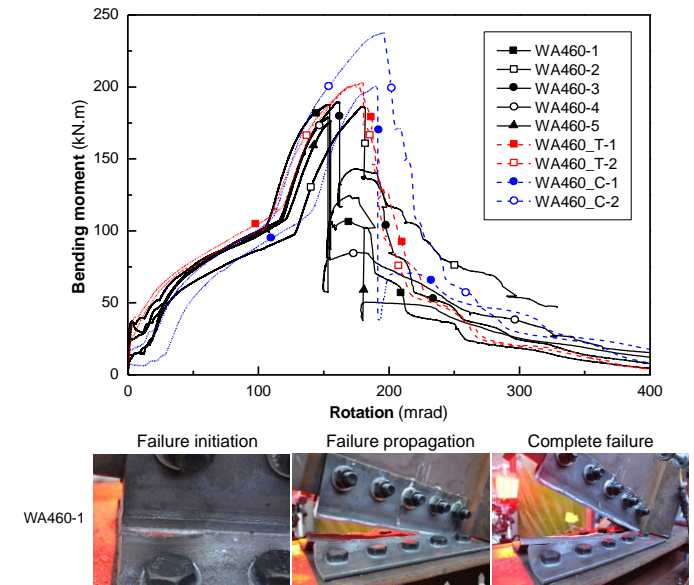


Fig. 10 Test results for WA460 series connections.

Table 7

Summary of WA360 series test results. [20]

Designation	Initial stiffness (kN·m/rad)	Ultimate resistance		Joint rotation at ultimate resistance (rad)	Joint ductility (rad)	Failure mode*
		Bending moment (kN·m)	Axial force [#] (kN)			
WA360-1	4550	93.7	20.6	0.277	0.500	WAF
WA360-2	2830	101	23.2	0.308	0.405	WAF
WA360-3	2970	87.3	18.6	0.261	0.438	WAF
WA360-4	3510	89.6	19.1	0.250	0.350	WAF
WA360-5	3630	98.6	22.9	0.287	0.511	WAF
WA360_T-1	3045	94.0	31.7	0.252	0.397 ^{##}	BSO
WA360_T-2	3211	90.3	30.6	0.239	0.551	BSO
WA360_C-1	4293	92.3	-18.8	0.215	0.377	WAF
WA360_C-2	4704	104	-19.9	0.275	0.408	WAF

* WAF = Web angle fracture; BSO = Bolt shear-out

Positive values indicate tension; negative values indicate compression

Loading was terminated when fracture in web angle propagated to the bottom bolt row; this rotation was the last recorded rotation

Table 8

Summary of WA460 series test results. [20]

Designation	Initial stiffness (kN·m/rad)	Ultimate resistance		Joint rotation at ultimate resistance (rad)	Joint ductility (rad)	Failure mode*
		Bending moment (kN·m)	Axial force [#] (kN)			
WA460-1	12000	188	26.7	0.154	0.288	WAF
WA460-2	9990	186	29.0	0.180	0.329 ^{##}	WAF
WA460-3	11900	190	27.0	0.161	0.326	WAF
WA460-4	11500	179	25.7	0.153	0.362	WAF
WA460-5	10400	176	23.6	0.155	0.343	WAF
WA460_T-1	10445	202	60.6	0.176	0.312	WAF
WA460_T-2	9047	203	62.7	0.180	0.296	WAF
WA460_C-1	10772	201	-45.3	0.203	0.390	WAF
WA460_C-2	12285	238	-50.6	0.216	0.361	WAF

* WAF = Web angle fracture

Positive values indicate tension; negative values indicate compression

Loading was terminated when fracture in web angle propagated to the bottom bolt row; this rotation was the last recorded rotation

2 connections, the additional tensile force also increased the ultimate bending resistance by about 10%. This was surprising as the additional tensile force was expected to accelerate the failure of the tensile part of the connection, leading to a lower ultimate strength. Further investigations involving finite element fracture simulations are needed in order to explain this result.

5.3. Failure mechanism

The tested double web angle connections showed two failure modes, i.e. the web angle fracture (WAF) mode as shown in Fig. 11 and the bolt shear-out (BSO) mode as shown in Fig. 12. Both failure modes were induced by the tensile load transferred through the tensile (top) part of the angles. The connection would fail in the mode associated with the lowest ultimate resistance.

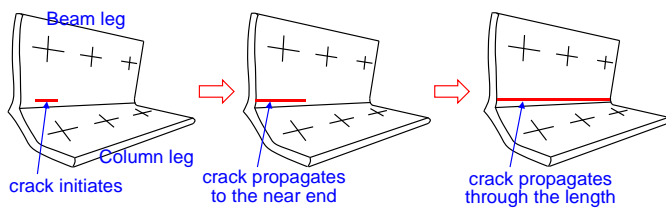


Fig. 11 Web angle fracture failure mode.

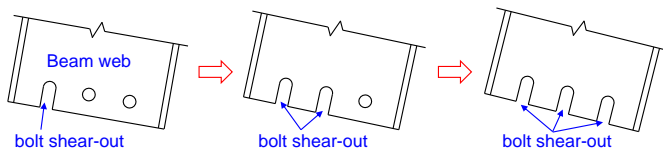


Fig. 12 Bolt shear-out failure mode.

The WAF failure mode dominated in the connections in which the web angle had a comparatively smaller resistance. In this failure mode, the crack occurred near the root of the angle cleat where the cleat thickness changed, which was similar to the TAF failure mode observed in the TSA series connections. But unlike in the TSA connections in which the crack could form either in the column leg or in the beam leg of the angle cleat, the crack in the

WA connections consistently formed in the beam leg, as shown in Fig. 11.

For the connections in which the bolts in bearing had smaller resistance than the web angle in bending, the BSO failure mode occurred, as shown in Fig. 12. Prior to the bolt shear-out, significant plastic bearing deformations developed at the edges of the bolt holes in the beam web.

6. Conclusions

This paper summarises recent experimental studies undertaken at the University of Sydney aiming at determining the full-range behaviour of three types of steel beam-to-column connections.

The experimental program comprised tests of 13 bolted extended end-plate (EP) connections, 18 top-and-seat angle (TSA) connections and 18 web angle (WA) connections. The connections were subjected to a variety of load combinations, including major-axis bending, combined bending and axial force, and bi-axial bending. Each connection was tested well into the post-ultimate range until complete failure, and thus the full-range behaviour of the connection was obtained, including the initial linear response, the non-linear behaviour resulting from the gradual yielding of the connection components, and the ultimate state and post-ultimate softening and fracture behaviour. Moreover, for the TSA and WA connections, multiple tests were conducted on nominally identical connections, so as to investigate the uncertainties in the full-range joint behaviour due to random variations in geometric and material properties.

The observed failure modes of the connections and experimental data defining the full-range moment-rotation curves are summarised. The tested EP10 connections showed the end-plate fracture failure mode featuring propagation of fracture along welds, while the tested EP20 connections failed in the column web buckling failure mode associated with a gradual resistance reduction in the post-ultimate range. The tested TSA connections failed in a top angle fracture failure mode, in which the fracture initiated and propagated quickly along the root of the cleat, leading to an instant drop of the bending resistance for the connections. The tested WA360 connections showed two failure modes, including the web angle fracture failure mode and the bolt shear-out failure mode. Both failure modes resulted from the tensile load transmitted through the top part of the angles. Similar ultimate bending resistances and post-ultimate responses were observed for the two failure modes. The WA460 connections all failed in the web angle fracture failure mode.

Acknowledgement

The work presented in this paper was funded by the Australian Research Council, Discovery Project DP150104873.

References

- [1] de Lima L.R.O., Simões da Silva L., da S. Vellasco P.C.G. and de Andrade S.A.L., "Experimental evaluation of extended endplate beam-to-column joints subjected to bending and axial force", *Engineering Structures*, 26 (10), 1333-1347, 2004.
- [2] Girão Coelho A.M., Bijlaard F.S.K. and Simões Da Silva L., "Experimental assessment of the ductility of extended end plate connections", *Engineering Structures*, 26, 1185-1206, 2004.
- [3] Cabrero J.M. and Bayo E., "The semi-rigid behaviour of three-dimensional steel beam-to-column joints subjected to proportional loading. Part I. Experimental evaluation", *Journal of Constructional Steel Research*, 63 (9), 1241-1253, 2007.
- [4] Stelmack T.W., Marley M.J. and Gerstle K.H., "Analysis and tests of flexibly connected steel frames", *Journal of Structural Engineering*, 112 (7), 1573-1588, 1986.
- [5] Pirmoz A., Khoei A.S., Mohammadrezapour E. and Daryan A.S., "Moment-rotation behavior of bolted top-seat angle connections", *Journal of Constructional Steel Research*, 65(4), 973-984, 2009.
- [6] Pirmoz A., Danesh F. and Farajkhah V., "The effect of axial beam force on moment-rotation curve of top and seat angles connections", *Structural Design of Tall and Special Buildings*, 20(7), 767-783, 2011.
- [7] Hong K., Yang J.G. and Lee S.K., "Moment-rotation behavior of double angle connections subjected to shear load", *Engineering Structures*, 24(1), 125-132, 2002.
- [8] Abolmaali A., Kukreti A.R. and Razavi, H., "Hysteresis behavior of semi-rigid double web angle steel connections", *Journal of Constructional Steel Research*, 59(8), 1057-1082, 2003.
- [9] Gong Y.L., "Single-angle all-bolted shear connection", *Journal of Constructional Steel Research*, 65(6), 1337-1345, 2009.
- [10] Asawasongkram N., Chomchuen P. and Premthamkorn P., "Development and application of a mechanical model of beam-to-column connections of steel storage racks", *Advanced Steel Construction*, 15(3), 297-305, 2019.
- [11] Zhang Y., Li Q., Huang W., Jiang K. and Sun Y., "Behavior of prefabricated beam-column connection with short strands in self-centering steel frame", *Advanced Steel Construction*, 15(2), 203-214, 2019.
- [12] Torbaghan M., Sohrabi M. and Kazemi H., "Investigating the behavior of specially prefabricated steel moment connection under cyclic loading", *Advanced Steel Construction*, 14(3), 412-423, 2018.
- [13] Simões da Silva L., Coelho A.G. and Lucena Neto E., "Equivalent post-buckling models for the flexural behaviour of steel connections", *Computers & Structures*, 77(6), 615-624, 2000.
- [14] Lee S.S. and Moon T.S., "Moment-rotation model of semi-rigid connections with angles", *Engineering Structures*, 24(2), 227-237, 2002.
- [15] Yang J.G. and Lee G.Y., "Analytical models for initial stiffness and ultimate moment of a double angle connection", *Engineering Structures*, 29(4), 542-551, 2007.
- [16] CEN (European Committee for Standardization), EN 1993-1-8, Eurocode 3: design of steel structures, Part 1-8: design of joints, European Committee for Standardization, Brussels, 2010.
- [17] Zhu C., Rasmussen K.J.R. and Yan S., "Generalised component model for structural steel joints", *Journal of Constructional Steel Research*, 153, 330-342, 2019.
- [18] Zhu C., Rasmussen K.J.R., Yan S. and Zhang H., "Experimental full-range behavior assessment of bolted moment end-plate connections", *Journal of Structural Engineering*, 145(8), 04019079, 2019.
- [19] Yan S., Jiang L., Rasmussen K.J.R. and Zhang H., "Full-range behaviour of top-and-seat angle connections", submitted to *Journal of Structural Engineering*.
- [20] Yan S., Jiang L., Rasmussen K.J.R., "Full-range behaviour of double web angle connections", *Journal of Constructional Steel Research*, 166, 105907, 2020.
- [21] Standards Australia, AS/NZS 3679.1, Structural steel Part 1: Hot-rolled bars and sections, Standards Australia, Sydney, Australia, 2010.

SEISMIC RESPONSES OF RC BRACED FRAMES WITH BUCKLING-RESTRAINED BRACES CONNECTED TO CORBELS

An-chin Wu¹, Keh-chyuan Tsai^{2,*}, Ting-li Lin³, Ching-yi Tsai⁴ and Kung-juin Wang⁵

¹ Associate researcher, National Center for Research on Earthquake Engineering, Taipei, Taiwan, China

² Professor, Department of Civil Engineering, National Taiwan University, Taipei, Taiwan, China

³ Research assistant, Department of Civil Engineering, National Taiwan University, Taipei, Taiwan, China

⁴ Post doctor, Department of Civil Engineering, National Taiwan University, Taipei, Taiwan, China

⁵ Technologist, Department of Civil Engineering, National Taiwan University, Taipei, Taiwan, China

*(Corresponding author: E-mail: ketsai@ntu.edu.tw)

ABSTRACT

The paper is a continuation of the investigation on a newly developed bracing system featured by the zigzag configured braced frame for reinforced concrete (RC) constructions. A 12-story RC frame equipped with buckling-restrained braces (BRBs) is investigated as a prototype building. The feasibility and performance of the proposed BRB-to-RC connection are investigated using a cyclic loading procedure on a full-scale beam-to-column sub-assembly specimen selected from the typical floor. No failure was observed in the steel gusset bracket or at the RC corbels throughout the tests. Seismic performance of the prototype building was further studied using a total of 240 ground accelerations in the building response history analyses. Analytical results suggest that the effects of system's high mode vibrations are moderate. The peak horizontal tension force demand on the steel gusset bracket is found about 70% of the sum of the two maximum horizontal strength components computed from the two joining BRBs.

ARTICLE HISTORY

Received: 24 July 2019
Revised: 7 February 2020
Accepted: 7 February 2020

KEYWORDS

Buckling-restrained brace;
reinforced concrete building;
corbel;
beam-to-column joint;
nonlinear response history analysis

Copyright © 2020 by The Hong Kong Institute of Steel Construction. All rights reserved.

1. Introduction

Buckling-restrained braces (BRBs) are characterized by symmetric hysteresis behavior, high ductility, and stable energy dissipation capability [1,2], which has led to extensive research and applications in various structural systems [3]. However, the research and applications that adopt BRBs for reinforced concrete (RC) constructions appear to be rather limited and confined to the retrofitting of existing RC structures. Several methods of using BRBs to strengthen RC buildings have been proposed, such as connecting BRB end gussets to RC frame corners directly [4], positioning a braced steel frame inside the RC structure [5], and attaching a local or global bracing system to the exterior RC frame [6,7]. For new RC buildings, the connection between braces and RC members can be achieved with more choices. Steel brackets with BRB gussets have been embedded into the beam-to-column joints to brace a new RC parking structure at an airport [8]. A new building was constructed using BRBs in precast RC frames to resist lateral earthquake loads [9]. Seismic responses of a full-scale RC frame with steel cast-in anchor brackets to connect BRBs and RC members was verified through hybrid and cyclic loading tests [10]. Even though the performance of various BRB connections can be found in these reports, the detailing and construction procedures of the BRB end brackets and the RC frames are still very challenging. In addition, BRBs can develop significant axial forces, which may impose the adjacent RC members with rather complicated and unfavorable loads. They may even significantly alter the expected force distribution of the adjoining members. Furthermore, the damage to adjacent RC members during earthquakes may gradually impair the expected BRB performance.

To resolve some of the aforementioned unfavorable issues when applying BRBs in new RC constructions, a Japanese research team proposed a novel bracing system [11]. As shown in Fig. 1, the BRBs are structured continuously along the height of the braced span. Each two adjacent BRBs share the same gusset, attached immediately adjacent to the RC beam-to-column joint. In such configuration, the beams in the braced span are not used. The BRB gusset connection consists of pre-installed bolts to transmit the horizontal tensions, and two RC corbels to resist the vertical shears induced from the BRB forces. In comparison with BRB gussets installed at the frame corners, gussets in this system are affixed to the side of the beam-to-column joints, reducing the potential for unfavorable shear failure in the braced column because of the impairment of the column slenderness. Seismic performance of the innovative BRB-to-RC frame connection was verified through cyclic loading tests on four half-scale sub-assemblies [11]. Nonlinear response history analyses (NLRHA) of a 12-story building were performed to

assess the influence of the BRB connection flexibility on the dynamic response of the new bracing system [12]. The results showed that the deformations of the corbels may lead to a slight increase of the inter-story drift demands on the entire building. The tensile force demands on the BRB connections could be significantly affected by the higher mode effects of the structural system after the yielding of the braces. This might be unnoticed from a static point of view, leading to an unconservative bolt design. However, the horizontal tension force demands were not quantified in their study. In addition, the gap between the gusset bracket and the corbels had to be filled with high-strength non-shrink grout after the gusset bracket was properly fastened by the pre-stressing bolts. Thus, the corresponding side surface of the RC column must be constructed sufficiently flat and plumb.

In this study, the locations of the BRB-to-RC frame connection proposed by [11] are adopted, but the gusset-to-column connection details and the construction procedures are modified (Fig.2). This could provide an alternative in implementing connection design for the aforementioned novel bracing system. During the construction, the BRB gusset bracket is placed adjacent to the beam-to-column joint as part of the concrete formworks and connected to the beam longitudinal reinforcements through the couplers welded to the back of the gusset bracket. After the concrete hardens, the gusset bracket, the column, and the corbels are integrated together without gaps. This construction process is quite common in typical steel reinforced concrete construction. To investigate the influence of the static and dynamic responses of the structural system on the design force demands of the modified connection, a 12-story RC building was considered as a prototype (Fig. 1). NLRHA were conducted using a PISA3D [13] model and a total of 240 ground accelerations. Cyclic loading test was conducted on a beam-to-column joint sub-assembly specimen selected from the tenth floor (Fig. 2) to verify seismic performance of the proposed connection. The particular objectives of this study: (1) develop the design and construction procedures for connections of BRBs zigzag configured in RC frames; (2) conduct a proof-of-concept test for the proposed connection details; (3) investigate the seismic efficiency of BRBs in the RC structure and the higher mode effects of the structural system on RC beams adjacent to BRBs; (4) create a test setup using electro-servo hydraulic actuators to simulate the BRB force components and control the variation of the beam axial forces; and (5) inspect the effects of beam longitudinal reinforcements anchored to the gusset bracket on the beam response and the corbel shear resistance.

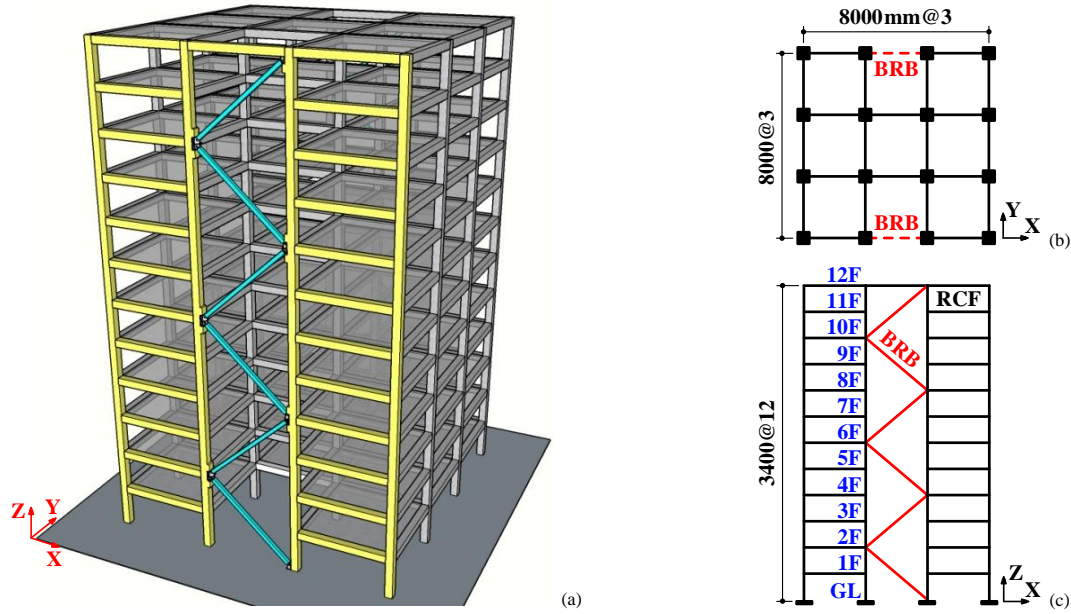


Fig. 1 (a) Structural perspective and BRB configuration, (b) structural floor plan, and (c) frame elevation in the X-direction of the prototype building

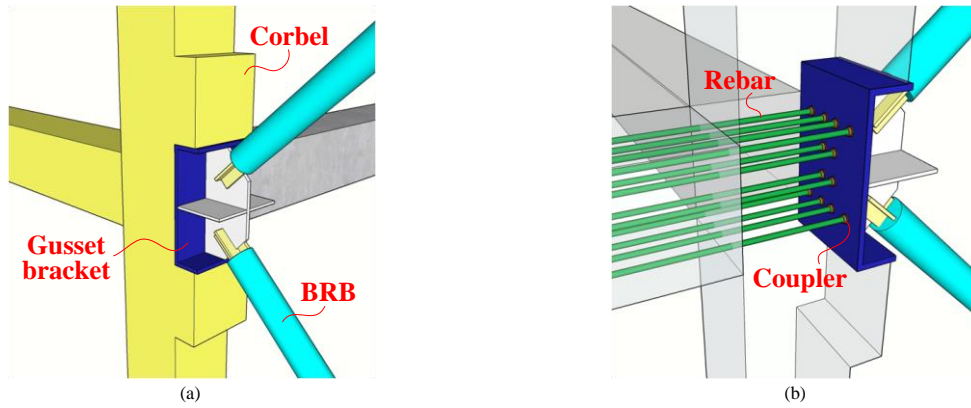


Fig. 2 Details of the (a) BRB-to-gusset bracket and (b) beam-to-gusset bracket connections

2. Design of a 12-story RC prototype building

A 12-story RC building located in Chiayi City was planned as a hospital with consideration of the typical architecture layout of new RC structures in Taiwan. As shown in Fig. 1, the structural plane was configured as an H-shape with each span of 8 m in both directions. Each story height was 3.4 m with a 150 mm thick RC floor slab. The dual structural system in the X-direction consisted of moment resisting frames and BRBs, while only moment resisting frames were adopted in the Y-direction. Instead of adopting link beams, the BRBs were configured in a zigzag in the two exterior X-directional middle bays. Each BRB was arranged to pass through two stories to diminish the effect on the lighting and a top beam was placed to increase the efficiency of the top BRB. The design concrete compressive strength was 35 MPa, and CNS SD420 steel (420 MPa as the nominal yield strength) was adopted for the reinforcements.

In comparison with the steel structure, the overall stiffness ratio of entire structural frames to BRBs in the combined system is typically higher. Thus, engineers are recommended arranging a sufficient number of BRBs to improve the lateral force resisting efficiency of BRBs in the structural system. In this case, the lateral forces for BRBs and moment frames in the two braced frames were designed to be 40% of the total X-directional stiffness, and the BRBs were designed to have 70% of the lateral forces in a single braced frame. As a result, the BRBs in the two braced spans were responsible to resist 28% of the total X-directional story shears. The BRB steel core was designed using CNS SN490B steel (325 MPa as the nominal yield strength) and the corresponding effective stiffness factor [2] was specified as 1.3. When the structural system is subjected to the higher mode effects, the two adjacent BRBs connected to the same gusset may be subjected to tension or compression forces simultaneously, leading to a significant axial force demand on the braced beam. Based on the capacity design concept, the maximum tensile (T_{max}) and compressive (C_{max}) force demands of the braced beam could be conservatively taken as the horizontal resultants induced from

the two maximum tensile and compressive strengths ($P_{T,max}$ and $P_{C,max}$) developed in the pair of BRBs, respectively. Nevertheless, local tension or compression demands arising from higher mode vibrations were found to not coincide with the peak inter-story drifts of the structural system [12]. Because of the essential difference between the force resisting capacities of the RC member in tension and compression, it appears that the tensile resistance of the braced beam should be specifically investigated. In order to avoid an over-conservative and uneconomical design, the longitudinal reinforcements in the braced beam were designed to sustain a reduced tension demand of $0.7T_{max}$. The adopted force factor of 0.7 was based on the NLRHA results of the structural system as illustrated later in this paper.

The commercial software SAP2000 [14] was adopted for the structural design and elastic analysis of the prototype building. The RC beams and columns were modeled by line elements, and the beam and column ends were specified with full rigid end zones. The flexural rigidity for all RC members was specified as 70% of the product of the modulus of elasticity of the concrete and the gross moment inertia. The BRBs were represented by truss elements. A short rigid beam was established to link the BRB work point on the column surface and the beam-column intersection (Fig. 3). The floor slabs were modeled using membrane elements to distribute vertical loads to beams. These membrane elements were constrained as a rigid diaphragm, but the rigid constraints at the nodes next to BRB work point nodes were released to allow variations of the braced beam axial forces. The P-Delta effects and a 5% eccentricity for the effects of accidental torsion were considered in the analysis. RC member sizes and the story weight are listed in Tables 1 and 2. The cross-sections of the braced beams were larger than those of other beams in the same level because of the significant axial force demands from the BRBs. The design capacities of the BRBs and braced beams are shown in Table 3. Factors of 1.2 for material overstrength, 1.3 for strain hardening, and 1.15 for compression strength adjustment were considered to estimate the

expected BRB maximum strengths ($P_{T,max}$ and $P_{C,max}$). The structural design results complied with the requirements for beam and column moment, beam-to-column joint shear capacities, and strong column-weak beam in the model seismic building codes [15]. The modal analysis results indicated that the first, second, and third mode vibration periods were respectively 1.37 (Y-directional translation), 1.28 (X-directional translation), and 1.08 seconds (torsion).

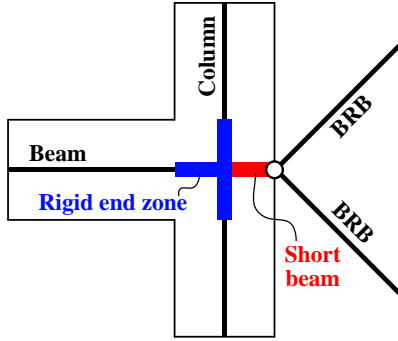


Fig. 3 Analytical model for the beam-to-column joint

Table 1
Floor weights and RC member sizes in the Y-direction

Story	Weight (kN)	Weight per unit area (kN/m ²)	Column section			Beam section		
			<i>b</i> (mm)	<i>h</i> (mm)	ρ (%)	<i>b</i> (mm)	<i>h</i> (mm)	ρ (%)
12F	4573	10.21	600	600	2.25	500	600	1.69
11F	4719	10.53						
10F	4748	10.60						
9F	4719	10.53						
8F	5276	11.78						
7F	5420	12.10	800	800	2.54	500	800	2.04
6F	5545	12.38						
5F	5512	12.30						
4F	5545	12.38						
3F	5512	12.30						
2F	5599	12.50	900	900	2.81			
1F	5708	12.74						
Base	560	11.80						

Note: *b* and *h* are the RC member width and depth, respectively; ρ is the steel ratio.

Table 2
RC member sizes in the X-direction

Story	Column section			Beam section			Braced beam section		
	<i>b</i> (mm)	<i>h</i> (mm)	ρ (%)	<i>b</i> (mm)	<i>h</i> (mm)	ρ (%)	<i>b</i> (mm)	<i>h</i> (mm)	ρ (%)
12F	600	600	2.25	400	600	2.11	500	600	2.03
11F							—	—	—
10F							500	600	2.03
9F							600	700	2.33
8F							600	700	2.33
7F	800	800	2.54	500	700	1.74	600	700	2.71
6F							600	700	2.71
5F							600	700	2.71
4F							600	700	2.71
3F							600	700	2.71
2F	900	900	2.81				—	—	—
1F							—	—	—

Table 3
Design capacities of the BRBs and the braced RC beams

Story	BRB			Braced RC beam		
	A_c (mm ²)	P_y (kN)	$P_{T,max}$ (kN)	$P_{C,max}$ (kN)	$0.7T_{max}$ (kN)	$0.7T_{max}/A_sF_{yn}$
12F	900	293	456	525	—	—
11F					1176	0.47
10F	3600	1170	1825	2099	1986	0.49
9F					2718	0.68
8F	4000	1300	2028	2332	4286	0.91
7F					4286	0.91
6F	6400	2080	3245	3732	—	—
5F					—	—
4F	10000	3250	5070	5831	—	—
3F					—	—
2F	6400	2080	3245	3732	—	—
1F					—	—

Note: A_s and F_{yn} are the total cross-sectional area and nominal yield strength of the reinforcement, respectively.

3. Test program

3.1 Subassembly Specimen

The sub-assembly specimen included a pair of RC corbels and a BRB gusset bracket. It had a 2470-mm-span beam and a column extending 1800-mm high and 2010-mm high, respectively, above and below the joint. The reinforcement layout and detailed dimensions of the specimen are illustrated in Fig. 4. The beam cross section was 500×600 mm and reinforced with 8-D25 longitudinal bars, while the column cross section was 600×600 mm and reinforced with 16-D25 longitudinal bars. The column hoops and beam stirrups were D13 and D10 bars, respectively, spaced at 100 mm on centers in the plastic hinge zones, which increased to 150 mm outside the plastic hinge zones. Table 4 summarizes the averaged material strengths from the material tests.

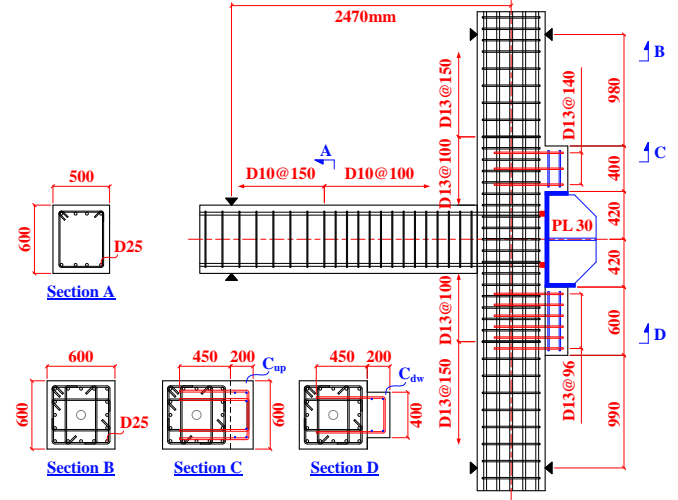


Fig. 4 Dimensions and reinforcement layout of the specimen

Table 4
Material test results

Material	F_{yn} (MPa)	F_y (MPa)	F_u (MPa)	f_c (MPa)
Longitudinal rebar, D25 (SD420)	—	454	669	—
Column and corbel stirrup, D13 (SD420)	420	451	686	—
Beam stirrup, D10 (SD420)	—	437	663	—
Gusset and bracket plate (A572 GR50)	350	370	498	—
Concrete	—	—	—	47

Note: F_y and F_u are the steel yield strength and tensile strength, respectively; f_c is the concrete compressive strength on the day of testing.

3.1.1 Design of gusset bracket

In a traditional buckling-restrained braced frame, the BRB corner gusset is subjected to not only brace forces but also frame actions, which may lead to the premature failure of gusset connections and the impairment of the seismic performance of the system. In the proposed bracing system, there is no beam in the braced span. The gusset bracket connected with the two adjacent BRBs is attached to the side surface of the beam-to-column joint, thus preventing the frame action on the gusset. The gusset bracket is composed of a gusset plate joined to the BRBs and a U-shaped steel connected to the RC frame. It is designed as a force-controlled element to remain essentially elastic when the BRBs reach their expected maximum capacities. ASTM A572 GR50 steel (350 MPa as the nominal yield strength) was adopted for the gusset bracket of the specimen. The gusset plate was detailed on the basis of the BRB ends with the welded end-slot connection [2]. The design limit states, including tensile yielding, compressive buckling, and block shear failure [16], were considered to resist the design force demands. Welding between the gusset plate and the U-shaped steel was designed to transfer the vertical resultant V_{max} from the two adjacent BRBs to the RC corbels and transfer the horizontal resultant of $0.7T_{max}$ to the longitudinal reinforcements of the braced RC beam. Dimensions of the gusset bracket specimen are shown in Fig. 4. Instead of applying two physical BRB members, four electro-servo hydraulic actuators were used to simulate the horizontal and vertical resultants developed from the BRBs. Thus, to transfer the gusset normal forces from a pair of actuators, a transfer plate was welded onto the gusset free edge of the gusset and U-shaped steel bracket assembly. The U-shaped steel end plate was also extended outward and properly stiffened, as shown in Fig. 5, to attach another pair of actuators for applying the corbel shear.

3.1.2 Design of corbel

The RC corbels in the structural system are also considered as the force-controlled element, which are expected to resist the vertical shear demand of V_{\max} coming from the gusset bracket. When the two adjacent BRBs reached their maximum capacities $P_{T,\max}$ and $P_{C,\max}$ (Table 3), the calculated shear demands of the corbels above and below the specimen gusset bracket were 1729 and 1590 kN, respectively. In the proposed connection, however, the gusset bracket is connected to the beam longitudinal reinforcements via the couplers. The beam longitudinal reinforcements can resist the horizontal tension from the BRBs directly and provide vertical shear resistance indirectly. Thus, the shear demands on the pair of corbels are reduced. To prevent an excessively conservative design result, the target shear capacities of the upper (C_{up}) and lower (C_{dw}) corbels were designed as 60% and 70% of the above-mentioned shear demands, respectively. As shown in Table 5 and Fig. 4, the depths (H) of corbels C_{up} and C_{dw} were 400 and 600 mm, while their widths (B) were 600 and 400 mm, respectively. The lengths (L) of both corbels were 200 mm, and the length-to-depth ratios L/H were 0.5 and 0.33, respectively. Corbel C_{up} was reinforced by 140 mm spaced D13 U-shaped double stirrups, while Corbel C_{dw} was reinforced by 96 mm spaced D13 U-shaped single stirrups. The corbel stirrups were 450 mm embedded into the column surface and were secured by framing bars.

The shear resisting capacity V_u of the corbels was assessed considering the modified strut-and-tie model [17]:

$$V_u = \sigma_d B l \cos \theta \quad (1)$$

where σ_d , θ , and l are the softened compressive strength, inclination, and depth of the concrete strut, respectively.

$$\sigma_d = \begin{cases} \frac{0.9 f_c}{\sqrt{1 + 400 f_{ct} / E_c}} & \text{for } f_c < 42 \text{ MPa} \\ \frac{5.8 \sqrt{f_c}}{\sqrt{1 + 400 f_{ct} / E_c}} & \text{for } f_c \geq 42 \text{ MPa} \end{cases} \quad (2)$$

$$l = kd = \left(\sqrt{(n \rho_s)^2 + 2n \rho_s} - n \rho_s \right) d \quad (3)$$

$$\theta = 2 \tan^{-1} \left(\frac{-1 + \sqrt{(a/d)^2 + (1+k^2/4)}}{a/d - k/2} \right) \quad (4)$$

where f_{ct} is the concrete tensile strength; $n = E_s / E_c$ is the ratio of steel to concrete elastic moduli; d and ρ_s are the corbel effective depth and primary stirrups ratio, respectively; and a is the applied force center-to-column surface distance. According to the assumption of the stirrup stress distribution along the corbel depth in this approach, the effective depth of the tie and the effective stirrup ratio can be calculated as follows:

$$d = \frac{2}{3} H \quad (5)$$

$$\rho_s = 0.5 \frac{n_{leg} A_{s1}}{Bd} \quad (6)$$

where n_{leg} and A_{s1} are the number of stirrup legs and the cross-sectional area of a single stirrup leg, respectively. The concrete tensile strength f_{ct} was specified as $0.1 f_c$, while the steel and concrete moduli were assumed to be $E_s = 200$ GPa and $E_c = 4.7 \sqrt{f_c}$ (MPa) GPa. As a result, the shear resisting capacities of corbels C_{up} and C_{dw} were determined to be 1079 and 1097 kN (Table 5). On the other hand, simple design provisions based on shear friction theory are provided in ACI 318-11 to evaluate the corbel shear resistance V_n [15]:

$$V_n = A_v F_y \mu \leq (0.2 f_c A_{con}, 5.5 A_{con}) \quad (7)$$

where A_{con} is the area of concrete section resisting shear transfer; μ and A_v are the friction coefficient and the area of shear-friction reinforcement. All the U-shaped stirrups in the corbel were accounted for the area of the shear-friction reinforcement, while the friction coefficient of 1.4 was adopted for monolithically cast concrete. Consequently, the shear resistance of corbels C_{up} and C_{dw} was 877 kN, which is more conservative than the resistances evaluated using the former method.

Table 5
Corbel design results

Corbel	L (mm)	H (mm)	B (mm)	a (mm)	n_{leg} (mm)	k	ρ_s (%)	θ	V_u (kN)
C_{up}	200	400	600	50	12	0.23	0.48	17°	1079
C_{dw}	200	600	400	50	12	0.23	0.48	14°	1097

3.2 Test Setup and Loading Procedure

As shown in Figs. 4 and 5, the sub-assembly specimen was rotated 90° to have corbels C_{up} and C_{dw} located at the north and south sides, respectively. Two assumed inflection points of the column were constrained using steel fixtures to simulate the north and south ends as a pin and a roller supports, respectively. The column was compressed to 700 kN using a post-tensioned rod through the column center to simulate the gravity load effect. The displacement-controlled horizontal actuator (BD) was connected to the beam end to simulate the equivalent inter-story drifts when the structural frame was subjected to lateral loads. The corbel shear resulting from the vertical resultant of the two BRBs was imposed to the specimen using two horizontal force-controlled actuators connected to the east and west sides of the gusset bracket (V1 and V2). A stiffened steel transfer beam, attached to the transfer plate on the gusset free edge, was connected with two vertical actuators installed on the strong floor (H1 and H2) to impose the horizontal resultant of the BRBs. Another steel transfer beam, attached to the cantilever beam end, was connected with two other vertical actuators (BA1 and BA2) to allow the imposition of axial force variations to the RC beam through the above-mentioned transfer beam attached to the gusset. The applied horizontal resultants of the BRBs were the sum of the forces from the four actuators, H1, BA1, BA2, and H2, while the beam axial loads were only from actuators BA1 and BA2. All actuators have a push or pull force capacity of 980 kN. The test setup adopted by Qu *et al.* [11] included the BRB members, which is trusted to be the state-of-the-art approach for evaluation of BRB connections. Test results confirmed that the gusset connection in the novel bracing system performed well despite the BRB end rotational demands induced by the beam-to-column joint translation and rotation. It is judged that the rotational demands imposed from the BRB end gussets on the proposed connection are less critical in the current study as the gusset bracket is fully anchored into the RC beam-to-column joint using beam longitudinal reinforcements. The flexural capacity of the BRB core can be conveniently computed and incorporated into the beam reinforcement design to resist the additional force from such rotational demand. Thus, in order to simplify the test setup, only shear and tension are imposed on the proposed connection without rotations.

The 12-story prototype building was analyzed using a detailed PISA3D model with the specified elements and material properties described in the next section. A cyclic loading analysis was conducted on the PISA3D building model by applying three cycles to each with roof or story drift ratios of 0.2%, 0.25%, 0.35%, 0.5%, 0.75%, 1.0%, 1.4%, 1.75%, 2.2%, 2.75%, and 3.5% in sequence, as prescribed in ACI 374.1-05 [18]. Using the aforementioned seven actuators, the sequence of the loading amplitudes for the sub-assembly specimen was based on the PISA3D analytical results to impose cyclic drifts to the cantilever beam end, the corresponding BRB force resultants, and the beam axial forces on the beam-to-column joint. As shown in Figs. 1(c) and 5, loadings toward the X-direction of the structural frame, the north, and the upward directions of the specimen were taken to be positive.

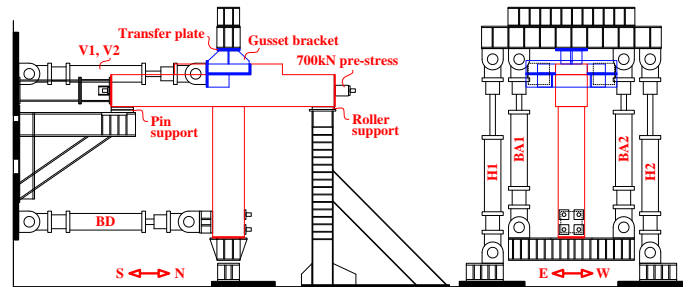


Fig. 5 Test setup

4. Experimental results and discussion

4.1 RC Member Response

During the loadings with 0.5% drift ratio, the beam and column elements remained essentially elastic as expected and no evident crack was observed on the sub-assembly. The free body diagram of the specimen is depicted in Fig.

6. The work point of the two BRBs was set at the column surface rather than the column centerline. Therefore, the vertical resultant V_{BRB} from the gusset bracket provided a moment demand of $V_{BRB} \times h/2$ on the column. Although the arm was short, significant forces in the BRBs were able to make the resultant moment contribution comparable to that of the eliminated beam. This moment demand on the column must be considered. The total column moment resistance $V_{c1} \times H_1 + V_{c2} \times H_2$ in the sub-assembly was obtained by combining the contribution of the beam moment $V_b \times L_b$ (L_b is measured from the cantilever load to the column centerline) and that of the BRBs $V_{BRB} \times h/2$. As shown in Fig. 7(a), the maximum moment contribution of the BRBs was about half that of the beam and about one-third of the total moment resistance of the specimen. Fig. 7(b) compares the test results with the P-M curves computed from the beam section analysis; the beam moment responses agreed with the predicted yielding surface. When the frame roof drift was positive, the corresponding beam end deformation of the specimen was negative, and the beam was compressed by the BRB horizontal resultant. Both analytical and experimental results indicated that the beam moment resistance in compression was larger than that in tension. Specimen damage conditions (Fig. 8) at the end of the test revealed that concrete spalling occurred at the beam fixed end, which is in compliance with the strong column-weak beam design principle. The flexural-shear cracks of the column appeared only within the range between the two corbels. Thus, it appears from the beam P-M responses that the flexural behavior of the beam was not evidently

influenced despite its longitudinal reinforcements are connected to the gusset bracket.

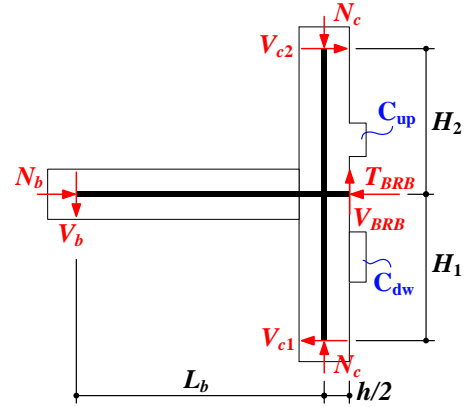


Fig. 6 Free body diagram of the sub-assembly specimen

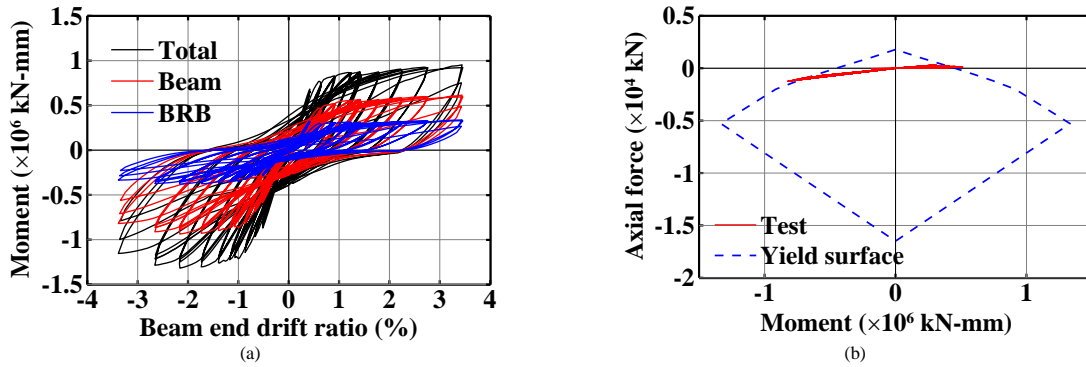


Fig. 7 (a) Bending moment components in the sub-assembly specimen and (b) comparison of the experimental beam axial force versus moment relationships with the P-M yield surface

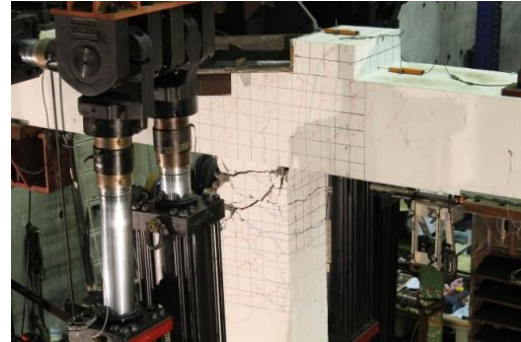
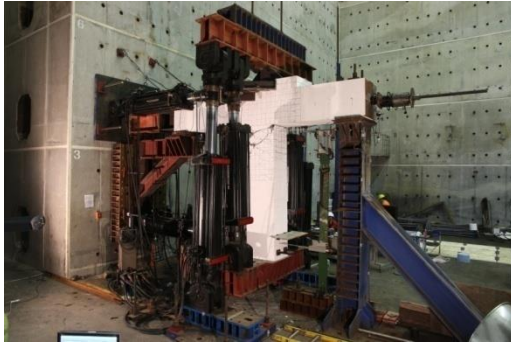


Fig. 8 Damage condition of specimen at the end of testing

4.2 Gusset Bracket and Corbel Response

The gusset bracket remained elastic and worked rather well throughout the entire test. The gusset bracket force versus displacement relationships in the direction normal to the column surface are shown in Fig. 9(a). The maximum displacement measured was less than 0.5 mm, which was small enough to be ignored. When the gusset bracket was compressed, the measured small positive normal displacements, shown in Fig. 9(a), were most likely caused by the slip of the measurement gauges or the local elastic deformation of the gusset bracket. Cyclic upward pull tests on the gusset bracket were continued after the prescribed cyclic loading test on the sub-assembly. At the end of test, the maximum tensile force sustained by the gusset bracket was about 1800 kN without nonlinear behavior observed. Corbel shear versus deformation relationships for C_{up} and C_{dw} are shown in Fig. 9(b). During the

entire tests, there was almost no crack found on the two corbels and only slight crush of the concrete was observed at the corbel edges due to bearing pressure from the gusset bracket. After the cyclic loading test, both corbels were monotonically pushed until the actuators reached their maximum capacities. No evident damage to the two corbels was observed before the end of testing. This could be attributed to the fact that the gusset bracket was cast with the column and corbels at the same time, there is no gap or non-shrink grout between the steel bracket and concrete surface. The behavior of the corbels was not affected by the deformation and flexural-shear cracks in the column adjacent to the corbels and in the panel zone. Test results confirm that the two corbels can carry much more shear resistance than the expected design capacity. It appears that the beam longitudinal reinforcements anchored on the back of the gusset bracket had provided a significant additional shear friction resistance.

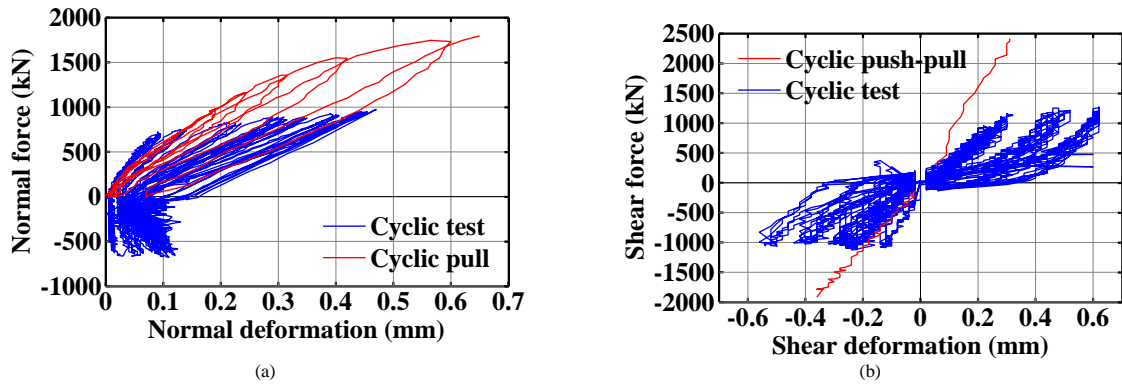


Fig. 9 (a) Gusset bracket normal force versus displacement relationships and (b) corbel shear versus deformation relationships

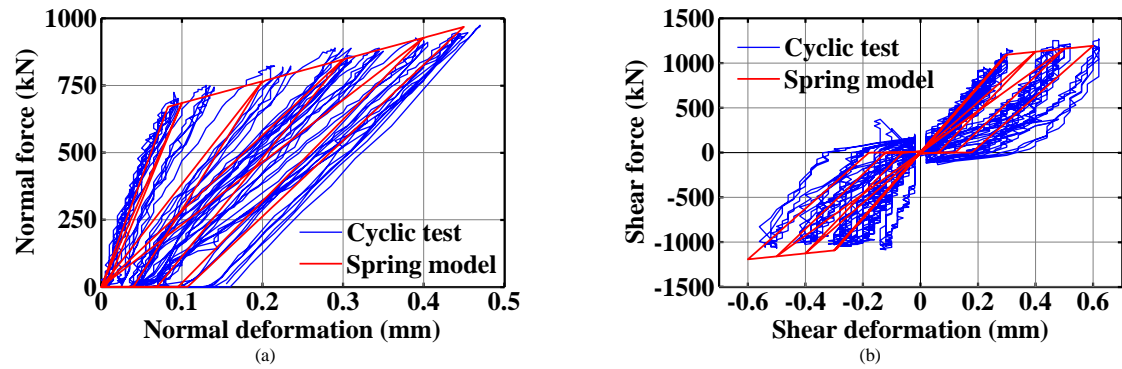


Fig. 10 Spring models for (a) the gusset bracket and (b) the corbels

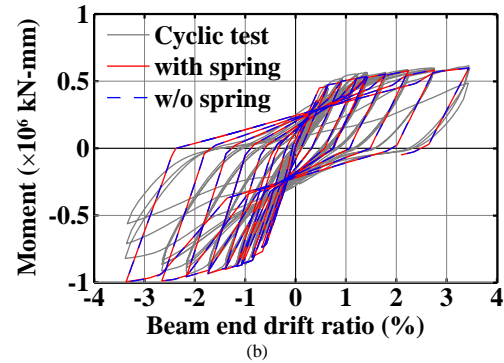
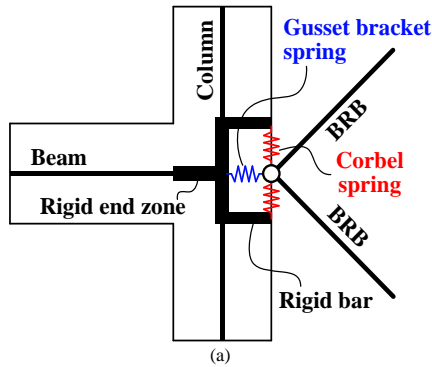


Fig. 11 (a) Equivalent springs for the proposed BRB connection and (b) experimental and analytical results of the specimen

4.3 Numerical Modeling of the Connection between the BRB and RC Frame

The effectiveness of BRB-to-RC frame connections is critical to the seismic performance developed from the BRBs during earthquakes. In this section, the force-deformation behavior of the gusset bracket and corbels is simulated using equivalent spring models to investigate the effects of connection flexibility on seismic responses of the entire system. The built-in degrading material in PISA3D was adopted for the equivalent spring to simulate the stiffness degradation and residual deformation of the gusset bracket tension behavior (Fig. 10(a)). This degrading material was also adopted to model the shear responses of corbels (Fig. 10(b)). A detailed PISA3D analytical model of the sub-assembly specimen, as shown in Fig. 11(a), was then constructed with and without the above-mentioned equivalent springs placed at the BRB work point. The adopted elements and material properties will be described in the next section. The boundary conditions and loading procedures in the analytical model were arranged in accordance with the test setup. Analytical results shown in Fig. 11(b) indicate that both PISA3D models with and without the equivalent springs capture the specimen behavior satisfactorily. The minor differences between the responses of the two models confirm that the proposed connection effectively suppress the unfavorable influence of the connection flexibility on the system behavior.

5. Analytical investigation of the prototype

The composite sections of RC members were simulated using fiber beam-column elements. Reinforcing bars were modelled using the three-parameter degrading material to simulate the concrete bond slip and pinching behavior of the hysteresis loop, as shown in Fig. 12. The Popovics [19] and Karsan-Jirsa [20] models were adopted to define the concrete compressive stress-strain response envelope and the degrading linear unloading/reloading stiffness, respectively. BRBs were represented by truss elements and defined as a hardening material, which takes the combined effects of the isotropic and kinematic hardening into account [2]. The BRB work points, the arrangements for the rigid ends at the beam-to-column joints, the concrete floor slab elements, and the constraint conditions in the PISA3D model were the same as those in the above-mentioned SAP2000 model. As illustrated previously, it is verified that the proposed connection deformation responses due to the gusset bracket normal force and corbel shear are small enough to be neglected. Thus, the equivalent springs representing the connection behavior were excluded in the analytical model to improve the computational efficiency. The dynamic analyses were conducted using a total of 240 earthquake records [21] with 80 for each of the service-level earthquake (SLE), design-basis earthquake (DBE), and maximum-considered earthquake (MCE) levels. These ground motions, including near-fault events, were normalized according to the estimated fundamental period of the building and the design response spectrum for Chiayi City (Fig. 13).

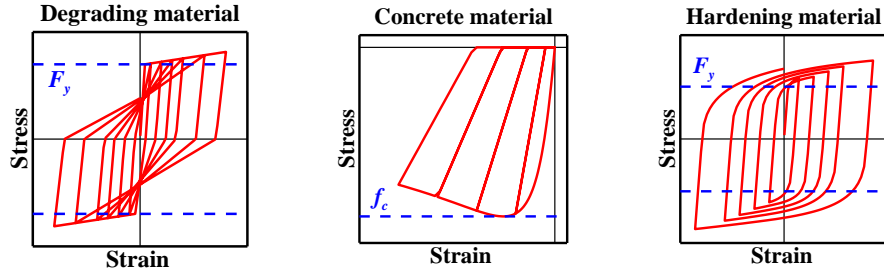


Fig. 12 Material properties for the PISA3D model

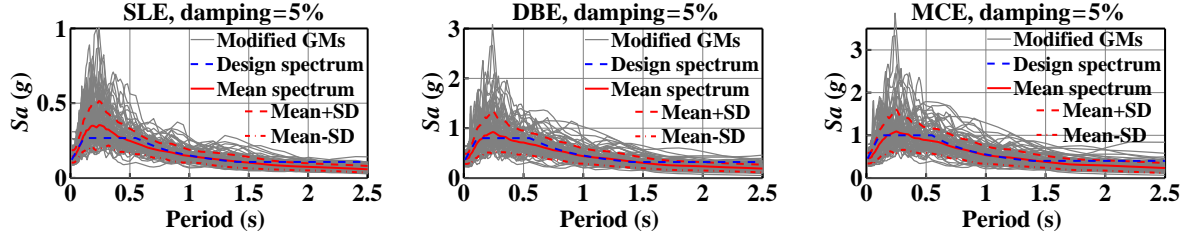


Fig. 13 Modified ground motions for the three hazard levels

5.1 Overall Structural Response

Fig. 14(a) shows that the maximum inter-story drift responses under SLE, DBE, and MCE events were 0.55%, 1.82%, and 2.32%, while the averaged ratios were 0.33%, 0.9%, and 1.11%, respectively. It appears that lateral deformations of this prototype building were effectively controlled because of the BRB stiffness contribution and the design safety requirements for hospitals. The mean values of the maximum base shears (Fig. 14(b)) were 8404, 18220, and 20630 kN under SLEs, DBEs, and MCEs, respectively. In comparison with the design base shear of 7517 kN, the system overstrengths were 1.1, 2.4, and 2.7 for the three hazard levels, respectively. Fig. 15(a)

shows the maximum horizontal shears provided by the pair of bottom BRBs, which indicate that the BRBs exceeded their yield strengths under DBEs and MCEs. The maximum ratios of the total BRB shears (horizontal resultants) to their corresponding base shears, shown in Fig. 15(b), had mean values of around 19% (MCE), 21% (DBE), and 23% (SLE). Analytical results reveal that the BRBs remained elastic and the BRB shear contribution to the base shear was close to the design value of 28% during small earthquake events. During moderate and strong earthquakes, the BRBs absorbed seismic energy by yielding and the BRB shear contribution was then reduced with a rising shear contribution from the RC moment frame.

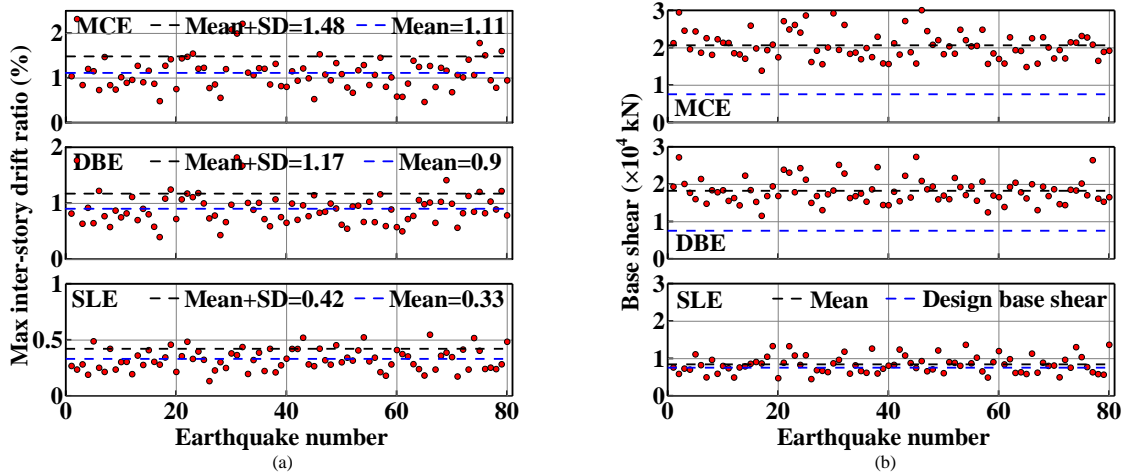


Fig. 14 Maximum (a) inter-story drift ratios and (b) base shear responses

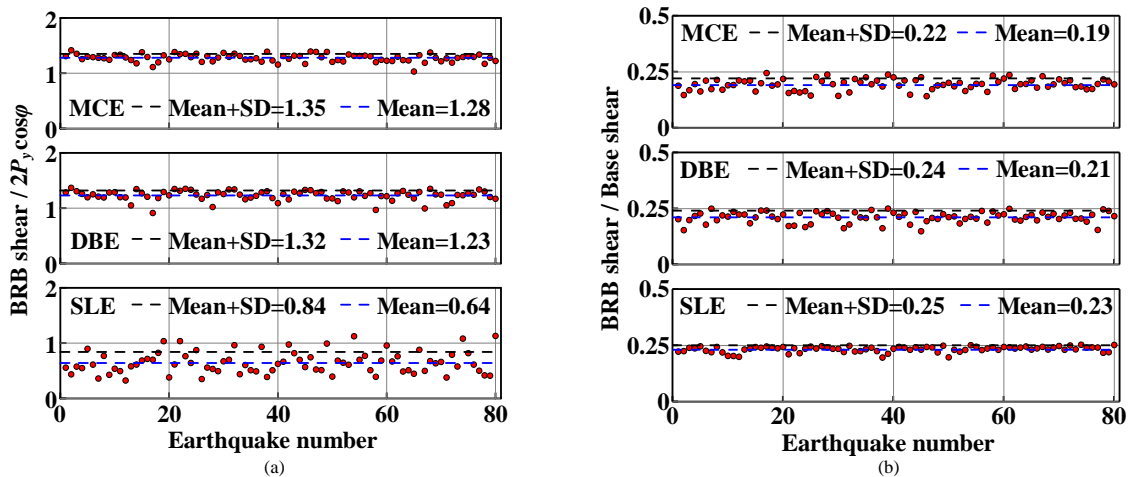


Fig. 15 Maximum BRB (a) shear responses and (b) shear contributions

5.2 BRB to RC Frame Nodal Force Response

When the structural system is subjected to the first-mode vibration, the two adjacent BRBs are subjected to tension and compression. The shear demand V_{\max} of corbels is considered as the vertical resultant induced from the BRB maximum strengths $P_{T,\max}$ and $P_{C,\max}$. The dynamic analyses shown in Fig. 16(a) indicate that the maximum vertical resultant V_{BRB} reached $0.96V_{\max}$ during MCEs as expected. Without considering the higher modes of

the system, the horizontal components of the two adjacent BRBs counteract each other and thus impose very small demands on the braced beam. However, significant horizontal resultants caused by the BRBs may arise due to the system higher mode vibrations, especially after the BRBs yield and the first mode vibration is greatly suppressed. As shown in Fig. 16(b), the maximum horizontal tension (T_{BRB}) and compression (C_{BRB}) reached $0.7T_{\max}$ and $0.68C_{\max}$ during MCE events, respectively.

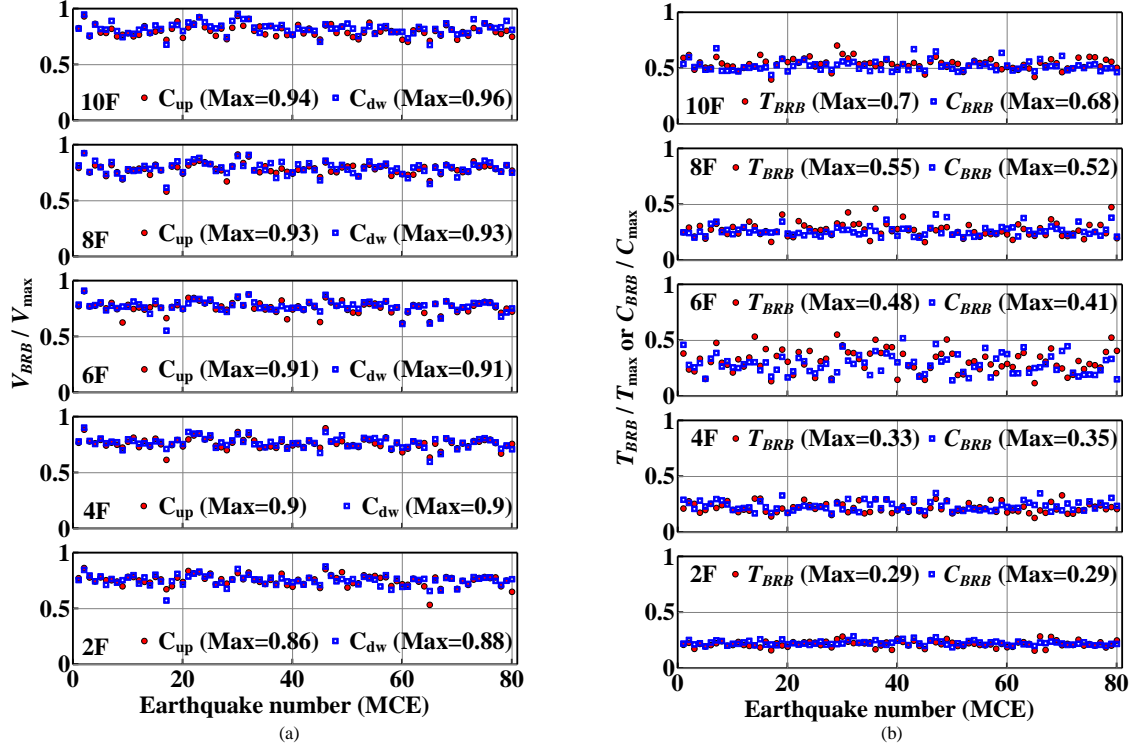


Fig. 16 Maximum BRB (a) vertical and (b) horizontal resultants

5.3 Braced Beam Response

In this section, the analytical results of the ground acceleration MCE No. 2 with the maximum inter-story drift response among the 80 sets of analyses (Fig. 14(a)) are selected to illustrate the braced beam's seismic response. The beam axial force versus moment response for the tenth floor braced beam (Fig. 17) was satisfactorily bounded by the calculated yield surface, showing the accuracy of the PISA3D fiber beam-column elements in the simulation of the RC member's P-M interactions. The time histories of the BRB horizontal resultant and the braced beam axial force at the tenth floor joint are compared in Fig. 18(a). When the BRB horizontal resultants were toward the braced beam as negative values in the plot, the BRB nodal forces could be transferred into the braced beam directly. However, when the BRB horizontal resultants were outward, the nodal forces could not be balanced by the braced beam tensile forces and the margins must be transmitted into the column shears. The analytical results, using the same ground motion of MCE No. 2 but applied in the reversed direction, are shown in Fig. 18(b). The seismic peak response of the BRB horizontal resultant and the braced beam axial force were somewhat different than those computed from the same ground motion

imposed in the opposite direction. This is because the RC beam axial stiffness under tension is smaller than that under compression.

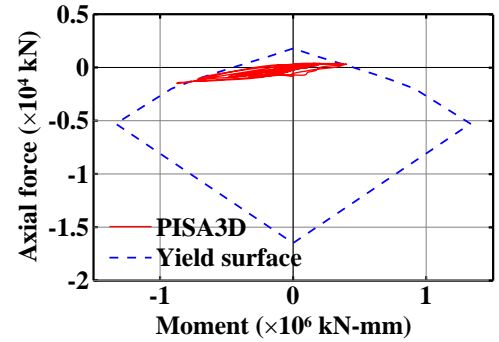


Fig. 17 Beam moment responses at the tenth floor beam-to-column joint

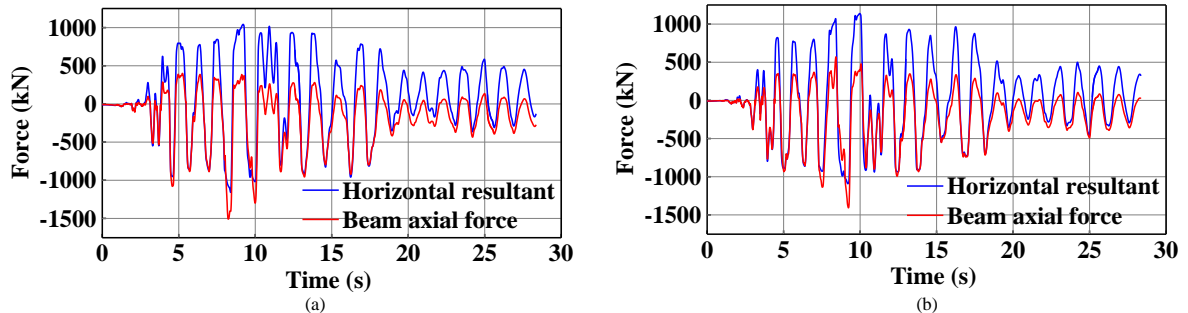


Fig. 18 Time histories of BRB horizontal resultants and braced beam axial forces under (a) MCE No. 2 and (b) reversed MCE No. 2 ground motions

6. Conclusions

1. This proof-of-concept test confirms the feasibility of the proposed system for practical applications. Test results indicate that the beam moment resistances were in compliance with the predicted yield surface. No evident damage to the two corbels was observed before the end of testing. This could be attributed to the fact that the gusset bracket was cast with the column and corbels at the same time, there is no gap or non-shrike grout between the steel bracket and concrete surface.

2. The design shear capacity computed using ACI specifications for the proposed connection corbels is very conservative. It is confirmed that the beam longitudinal reinforcements anchored on the gusset bracket can provide a significant additional shear friction resistance. Test results indicate that the proposed gusset anchor details can lead to a much stronger connection than that tested by others. However, RC corbels may fail in a very brittle manner under shear. It is recommended that the corbel shear resistance be at least computed from the modified strut-and-tie model to ensure an effective connection between the BRB and RC frame.

3. NLRHA results of the prototype building show that the maximum ratios of the total BRB shear to base shear are 23%, 21%, and 19% in the SLE,

DBE, and MCE events, respectively. BRBs remain elastic during the SLEs and go into the inelastic range to dissipate seismic energy under the DBEs and MCEs as expected.

4. NLRHA results suggest that the horizontal tension demand of the proposed gusset connection due to the system higher mode vibrations can be taken as 70% of the maximum tensile strengths ($0.7T_{max}$) of the two adjacent BRBs. However, for the design of higher or more irregular buildings than the proposed prototype, it is recommended that the effects of the system dynamic responses on the BRB connections be evaluated specifically.

5. Significant horizontal force demands could occur on the BRB connection at the top and bottom stories, or when the two adjacent BRBs have notably different strengths. In addition, for BRBs connected to the top and bottom beams or columns without using corbels, the shear failure of the RC discontinuity regions due to the concentrated loads from the BRB must be prevented.

6. Imposing the same ground motions in two opposite directions, the magnitudes of the peak BRB horizontal resultant and the braced beam axial force responses were different. This is because the RC beam axial stiffness under tension is smaller than that under compression.

References

- [1] Wada A. and Nakashima M., "From infancy to maturity of buckling restrained braces research", Proceedings of the 13th World Conference on Earthquake Engineering, Vancouver, B.C., Canada, 2004.
- [2] Tsai K.C., Wu A.C., Wei, C.Y., Lin P.C., Chuang M.C. and Yu Y.J., "Welded end-slot connection and debonding layers for buckling-restrained braces", *Earthquake Engineering & Structural Dynamics*, 43(12), 1785-807, 2014.
- [3] Takeuchi T. and Wada A., "Buckling-Restrained Braces and Applications", The Japan Society of Seismic Isolation, 2017.
- [4] Mahrenholtz C., Lin P.C., Wu A.C., Tsai K.C., Hwang S.J., Lin R.Y. and Bhayusukma M.Y., "Retrofit of reinforced concrete frames with buckling-restrained braces", *Earthquake Engineering & Structural Dynamics*, 44(1), 59-78, 2015.
- [5] Pan K.Y., Wu A.C., Tsai K.C., Li C.H. and Khoo H.H., "Seismic retrofit of reinforced concrete frames using buckling-restrained braces with bearing block load transfer mechanism", *Earthquake Engineering & Structural Dynamics*, 45(14), 2303-2326, 2016.
- [6] Takeuchi T., Yasuda K. and Iwata M., "Studies on Integrated building facade engineering with high-performance structural elements", Proceedings of International Association for Bridge and Structural Engineering Symposium, Budapest, Hungary, 2006.
- [7] Robinson K., "Novel uses for the buckling restrained brace", *Structure Magazine*, August, 2012.
- [8] Richards J., "\$48.5 million parking structure at John Wayne Airport is braced for the future", *Airport Improvement Magazine*, March-April, 2011.
- [9] Viano J.D. and Schaeffer T.C., "Novel use of buckling-restrained braces in precast concrete frames", *PCI Journal*, 62(5), 28-34, 2017.
- [10] Wu A.C., Tsai K.C., Yang H.H., Huang J.L., Li C.H., Wang K.J. and Khoo H.H., "Hybrid experimental performance of a full-scale two-story buckling-restrained braced RC frame", *Earthquake Engineering & Structural Dynamics*, 46(8), 1223-1244, 2017.
- [11] Qu Z., Kishiki S., Sakata H., Wada A. and Maida Y., "Subassemblage cyclic loading test of RC frame with buckling restrained braces in zigzag configuration", *Earthquake Engineering & Structural Dynamics*, 42(7), 1087-102, 2013.
- [12] Qu Z., Kishiki S., Maida Y., Sakata H. and Wada A., "Seismic responses of reinforced concrete frames with buckling restrained braces in zigzag configuration", *Engineering Structures*, 105, 12-21, 2015.
- [13] Lin B.Z., Chuang M.C. and Tsai K.C., "Object-oriented development and application of a nonlinear structural analysis framework", *Advances in Engineering Software*, 40(1), 66-82, 2009.
- [14] Computers and Structures, Inc. <https://www.csiamerica.com/products/sap2000>.
- [15] ACI, Building code requirements for structural concrete and commentary (ACI 318-11), American Concrete Institute, Farmington Hills, Michigan, 2011.
- [16] Chuang M.C., Tsai K.C., Lin P.C. and Wu A.C., "Critical limit states in seismic buckling-restrained brace and connection designs", *Earthquake Engineering & Structural Dynamics*, 44(10), 1559-1579, 2015.
- [17] Qu Z., Maida Y., Kishiki S. and Sakata H., "Shear resistance of reinforced concrete corbels for shear keys", Proceedings of the 9th International Conference on Urban Earthquake Engineering and 4th Asia Conference on Earthquake Engineering, Tokyo, Japan, 2012.
- [18] ACI, Acceptance criteria for moment frames based on structural testing and commentary (ACI 374.1-05), American Concrete Institute, Farmington Hills, Michigan, 2005.
- [19] Popovics S., "A numerical approach to the complete stress-strain curve of concrete", *Cement and Concrete Research*, 3(5), 583-599, 1973.
- [20] Karsan I.D. and Jirsa J.O., "Behavior of concrete under compressive loadings", *Journal of the Structural Division*, 95, 2543-2563, 1969.
- [21] Baker J.W., Lin T., Shahi S.K. and Jayaram N., New ground motion selection procedures and selected motions for the PEER transportation research program, Pacific Earthquake Engineering Research Center, Berkeley, California, 2011.